Universidad de Valladolid

Escuela de Doctorado Universidad de Valladolid

PROGRAMA DE DOCTORADO EN FÍSICA

FACULTAD DE CIENCIAS DEPARTAMENTO DE FÍSICA TEÓRICA, ATÓMICA Y ÓPTICA

TESIS DOCTORAL:

Desarrollo de nuevos métodos y herramientas para la caracterización avanzada de aerosoles atmosféricos a partir de medidas de teledetección.

Development of new methods and tools for advanced characterization of the atmospheric aerosol based on remote sensing measurements

Presentada por David Fuertes Cocho para optar al grado de doctor por la Universidad de Valladolid

Dirigida por:
Dr. Carlos Toledano
Dr. Benjamín Torres

Tutor Internacional:
Oleg Dubovik

Este trabajo ha sido realizado en el

Grupo de Óptica Atmosférica de la Universidad de Valladolid

Certificado

Dr. Carlos Toledano Olmeda, profesor contratado doctor del departamento de Física Teórica, Atómica y Óptica de la Universidad de Valladolid, como Tutor y Director del presente trabajo, y el Dr. Benjamin Torres Rodríguez, profesor asociado de la Universidad de Lille, como Director del presente trabajo

CERTIFICAN:

Que la memoria titulada: “Desarrollo de nuevos métodos y herramientas para la caracterización avanzada de aerosoles atmosféricos a partir de medidas de teledetección”, presentada por Don David Fuertes Cocho para optar al grado de Doctora en Física por la Universidad de Valladolid, ha sido realizada bajo nuestra dirección en el Departamento de Física Teórica, Atómica y Óptica de la Universidad de Valladolid.

Y para que conste, y en cumplimiento de la legislación vigente, firmamos el presente certificado en Valladolid, a 1 de Junio de 2018.

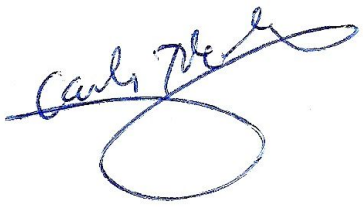

Fdo.: Dr. Carlos Toledano Olmeda Fdo.: Dr. Benjamín Torres Rodríguez

Agradecimientos

A todos los que están, estuvieron y estarán.

Especialmente a los que cumplen las tres condiciones.

Acknowledgments

To those who were, are and will be.

Especially to those that fulfill all three cases.

Índice

Publicaciones

Compendio de artículos de la tesis doctoral

1. David Fuertes, Carlos Toledano, Ramiro González, Alberto Berjón, Benjamín Torres, Victoria Eugenia Cachorro and Ángel Máximo de Frutos: CÆLIS: Software for assimilation, management and processing data of an atmospheric measurement network, Geosci. Instrum. Method. Data Syst., 7, 67-81, 2018. doi:10.5194/gi-7-67-2018.

   Índice de impacto 1.023 (2016), 1.557 (5 años). Categoría:
   - Geosciences, multidisciplinary: 147 de 188 (Q4)
   - Meteorology & Atmospheric sciences: 69 de 85 (Q4)

2. Carlos Toledano, Ramiro González, David Fuertes, Emilio Cuevas, Thomas F. Eck, Stelios Kazadzis, Natalia Kouremeti, Julian Gröbner, Philippe Goloub, Luc Blarel, Roberto Román, África Barreto, Brent N. Holben, and Victoria E. Cachorro: Assessment of Sun photometer Langley calibration at the high-elevation sites Mauna Loa and Izaña. Atmos. Chem. Phys., accepted, 2018.

   Índice de impacto 5.318 (2016), 5.896 (5 años). Categoría:
   - Meteorology & Atmospheric sciences: 4 de 85 (Q1)

3. Benjamin Torres, Oleg Dubovik, David Fuertes, Gregory Schuster, Victoria Eugenia Cachorro, Tatsiana Lapyonok, Philippe Goloub, Luc Blarel, Africa Barreto, Marc Mallet, Carlos Toledano, and Didier Tanré: Advanced characterisation of aerosol size properties from measurements of spectral optical depth using the GRASP algorithm, Atmos. Meas. Tech., 10, 3743–3781, 2017

   Índice de impacto 3.089 (2016), 3.7 (5 años). Categoría:
   - Meteorology & Atmospheric sciences: 24 de 85 (Q2)

Resumen

Los aerosoles atmosféricos son partículas en estado sólido o líquido es supensión en la atmósfera. Estas partículas, de origen natural o antropogénico, afectan al clima, a la actividad humana y a la salud. Es por ello que la monitorización y evaluación de los aerosoles es de suma importancia dentro de los estudios atmosféricos. En las últimas décadas distintas iniciativas tratan de obtener más y mejores datos para la caracterización de los aerosoles. Las redes en tierra son capaces de obtener sus propiedades con gran calidad, mientras que diferentes misiones satelitales son capaces de tomar grandes volúmenes de datos con una excelente cobertura espacial. A partir de las medidas y mediante la aplicación de complejos algoritmos se pueden obtener las propiedades ópticas y microfísicas de los aerosoles. GRASP es un reciente algoritmo de inversión que nace como una evolución del algoritmo utilizado por la red AERONET, y que puede aplicarse a diversos tipos de instrumentos (desde instrumentos de laboratorio, redes en tierra o sensores de satélites) e incluso sus sinergias (combinando las medidas de varios de ellos). Además, incluye modernas metodologías como la inversión multi-pixel, que permite añadir restricciones a priori sobre la variabilidad temporal o espacial.

En la actualidad existen numerosos retos asociados a mejorar el conocimiento de los aerosoles, desde el reto tecnológico de cómo manipular las grandes volúmenes de información generados hasta la mejora de los algoritmos existentes para su caracterización. La presente tesis trata de ahondar en el estudio y análisis de los aerosoles mediante el uso de herramientas informáticas avanzadas. Se presenta el desarrollo de CÆLIS, herramienta de gestión que permite a la red liderada por la universidad de Valladolid el control y mantenimiento de la instrumentación así como el estudio de los datos recibidos y su procesado. Esta herramienta es de gran ayuda la hora de mejorar la calidad de las medidas obtenidas por la red así como para procesar los datos con algoritmos avanzados y estudiar sus resultados. Como ejemplo de aplicación de estas técnicas se desarrolla un estudio comparativo de las estaciones de Izaña y Mauna Loa. Más de 20 años de datos de las redes AERONET y PFR-GAW en estas estaciones han sido analizados con el objetivo de comprender mejor la calidad de las estaciones y la precisión de la calibración por el método de Langley de los instrumentos de referencia. Las climatologías muestran que el AOD (500nm) promedio en Mauna Loa es de 0.016 y en Izaña es de 0.054. El análisis establece el número de días aptos para este tipo de calibraciones a lo largo del año en ambas estaciones, siguiendo los estrictos protocolos establecidos por ambas redes.

Por último, este trabajo desarrolla una aplicación específica del algoritmo GRASP: el desarrollo de una inversión para medidas de espesor óptico de aerosoles. Los resultados muestran que se pueden separar los modos fino y grueso dentro de un error menor del 1% del valor de la medida de espesor óptico. La modelización del modo fino es más precisa si se aporta información del índice de refracción real. El modo grueso es menos estable pero mejora si se aporta información extra, como el índice de refracción complejo.

Abstract

Atmospheric aerosols are liquid or solid particles suspended in the atmosphere. These particles, from natural or anthropogenic sources, affect the climate, human activities and human health. Therefore, its monitoring and analysis is of great importance in atmospheric studies. In the last decades many different initiatives attempt to obtain more and better data to be used in the aerosol characterization. Ground-based networks are able to collect high quality data, whereas satellite missions are able to provide large amounts of data, providing very good spatial coverage. From measurements and by applying complex algorithms, it is possible to retrieve optical and microphysical properties of the aerosols. GRASP is a new inversion algorithm developed as an evolution of the algorithm used by the AERONET network. This new developments include a generalization from the point of view of the instruments (it is able to retrieve data from either laboratory experiments, ground based instruments or satellite sensors), and many other novel approaches, e.g. the new multi-pixel concept which allows to add a-priori constraints about the spatial and temporal variability of the parameters.

Currently, there exist many different challenges related to the improvement of the knowledge of the aerosol, both the technological challenge of handling huge amounts of measured data and the improvement of the existing algorithms for its characterization. This PhD Thesis attempts to deepen in the study and analysis of atmospheric aerosols by the use of advanced software tools. The CÆLIS platform is described. It consists of a management tool that allows the photometer network leaded by the University of Valladolid to control and maintain the instrumentation and to process and analyze the data. This tool is helpful for checking the quality of the measurements and for processing the data with advanced algorithms. As example of application of the methodology developed with the CÆLIS system, it is developed a comparison study for the measurement sites of Izana and Mauna Loa. More than 20 years of data from AERONET and GAW-PFR networks have been analyzed with the aim of improving the understanding of the quality of the calibration of the master instruments using the Langley plot method. The climatology shows average aerosol optical depth (500nm) of 0.015 for Mauna Loa and 0.054 for Izana. The analysis shows the number of days suitable for this calibration procedure per year in both stations, following the strict protocols established by the networks

Finally, this work develops an specific application of GRASP code: inversion of aerosol optical depth measurements. The results show that from extinction measurements it is possible to split the AOD of the fine and coarse modes of the size distribution, within an error lower than 1% of the input measurements. The retrieval of the fine mode is more stable if a priori information of the real part of refractive index is available. The retrieval of the coarse mode is less stable but it significantly improves if extra a priori information is provided, i.e. complex refractive index.

1. Introducción

1.1 Los aerosoles atmosféricos

Los aerosoles atmosféricos son partículas sólidas o líquidas en suspensión en la atmósfera. El tamaño de de estas partículas va desde algunos nanómetros hasta los decenas de micrómetros. Por origen, los aerosoles se pueden clasificar en aquellos de origen natural (arena del desierto, volcanes, sal del mar, etc.) y aquellos de origen antropogénico (combustión de carbón, petróleo, emisiones industriales, etc.). Las partículas de origen antropogénico son principalmente de un tamaño inferior a un micrómetro y representan las de mayor número en la atmósfera. Por el contrario, las partículas de origen natural son generalmente de mayor tamaño (mayores que un micrómetro) y son las que mayor masa aportan. Las partículas gruesas tienen un tiempo de vida relativamente corto porque de manera general la gravedad las deposita en la superficie. Por el contrario, las partículas pequeñas son capaces de permanecer mucho más tiempo en la atmósfera.

Es bien conocido que los aerosoles atmosféricos y los gases afectan a la calidad del aire, el clima y la salud humana. El fuerte aumento de la polución observado durante las últimas décadas en determinadas regiones del planeta está ligado sin duda alguna a las actividades humanas. Es, por tanto, de crucial importancia la monitorización y evaluación de los aerosoles atmosféricos a fin de poder tomar las adecuadas decisiones políticas ligadas al consumo de energía y las actividades económicas de manera global. Sin embargo, así como a día de hoy la evaluación de la contaminación debida a gases es bien conocida y monitorizada, la caracterización de los aerosoles continúa siendo incierta y por tanto necesita de un esfuerzo extra en su estudio. Esto se debe fundamentalmente a la inhomogeneidad tanto espacial como temporal de los aerosoles, que resulta del tiempo relativamente corto en el que los aerosoles residen en la atmósfera (de días a semanas) y la mencionada variabilidad tanto en composición como en tamaño de las partículas, resultante de la amplia gama de fuentes naturales y artificiales.

Los aerosoles atmosféricos influyen de manera importante en el clima mediante su efecto en el balance radiativo. El efecto que estos provocan depende de sus propiedades (distribución de tamaños, propiedades físico-químicas y morfología). La figura 1, extraída del último informe del IPCC, ilustra los aspectos clave de la contribución de las nubes y los aerosoles al cambio climático mediante efectos directos: el forzamiento asociado a los gases de efecto invernadero y los aerosoles modifican la temperatura de la superficie a través del balance radiativo global.

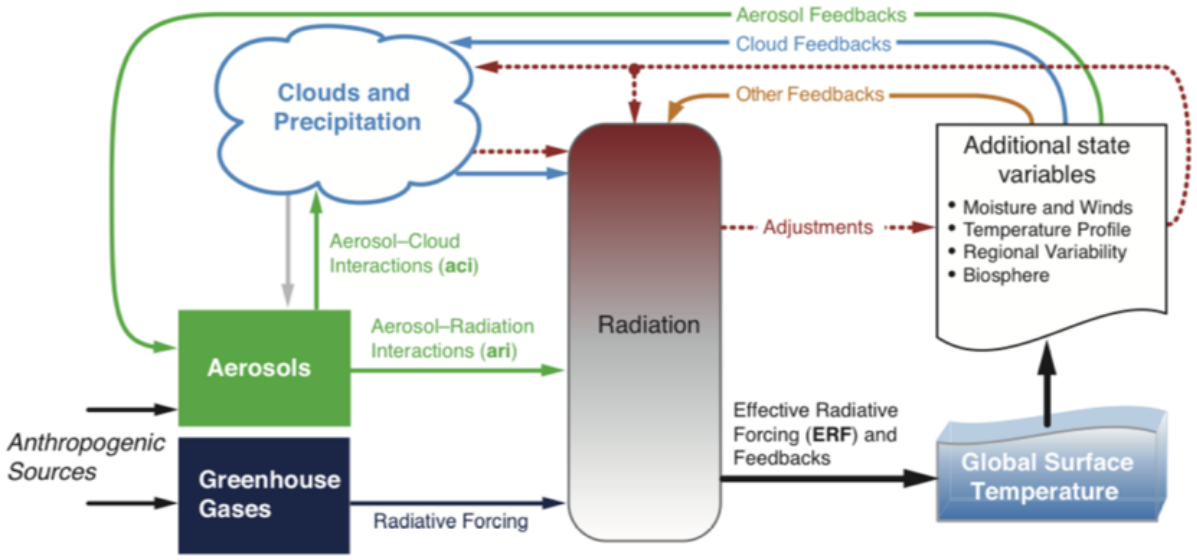

Figura 1: Descripción general de los procesos de forzamiento y retroalimentaciones de los gases de efecto invernadero, los aerosoles y las nubes. Los agentes del forzamiento están representados en las cajas verdes y azules. Cuando el forzamiento es modificado por ajustes rápidos, y por tanto independientes de los cambio de la temperatura superficial media, son indicados mediante flechas marrones de puntos. Las retroalimentaciones se representan por flechas curvadas (las azules representan el efecto de las nubes, las verdes el efecto de los aerosoles y las naranjas indican otros bucles de retroalimentación como los ligados al gradiente térmico, al vapor de agua y al albedo superficial). Imagen obtenida del IPCC 2013

Es importante tener en cuenta los ajustes rápidos (a veces también denominados respuestas rápidas) que ocurren cuando los aerosoles y los gases, modificando los flujos de energía internos del sistema, afectan a las nubes y otros componentes del sistema produciendo modificaciones en el balance radiativo global. Estos son los conocidos como efectos indirectos. Debido a que los cambios no afectan a la temperatura superficial global (que son cambios más lentos debido a la respuesta térmica de los océanos) son generalmente más rápidos y se cree que ocurren en pocas semanas. Por lo tanto, se debe distinguir entre el concepto tradicional de forzamiento radiativo y el concepto relativamente nuevo de forzamiento radiativo eficiente (ERF), que también incluye estos ajustes rápidos.

La estimaciones de los efectos radiativos directos de los aerosoles puede ser modelizada, como primera aproximación, por la ecuación de Chylek and Wong (1995):

$$\frac{\Delta F_{aer}}{\tau} = -\frac{S_0}{2} T_{atm}^2 (1 - A_{cld}) \left[\bar{\beta} \omega (1 - R_{surf})^2 - 2(1 - \omega_o) R_{surf} \right]$$

Ecuación 1: Estimación del efecto radiativo directo de los aerosoles.

Donde S_0 es la constante solar, T^2_{atm} es la transmitancia de la atmósfera por encima de la capa de aerosol, A_{cld} es la fracción de la cobertura de nubes, ω_0 es el albedo de dispersión simple del aerosol, definido como la relación entre la extinción (dispersión más absorción) y la dispersión de aerosoles, R_{SURF} es la reflectancia superficial y β la fracción de la radiación dispersada por los aerosoles para el hemisferio iluminado por el sol en la Tierra. Este último parámetro se define a partir de la función de fase del aerosol. En términos generales, la

ecuación 1 indica que los aerosoles dispersan parte de la luz solar hacia el espacio y producen un enfriamiento. Además, los aerosoles absorbentes son capaces de captar energía solar de manera eficiente y esta absorción puede cambiar el signo del impacto radiativo de los aerosoles, pasando del enfriamiento al calentamiento en áreas donde los aerosoles están presentes. Este efecto es aún más pronunciado cuando los aerosoles se encuentran por encima de superficies altamente reflectantes, como la nieve o las nubes. Por lo tanto, podemos concluir que el efecto radiativo directo de los aerosoles se puede caracterizar a partir de la cantidad, de la forma (parámetros microfisicos) y las características ópticas del aerosol (especialmente de la absorción), así como del albedo de la superficie terrestre donde se encuentran.

1.2 Medidas en teledetección

Como se observa en la figura 2, extraída del informe de 2013 del IPCC, la incertidumbre sobre los aerosoles es la mayor de todos los componentes que afectan al forzamiento radiativo. La incertidumbre sobre el impacto y efecto de los aerosoles sobre el clima está claramente relacionado con la dificultad de su caracterización de una manera precisa y global. Es especialmente importante (ver ecuación 1) disponer de una buena información sobre la cantidad de aerosol, que nos indicará la magnitud del impacto radiativo, y de la absorción, que nos determinará el signo de este impacto. En este contexto, la teledetección se muestra como la mejor herramienta para estudiar las interacciones de la radiación solar con los componentes atmosféricos, en particular los aerosoles, y la superficie terrestre, así como su influencia en el balance radiativo.

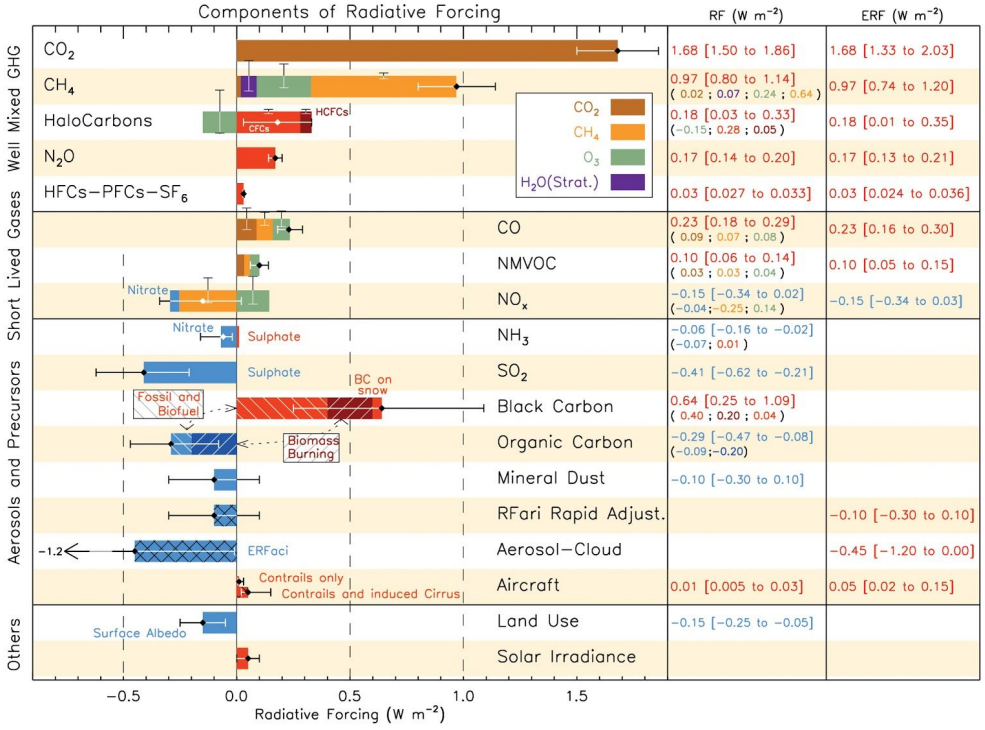

Figura 2: Forzamiento radiativo (RF) del cambio climático durante la era industrial mostrado a través de los componentes emitidos entre 1750 y 2011. La mejor estimación para los totales y los componentes individuales (de izquierda a derecha) de cada respuesta es mostrada en la columna de la derecha. Imagen obtenida del IPCC (2013).

Durante las últimas décadas, sensores integrados en satélites, redes de estaciones fijas en tierra y sensores a bordo de aviones o barcos han sido utilizados con éxito para medir las propiedades radiativas de la tierra, océanos, gases atmosféricos, aerosoles, nubes, etc. Grandes colecciones de datos han permitido mejorar el conocimiento sobre los procesos que ocurren tanto a nivel local como global. Como ejemplo, la figura 3 muestra una de estas colecciones de datos, en concreto el valor medio del espesor óptico de aerosoles medido a lo largo del año 2008 por el sensor satelital francés POLDER (POLarization and Directionality of the Earth's Reflectances) procesado mediante el algoritmo de inversión GRASP (Generalized Retrieval of Atmosphere and Surface Properties). Los datos de espesor óptico de aerosoles (aerosol optical depth, AOD) y absorción (generalmente a través del albedo de scattering simple) son fundamentales para el cálculo del forzamiento radiativo de los aerosoles. Sin embargo, todavía hay un sesgo significativo asociado a las propiedades de los aerosoles, tanto por las limitaciones asociadas al modo de observación como a los algoritmos de inversión. Los instrumentos en estaciones en tierra presentan alta precisión y una gran cobertura temporal del sitio pero carecen de cobertura espacial. En cambio, los sensores a bordo de satélites son capaces de obtener datos de grandes áreas geográficas, pero con una mala cobertura temporal y en general menor precisión que las medidas en Tierra. Por otro lado, como se ha mencionado, existen también limitaciones en los complejos algoritmos de inversión utilizados para obtener las propiedades ópticas, microfísicas y químicas. Estos algoritmos requieren de gran cantidad de información de entrada para producir resultados de calidad. En la actualidad, el número de medidas sobre un parámetro básico para el entendimiento del forzamiento radiativo como es la absorción, sigue siendo limitado.

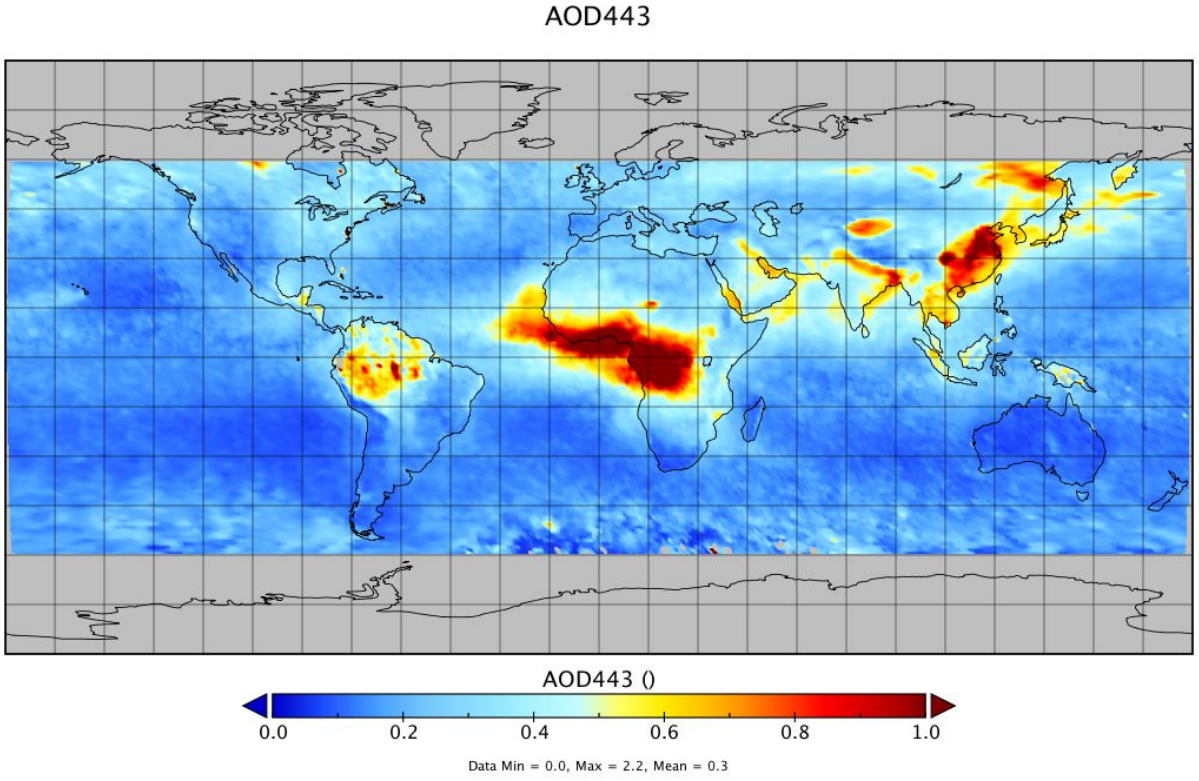

Figura 3: Espesor óptico de aerosoles medio para el año 2008 a partir de medidas del sensor satelital POLDER, procesado mediante el algoritmo GRASP.

Cabe destacar otro de los grandes retos de los estudios de clima a nivel global: la cantidad de datos que deben ser procesados. Si bien es cierto que en el caso de las redes en tierra el número de instrumentos es limitado, y por tanto varios órdenes de magnitud más manejable que en los datos de los satélites, no es, sin embargo, nada despreciable el volumen de información medido por los instrumentos. En el caso de las misiones satelitales esto se complica de forma drástica. Por citar algún ejemplo que ilustre la cantidad de información medida, las misiones Sentinel en conjunto producen alrededor de 4Tb de datos al día.

1.3. La red AERONET

Una de las redes fundamentales para la medida y validación de los aerosoles es la red AERONET (AErosol RObotic NETwork, Holben et al., 1998). La red AERONET (https://aeronet.gsfc.nasa.gov), creada en los años 90, es una red de medidas fotométricas impulsadas por la NASA y el Laboratorio de Óptica Atmosférica de la Universidad de Lille. La red tiene por objetivo la obtención rutinaria de medidas fotométricas a nivel global para el estudio de los aerosoles y la validación de las medidas satelitales. La red AERONET funciona como una federación de redes, con centros dedicados a la calibración y mantenimiento de los instrumentos en NASA-Goddard, Lille y Valladolid. Dentro del conjunto del subredes federadas, el GOA-UVa se encarga desde Valladolid de la calibración y monitorización de unos cincuenta equipos situados principalmente en la península Ibérica y Europa pero con algunas estaciones situadas en otros sitios más lejanos como Cuba o la Antártida. Desde el año 2008 el GOA-UVa emplea CÆLIS (www.caelis.uva.es; Fuertes et al. 2018) como herramienta interna tanto para el mantenimiento y calibración de la red como para el procesado de los datos y su explotación con fines científicos.

La red AERONET establece estrictos protocolos de calibración y mantenimiento, usando siempre un mismo instrumento estándar y un procesado centralizado. Como resultado se obtiene un registro de medidas de gran calidad y homogeneidad. El instrumento elegido para la red es el fotómetro de la empresa francesa CIMEL Electronique capaz de realizar medidas de irradiancia directa del sol y la luna, utilizando 9 filtros interferenciales en el rango de 340nm a 1640nm. Además el instrumento realiza medidas de radiancia del cielo en diferentes geometrías en el rango espectral de 380 nm hasta 1640 nm (existen algunas diferencias dependiendo de la versión del instrumento).

A partir de las medidas de irradiancia directa se puede calcular la atenuación de la radiación solar (o lunar) a su paso por la atmósfera. La atenuación viene definida por la ley de Beer-Bouguer-Lambert, de la siguiente forma:

$$F(\lambda) = F_0(\lambda)e^{-m_s\tau}$$

Ecuación 2: Ley de Beer-Bouguer-Lambert.

Donde F_0 es el flujo extraterrestre total - solar o lunar - (cantidad de radiación que llega a la parte más externa de la atmósfera), m_s es la masa óptica que puede ser calculada usando la fórmula de Kasten (Kasten and Young 1989) y τ es el espesor óptico total, que viene

determinado por el tamaño, la composición y la cantidad de los diferentes componentes atmosféricos: moléculas, aerosoles y gases absorbentes.

En ausencia de nubes, el espesor óptico total (τ) puede ser descompuesto en sus distintos componentes, es decir, la contribución debida los aerosoles (τ_a), al la absorción de los gases (τ_g) y a la dispersión de Rayleigh producida por las moléculas de aire (τ_R). Por tanto:

$$\tau_a = \tau - \tau_g - \tau_R$$

Ecuación 3: Espesor óptico de aerosoles a partir del espesor óptico total derivado de la ley de Beer-Bouguer-Lambert.

Finalmente teniendo en cuenta que la dispersión de Rayleigh es conocida para una atmósfera estándar a nivel del mar (P_0=1013.25hPa) y que la masa óptica es distinta para cada componente (moléculas, aerosoles y gases), obtenemos la fórmula de la ley de Beer-Lambert que AERONET usa para el cálculo del espesor óptico de aerosoles:

$$F(\lambda) = F_0(\lambda) e^{(-\tau_a m_a - \tau_R \frac{P}{P_0} m_R - \tau_g m_g)}$$

Ecuación 4: Ley de Beer-Bouguer-Lambert desarrollada; muestra explícitamente el espesor óptico de aerosoles así como masas ópticas diferenciadas para aerosoles, moléculas y gases absorbentes.

En cuanto a las medidas de radiancia del cielo, el fotómetro Cimel utiliza una serie de geometrías (almucantar, plano principal, híbrido) para medir la luz dispersada en distintos ángulos de scattering y en 6 canales espectrales en el rango 440-1640nm. En la medida de almucantar el ángulo cenital permanece constante e igual al ángulo cenital solar y el instrumento barre todo el rango de ángulos acimutales. En la medida de plano principal el ángulo acimutal es el que permanece constante e igual al del sol, y el ángulo cenital barre distintos ángulos de elevación desde 6º por debajo del sol hasta 150º. El híbrido es una combinación de ambas geometrías, variando los ángulos cenital y azimutal para un conjunto predeterminado de ángulos de scattering. La geometría condiciona el rango de ángulos de scattering que se pueden medir por lo que el almucantar es más adecuado para elevaciones solares bajas, mientras que el plano principal y el híbrido se aplican en torno al mediodía solar.

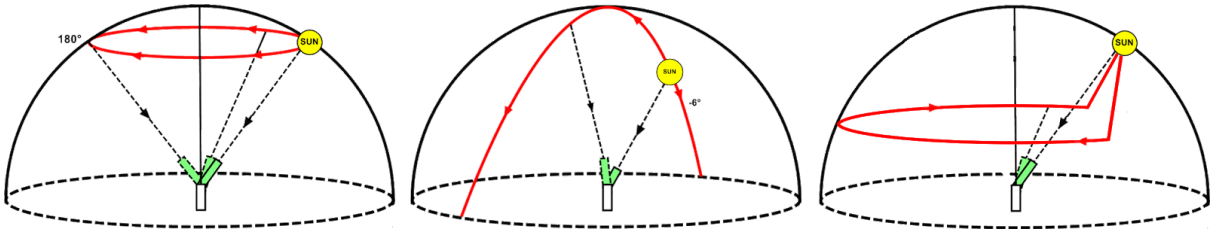

Figura 4: Geometrías del fotómetro Cimel. La primera representa el almucantar, la segunda el plano principal y la tercera el híbrido. Las dos primeras imágenes han sido extraídas del manual de usuario del instrumento así como la tercera ha sido una composición de de las otras.

Estas medidas de radiancia multi-espectrales y multi-angulares se introducen junto con el espesor óptico de aerosoles en los algoritmos de inversión (Dubovik et al., 2000; 2014) para

obtener un conjunto de parámetros microfísicos y radiativos de los aerosoles: distribución de tamaños, esfericidad, índice de refracción, función de fase, etc.

Los criterios para obtener una inversión fiable exigen un número suficiente de medidas libres de nubes a lo largo del rango de ángulos de scattering (https://aeronet.gsfc.nasa.gov/new_web/Documents/AERONETcriteria_final1.pdf), lo que en general constituye un nivel de requerimiento muy alto en cuanto a las condiciones de cielo despejado. Esto puede llegar a ser una limitación severa en regiones en las que existe mucha nubosidad, ya que difícilmente se podrá obtener un muestreo significativo del sitio mediante medidas de radiancia del cielo. Por ello la inversión de espesor óptico de aerosoles (sin radiancias), descrita en el tercero de los artículos, puede llegar a jugar un papel relevante, aunque la falta de información sobre la función de fase limita la posibilidad de obtener determinados parámetros como el índice de refracción.

La calibración de los canales de medida directa al sol y a la luna se hace mediante dos métodos distintos: una calibración absoluta para una serie de instrumentos usados como referencia (llamados máster) y una calibración por intercomparación usando los anteriormente citados másteres. La calibración por intercomparación se realiza en las estaciones de calibración, donde siempre hay dos instrumentos máster (doble verificación) y donde cada instrumento es enviado una vez al año para su calibración y mantenimiento. Así como las condiciones específicas de una estación de calibración por el método de intercomparación no son muy restrictivas, tan solo se necesita un AOD bajo-medio y estable, condiciones que son relativamente fáciles de encontrar en muchos sitios, las estaciones de calibración de los másteres deben reunir unas condiciones muy singulares. La calibración absoluta se realiza mediante la aplicación del método de Langley (Shaw, 1983) que deriva la señal total fuera de la atmósfera usando la media de un conjunto de observaciones a distintas masas ópticas:

$$\ln F(\lambda) = \ln F_0(\lambda) - \tau m_s$$

Ecuación 5: Ley de Beer-Bouguer-Lambert linealizada para aplicar el método de Langley.

Las medidas proporcionan una línea recta (ln F contra m_s) donde la intersección es F_0. Para conseguir medidas a distintas masas ópticas se deben realizar medidas con el sol a distinta elevación, por ejemplo a lo largo de una mañana (salida del sol) o tarde (puesta de sol). Durante este tiempo se asume que el espesor óptico total de la atmósfera permanece estable. Conociendo las asunciones del método es fácil entender las condiciones que deben cumplirse en las estaciones de calibración por el método de Langley: rápida y amplia variación de la masa óptica (lugares cerca del ecuador) y espesor óptico total bajo y estable (lugares a gran altitud). Existen pocos lugares con la infraestructura adecuada que cumplan estas condiciones. En concreto en la red AERONET utiliza las estaciones de Mauna Loa (19,5˚N 155,6˚O, 3397 metros sobre el nivel del mar) e Izaña (18,3˚N - 16,5˚O, 2373 metros sobre el nivel del mar) para realizar este tipo de calibraciones. El segundo de los artículos de esta tesis incide sobre las condiciones y la precisión de las calibraciones realizadas por este método, que constituyen la referencia absoluta y determinan la precisión de las medidas de AOD en la red AERONET.

En cuanto los canales de medida de radiancia del cielo, la calibración se realiza mediante una esfera integrante calibrada de manera absoluta en radiancia. En este caso, la referencia primaria es una esfera calibrada por NIST y ubicada en el Goddard Calibration Facility de NASA. Esta calibración se transporta a las esferas dedicadas a la calibración rutinaria de fotómetros de la red en NASA, Universidad de Lille, observatorio de Izaña y Universidad de Valladolid.

1.4. Métodos de inversión

Los métodos de inversión se refieren a algoritmos complejos que son capaces de calcular propiedades ópticas y microfísicas del aerosol a partir de distintas observaciones. Los algoritmos de inversión se fundamentan en un modelo hacia delante, capaz de modelizar las medidas a partir de unos parámetros atmosféricos; y la estrategia de inversión, capaz de, a partir de un conjunto de parámetros que modelizan la atmósfera y un conjunto de medidas, obtener un conjunto de parámetros resultado que minimiza el error (o distancia) a las medidas originales. A lo largo de las últimas décadas estos algoritmos se han ido perfeccionado de forma que son capaces de tener en cuenta más parámetros a la hora de modelar la atmósfera y de invertir nuevos tipos de medidas.

Dentro del área de los aerosoles atmosféricos, se han desarrollado numerosos algoritmos de inversión. En base a su repercusión, es posible hacer un pequeño resumen histórico de su evolución. El primer algoritmo que citamos es el desarrollado en 1978 por King et al., capaz de invertir medidas espectrales de espesor óptico para obtener la distribución de tamaños de las partículas. Nakajima et al. (1983, 1996) añadieron la capacidad de invertir la distribución angular de la radiancia del cielo, de forma que al disponer de más información de entrada, se obtiene una mejora en la calidad de los resultados. Dubovik y King en el año 2000 elaboraron el modelo de inversión que utiliza la red AERONET. Este modelo, además de mejorar el modelo hacia adelante añadiendo un modelo de esferoides, mejora la estrategia de inversión de forma que minimiza todas las medidas a la vez que sus errores. Finalmente, como última evolución de estos algoritmos, presentaremos GRASP.

GRASP (Dubovik et al, 2014) es un algoritmo de inversión de última generación para la inversión de medidas atmosféricas y de parámetros de la superficie. GRASP está basado en sólidos conceptos físicos y matemáticos ofreciendo un algoritmo altamente configurable capaz de invertir instrumentos de diversa índole (desde medidas de laboratorio, pasando por instrumentos de las redes en tierra hasta los sensores satelitales). GRASP es código abierto y puede ser descargado desde su página web www.grasp-open.com. GRASP es utilizado en esta tesis en la elaboración del tercer artículo. Por ello será más ampliamente descrito en la sección de metodología (apartado 2.3)

1.5. Objetivos

La hipótesis de partida de este trabajo, como se puede deducir de los antecedentes expuestos, es la conveniencia del uso de herramientas informáticas y algoritmos de procesado avanzados, para poder controlar la calidad y explotar adecuadamente la información contenida en la enorme cantidad de instrumentos en tierra y satélite dedicados a la observación de la composición de la atmósfera, en particular de los aerosoles.

El Grupo de Óptica atmosférica de la Universidad de Valladolid (GOA-UVa, http://goa.uva.es/), lleva años dedicado al estudio de los aerosoles atmosféricos. Creado en 1995, tiene por objetivo el estudio de la composición de la Atmósfera mediante métodos ópticos: espectroradiometría, instrumentación óptica in-situ, teledetección activa y pasiva. Este grupo mantiene una larga colaboración científica con el Laboratorio de Óptica Atmosférica de la Universidad de Lille, el cual cuenta con una dilatada experiencia en óptica atmosférica y transferencia radiativa, así como con la empresa GRASP-SAS, spin-off de la Universidad de Lille y expertos en el algoritmo de inversión GRASP, con la que el GOA-UVa mantiene un convenio de colaboración. Los investigadores de estas tres instituciones han constituido el respaldo científico para este trabajo de tesis doctoral y han aportado los medios para hacer posible su realización.

En este contexto, el objetivo del presente trabajo es el desarrollo de nuevos métodos y herramientas para la caracterización avanzada de aerosoles atmosféricos a partir de medidas de teledetección. Para la consecución de este objetivo se plantean los siguientes objetivos específicos:

- Desarrollo de una sistema informático que ayude a la calibración y mantenimiento de una red de medidas así como a la explotación de los datos recibidos.
- Evaluación de la estaciones de Mauna Loa e Izaña como centros de calibración de referencia para medidas fotométricas mediante el método de Langley.
- Estudio de la caracterización de la distribución de tamaños de los aerosoles a partir de medidas espectrales de espesor óptico de aerosoles usando GRASP

1.6. Estructura de la tesis

Esta tesis presenta en su introducción el contexto actual del estudio de los aerosoles, indicando después los objetivos y la metodología propuestos para la realización del trabajo de investigación. Posteriormente se presentan tres trabajos específicos que ayudan a la consecución de los objetivos. El primer trabajo expone el desarrollo de un sistema informático para la gestión y mantenimiento de una red de medidas de aerosoles así como la explotación de sus datos con fines científicos (Fuertes et al., 2018). El segundo artículo utilizará el sistema informático desarrollado para el estudio de las dos estaciones principales de AERONET, puesto que son las dos únicas en las que en la actualidad se realizan calibraciones absolutas mediante el método de Langley: Izaña y Mauna Loa. Este artículo describe los requisitos necesarios para realizar una calibración absoluta y luego comparar estadísticamente las dos estaciones para mostrar las excelentes y singulares condiciones que estos sitios ofrecen (Toledano et al., 2018). Por último, se estudia el algoritmo GRASP y

se propone una aplicación específica, la inversión de las medidas de extinción (Torres et al. 2017). Este algoritmo se podría aplicar luego a gran escala gracias a herramientas como las desarrolladas en el primer artículo.

El presente trabajo pretende presentar de manera adecuada y ordenada los artículos científicos mostrando entre ellos un hilo argumental que lleva a la la consecución de los objetivos planteados por la tesis. Además, este trabajo se apoya en las publicaciones científicas citadas para extender con más información, estudios o aplicaciones al respecto.

2. Metodología

Esta sección desarrolla los métodos y herramientas más importantes utilizados a lo largo de los artículos presentados.

2.1. CÆLIS

Como se ha explicado en la sección 1.3, la gestión de las redes en tierra es fundamental para la monitorización y validación de los aerosoles. CÆLIS nace como respuesta las necesidades del Grupo de Óptica Atmosférica de la Universidad de Valladolid para la gestión de una subred federada a AERONET. Para garantizar la calidad de los datos, grandes volúmenes de información deben ser procesados en tiempo real y analizados para verificar el correcto funcionamiento de la red. Además, el sistema proporciona las herramientas para el estudio de los datos recibidos.

En este trabajo de tesis el sistema CÆLIS es descrito en profundidad dentro del primer artículo; en el segundo artículo se emplea como parte de la metodología; y en el tercero como futura aplicación. En consecuencia es redundante en esta sección volver a describir el sistema pero, dada la importancia de CÆLIS en el conjunto de la tesis, en esta sección se extiende la información ya aportada por los artículos mostrando el potencial del sistema como metodología/herramienta para la investigación.

CÆLIS ofrece visualizaciones de muchos de los productos calculados a través de la página web, pero incluso en las herramientas más genéricas propuestas, como las gráficas personalizadas que se puede ver en la figura 5, no son suficientes en muchos casos. Esto es porque la creatividad del trabajo científico no puede estar limitada a un número finito de opciones que una interfaz puede ofrecer. Por ello, cuando se quiere realizar un estudio en profundidad, las herramientas propuestas sirven como punto de partida para análisis inicial pero después se requiere desarrollar código a medida para el tratamiento específico que se quiera realizar con los datos.

Para realizar un análisis intensivo de los datos almacenados, CÆLIS propone una interfaz SQL a través del Sistema Gestor de Bases de Datos que lo maneja (MySQL). A través de esta interfaz, el usuario puede extraer los datos de una forma absolutamente flexible, realizando filtrados, relacionando diferentes tablas, etc. El artículo uno propone una serie de ejemplos utilizando esta interfaz. Este sistema cubre todos los casos de extracción de información pero puede suponer un límite cuando los datos que se quieren extraer no están previamente calculados. En este caso, CÆLIS se puede utilizar de dos formas: 1) extraer del sistema los datos de entrada necesarios para su posterior procesado fuera del sistema o 2) crear una nueva aplicación para el procesado de los datos dentro de CÆLIS. Esta segunda opción es la mejor cuando el resultado del nuevo procesado pueda ser de utilidad para otros usuarios. El artículo segundo, donde se analizan las estaciones de Mauna Loa e Izaña para ver sus capacidades como estaciones de calibración mediante el método Langley se pudo realizar con la primera aproximación pero se decidió que dichas calibraciones podían ser útiles si se calculan de manera rutinaria. Por ejemplo, se podría

pensar en programar algún tipo de alarma en función de la desviación de una calibración in-situ respecto a la realizada en el centro de calibración.

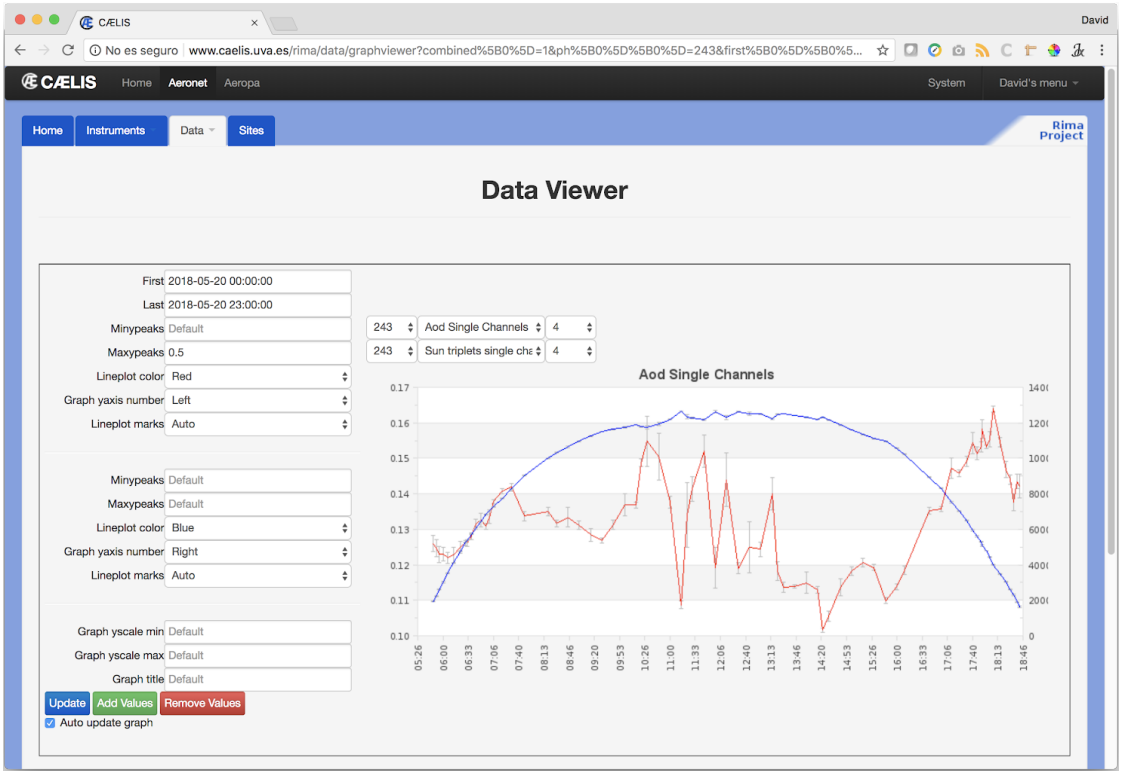

Figura 5: Captura de pantalla de la herramienta de graficado manual de CÆLIS. La gráfica muestra los datos de las cuentas digitales medidas por el canal 4 del instrumento #243 (eje derecho) a la vez de su transformación a espesor óptico de aerosoles (eje izquierdo)

Insertar nuevas aplicaciones para el procesado de datos en CÆLIS es fácil gracias a sus módulo NRT (near-real time). En este caso hay que desarrollar una aplicación, en un lenguaje de programación arbitrario pero que pueda ser ejecutado en la consola del servidor de CÆLIS y que acepte una serie de argumentos estándar como fecha de inicio y fin del procesado y estación o instrumento al que se aplica el procesado. Una vez dado de alta en el módulo NRT de CÆLIS, la nueva aplicación será lanzada dentro del esquema de procesado en tiempo real. Esta nueva aplicación se comunicará con CÆLIS a través de la base de datos, por tanto, cada vez que sea ejecutada leerá los datos entrada de la base de datos y escribirá ahí los datos de salida. Así pues, este nuevo producto estará disponible a través de la interfaz SQL y se podrá utilizar en estudios posteriores: filtrados, relaciones, estadísticos, etc. Además, la interfaz web puede disponer de los resultados para incluirlos en sus vistas que actúan a modo de informe dinámico mostrando gráficos o estadísticas. Esta es la metodología utilizada para conectar GRASP a CÆLIS. Se han desarrollado dos extensiones específicas que se compilan junto a GRASP y permiten leer la entrada y escribir la salida directamente de la base de datos de CÆLIS. Una vez los datos están procesados y forman parte de la base de datos del sistema, pueden ser utilizados tanto a través de la base de datos como desarrollando una interfaz específica de visualización. La figura 6 muestra un ejemplo de cómo los datos procesados mediante el algoritmo GRASP son visualizados en CÆLIS.

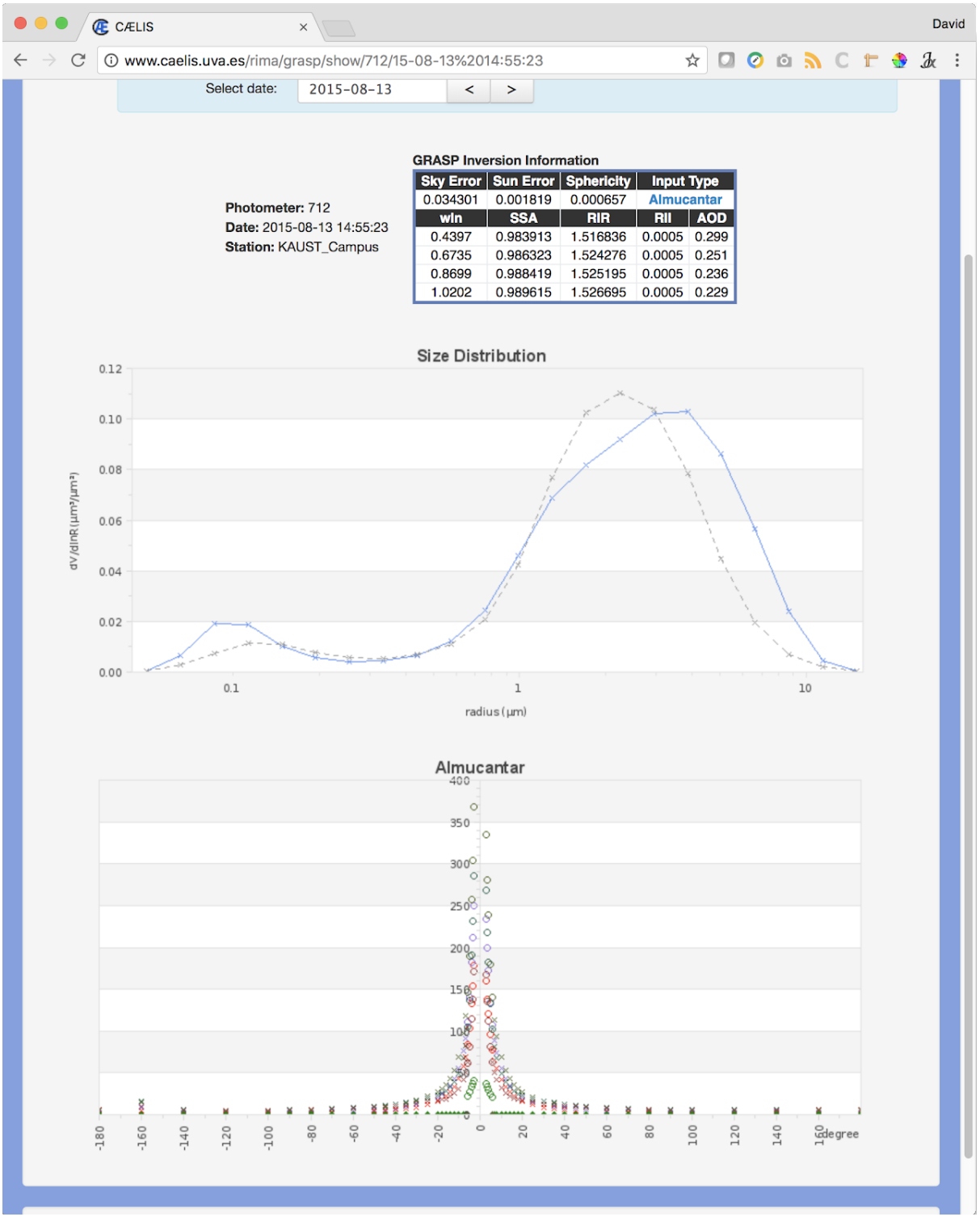

Figura 6: Captura de pantalla que muestra un ejemplo de datos procesados mediante GRASP y visualizados a través de la web CAELIS.

2.2. Las estaciones de Mauna Loa e Izaña

Como se ha explicado en la sección 1.3 los instrumentos en las redes de medida en tierra deben ser calibrados periódicamente y siguiendo protocolos estrictos. Para realizar calibraciones absolutas mediante el método de Langley se requieren condiciones muy especiales. Para que la ecuación 5 se pueda aplicar, se necesitan condiciones de gran estabilidad atmosférica y un significativo rango de variación de la masa óptica. Con estas premisas, las estaciones de calibración deben estar situadas a una gran altitud, que garantiza la estabilidad atmosférica y en los trópicos, donde se producen grandes variaciones de la masa óptica en breves espacios temporales. Las estaciones de Mauna Loa e Izaña son dos centros de referencia mundial de calibración porque cumplen con esas condiciones tan particulares.

El observatorio de Mauna Loa (19˚N, 155˚O) situado en Hawaii, Estados Unidos, se encuentra sobre el volcán Mauna Loa a 3397 metros sobre el nivel del mar. Fue creado en 1956 por el NOAA (National Oceanic and Atmospheric Administration)

El observatorio de Izaña (28˚N, 16˚O) situado en Tenerife, España, se encuentra sobre el volcán del Teide a 2373 metros sobre el nivel del mar. Fue fundado en 1916 pero su historia es mucho más extensa, puesto que el primer interés en la isla de Tenerife como sitio para la investigación de la atmósfera se remonta a 1643.

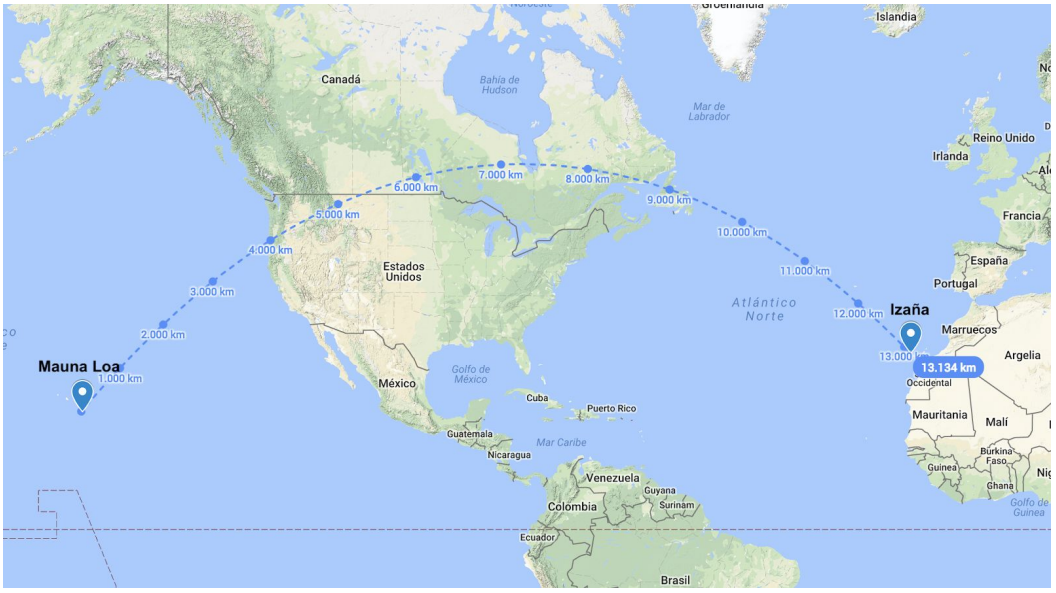

Figura 7: Mapa que muestra las estaciones de Mauna Loa e Izaña y la distancia entre ellas (13.000km)

Ambas estaciones cuentan con la infraestructura y personal cualificado que son necesarios para la operación de este tipo de instrumentación. En la actualidad, los instrumentos de referencia de las principales redes radiométricas de medidas desde tierra se encuentran en estas dos estaciones.

2.3. GRASP

GRASP (Generalized retrieval of Aerosol and Atmosphere Properties; Dubovik et al., 2014) es un programa de código abierto que puede ser descargado a través de su página web www.grasp-open.com. El software propone un paquete completo de inversión de productos atmosféricos y propiedades de la superficie a partir de las observaciones proporcionadas. Uno de los puntos fuertes de GRASP es que está basado en conceptos genéricos fundamentales permitiendo al algoritmo invertir multitud de instrumentos distintos, desde instrumentos de laboratorio hasta sensores satelitales pasando por redes de medidas en tierra, cualesquiera que sean el tipo de medidas que realizan. El modo general de funcionamiento, ilustrado en la figura 8, muestra cuales son los elementos fundamentales a la hora de su uso. Como entradas, GRASP requiere un archivo con las medidas y un archivo de configuración que permite definir la estrategia de inversión así como parámetros intrínsecos a la instrumentación utilizada. Como resultado, GRASP proporcionará los parámetros de la inversión más un conjunto extra resultado de modelizar el escenario utilizando el modelo de GRASP.

Figura 8: Esquema del flujo de datos de GRASP. Input data representa los datos de entrada del sensor. Settings file es la configuración del algoritmo que especifica la estrategia de inversión. La salida son los resultados de la inversión.

GRASP implementa un nuevo concepto llamado multi-pixel, el cual trata las medidas en conjunto en vez de individualmente. Esta aproximación permite al algoritmo añadir restricciones temporales (donde es conocido que la superficie cambia suavemente) y espaciales (donde es conocido que los aerosoles cambian suavemente), de forma que se completa la información de entrada permitiendo tener una salida más precisa o en situaciones realmente complicadas, como el caso de las medidas de satélite sobre superficies muy reflectantes. La figura 9 muestra cómo GRASP organiza los datos para su procesado. De todos los datos globales, el conjunto de datos procesado se le llama “tile” (baldosa 3D) que se subdivide en segmentos. Estos segmentos son la unidad de información que el módulo científico es capaz de manejar, es decir, el bloque de datos que procesa y sobre el que se permite añadir restricciones. Los segmentos a su vez, están formados por un grupo de observaciones, también llamados píxeles.

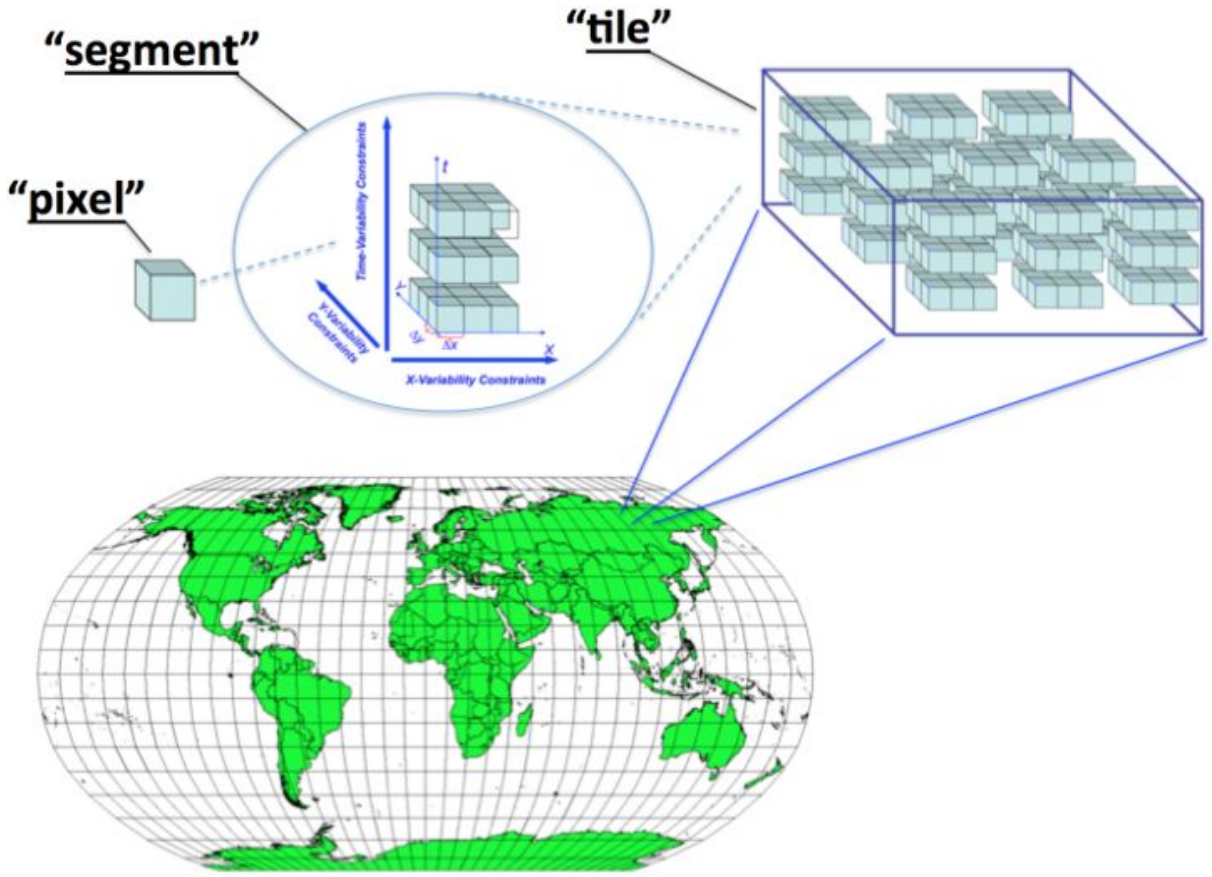

Figura 9: Organización de la información procesada por GRASP. Imagen tomada de la documentación oficial del algoritmo.

A nivel interno GRASP está organizado en forma de módulos. Podemos hablar de dos niveles de abstracción: 1) Alto nivel, ligado a la preparación de la entrada y la salida para el algoritmo científico y 2) Nivel algorítmico, donde de desarrollan específicamente el modelo directo o hacia delante y la inversión.

La figura 10 ilustra los módulos que componen GRASP desde un punto de abstracción de alto nivel. Estos son los encargados de la entrada, la salida, la gestión de la configuración, algoritmo científico y el controlador encargado de la coordinación y comunicación entre todos los anteriores.

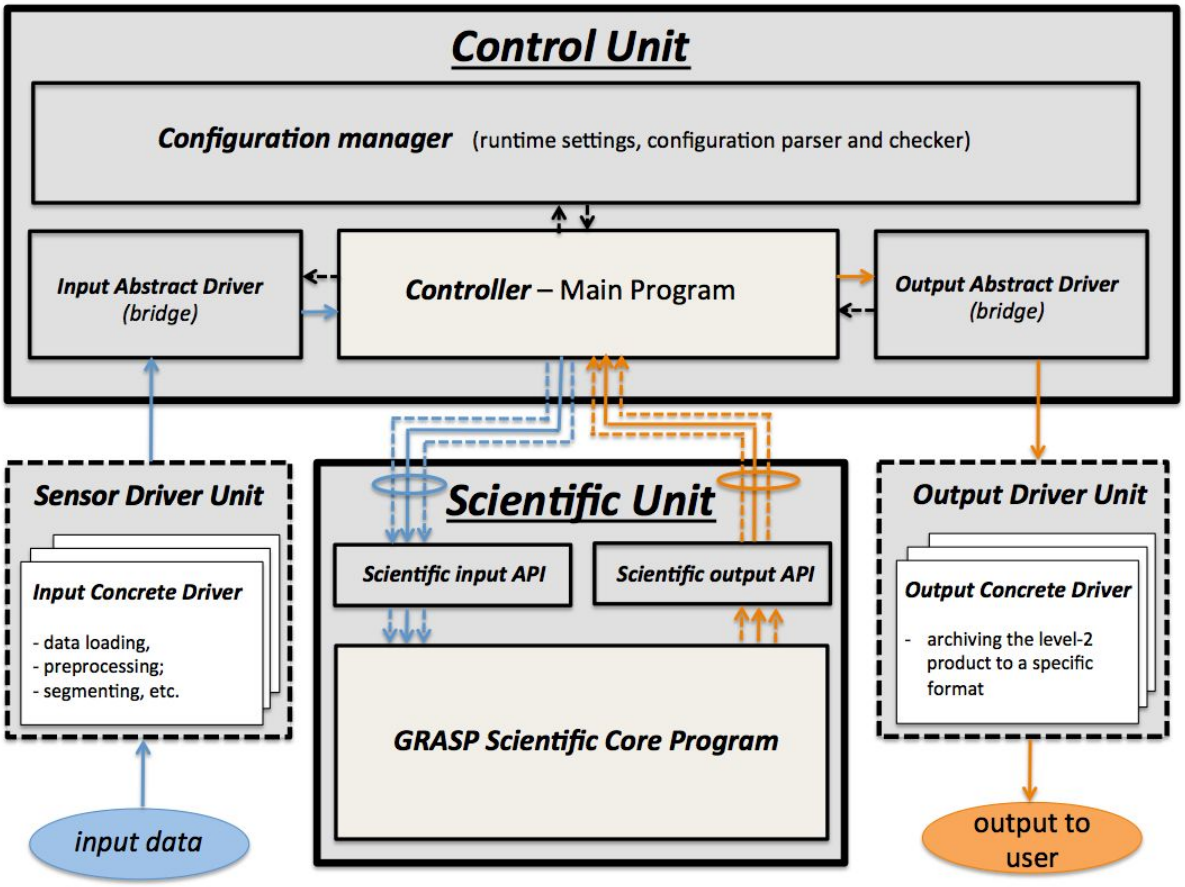

Figura 10: Esquema general de los módulos que componen GRASP, extraído de la documentación oficial.

Respecto a este nivel de detalle del software cabe destacar la abstracción de la entrada y salida que GRASP propone. El software define una API (Interfaz de programación de aplicaciones) para comunicar con las estructuras internas del software. Está API puede ser utilizada para el desarrollo de extensiones en tiempo de compilación que permitan al software adaptarse a una aplicación en concreto. Por tanto, incluso si GRASP ofrece unos formatos determinados tanto de entrada como de salida, estos se pueden ajustar a un escenario concreto. Este detalle toma gran importancia cuando se aplica el código a grandes volúmenes de datos (por ejemplo medidas de satélite) donde la optimización del proceso es primordial. Estas adaptaciones del código permiten que todo el proceso de inversión ocurra en memoria evitando así el uso de ficheros intermedios y acelerando el proceso de manera global.

El controlador es el encargado de orquestar la comunicación entre los distintos módulos de forma ordenada. La figura 11 muestra un diagrama de secuencia donde se puede ver el orden de las llamadas que el controlador organiza: primero lee el archivo de configuración para saber qué tipo de inversión se va a realizar, luego inicializa los módulos de entrada, salida y científico para luego proceder a cargar los datos e iterar sobre cada segmento, realizando la inversión. La salida de cada segmento es recogida y organizada para posteriormente llamar al módulo encargado de tratarla.

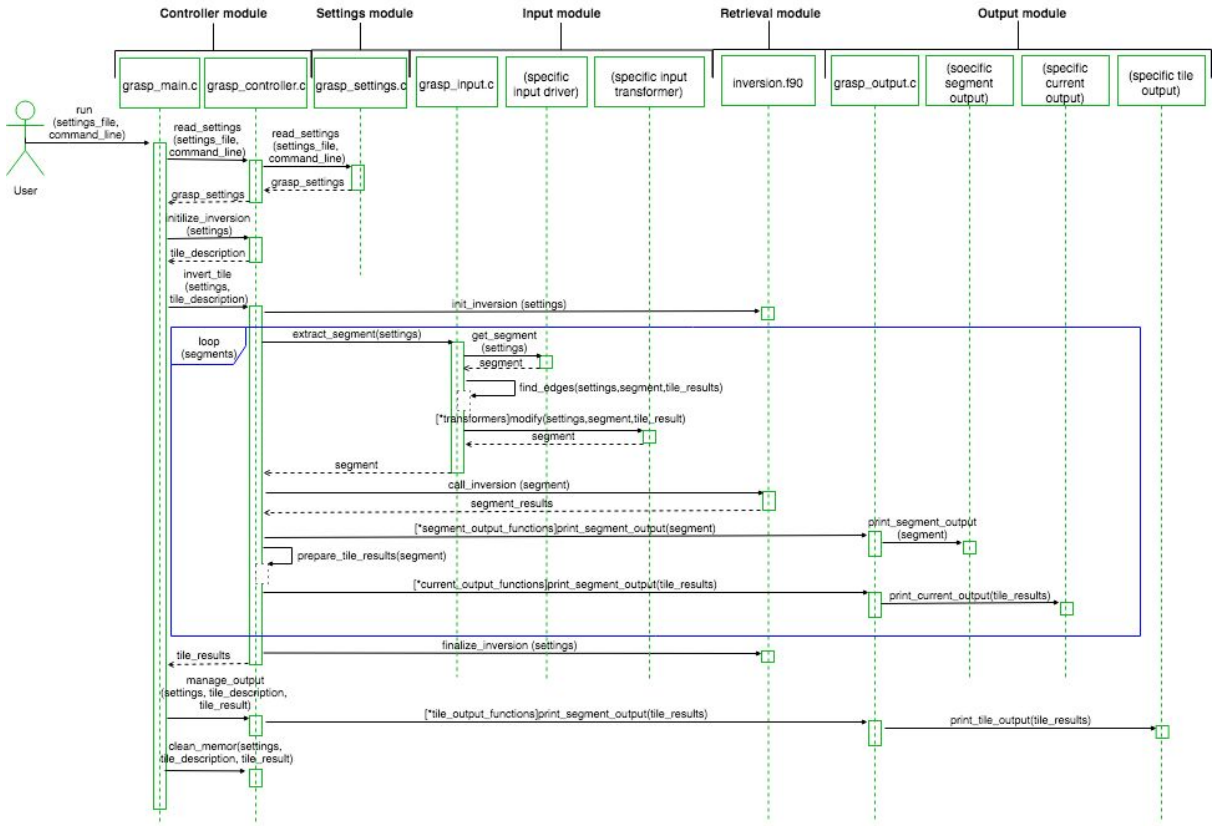

Figura 11: Diagrama de secuencia general, muestra cómo el controlador dirige el proceso de inversión.

La figura 12 muestra el funcionamiento general del módulo científico. Se parte de una serie de observaciones y unos parámetros de configuración que describen el comportamiento y el valor de las constantes que corren dentro de la librería científica. El modelo de directa simula una serie de medidas que son comparadas con las de inicio y ajustadas estadísticamente para minimizar el error. En la figura 12 se observa:

- **f*** es el vector de las medidas que se desean invertir
- **f($\mathbf{a}^p$)** es el vector de las medidas invertidas después de p iteraciones
- $\mathbf{a}^p$ es el vector de incógnitas en p iteraciones

En la última iteración $\mathbf{a}^p$ es $\mathbf{a}^{p\ -\ final}$, es decir, el vector de parámetros que contiene la solución.

El vector de parámetros (incógnitas) está compuesto por distintos elementos dependiendo del tipo del instrumento a invertir y de tipo de inversión a realizar. Normalmente estos parámetros son la distribución de tamaños, índices de refracción real e imaginario, esfericidad (fracción de partículas esféricas), parámetros de superficie, perfil vertical y concentración. El modelo directo (forward model) es a su vez también modular, de forma que dependiendo del tipo de medidas se activarán o no distintos módulos. Por ejemplo, en las medidas de satélite el módulo de modelización de superficie estará presente, así como en el caso de medidas de lidar el módulo de superficie puede ser desactivado y el módulo de modelización del perfil vertical estará presente. GRASP está diseñado de forma que sea sencillo añadir nuevos módulos para en el futuro invertir otro tipo de medidas.

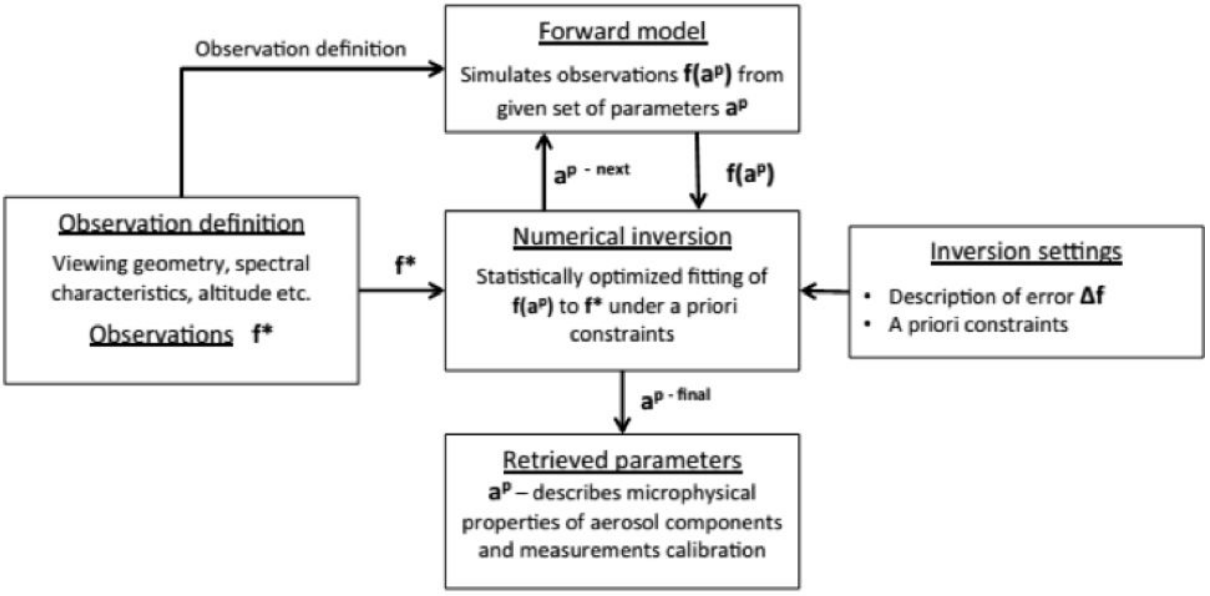

Figura 12: Funcionamiento general del algoritmo de inversión GRASP.

3. Resultados

Artículo 1: CÆLIS: software for assimilation, management and processing data of an atmospheric measurement network

Resumen y comentarios

Dado el contexto planteado en la introducción donde se exponen las necesidades de una red de medida de aerosoles, este primer artículo plantea la descripción de una solución informática que resuelva los requisitos planteados. De manera resumida, las funcionalidades que debe cubrir el sistema son:

1. Ayudar a la gestión y mantenimiento de una red de medidas fotométricas
2. Proponer un sistema de procesado de datos
3. Facilitar a los investigadores la explotación de los resultados con fines científicos.

El artículo hace una descripción del sistema CÆLIS y cómo este cubre los requisitos esperados. Se describen con detalle las tecnologías informáticas empleadas, ya que la revista así lo promueve para facilitar que otros grupos de investigación conozcan detalles que en otro tipo de publicaciones no es posible proporcionar. Además el artículo plantea una serie de ejemplos prácticos de utilización de sistema que muestra la potencia y flexibilidad de este.

La flexibilidad de CÆLIS se apoya también en su carácter modular. Si bien nació para responder al reto de gestionar una red de fotómetros dentro de AERONET, es sencillo incorporar otros instrumentos, como los fotómetros PFR de la red GAW usados en el artículo 2º de esta tesis. CÆLIS está en constante desarrollo y ya se están incorporando medidas de ceilómetro y lidar de 1 longitud de onda, lo que abre todo un horizonte de aplicaciones y combinaciones de medidas.

Así mismo el módulo de procesado asimila de manera rutinaria datos auxiliares que son necesarios para el procesado de las medidas, como mapas de análisis meteorológico, etc. CÆLIS desde su origen sirve a redes de medida con grandes volúmenes de datos, para realizar procesados no para un instrumento o una estación, sino a escala de red y con suficiente fiabilidad y robustez para ser empleado como herramienta operacional.

Artículo 1

CÆLIS: software for assimilation, management and processing data of an atmospheric measurement network

David Fuertes[1,2], Carlos Toledano[1], Ramiro González[1], Alberto Berjón[1], Benjamín Torres[2], Victoria E. Cachorro[1], and Ángel M. de Frutos[1]

1. Group of Atmospheric Optics, University of Valladolid (GOA-UVa), Valladolid, Spain

2. GRASP-SAS, Lille, France

Correspondence: David Fuertes (david@goa.uva.es)

Received: 30 June 2017 – Discussion started: 4 August 2017 Revised: 22 November 2017 – Accepted: 17 December 2017 – Published: 16 February 2018

Abstract. Given the importance of the atmospheric aerosol, the number of instruments and measurement networks which focus on its characterization are growing. Many challenges are derived from standardization of protocols, monitoring of the instrument status to evaluate the network data quality and manipulation and distribution of large volume of data (raw and processed). CÆLIS is a software system which aims at simplifying the management of a network, providing tools by monitoring the instruments, processing the data in real time and offering the scientific community a new tool to work with the data. Since 2008 CÆLIS has been successfully applied to the photometer calibration facility managed by the University of Valladolid, Spain, in the framework of Aerosol Robotic Network (AERONET). Thanks to the use of advanced tools, this facility has been able to analyze a growing number of stations and data in real time, which greatly benefits the network management and data quality control. The present work describes the system architecture of CÆLIS and some examples of applications and data processing.

1 Introduction

The atmospheric aerosols are defined as solid or liquid particles suspended in the atmosphere. Many studies have shown the importance of aerosols, which play an important role in global energy balance and human activities. Upon direct impact the aerosol particles produce radiative forcing in the atmosphere, provide nutrients to the oceans and affect human health. Aerosols generally produce a cooling effect, although the aerosol can also locally warm up the atmosphere depending on its type, height above the surface and timescale under consideration. Upon indirect impact they change the chemical composition of clouds and therefore their radiative properties, lifetime and precipitation. To improve the knowledge about the distribution and composition of aerosols is one of the emerging challenges highlighted by the last IPCC report (IPCC, 2014), where it is shown that they have the largest uncertainty for the estimates and interpretations of the Earth's changing energy budget.

Ground-based and orbital instruments have been applied to monitor aerosol properties. Combining instruments is also possible to maximally exploit synergies. For example, satellites have demonstrated the potential of high spatial coverage and resolution, and standardized ground-based networks have the benefit of high accuracy. A common exercise is to validate satellite data with ground-based networks.

One of these ground-based networks is the Aerosol Robotic Network (AERONET; Holben et al., 1998). Led by NASA (National Aeronautics and Space Administration; http://aerosnet.gsfc.nasa.gov) and PHOTONS (PHOtométrie pour le Traitement Opérationnel de Normalisation Satellitaire; http://loaphotons.univ-lille1.fr/),

AERONET is built as a federation of sub-networks with highly standardized procedures: instrument, calibration, processing and data distribution. It was created in the 1990s with the objective of global monitoring of aerosol optical properties from the ground, as well as validating satellite retrievals of aerosols. The standard instrument used by the network is the photometer Cimel318. It is an automatic filter radiometer with two-axis robot and nine spectral channels covering the spectral range of 340 to 1640 nm. It collects direct solar and lunar measurements, and sky radiances in the almucantar, principal plane and hybrid geometrical configurations. Once the data are validated through instrument status and cloud screening, aerosol optical depth (AOD) can be obtained as direct product for the nine wavelengths. Using inversion algorithms (Dubovik and King, 2000; Dubovik et al., 2006), many other parameters can be retrieved, such as size distribution, complex refractive index, portion of spherical particles and single-scattering albedo.

The Group of Atmospheric Optics at Valladolid University (GOA), Spain, is devoted to the analysis of atmospheric components by optical methods, mainly using remote sensing techniques such as spectral radiometry and lidar. One of the main tasks of the group is the management of an AERONET calibration facility since 2006, which is now part, together with the University of Lille, France, and the Spanish Meteorological Agency, of the so-called Aerosol Remote Sensing central facility of the Aerosols, Clouds, and Trace gases Research Infrastructure (ACTRIS). Since 2016, ACTRIS has been included in the road map of the European Strategy Forum for Research Infrastructures (ESFRI). The GOA calibration facility is in charge of the calibration and site monitoring of about 50 AERONET sites in Europe, North Africa and Central America.

AERONET standards stands for annual instrument calibration, maintenance and weekly checks on the observation data. The calibration process takes about 2–3 months and includes post-field calibration for sun, moon and sky channels, maintenance of the instrumentation and pre-field calibration for the next measurement period. In order to avoid gaps in the data sets during calibration periods, frequently one instrument is swapped out with a freshly calibrated one. The network management determines where each instrument is located, what its exact configuration and calibration coefficients are and how many days remain until the next calibration is needed. During the regular deployment period the instrument has to be regularly checked to guarantee the data quality. A routine maintenance protocol is performed by the site manager, but the network is ultimately responsible for data quality. The routine maintenance helps in reducing instrument failure and data errors, but even with the best daily protocol, instrumentation problems may occur. Data monitoring at the calibration center helps in early identification of instrument issues. However such work cannot be accomplished manually in near-real time (NRT) for a large number of sites.

In this context, it was necessary for the calibration facility at GOA to implement an automatic mechanism (in addition to the standard mechanism of AERONET) to help manage the network and facilitate weekly data checks needed to guarantee the quality of the data. The motivation of the CÆLIS system is to fulfill these two requirements. The system has to be designed to save all data, metadata and ancillary data (assimilated from other sources) in order to, on the one hand, support the management, maintenance and calibration of the network, and on the other hand, process the raw data in NRT with different algorithms and provide network managers, site managers and ultimately the scientific community with a very powerful and modern tool to analyze data produced at the observation sites. This work shows the fundamentals of CÆLIS system which have been developed since 2008, both with respect to the scientific background and the information technology employed. There was no predecessor software at Valladolid and these tasks were done manually before CÆLIS was developed. The other two AERONET calibration centers at NASA and University of Lille have their own tools. Some ideas implemented in CÆLIS are inspired by these tools.

2 General architecture

CÆLIS has been designed to run on a server which, connected to the internet, allows for external communication via a web interface. The software contains a “daemon” (a background process that offers a service) which is responsible for selecting and launching tasks. These tasks, later explained, are responsible for downloading new data whenever available and processing them. Each task reads the required input information from the database and writes the output there. Some tasks use direct internet access to retrieve data, e.g., downloading ancillary data from an FTP server. All information downloaded and treated by the CÆLIS tasks is

stored in the database. This allows for the following actions to retrieve all information required from the database (quick extraction). External users (organized by role with various privilege levels) can connect through the web interface to watch what tasks are being executed and explore the results of finished tasks. All actions required by the system administrators can easily be done through the web interface. Network management is also performed through the web interface which allows for, for example, setting up the installation of an instrument at a measurement station. The same information will be used by the system when data from the instruments reach the server and CÆLIS will compare the received information (instrument number, parameters, location, dates, etc.) with reference registers stored in the database (installation periods, configuration parameters, etc.) to know if the instrument is working properly and using the correct configuration.

External systems, such as measurement stations, can also be connected to the server and submit data. Thanks to the web interface, it can be done using port 80 (standard HTTP), which avoids many problems derived from security rules of the measurement stations and hosting institutions (some of which are in military areas).

The current system manages 120 users and 80 stations. Each station can send thousands of aerosol observations every year and the system is constantly growing. A benchmark has been applied to confirm that the current architecture can support a network 100 times bigger, so the database can grow safely in the future.

As shown in Fig. 1, CÆLIS is composed of a database, a processing module and a web interface. These modules can be deployed independently even in different computers. The users and the stations interact with the system through the web interface. In the database, the raw data and metadata are stored, as well as the retrieved products, ancillary data, user information, etc. The NRT processing module is composed of the system daemon and a set of processing routines that extract information from the database, calculate products and store them in the database. The web interface is the platform designed to manage the system, to manage the network and to provide visual access to the data and metadata, with tables, plots, searching capability, etc. Each of these elements will be explained in detail in the next sections.

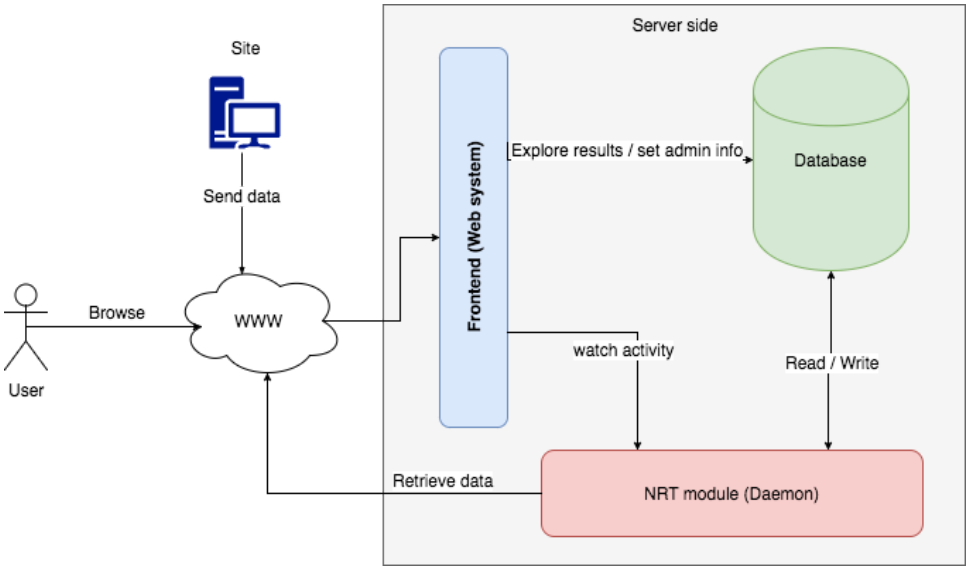

Figure 1. Diagram of CÆLIS architecture. Arrows indicate where the action is initiated (data flow is always bidirectional).

3 Database model

Databases are one of the main concepts developed in the 1980s in the computer sciences. Many different approaches in terms of technology and data models have been developed with varying success. There are many types of databases, classified depending on their characteristics. A database management system (DBMS) is software with an interface to a database system that provides the user with advanced characteristics such as the management of concurrency or a query language. The decision about what kind of database and which specific DBMS software to select is one of the main design decisions because all further development will be impacted by it.

Relational databases are a traditional and well-known model, and have been successfully applied to many different fields. In relational databases the information is organized in tables or relations which represent entity types (Chen, 1976). A good database modeler is able to identify those entity types that are relevant with the information that describes them. The tables or relations are composed of columns with the attributes that describe them, and rows which represent different individual entities that are identified by an unique key (one or more attributes that cannot be repeated in different rows). The tables are linked, creating a relational model. The keystone of a database is good design which needs to take into account the information targeted for modeling as well as the way in which the data is going to be accessed (to optimize performance). Complex models with many groups of entities need to be planned in advance by creating an entity– relationship diagram. This diagram then helps final implementation of the database, which can be a direct translation of the diagram just taking some implementation decisions about a balance between data redundancy and performance.

The main elements of the entity–relationship diagram of CÆLIS database are shown in Fig. 2. The central entity is the photometer, which produces raw data. The photometer, with given hardware configuration and calibration coefficients, is installed at one site of the network. The ancillary data for the site (e.g., meteorological data, ozone column, surface reflectance) need to be stored. Finally the measurement stations are supported by institutions, which can also own other instruments.

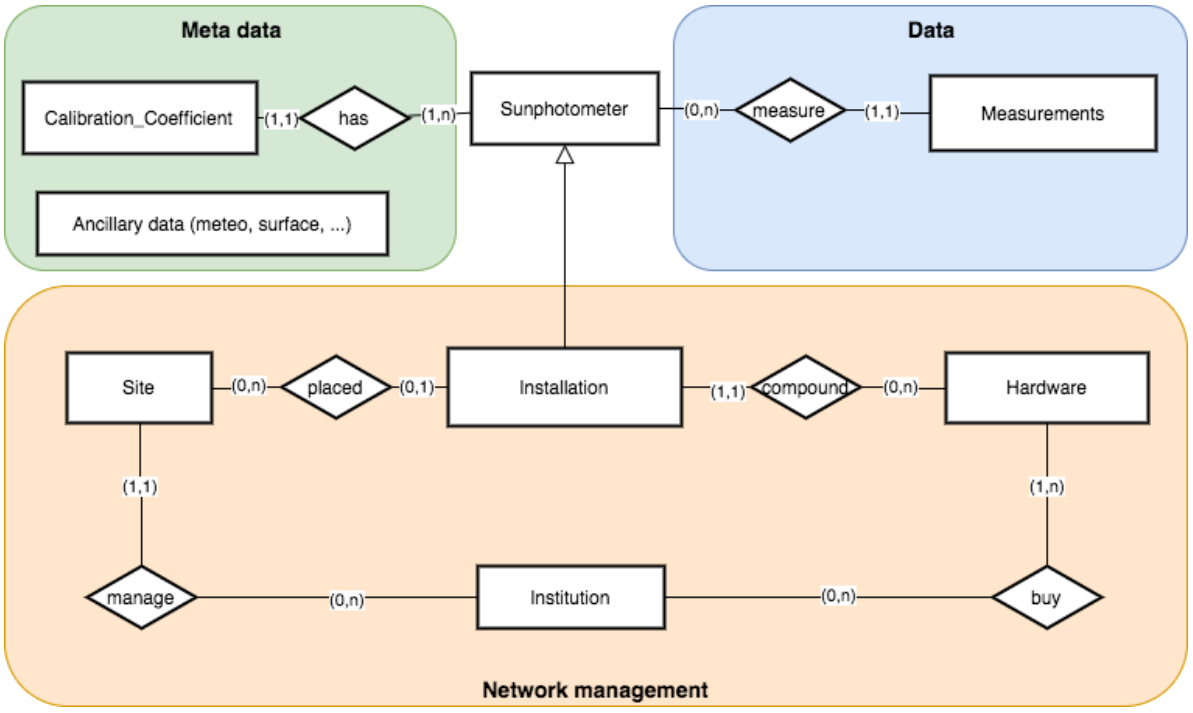

Figure 2. Entity–relationship diagram for CÆLIS (extract of the main elements). Entities have been divided into three logic blocks

Each of these elements is in many cases representing a group of entities. For instance, calibration coefficients include extraterrestrial signal for the different solar spectral channels, radiance calibration coefficients for sky channels, coefficients for temperature correction of the signals, instrument field of view, etc. Another example is the hardware, which includes the different parts (sensor head, robot, collimator, control box, etc.), the spectral filters with the corresponding filter response, and others.

The lower part of the diagram is closely related to the network management, with an inventory of all hardware parts identified with their serial numbers and related to the institution that owns them. The upper part is related to the raw data production, and its organization is optimized for data extraction (to create products) and is consistent with the physical meaning and relevance of the quantities. The installations are manually introduced by the network managers so that any data file submitted to the system from a measurement station can be validated.

Other tables contain ancillary information that is needed to process data, such as the list of stations (including coordinates), global climatologies for certain atmospheric components (ozone, nitrogen dioxide, etc.), solar and lunar extraterrestrial irradiance spectra and spectral absorption coefficients for several species (ozone, NO2, water vapor, etc.). Many different DBMS can be used to implement such a model: OracleDB, SQLite, PostgerSQL, etc. CÆLIS is based on a MySQL database. MySQL software is widely used by many different communities. Therefore the software is very robust, complete, stable and well documented, and it can be run in many different architectures.

The entity–relationship diagram for CÆLIS, illustrated using the model defined by Chen (1976), is shown in Fig. 2. This diagram shows the fundamental part of the database, called layer 0. On top of that, direct products – obtained with the combination of raw data, calibration coefficients and ancillary data – are stored. This represents "layer 1" products, physical quantities with their corresponding units and estimated uncertainties (derived from the calibration uncertainties). In our case, these products are basically aerosol optical depth, water vapor content, sky radiances and degree of linear polarization of the sky light. On top of layer 1, there are more sophisticated products, like those derived from inversion algorithms, as well as any flags or "alarms" that are produced to help in NRT data quality control. Layer 2 products use and combine previous layer quantities to retrieve other parameters, but no longer go down to the raw data. For instance, the inversion codes by Dubovik and King (2000) and Nakajima et al. (1996) use spectral aerosol optical depth and sky radiances to retrieve aerosol particle size distribution, refractive indices, single-scattering albedo, etc. More advanced products that combine photometer data with other aerosol data (e.g., lidar) also belong to this group, named "layer 2" products. A clear example is the GRASP algorithm (Dubovik et al., 2014, http://www.grasp-open.com/), which is able to digest data from different sensors (satellite and ground-based, active or passive) to provide a wide set of aerosol and surface parameters. The system architecture as described here is shown in Fig. 3.

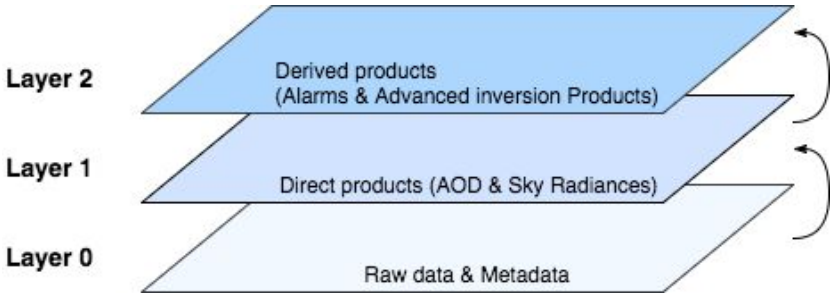

Figure 3. Different logic data layers. Each layer is based on the information of the previous layer.

4 Processing chain and near-real-time module

CÆLIS system provides many different data products. To provide each product, some input data has to be processed in a specific way. This is what we call a "task". The job is divided into a set of simple tasks. The system works as a state machine: one task cannot start until the previous one is finished, no matter if the second task is dependent on or independent of the previous one. When many tasks work sequentially to achieve a common objective, we create a chain of tasks. The daemon running in the server is responsible for coordinating the different tasks, as it will be explained in the next section.

The main processing chain in CÆLIS is the set of the tasks that are performed once new photometer data are uploaded into the system, as shown in Fig. 4.

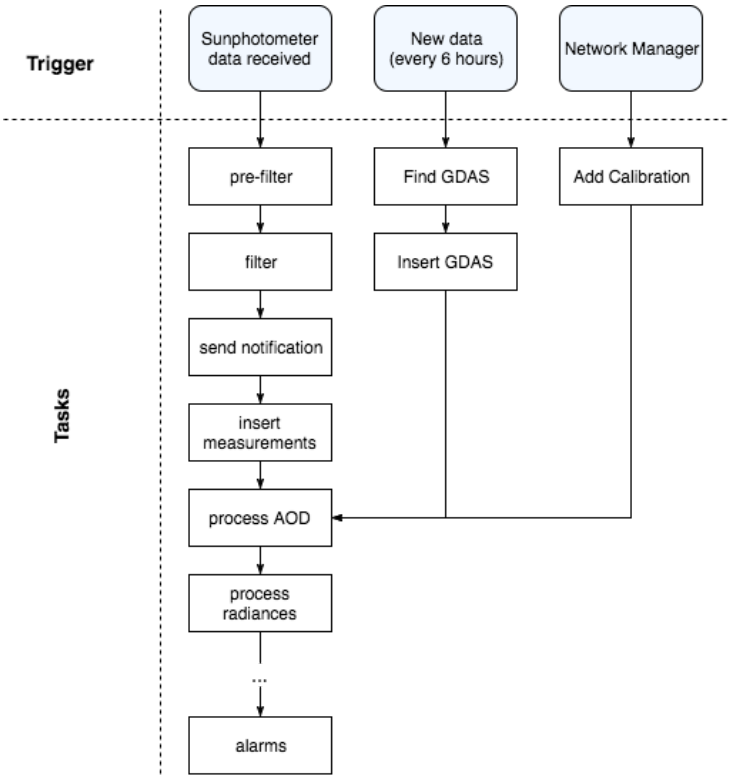

Figure 4. Different processing chains and their relationships. An action triggers a task and then the actions bubble up.

The pre-filter checks that the file uploaded to the server is a valid data file pertaining to the AERONET instruments managed by CÆLIS. If this is true, the "filter" checks that the basic information (instrument number, coordinates and dates, configuration parameters) is in accordance with the stored information about instrument installations. If any of these parameters do not correspond to its expected value, the data file is put to quarantine and the network managers receive an email notification ("send notification"). If all parameters are correct, the measurements are inserted in the database and the data file is forwarded to any desired destination: our data file repository, an AERONET server at NASA, etc. With the raw measurements inserted in the database, the processing of layer 1 products is triggered: the aerosol optical depth, water vapor and radiances in several geometries (almucantar, principal plane, etc.). With all raw data and layer 1 products, a set of flags concerning data quality control are produced by the alarms task. These flags are produced in near-real time, as soon as new data are submitted to CÆLIS from a particular site. Since the automated quality control (QC) analysis needs all available information, the alarms task is always the last one in the processing chain. The QC flags in near-real time are a very important element in the network management. More details are given in Sect. 7.2.

Any new implementation, for instance a new layer 1 product, needs to be inserted in the processing chain taking into account its dependency on any other elements in the chain. The last step in a certain task is to trigger the next one in the chain.

Whenever new data are found (photometer, ancillary, other) or new information is inserted by the managers (new calibration, installation, etc.), a processing chain is triggered. The management of all chains in CÆLIS is carried out by the daemon, which is explained in detail in the next section. This kind of task organization is highly modular, so new elements in CÆLIS, either data or different instruments can be added by creating new chains that can be connected or not to the existing ones.

The near-real-time processing module (see Fig. 1) is composed of a set of programs and libraries that are related to all the above mentioned tasks. These are programmed mainly in C for fast computation with large data sets and interoperability with other technologies, allowing for the use of other languages in the future. A Git repository is used to facilitate version control and deployment of the software.

5 Daemon

The daemon is responsible for organizing the tasks and deciding which process has to be run in each moment. It has to address different challenges:

1. running scheduled tasks according to their priority;
2. knowing which task must trigger other tasks;
3. maintaining the sequence;
4. optimizing the server processing capability and running less important tasks when the CPU is idle.

The tasks are stacked in the system. Figure 5 is a representation of the stack of the tasks, where the green tasks are actions that can be executed right now and the red tasks are disabled until the "activation time" arrives. Each task is described by the following information.

1. Group: classification of the task.
2. Name: name of the task.
3. Object: if it exists, this defines the target where the task will be applied (for example, one file, one particular instrument, one site).
4. Date range: if defined, the task can be applied to a specific time range.
5. Date/time of activation: this mark allows organizing when the task can be run (note that some tasks can be defined to be executed in the future).
6. Priority: defines the importance of the task.

Acc	Sub acc	Object	First	Last	Valid	PRTY
cimel	sendaeronet	20170510_p382_1218.K7			2017-05-10 13:59:26	4420
cimel	processaod	382	2017-05-10 08:23:27	2017-05-10 12:13:09	2017-05-10 13:59:26	4410
caelis	sitecheck				2017-05-10 13:59:26	3900
cimel	finddata				2017-05-10 14:12:03	4400
gdas	finddata				2017-05-10 17:02:43	4050

Figure 5. Example of CÆLIS task stack. Ordering is related to the next task to be executed. Green indicates tasks that can be already selected to be executed. Red indicates tasks to be executed in the future (when "valid" time arrives). The example is captured at 14:00 UTC on 10 May 2017.

Frequently, several tasks can be activated at the same moment. In these cases, the priority flag indicates the system the order in which the tasks should be run. At the same time, the processing chains (commented in Fig. 4) used this mark to indicate the order of the tasks to the daemon. When a task is executed, if it is part of a chain, it will introduce the next actions in the stack (sorted by priority). This is the procedure to keep the system alive and always working.

In every moment, the stack contains the current tasks that can be executed right now, as well as the tasks that are scheduled to be run in the future. This is the method used by the system to repeat tasks: if a task is intended to be repeated every 15 min, once it is executed the system will remove it from the stack but will add it again with the activation time set to 15 min later.

After a task is executed, the information on the execution is saved into a log. This allows the system administrator to study the behavior of the system, to know what has been executed, to foresee the future use of the system and to tune the parameters of CÆLIS to balance between NRT actions and the load of the system. Figure 6 shows the log of actions and their statistics. Thanks to the log and system statistics, the system administrators can know how much time a specific task takes every day and how many times each task is executed. This information is crucial for system administrators and developers because they can analyze which tasks take more time and why (in the cases when a defined task is too slow or is called many times, etc.) and create plans to optimize the system.

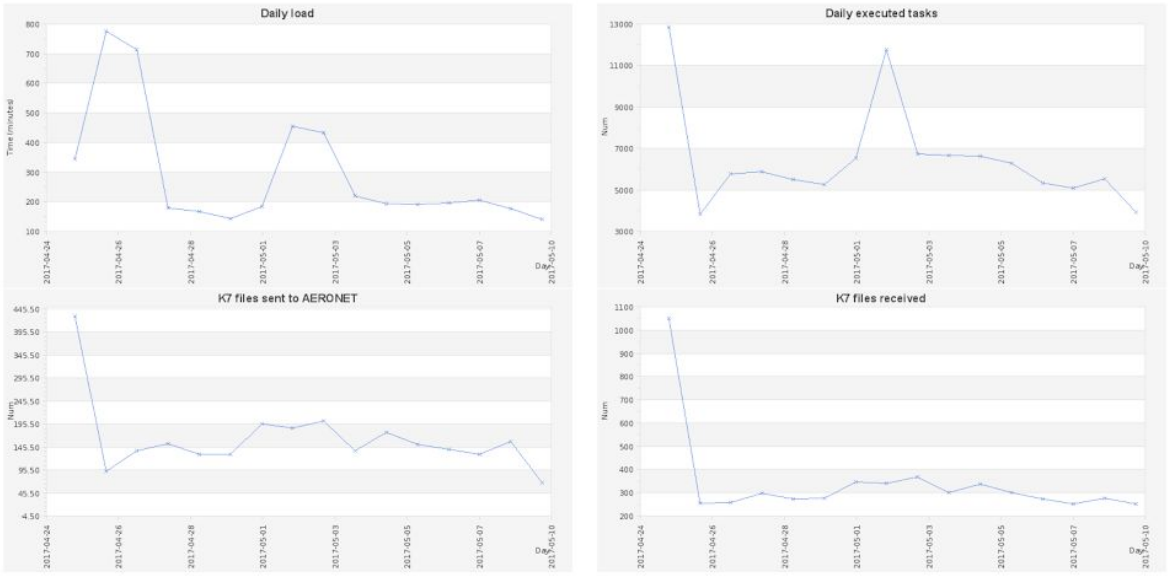

Acc	Sub acc	Object	First	Last	Valid	Time to Start	PRTY	Start	Duration	Status
cimel	processaod	243	2017-05-09 19:03:44	2017-05-10 10:17:56	2017-05-10 11:08:22	25 seg	4410	2017-05-10 11:08:47	0.5 seg	OK
cimel	sendaeronet	20170510_p243 _1008.K7			2017-05-10 11:08:22	23 seg	4420	2017-05-10 11:08:45	2.3 seg	OK
caelis	sitecheck				2017-05-10 11:03:26	3 min	3900	2017-05-10 11:06:33	1.5 min	OK
...										

Figure 6. Plots represent CÆLIS load from different measurements: minutes of CPU per day, number of tasks executed per day and number of photometer raw data files sent to AERONET and received from stations. Those plots are constructed based on log information. The table at the bottom shows an example of the log. Delay indicates the difference between actual start and valid time therefore indicating NRT capabilities.

In a regular situation, the system works automatically. For instance, when the daemon starts, the common operations are introduced in the stack of tasks. One of these common operations will look for new data and metadata with a certain frequency (e.g., once per hour). Then, if new data are found by the corresponding task, it will add new tasks to process those data, triggering the processing chain. If there are no new data, the task will add the same task to find new data some minutes later.

The system administrators can add tasks manually and they can change the priority of the current tasks in the stack. One of the main manual tasks that the administrator can add is the “stop” action. The stop action has a duration of a few seconds and, once it finishes, it re-enters itself in the stack. This process continues until the administrator erases the task manually from the stack. Depending on the priority assigned to the stop action, the system can be completely blocked or it can allow some tasks with high priority to be undertaken. Another main action is to shut down the system. If the system administrator wants to shut down the daemon, this task should be introduced. This guarantees that the system is turned off when idle and no task is interrupted abruptly.

The system is also prepared for a sudden shutdown (for example, power outage). Given that the system only removes the tasks from the stack when they are finished, once the server is turned on, the first task to be executed will be the one that could not be completed. The fact that all these scenarios are taken into account by the stack of tasks, makes CÆLIS a robust system and easy to maintain.

The system executes maintenance tasks regularly. For example, a daily backup is performed. This task is scheduled every night thanks to activation time information. The maintenance tasks can cover many different activities that need to be done regularly in the system. Other examples of the maintenance tasks include the optimization of the database and regular re-booting.

The current implementation of the daemon is developed using bash scripts. This characteristic allows running tasks written in any language. It is planned to improve the current implementation by using Python and to introduce parallelism into the task chain. If this has not yet been undertaken, it is due to the relatively low load of the system. Processing in sequential mode is still sufficient to provide data in NRT. When more sophisticated algorithms will be run (such as inversion retrieval algorithms) a new implementation of the daemon will be needed. Alternatively, tasks can be launched in a server farm allowing the system to only organize tasks, keeping its load very low. The tasks are currently implemented mainly in C because of its high performance, but any compilable language is allowed in the server.

6 Web tool

CÆLIS system offers users a web interface (http://www. caelis.uva.es). The web interface is a high level view of the data model, and thus it shows information in real time, as soon as it is processed. The web system is secured with private access, only for registered users. During the registration process a "role" is assigned to each user. The roles allow identifying groups of users with different permissions into the system, for example, regular users (site managers or researchers) that can access its data or a system administrator that can handle the stack of tasks of the system or reboot it.

The web interface provides high-level access to the database. It can extract and relate different data and show them all together as an online real-time report. CÆLIS has implemented many different use cases which are sufficient for common user actions. The system offers different tools depending on the role of the user. For example, a site manager can check the performance of one instrument, a network manager can modify the location of an instrument and a system administrator can check the tasks that the NRT module is executing. The web interface allows the user to explore the database showing tables and customized plots. Some of these use cases are described below in the example section. The web interface allows one to query information as well as inserting new information. This is specially interesting because it constitutes the second way to insert data into the system: data inserted by the users (data can also be registered by the tasks controlled by the daemon; see previous section). In the case of users, since they work via web interface, the actions can be controlled in two senses: (1) the user has the permission to introduce the information, and (2) the information introduced is validated. Moreover, the fact that manual information is registered by means of the web interface allows the system to launch "derived tasks" for an specific action. For example, when a new measurement site is created, the system can add the action of "insert climatology data for the new coordinates". Everything is triggered automatically and controlled by the logic implemented in the web interface. The web interface has been developed using PHP through the Symfony framework, Bootstrap as CSS framework and jQuery as JavaScript framework (used for asynchronous actions and to make the interface more dynamic). The choice for PDO (PHP Data Object) is Propel. Every technology selected in the development has been highly studied:

- PHP is a widely developed language for web development. It shows very good performance and popular websites have been developed using it. It has a big community behind, which offers helpful support. The ecosystem (libraries implemented to be used with PHP) is one of the best for web computing and includes libraries for graphical representation, mathematics, etc.
- Symfony framework: at present, for quick development the use of this framework is heavily development. This allows developers to stay focused on main issues and reduce the complexity of common tasks: user management, database access, etc. The selection of Symfony over other alternatives was because it became very popular at the moment web interface development began and the community was very active. Moreover, it is easy to use, contains hundreds of libraries, is powerful and flexible and it performs well.
- JavaScript is used for asynchronous connections with the server in order to offer a very dynamic interface. JavaScript is undisputedly the best for this purpose.
- jQuery is used as JavaScript framework. There are alternatives but jQuery is very well integrated with Symfony, it is widely used and fulfills all system requirements.
- Propel was selected for the PDO library because it allows one to have primary keys with multiple fields. CÆLIS database has been deeply optimized and the use of multi-field primary keys greatly

improves performance in comparison with an auto increment ID (common alternative). At the decision time, only Propel managed such kind of keys.

The web interface has been structured and designed to grow, being able to add the management of other measurement networks or scientific projects. Those projects can share the core of the developed code. This allows one to start projects from existing code instead of starting from scratch, making it quick to add new features. For example, one of these common utilities is the plotting tool. CÆLIS has a very powerful and flexible tool to plot the data. The tool is implemented on the server side using PHP. The benefit of this approach is that, when plotting very huge pieces of data, the plotting is still quick since the data is not transferred to the client (the web browser). Instead, the plot is created in the server and only some tens of kilobytes are transferred to the users. This solution is optimal for treating large pieces of information. A disadvantage of this approach is that the result is less dynamic than an implementation on the client side.

The web interface also implements web services for machine-to-machine communication. These web services allow one to perform common operations such as data transfer from the measurement sites to the server. A great advantage of this approach is that even well-secured external machines can connect to a HTTP server. In some cases, e.g., instruments installed in military bases, they need special permission to set up internal proxies and allow access to the system, but it is widely accepted that HTTP protocol on port 80 can be used everywhere. Alternatively CÆLIS can offer other data transfer alternatives, such as FTP or via e-mail, but the most common is to use the web service.

7 Examples of application

In order to illustrate the capabilities of the system, we will now show a set of examples, focusing on the typical needs of the different users: site managers, network managers (calibration center) and researchers.

7.1 Site manager use case

Site managers are interested in knowing the status of their instruments and retrieving general information about the instruments and their sites. This example will illustrate how a site manager can access all this information.

CÆLIS offers access to all metadata related to each instrument: calibration coefficients, temperature corrections, configuration parameters, filters, etc. The metadata are in general different for each deployment period.

Figure 7 shows the description of the photometer #783 of the AERONET network (registered in CÆLIS and calibrated by GOA). There are three blocks of information: (1) metadata such as calibration coefficients or configuration, (2) network management information such as deployment periods (sites, dates), and (3) administrative information such as hardware inventory of all parts of the instrument.

The continuity of the data sets is an important issue in AERONET. In order to avoid (or minimize) data gaps, often a calibrated instrument is sent to a site to replace an instrument that needs to be calibrated. Hence a number of instruments are rotating inside the network, from site to site. This fact makes it difficult to monitor which instrument is where. CÆLIS offers the information about each site, with the list of instruments and deployment dates in that particular site. This is all easily accessible to site managers.

The illustration in Fig. 8 shows the information of the measurement site placed in Madrid, Spain. Some general information is shown on top of the page, followed by the list of instruments and measurement periods. This information is linked with the instrument information showed in the previous figure so that it is very easy to browse all the information.

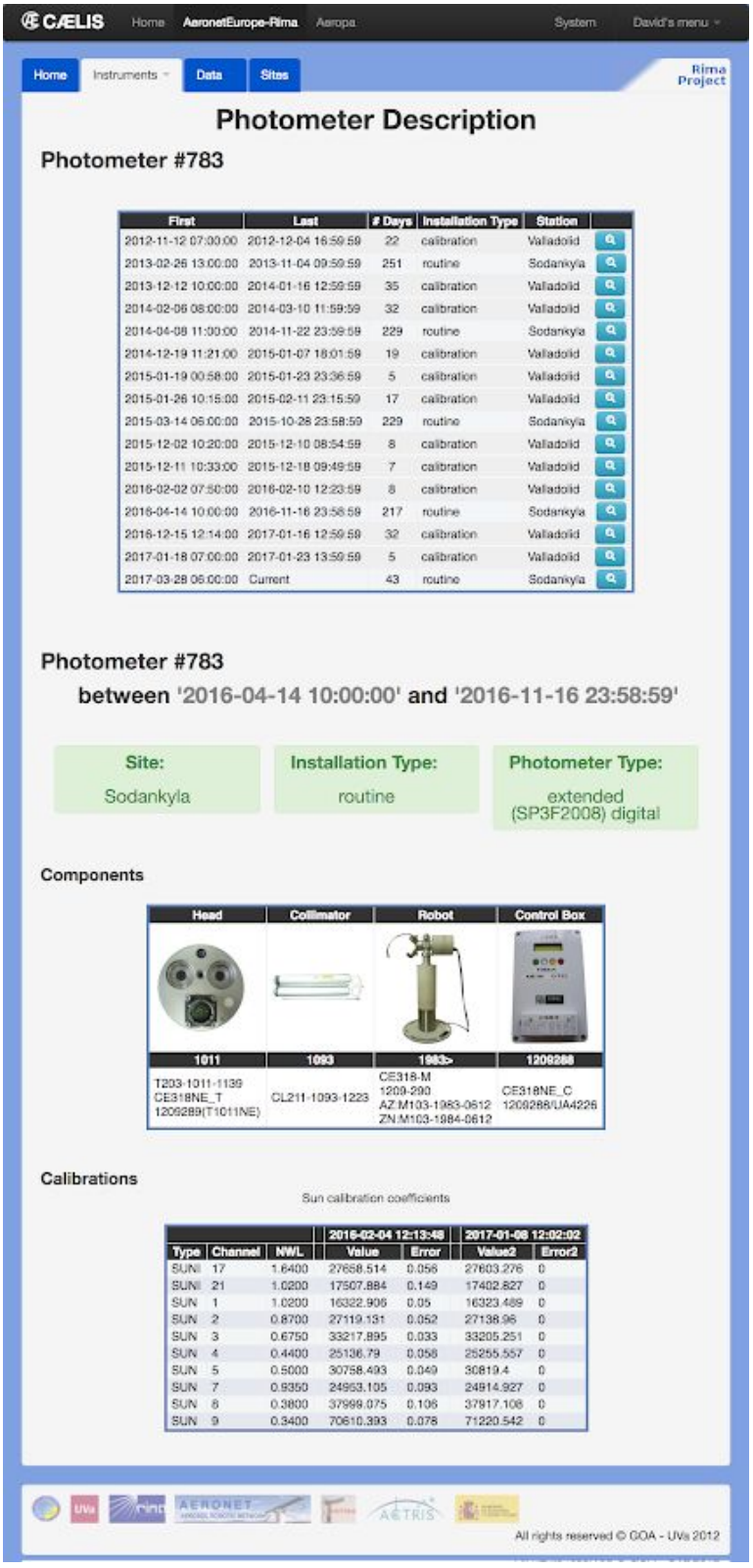

Figure 7. Screenshot (cut and abbreviated) of the photometer description for AERONET photometer #783.

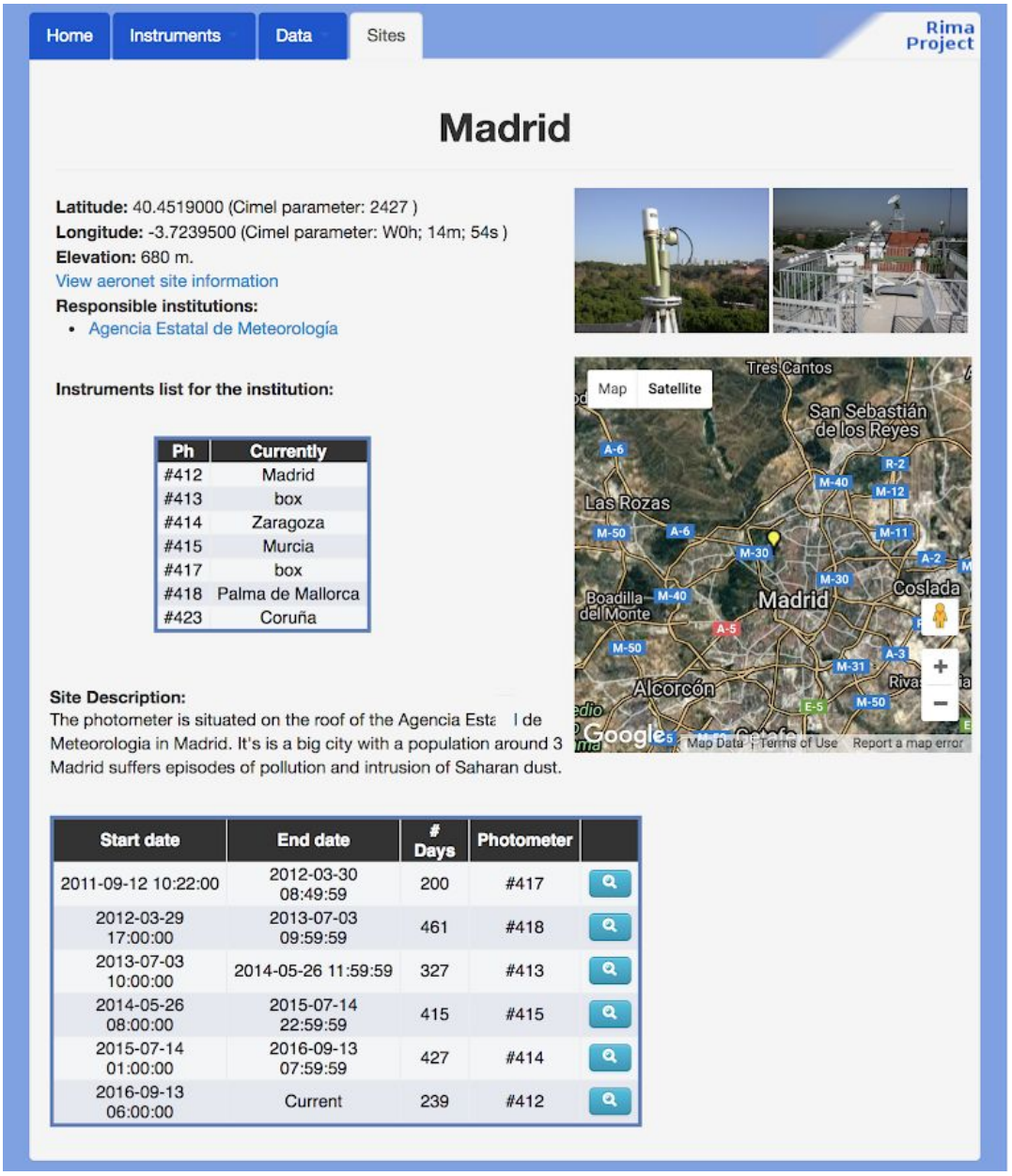

Figure 8. Screenshot of the Madrid site description.

7.2 Network manager use case

One of the most important applications of CÆLIS is the realtime data monitoring. This information is used by the network managers (as well as site managers) and it provides useful information about the instrument performance. The biggest benefit of this powerful tool is that it allows identifying problems in the instrumentation as soon as they appear, raising a flag automatically. The network managers at the calibration center can send a warning to the site managers. If site managers can solve problems quickly, this is of great benefit to data quality and continuity, and thus network quality. The calibration center is continuously monitoring this information in order to warn and assist the site managers if a problem is not quickly solved.

When the system receives new data files from a measurement site, it processes the data, generating new products. From raw measurements it calculates the aerosol optical depth, sky radiances and other products. The last product in the processing chain triggered by the arrival of new data is the alarms. This product studies the new data, metadata and derived products in order to identify malfunctions in the instrumentation.

Figure 9 shows a screenshot of CÆLIS web interface where we can see the status of a specific site over 6 days (this is a calibration site so it has more than one instrument). This page can be customized thanks to filters (sites, instruments, dates, etc.). Finally, useful information can be obtained by simply clicking on specific places. For example, when the photometer number is clicked, instrument status information is shown in graphs (battery voltage, internal temperature, etc.), and when a specific day is selected the user can explore all information (raw data, products) received and processed for that particular day.

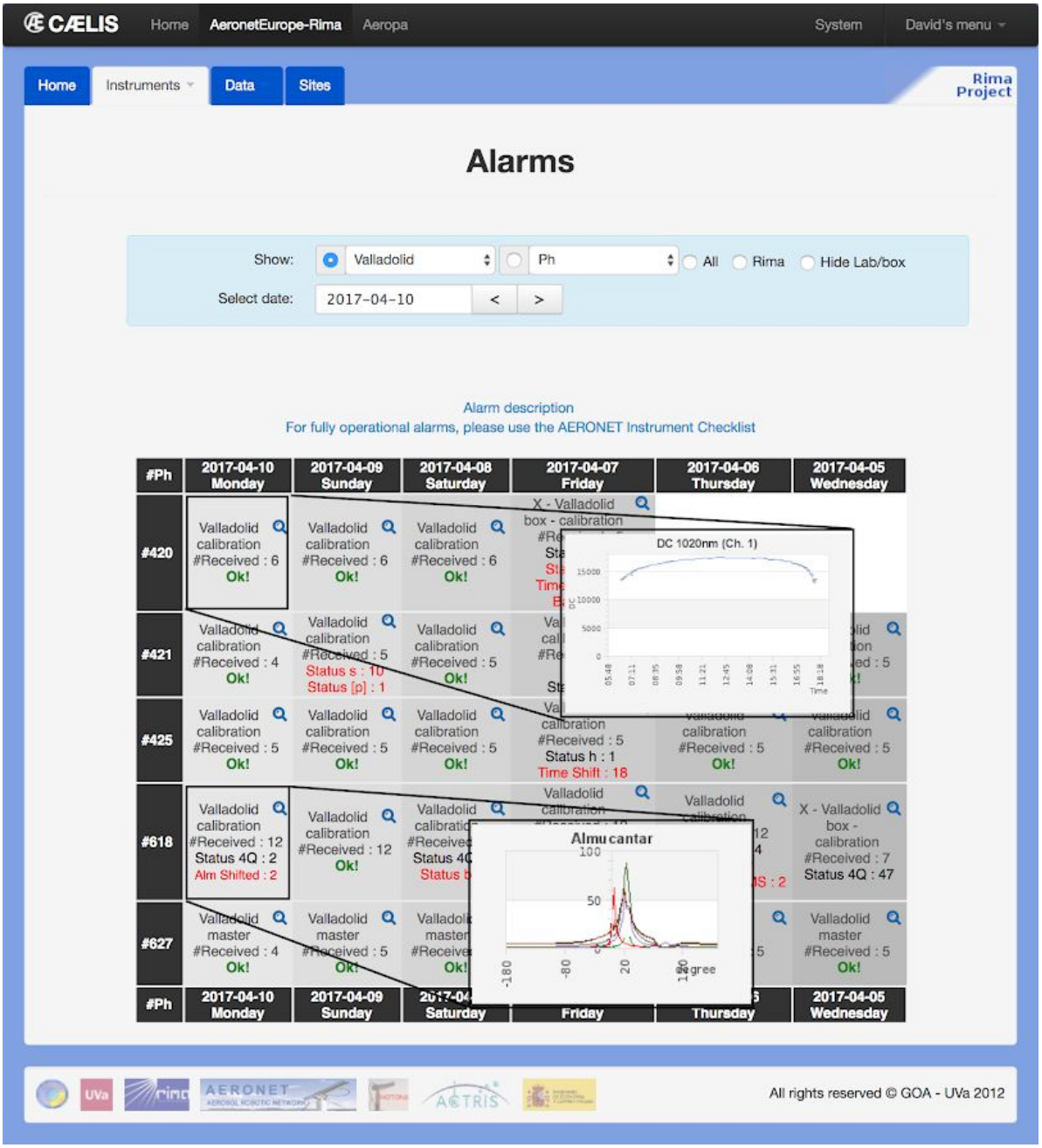

Figure 9. View of real-time flags (alarms) for a specific day at Valladolid site. A zoomed-in view shows how the signal of a good day appears and how a problem is automatically identified. Specifically, photometer #618 on 10 April 2017 has an almucantar where the sun is not in the center (usually from cable tangling).

Every day, calibration centers need to solve instrument issues and multiple questions and this is only possible thanks to deep knowledge of the instrumentation. CÆLIS helps with routine problems and provides very useful information about the data contained in the database. In the case of new issues, the system offers a data viewer which allows one to customize the data to be displayed in a very flexible and powerful way.

Figure 10 shows setting up a specific case in which data from different sources are shown in the same plot in order to help the network manager to understand the problem. We can select one or multiple variables (all available raw data and data products) from one or multiple instruments, and display them for a particular date/time range, with full flexibility in plot configuration (colors, axis, etc.). Specifically, the example shows battery voltage and robot errors. The plot clearly indicates that the power supply stopped working; therefore, the battery is losing charge and the robot cannot operate normally and returns robot errors coinciding with the decreasing battery voltage trend.

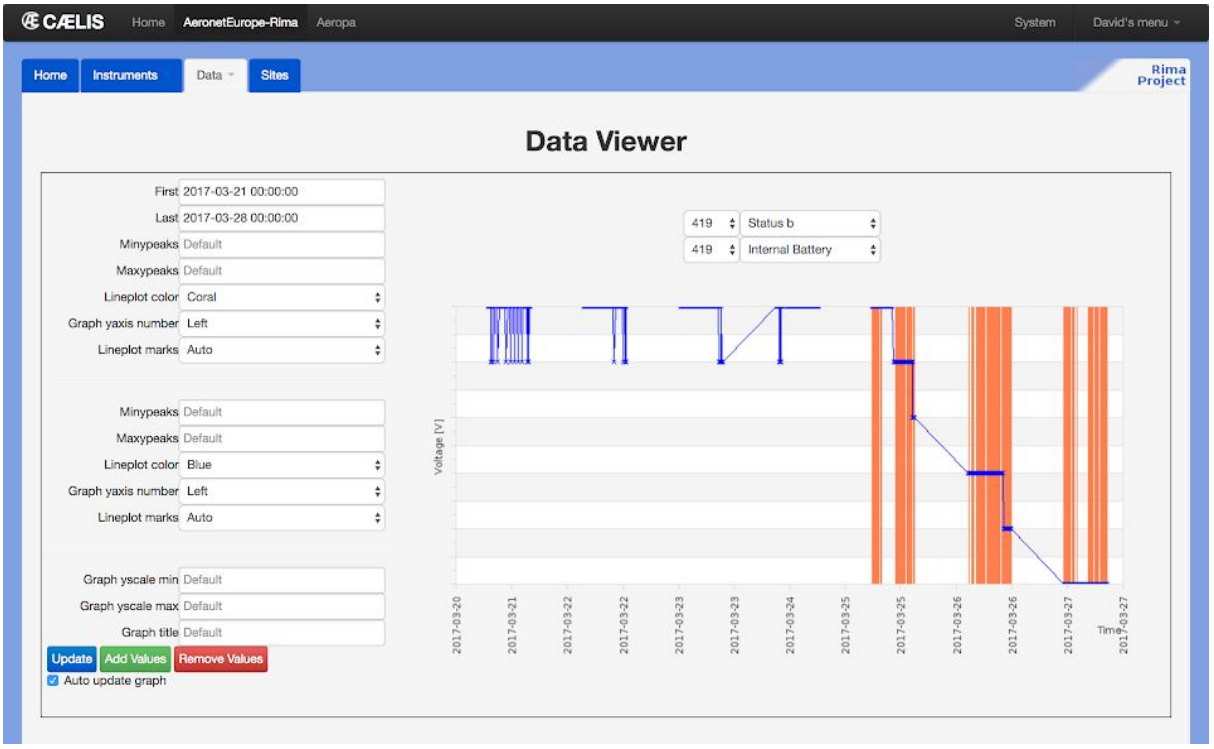

Figure 10. An example of data viewer where an instrumental error can be identified. The power supply is disconnected and the internal battery decreases. When energy it is not enough to move the robot, "status b" (robot) errors appear. Each orange vertical line represents a status error in an specific time.

7.3 Research applications

The following example will show a specific project of the research group with the aim of studying the AERONET database. As part of this project, a relational database which organizes AERONET data was created. By querying this database the user can answer general questions about AERONET sites, including the following: since when has an AERONET site been active? How much data (and at what quality) does a site have? This project re-uses at maximum the core of the system (user access, plot tools, etc.) and lets the developers create a new tool quickly. CÆLIS has been used as "framework" for data analysis. The effort required to develop this system is far less than starting from scratch. The features needed in this development are a tool to assimilate the new data and the specific views that show the results. Additionally, CÆLIS can re-use the database added here in other projects.

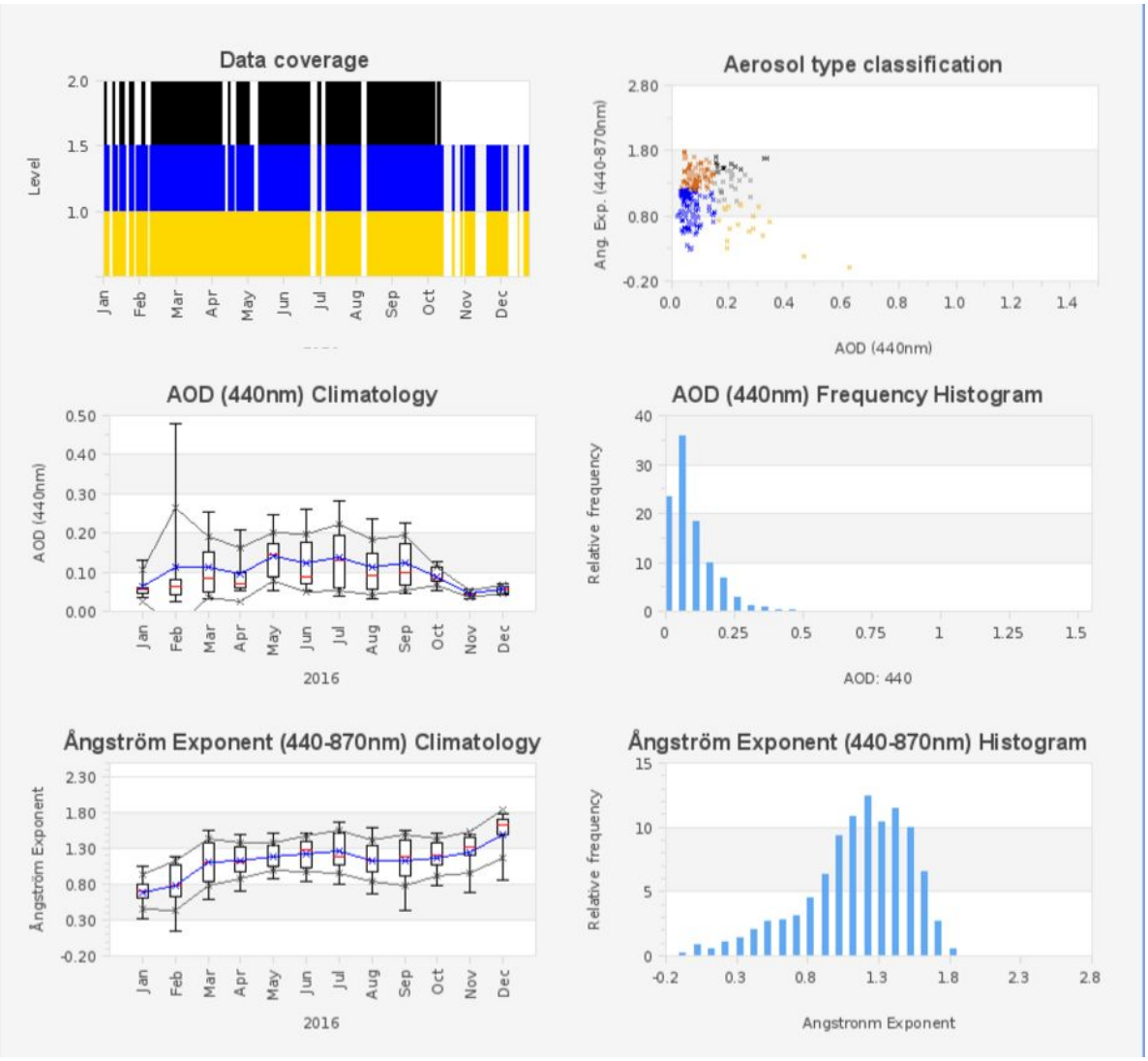

Figure 11. Statistical analysis of aerosol optical depth (AOD) and Ångström exponent (AE) derived from AERONET for Palencia site in 2016: (a) data coverage for level 1.0, 1.5 and 2.0 of the AERONET database; (b) aerosol type classification based on the AOD vs. AE scatter plot. (c) AOD (440 nm) monthly statistics using box plot; (d) frequency histogram for AOD (440 nm); (e) AE monthly statistics using box plot; (f) frequency histogram for AE.

Figure 11 shows the automated aerosol data analysis of an AERONET site (Palencia, Spain). In it, we can see the data coverage (for level 1.0, 1.5 and 2.0 of the AERONET database), monthly statistics of aerosol optical depth and Ångström exponent, frequency histograms and AOD vs. AE scatter plot providing basic aerosol type classification. These plots provide a general overview of the site characteristics in terms of data coverage, aerosol statistics and type classification, which can be used as a first approach in order to select a site for some particular study. Then, based on this general information, the researcher can ask other questions that can be solved by interrogating the database directly. In order to illustrate how it can be done, the next part of the example will show how to identify special aerosol events at the Palencia AERONET site. For this purpose, we need to explore the CÆLIS database. The starting point will be the following questions: how many days of high turbidity occur at the site? How many of these can be classified as desert dust events? To answer these questions we will use the previous (overall) climatology and we will make some assumptions. First, we are going to assume that "a high-turbidity event" takes place when the AOD average is larger than the climatological mean plus 2SD (standard deviations). Based on that assertion, we can write an SQL query that is launched in the system database and will review every single value and return the result. To create this SQL query it is important to have accurate knowledge of the database model in order to obtain the expected results and within a reasonable time. For our particular case, we will use the cml-aod table which contains the general information

about each AOD measurement, and the cml-aod channel which contains AOD information about each specific wavelength channel. First, we check how many days with AOD measurements we have for Palencia AERONET site:

```
SELECT COUNT (a. `date`) FROM `cml-aod` a WHERE station= 'Palencia' GROUP BY DATE (a.
`date`)
```

—

```
Result= 2730
```

Now, we can filter this result by checking during how many days does the AOD (440nm wavelength) have at least 10 observation points greater than 0.31 (climatological average =0.13 and SD=0.09):

```
SELECT DATE (a. `date`) FROM `cml-aod` a LEFT JOIN `cml-aod-channel` c ON a. `ph`=c. `ph`
AND a. `date`=c. `date` WHERE station='Palencia' and c. `wln`= 0.44 and c. `aod`>0.31 and
cloud-screening-v2='cloud-free' GROUP BY DATE (a. `date`) HAVING COUNT(*)> 10 ORDER BY DATE
(a. `date`)
```

—

```
Result 285 days: 12 February 2004, 14 February 2004,..., 14 March 2017
```

Finally, we make another assumption: a desert dust event must have a low Ångström exponent value, lower than the average minus 2 times the standard deviation (climatological average= 1.29, SD=0.37):

```
SELECT DATE (a. `date`) FROM `cml-aod` a LEFT JOIN `cml-aod-channel` c ON a. `ph`=c. `ph`
AND a. `date`=c. `date` WHERE station= 'Palencia' and c. `wln`=0.44 and c. `aod`> 0.31 and
a. `alpha-440-870`<0.55 GROUP BY DATE (a. `date`) HAVING COUNT(*)>10 ORDER BY DATE (a.
`date`)
```

```
— Result= 65
```

These are very strong conditions, which identify the most intense dust event days over the site. Finally, we will show for one selected year (2016), the number of dust event days per month as identified by our assumptions:

```
SELECT MONTH (`date`), COUNT(*) FROM (SELECT DATE (a. `date`) AS `date` FROM `cml-aod` a
LEFT JOIN `cml-aod-channel` c ON a. `ph`= c. `ph` AND a. `date`=c. `date` WHERE station=
'Palencia' AND YEAR (a. `date)=2016 AND c. `wln`=0.44 AND c. `aod`> 0.31 AND a.
`alpha-440-870`<0.55 AND cloud-screening-v2='cloud-free' GROUP BY DATE (a. `date`) HAVING
COUNT(*)>10 ORDER BY DATE (`date`)) dd GROUP BY month (`date`)
```

The result is shown in Fig. 12, where we can see the two peaks of occurrence of Saharan dust episodes over Spain, i.e., February–March (early spring) and May through September, basically the summer months.

This example shows the flexibility and power of a relational database to make data analysis. Using SQL queries, very complex customized questions can be asked and the data can be easily extracted from the database.

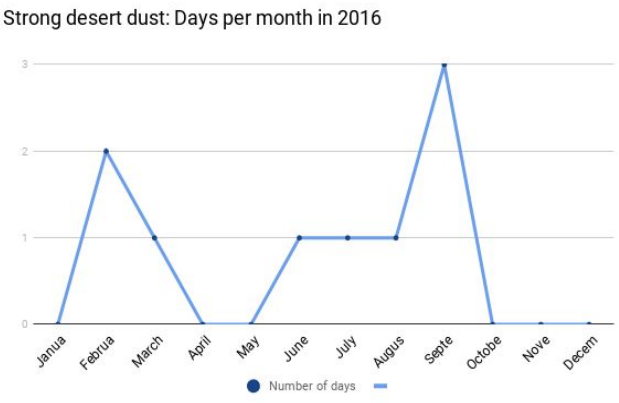

Figure 12. Number of strong Saharan dust event days for each month of the year 2016 over the Palencia AERONET site (Spain) derived from a query to the CÆLIS relational database (see text in Sect. 7.3).

8 Summary and conclusions

The atmospheric aerosol particles are one of the most important contributors to the climate forcing uncertainty. They are currently extensively measured from ground and space, with very different techniques. It is therefore important to develop tools using modern technologies to monitor (quality control), process, analyze and combine those data.

This paper has described the CÆLIS software tool, which has been developed for the management of the photometers that are calibrated and monitored by the calibration facility at the University of Valladolid, Spain, as part of AERONET. CÆLIS is intended to provide management for the photometer network, archive the data and allow data analysis and research. Previously to the development of CÆLIS, these tasks were done manually. The use of this kind of advanced system has reduced the number of human errors and allowed one to perform more in-depth and exhaustive analysis. Thanks to CÆLIS, we are currently receiving and analyzing data from 80 sites, with a quality control system that provides flagging of the data in real time. This provides great benefits to the network management and allows immediate response to instrument malfunction.

The core of the CÆLIS system is built in a relational database. It stores user information (with its privileges), data, meta-data, etc. Around this database, different modules use it and offer different services: a web interface to explore the database and a NRT module to perform processing. All this software can be re-used for extending the system, for instance with other instrument types.

The construction of the database requires a balance between normalization and redundancy. The current system has three different layers of data. Layer 0 contains the raw data and the network management information, layer 1 contains direct products, and layer 2 contains advanced derived products that can be calculated. Each layer is based on the information of the previous one. A keystone of the system is to have correct model of the first layer, i.e., normalized and without redundancy. This helps maintain the congruence of the system. Based on these data, other products can be developed. Depending on the use of these products, some redundancy may be necessary. For instance, pre-calculated products can allow for fast visualization in the web interface, which would be too slow if done on the fly.

The existence of redundancy implies that automated tasks are needed to maintain congruence. This is done by the NRT module, which organizes the actions in separated tasks. The NRT module is always running, thanks to a daemon which is based on a stack of tasks organized by priority, and that decides in every moment what must be done.

Users (site managers, calibration centers, researchers, etc.) can use the web interface for quick access and visualization of data. The relational database is shown to be an appropriate tool for research because it allows one to perform queries and extract data in a fast and very flexible way.

Acknowledgements. The authors gratefully acknowledge the effort of NASA to maintain the AERONET program. This research has received funding from the European Union's Horizon 2020 Research and Innovation Programme under grant agreement no. 654109 (ACTRIS-2). The funding by MINECO (CTM2015-66742-R) and Junta de Castilla y León (VA100P17) is also acknowledged. We thank all the users of CÆLIS for their feedback, especially Emilio Cuevas, Carmen Guirado and Roberto Román.

References

See references section of the PhD Thesis

Artículo 2: Assessment of Sun photometer Langley calibration at the high-elevation sites Mauna Loa and Izaña

Resumen y comentarios

El siguiente artículo hace una descripción de las principales estaciones de calibración de la red AERONET, Mauna Loa e Izaña. Estas estaciones reúnen características únicas que hacen que sean las propuestas por la red AERONET para realizar calibraciones absolutas por el método de Langley que luego son transferidas al resto de instrumentos de la red mediante intercomparación. El artículo es de especial interés en el marco de esta tesis puesto que muestra un ejemplo concreto de cómo el sistema CÆLIS puede ser explotado con fines científicos. Para el desarrollo de este estudio científico, un módulo extra fue implementado en CÆLIS. Este se encarga de calcular las calibraciones por el método de Langley a las medidas tomadas por las estaciones de la red de medidas. Una vez desarrollado el módulo, mediante el uso de consultas SQL, los estadísticos necesarios son fácilmente calculados y extraídos. Esto ha permitido cuantificar en primer lugar las capacidades en número de días adecuados para realizar Langleys en cada estación, y en segundo lugar la incertidumbre de dichas calibraciones.

Las condiciones de Mauna Loa e Izaña para las calibraciones y medidas radiométricas y atmosféricas en general son conocidas desde hace décadas. Sin embargo mientras que la literatura sobre Mauna Loa y sus características es extensa, no lo es sobre Izaña con respecto a las calibraciones de este tipo. Este artículo establece por primera vez las características de Izaña como centro de calibraciones radiométricas, incluyendo su climatología de espesor óptico y un breve análisis de la incidencia de episodios de aerosol Sahariano, su frecuencia y estacionalidad. Una vez descontados este tipo de eventos, se pueden establecer las condiciones de fondo, con gran transparencia y estabilidad de la atmósfera, que permiten aplicar con garantías el método de Langley.

Actualmente estas dos estaciones operan y calibran los instrumentos de referencia de numerosas redes dedicadas a la observación de la atmósfera y la radiación solar. La incertidumbre de las calibraciones es una pieza clave para la calidad de las medidas de esas redes. En el artículo se aborda un tratamiento exhaustivo de las incertidumbres asociadas a los instrumentos, la atmósfera y el propio método, identificando y estimando los errores aleatorios y sistemáticos que están presentes. El aerosol es el factor más importante para asegurar la estabilidad de la transmitancia de la atmósfera durante una calibración Langley, lo que en último término justifica los emplazamientos elegidos. El estudio además viene respaldado por las series de datos de AOD de mayor calidad disponibles, y que han puesto de manifiesto además la excelente operatividad de las redes GAW-PFR y AERONET así como la estabilidad de los instrumentos de referencia utilizados.

Artículo 2

Assessment of Sun photometer Langley calibration at the high-elevation sites Mauna Loa and Izaña

Carlos Toledano[1], Ramiro González[1], David Fuertes[1,2], Emilio Cuevas[3], Thomas F. Eck[4,5], Stelios Kazadzis[6], Natalia Kouremeti[6], Julian Gröbner[6], Philippe Goloub[7], Luc Blarel[7], Roberto Román[1], África Barreto[8,3,1], Alberto Berjón[1], Brent N. Holben[4], and Victoria E. Cachorro[1]

[1] Group of Atmospheric Optics, University of Valladolid (GOA-UVa), Spain
[2] GRASP-SAS, Lille, France
[3] Izaña Atmospheric Research Center, Meteorological State Agency of Spain (AEMET), Tenerife, Spain
[4] NASA Goddard Space Flight Center, Greenbelt, MD, USA
[5] Universities Space Research Association, Columbia, MD, USA
[6] Physikalisch-Meteorologisches Observatorium Davos, World Radiation Center – PMOD/WRC, Davos, Switzerland
[7] Laboratory of Atmospheric Optics, University of Lille, Villeneuve d'Ascq, France
[8] Cimel Electronique, Paris, France

Correspondence to: Carlos Toledano (toledano@goa.uva.es)

Abstract. The aim of this paper is to analyze the suitability of the high-mountain stations Mauna Loa and Izaña for Langley plot calibration of Sun photometers. Thus the aerosol optical depth (AOD) characteristics and seasonality, as well as the cloudiness, have been investigated in order to provide a robust estimation of the calibration uncertainty, as well as the number of days that are suitable for Langley calibrations. The data used for the investigations belong to AERONET and GAW-PFR networks, which maintain reference Sun photometers at these stations with long measurement records: 22 years at Mauna Loa and 15 years at Izaña. In terms of clear sky and stable aerosol conditions, Mauna Loa (3397m a.s.l.) exhibits on average of 377 Langleys (243 morning and 134 afternoon) per year suitable for Langley plot calibration, whereas Izaña (2373m a.s.l.) shows 343 Langleys (187 morning and 155 afternoon) per year. The background AOD(500nm) values, on days that are favorable for Langley calibrations, are in the range 0.01-0.02 throughout the year, with well defined seasonality that exhibits a spring maximum at both stations plus a slight summer increase at Izaña. The statistical analysis of the long-term determination of extraterrestrial signals yields to a calibration uncertainty of ~0.25-0.5%, this uncertainty being smaller in the visible and near infrared and larger in the ultraviolet wavelengths. This is due to atmospheric variability produced by changes in several factors, mainly the aerosol optical depth. The uncertainty cannot be reduced based only on quality criteria of individual Langely plots and averaging over several days is shown to reduce the uncertainty to the needed levels for reference sun photometers.

1 Introduction

The Langley plot method (Shaw, 1983) is widely used for absolute calibration of Sun photometers. The main requirement for the method to be successful is the atmospheric transmittance stability during the period in which direct Sun observations are acquired at varying solar elevations. Apart from the original (classic) approach, several variations have been developed (e.g. Herman et al., 1981; Forgan, 1994; Campanelli et al., 2004). These are mostly intended to reduce the uncertainty and calibration error in case of changes in the atmospheric transmittance during the observation period.

Sun photometer networks like the AErosol RObotic NETwork (AERONET, Holben et al., 1998), the Global Atmospheric Watch – Precision Filter Radiometer (GAW-PFR, Wehrli, 2005), Skyradiometer Network (SKYNET, Nakajima et al., 1996), use the Langley plot method to calibrate the direct Sun channels, i.e. obtain extraterrestrial signals (V_0), with the aim of calculating aerosol optical depth (AOD). Although some networks (e.g. SKYNET) perform Langleys 'on site' (Campanelli et al., 2007), networks like AERONET and GAW only use high altitude stations to provide accurate absolute calibration with the Langley plot method in the so-called master instruments. The calibration is later transferred to field instruments by comparison in a calibration platform.

The AERONET network currently has 3 calibration centers: Goddard Space Flight Center (GSFC, in Greenbelt, Maryland), Laboratory of Atmospheric Optics (LOA, in Lille/Carpentras, France) and Group of Atmospheric Optics (GOA, in Valladolid, Spain). The GSFC master instruments are calibrated at the Mauna Loa Observatory, in Hawaii. The LOA and GOA masters are calibrated at Izaña Observatory. The GAW-PFR network is managed by the Physikalisch Meteorologisches Observatorium Davos, World Radiation Center (PMOD/WRC) at Davos (Switzerland). It uses a triad of reference (PFR) instruments at Davos which are considered by the World Meteorological Organization (WMO-GAW) as the reference instrument triad for AOD measurements. It also operates permanent reference instruments at Izaña and at Mauna Loa, that return periodically (every six months) to PMOD/WRC and are compared with the reference triad (Kazadzis et al., 2018b).

Mauna Loa is a reference site for radiometric observations and calibrations. It was very early considered as an ideal place for calibration of Sun photometers using the Langley technique (Shaw, 1979), hence it hosts reference instruments of the main radiometric networks. Many studies have already reported the atmospheric aerosol characteristics at Mauna Loa (Bodhaine et al., 1981, 1992; Dutton et al., 1994; Andrews et al., 2011; Hyslop et al., 2013), to cite some. Numerous studies about aerosol characteristics at Izaña have also been conducted (e.g. Prospero et al., 1995; Rodríguez et al., 2011; García et al., 2016). Izaña is also commonly used for accurate Langley plot calibrations (even in Moon photometry, Barreto et al. (2013, 2016)), although the site performance has not yet been quantitatively evaluated in this sense.

After years of continuous Sun photometer observations at the Mauna Loa and Izaña observatories, long and high quality measurement records are available, and the quantification of the calibration performance can be accomplished with the support of robust datasets. Therefore, the aim of this paper is to analyze the capability of the two high-mountain stations Mauna Loa and Izaña for Langley plot calibration, in terms of aerosol characteristics, seasonality and cloudiness; and provide statistically robust quantification of calibration uncertainty. The data used for the investigations belong to AERONET and GAW-PFR networks, both having reference instruments at these stations with long measurement records. Several factors and physical processes affecting the performance of the Langley plots are analyzed.

2 Sites and instrumentation

2.1 The Mauna Loa and Izaña observatories

The atmospheric stability required for the Langley plot method is more easily achieved in remote, high-elevation locations, especially because the AOD is very low and stable. Several characteristics make Izaña and Mauna Loa Observatories to be unique for this purpose.

The Izaña Observatory (Tenerife, Spain, 28˚N, 16˚W) is located at the top of a mountain plateau, 2373 m above sea level, about 15 km away from the Teide peak. It is run by the Meteorological State Agency of Spain (AEMET, see http://izana.aemet.es). Izaña is normally above a strong temperature inversion layer and therefore free of local anthropogenic influence. It is a World Meteorological Organization (WMO) Global Atmospheric Watch (GAW) program station as well as WMO-CIMO Testbed for Aerosols and Water Vapour Remote Sensing Instruments (http://testbed.aemet.es). It hosts reference instruments of several radiometric networks (e.g. Regional Brewer Calibration Centre, GAW-PFR, AERONET, PANDORA, etc.). Details of the Izaña facilities and activities are described in Cuevas et al. (2017b).

The Mauna Loa Observatory (Big Island, Hawaii, 19˚N, 155˚W) is located on the slope of Mauna Loa volcano, 3397 m. above sea level. It was created in 1956 and run by the National Oceanic and Atmospheric Administration (NOAA, see https://www.esrl.noaa.gov/gmd/obop/mlo). It is the reference observatory for a wide set of atmospheric composition research programs (greenhouse gases, carbon cycle, aerosols, water vapor, ozone, trace gases, etc.) and has been continuously monitoring and collecting data related to the atmospheric change.

Both observatories are located in the free troposphere. The aerosol content above is very low (see section 3), as well as the water vapor column (PWV, precipitable water vapor) and the molecular (Rayleigh) optical depth, making it easier to ensure stable conditions during a Langley plot calibration. For instance the water vapor column at Izaña ranges from 0.2cm in winter to 0.7cm in summer (monthly averages, AERONET-derived, see Table S1) whereas in the nearby site 'Santa_Cruz_Tenerife' located at sea level, the PWV ranges from 1.5cm to 2.5cm. The atmosphere is therefore very stable, especially in the mornings. In the afternoon, local convection can rise the boundary layer up to the Observatory level, especially at Mauna Loa. The strong inversion associated to the Trade Wind at Izaña very often prevents from boundary layer to reach the observatory (Carrillo et al., 2015).

Another important feature to assure the success of the Langley calibration, is to reduce as much as possible the time needed to acquire Sun observations at a wide optical air mass range, in order to avoid possible atmospheric changes. The latitude of Mauna Loa and Izaña, close to the tropics, make the air mass to change rapidly from 7 to 2, i.e. solar elevations from 8˚ to 30˚ approximately, lasting about 1:35h to 2:15h depending on the season (the duration is few minutes shorter for Mauna Loa). Just for comparison, at 37˚ latitude, the time in winter to change from air mass 7 to 2 is more than 3h. At higher latitudes, air mass 2 is not reached in winter.

The cloudiness is another main aspect in performing Langleys. Even thin high clouds perturb the Langley calibration dramatically. To evaluate the sky conditions with the same methodology at both locations, a cloud satellite product has been used. In particular, the cloud products (GDP-4.8 version) of the algorithms OCRA and ROCCIN (Loyola R. et al., 2010) from GOME-2 onboard MetOp-A have been used to evaluate cloud fraction and cloud top height respectively. The cloud top height is a crucial parameter due to the high elevation of the observatories. The monthly mean cloud fraction and number of clear sky days, defined as cloud fraction < 0.1, have been evaluated over the period 2007-2014. If the cloud top height was lower than the site elevation, the cloud fraction was considered 0. The results are shown in Table 1. On average, Mauna Loa exhibits 24 clear sky days per month, whereas Izaña has 20. There is some seasonal variability, being the period between May and August the most sunny at both locations. However it is possible that very thin cirrus (optical depth < 0.1) are not detectable in these satellite products. This will be taken into account in the analysis of the Langley regressions (section 4).

Besides the necessary atmospheric conditions, the facility itself including permanent and trained staff, convenient access and easy logistics are also an important point to consider. Actually the capacity of the measurement platforms themselves is a limitation given that many radiometric networks have reference instruments in these two observatories. This limitation together with the relatively expensive shipping to such remote locations, is the main reason for AERONET (and many other networks) to calibrate master instruments with the Langley method at Izaña and Mauna Loa, and then transfer the absolute calibration to field instruments in calibration platforms located in much more accessible facilities at GSFC, Carpentras, Davos, Valladolid, etc. As example, 15 to 20 calibrations of AERONET master instruments are accomplished every year at Izaña. Of course the calibration uncertainty of the field instruments is therefore less than that of masters, but logistically it is not reasonable to ship several hundred instruments every year to Mauna Loa or Izaña. The AOD calibration uncertainty needed for field instruments (0.01 to 0.02 absolute error as recommended by Kazadzis (2016)) can be achieved by means of side-by-side inter-calibration (Holben et al., 1998; Eck et al., 1999). Possible instrument fluctuations due to shipping are controlled by using always a couple of masters that travel together and rigorous comparison of master instruments at the inter-calibration sites. Ratio of direct sun signals between the two masters must keep below 1% variability.

	Mauna Loa				Izaña			
	Mean Cloud cover fraction	Frequency of cloud cover < 0.1 (%)	Mean N. days fraction< 0.1	N days	Mean Cloud cover fraction	Frequency of cloud cover < 0.1 (%)	Mean N. days fraction< 0.1	N days
Jan	0.06	88.9	28	162	0.13	60.67	19	178
Feb	0.11	75.0	21	164	0.12	67.96	19	181
Mar	0.14	70.8	22	171	0.14	61.22	19	196
Apr	0.11	76.1	23	155	0.11	58.48	18	171
May	0.06	81.9	25	171	0.08	68.85	21	183
Jun	0.05	85.6	26	160	0.05	80.56	24	180
Jul	0.03	86.2	27	159	0.06	76.24	24	181
Aug	0.02	91.2	28	159	0.08	66.47	21	173
Sep	0.07	79.2	24	149	0.14	53.29	16	167
Oct	0.09	76.9	24	156	0.16	58.48	18	171
Nov	0.12	72.9	22	155	0.15	57.74	17	168
Dec	0.19	68.2	21	157	0.16	60.34	19	174
YEAR	0.09	79.4	290	1918	0.11	64.34	235	2123

Table 1. Cloud fraction and number of clear sky days over Mauna Loa and Izaña observatories, derived from GOME-2 cloud products (Loyola R. et al., 2010) over 2007-2014 . Clear sky is defined for the 8-year period is also provided.

2.2 Instrumentation and datasets

The AERONET standard instrument is the Cimel-318, that has been extensively described (e.g. Holben et al., 1998). It is an automatic radiometer equipped with a 2-axis robot, that collects both direct Sun and sky radiance observations at selected wavelengths in the range 340 to 1640nm. Three generations of Cimels have been used in AERONET: the first (starting the early 1990's) were analog instruments. After 2002 the digital version (Cimel 318N) came into play, and after 2013 the socalled Triple instruments (Cimel 318T, after Sun-Sky-Moon measurement capability) started to operate. All three types of instruments can still be found nowadays in AERONET.

The Precision Filter Radiometer of the GAW-PFR network is described in detail in Wehrli (2005). It uses four AOD channels at 368, 412, 500 and 862 nm and needs a separate solar tracker. It is designed for long-term stability, therefore the detectors are behind a shutter except for the brief sampling periods and the instrument is stabilized in temperature and hermetically sealed, having internal atmosphere of pressurized dry nitrogen.

Both instruments use interference filters to select the wavelengths, with full width at half maximum of about 2-10nm (filters are narrower in the ultraviolet wavelengths). The PFR uses one optical path and detector per channel, allowing simultaneous (and continuous) observation in the 4 channels. Conversely, the Cimel has a single detector (or 2 in the case of instruments with 1640nm channel) and the filters are mounted in a rotating filter wheel. The Cimel configuration allows more wavelength channels (up to 10) but they can only be measured sequentially. In automatic operation, the Cimel takes a triplet measurement (3 separate measurements in a 1-minute interval) every 15 minutes (or 3 minutes, in the high frequency sampling mode), although during the 'Langley sequence' –am or pm for air masses larger than 2– the Cimel measures at fixed solar elevations, with higher frequency.

The AERONET observations at Mauna Loa started in 1994. The observation period used in this study spans 20 years (1997-2016). Within this period, 210 deployments of 22 different master photometers were done. This gives an idea of the frequent swap of Cimel instruments, once per month on average. The AERONET measurements at Izaña started in 2003 and had 37 deployments (71 days on average, 16 different instruments) until January 2011, when instrument #244 was set as permanent reference. The GAW-PFR measurements started in 2000 and 2001 at Mauna Loa and Izaña respectively. The list of PFR radiometers deployed at each location is given in Table 2. The high long-term stability of these radiometers will be shown in section 4.

(a) Mauna Loa

Instrument	Start date	End date	N days
PFR #27	1-Jan-2000	1-Sep-2005	2070
PFR #22	2-Sep-2005	16-Jun-2010	1748
PFR #24	16-Jun-2010	31-Dec-2014	1659

(b) Izaña

Instrument	Start date	End date	N days
PFR #25	9-Jun-2001	25-Feb-2009	2818
PFR #06	14-May-2009	1-Jan-2013	1328
PFR #21	2-Jan-2013	30-Apr-2014	483
PFR #06	1-May-2014	31-Dec-2014	244

Table 2. Deployment periods of GAW-PFR instruments at Mauna Loa and Izaña. (a) Mauna Loa

The database tool 'CÆLIS' (Fuertes et al., 2017, www.caelis.uva.es), developed at the Group of Atmospheric Optics, University of Valladolid (GOA-UVa) since 2008, has been used to facilitate the organization and extraction of data. It consists of a relational database, a web interface and a real-time data processing module. The specific software used in this work will be better described in section 4.1. The 'demonstrat' software tool (Holben et al., 1998) was used to browse the AERONET data and construct the AERONET data sets at the two stations, given the frequent swap out of master instruments (every 3-4 months). Conversely the GAW-PFR data sets are composed by few instruments deployed for very long periods.

The two approaches have been therefore different, being AERONET priority to frequently recalibrate and maintain the master instruments, shipping them to the inter-calibration platforms, whereas GAW-PFR has prioritized the stability in the long-term observations, in order to facilitate the assessment of trends in the aerosol content, well in line with the GAW aims. However in the last years (since 2011) AERONET has a permanent instrument at Izaña, not involved in the rotation of masters between this site and the inter-calibration platforms.

3 Aerosol Climatology

The aerosol characteristics at Mauna Loa and Izaña observatories can be well established thanks to the long records of the AERONET and GAW-PFR networks. The very low aerosol optical depth is a general feature at Mauna Loa throughout the year. At Izaña, very clean days alternate with some desert dust intrusions, especially in spring and summer (Cuevas et al., 2017a). The overall statistics for aerosol optical depth at 500nm wavelength is provided in Figure 1 and Table S1. These are computed by averaging all available daily mean values in the investigated period within a certain month of the year. As indicated above, 20 years of continuous AERONET data are used for Mauna Loa and 13 years for Izaña. Version 2 AERONET data have been used in this analysis. A detailed description of the direct sun algorithm, including gaseous absorption spectral corrections, is provided in the AERONET website (see https://aeronet.gsfc.nasa.gov/new_web/publications.html). As for GAW-PFR data, 15 years are available at Mauna Loa and 14 years at Izaña. A detailed description of the AOD derivation is given by Kazadzis et al. (2018b). Both are depicted in Figure 1. Although the measurement periods are different, the long-term averages of AERONET and GAW-PFR differ less than 0.01 for all months, with mean absolute difference of 0.0035 for the monthly means.

The cloud screening methodologies of AERONET and GAW differ, thus contributing to differences in monthly means. AERONET uses the algorithm by Smirnov et al. (2000), based on temporal variance as utilized by AERONET. GAW data are cloud screened following the methodology by Wehrli (2008). Other authors have accomplished extensive comparison of Cimel and PFR observations (Kim et al., 2008; Kazadzis et al., 2014, 2016, 2018a) with excellent results.

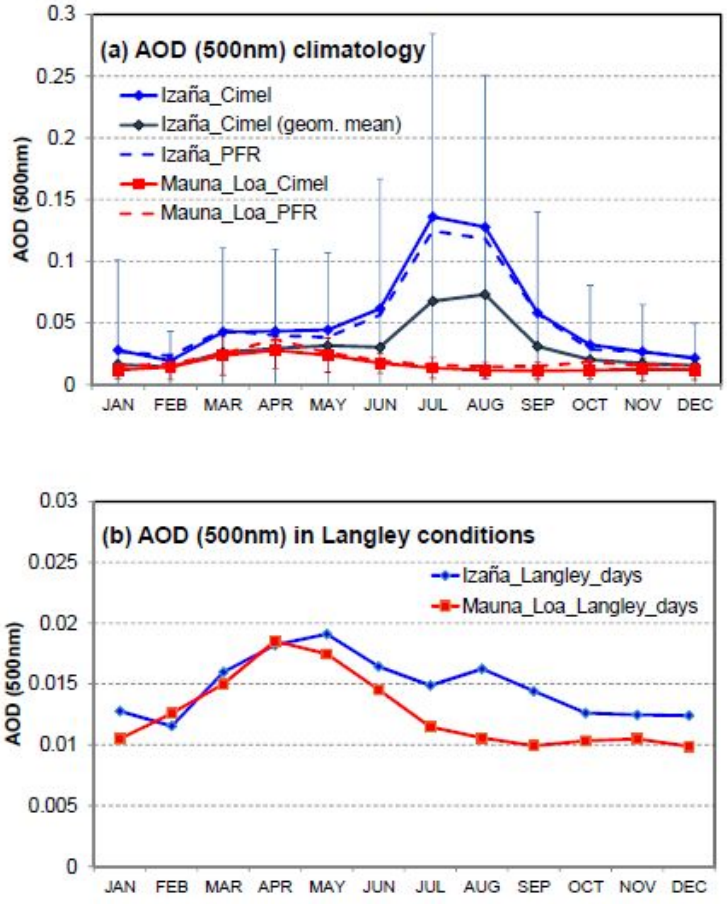

Figure 1. (a) Monthly mean aerosol optical depth (500nm) at Mauna Loa (1994-2016) and Izaña (2004-2016) for AERONET and GAW-PFR. Bars indicate ±1 monthly standard deviation. Black line indicates geometric mean values for AOD at Izaña (in contrast to the arithmetic mean for the other variables). (b) Monthly mean aerosol optical depth (500nm) for the days fulfilling the criteria for Langley calibration as given in section 4.1.

Regarding Mauna Loa (Fig. 1), the AOD (500nm) has a mean value of 0.016 (geometric mean 0.013), peaks in March with 0.028 and is minimum in August-September, with 0.011. The AOD (500nm) daily mean only exceeded 0.05 in 0.6% of the days. The monthly standard deviations indicate that the variability within each month is very low too. The largest variability is found from March through May, with monthly standard deviations about 0.015. The Ångström exponent AE(440-870nm), also given in Table S1, shows a mean value of 1.25, that is indicative of dominance by fine mode particles. The AE is slightly lower in May (1.02), indicating somewhat greater proportion of coarse mode particles. The spring peak in aerosol concentration at Mauna Loa is a well documented phenomenon and it is attributed to the advection of Asian dust (e.g. Bodhaine et al., 1981; Perry et al., 1999). The uncertainty in AE is very high at MLO since the uncertainty in AOD (about 0.002 − 0.003) is quite large in relation to the ~ 0.01 measured AOD. Thus the AE values at MLO should be in general taken with caution.

The low AOD makes it difficult to investigate any other aerosol optical and microphysical properties, in particular those derived from the inversion of sky radiances for the AERONET instruments using the Dubovik inversion code (Dubovik and King, 2000; Dubovik et al., 2006). Such properties, like single scattering albedo or complex refractive index, are generally not quality assured if AOD(440nm) is less than 0.4 (Holben et al., 2006). Given that the AOD stability is the main requirement for Langley calibrations, in-depth investigation of the aerosol properties is not in the scope of this work and will not be considered here.

The mean AOD (500nm) at Izaña Observatory is 0.054 (geometric mean 0.029), with important seasonal variability. The geometric mean is often more suitable for AOD statistics, because the log-normal probability

distribution is a better reference than a normal distribution for most aerosol types (O'Neill et al., 2000). Monthly means range from 0.02 –November through February– up to 0.14 in July and August (geometric means 0.07 on both months, see Fig. 1). The transport of Saharan dust over Izaña in Summer enhances the aerosol content and the variability, as indicated by the large monthly standard deviations up to 0.15 in July. The Ångström exponent, that has a mean value of 0.99, exhibits a clear decrease in the summer months down to 0.54 in August, confirming the predominance of coarse dust particles. Despite this variability, 25th percentile of AOD is < 0.03 in July and August, indicating a relevant portion of pristine days during the summer months.

In order to assess the dust event frequency over Izaña, the presence of dust has been investigated within the 13-year AERONET database. Following similar methodology that proposed by Toledano et al. (2007), dust events were identified by daily mean AOD(870nm) > 0.05 and AE < 0.6, which approximately correspond to the 75th and 25th percentiles of these magnitudes in the Izaña dataset. This simple approach results in the identification of 58 dust event days per year on average. The seasonal distribution is not even. On the contrary, dust events are very rare from October to February (1-2 days per month), while July and August, on average, exhibit 16 and 17 dust event days respectively, which cause the higher AOD values observed in these months (Fig. 1). Similar results, even with slightly different methodology, were achieved by Guirado-Fuentes (2015).

The dust occurrence over Izaña in summer may yield to the incorrect conclusion that, during several months each year, the Langley calibrations are not possible in this station. But as it was previously indicated, dust events alternate with very clean (background) conditions. To demonstrate this important feature, all daily means of AOD (440nm) over 2004-2014 have been plotted as a function of the day of the year (Figure 2b). For comparison, Figure 2a displays the same plot for Mauna Loa. As can be seen, most of the daily observations at Izaña (about 75%) correspond to background values. Higher daily means, corresponding to dust events, are evident from June to September. Dust events are less frequent and with lower AOD outside those months. Note that dust transport in winter occurs at much lower altitude than in summer, therefore the aerosol column above the observatory is minor in winter as compared to summer dust events, in which dust can reach 5 km height (Ansmann et al., 2011; Guirado-Fuentes, 2015; Cuevas et al., 2015). Izaña is therefore a privileged location for studying Saharan dust within the Saharan Air Layer.

Another feature of the AOD seasonal cycle is the increase of the background AOD (lowest values) from March to May, with maximum background of about day of the year equal to 120, i.e. beginning of May. This is not exactly in phase with the spring AOD peak at Mauna Loa (in April). The background AOD is in May about 0.016 (440nm), whereas the rest of the year it is as low as AOD=0.005. Interestingly, this enhanced background occurs both at Mauna Loa and Izaña (Figure 2), although it is unclear whether these two seasonal maxima have the same origin.

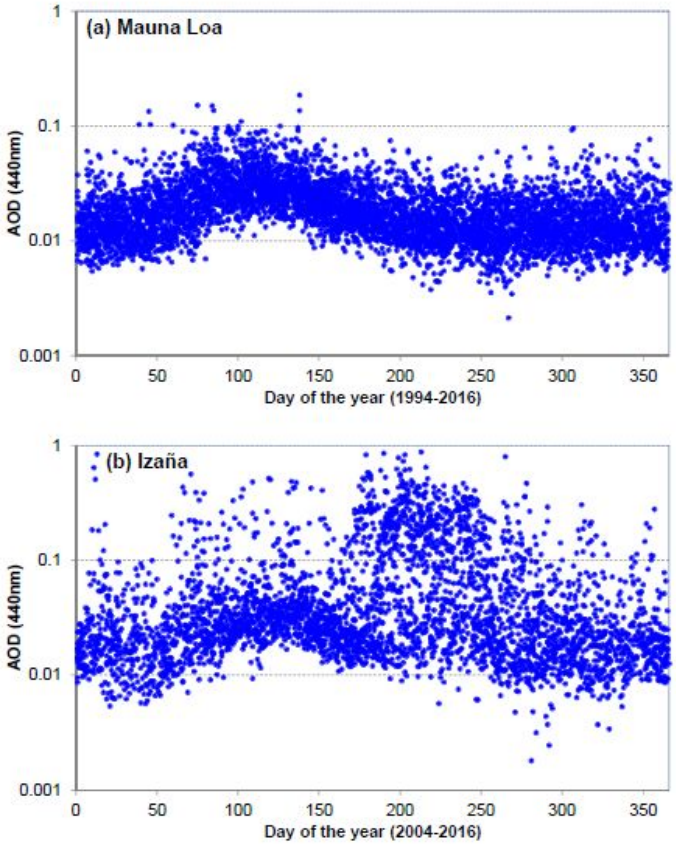

Figure 2. Daily means of aerosol optical depth (440nm) as a function of the day of the year at: (a) Mauna Loa (1994-2016) and (b) Izaña (2004-2016) using AERONET data.

4 Assessment of calibration capability

4.1 Langley plot analysis

In order to investigate the station capability for Langley calibration, a software tool has been developed and integrated in CÆLIS. It performs two Langley plots for each available day (morning and afternoon, i.e. 'am' and 'pm') and stores the resulting extraterrestrial signal together with a set of regression statistics: correlation coefficient, standard deviation of the fit (σ), number of valid points, air mass range, fitting error for slope and intercept, etc. The routine performs the linear fit from airmass 7 to 2 (This differs from the airmass range used in AERONET for Langley calibrations, i.e. 5 to 2, and 4 to 2 for the two UV channels (380 and 340 nm), thereby avoiding errors in optical airmass determination that increase significantly at larger airmass (Russell et al., 1993)), and analyzes the standard deviation of the fit. If the residual for some point is larger than 2σ, the point is eliminated and a new iteration starts until all points are within 2σ or the number of remaining points is less than 10. If $\sigma > 0.2$ or there is not enough number of points, the process stops.

This type of automatic and iterative analysis, allows identifying whether a certain day is suitable for Langley plot calibration according to pre-established quality thresholds. In our study, we have considered that for a certain period (morning or afternoon) within a particular day, the Langley calibration is possible if $\sigma < 0.006$, the number of valid points is > 33% of the initial number of observations (Harrison and Michalsky, 1994) and AOD(500nm) < 0.025. These criteria can be chosen based on experience (Kiedron and Michalsky, 2016), but they are not critical in this study because we do not intend to perform the calibration of any particular instrument. For instance, for calibration purposes a higher threshold in σ should be used for the UV wavelengths. However our purpose here is to analyze the number of suitable Langley plots in a climatological

sense. Other thresholds were tested and revealed no qualitative changes in the analysis. Other statistical indicators of the linear regression quality, such as the correlation coefficient, do not have enough sensitivity to be used for this purpose.

It is then straightforward to search the database for Langley periods fulfilling the indicated criteria. The results are given in Figure 3, in which the average number of Langley plots for each month is indicated, as well as the standard deviation resulting from the year-to-year variability. Morning and afternoon Langleys are given separately. It is common practice to use only mornings for Langley calibration, but in principle both periods are possible and therefore will be both considered in our study. Overall, Mauna Loa meets the selected criteria in 377 Langleys per year (243 'am' calibrations and 134 'pm'). This means, on average, about 20 morning Langleys and 11 afternoon Langleys per month. Izaña meets the criteria in 343 Langleys per year (187 'am' calibrations and 155 'pm'), which means 15 morning and 13 afternoon Langleys per month. There is a slight seasonality, with less suitable days in spring and fall at Mauna Loa and better conditions from May through September and December-January. At Izaña the dust events reduce the number of suitable days in July-August, and the best time of the year is May-June.

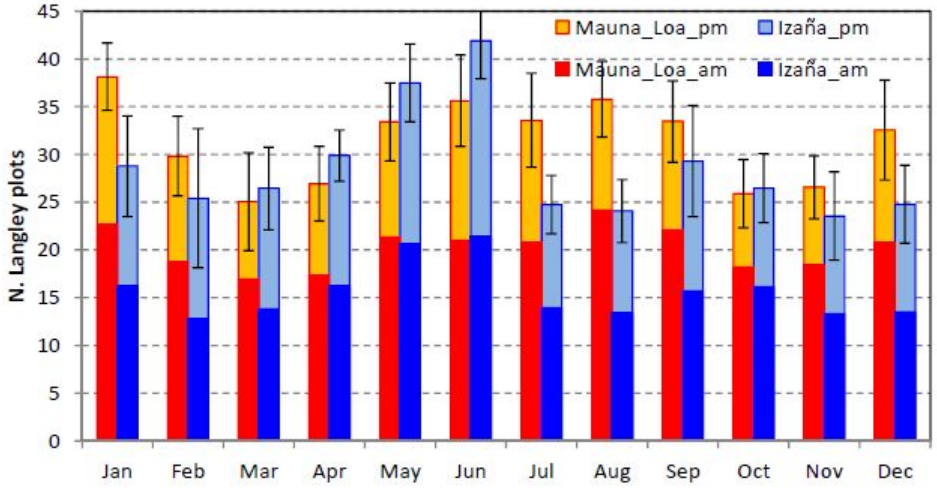

Figure 3. Mean number of suitable Langley calibrations per month at Mauna Loa and Izaña based on GAW-PFR and AERONET data (see text). Bars indicate ±1 standard deviation for each month due to year-to-year variability. Morning ('am') and afternoon ('pm') Langley plot calibrations are given separately.

The AOD (500nm) for the selected 'Langley' days, is given in Fig. 1b, in which monthly averages are calculated for comparison with the overall climatology (Fig. 1a). This plot provides the seasonality of the background AOD values, that exhibits a spring maximum at both stations plus a slight summer increase at Izaña.

4.2 Calibration and statistical uncertainty

A major issue pointed out by many authors is that, despite the available Langley plots can be screened with very strict criteria, a certain variability, i.e. uncertainty in the extraterrestrial signals, remains (Kazadzis, 2016). The noise is caused by small changes in atmospheric transmission having a hyperbolic (solar air mass) dependence, thus they do not affect the linearity of the Langley plot but may change the result (Shaw, 1976; Cachorro et al., 2004). These changes in atmospheric transmission are mainly due to AOD variations, which affect the slope and/or y-intersect of the Langley plots and cannot be identified with Langley plots alone (Marenco, 2007). For instance, a small variation of 0.005 in AOD could produce ~0.5% departure in the extraterrestrial signal. Other components like ozone, NO_2 or water vapor, would need unrealistically large changes during the Langley period to produce significant changes in the plot y-intersect. Only changes in pressure > 5hP a during the Langley period would produce a significant change in the shorter wavelengths (< 400nm).

This uncertainty is well illustrated in Figure 4, in which the GAW-PFR data at Mauna Loa have been selected. These data are very appropriate for this analysis due to the long deployment periods. We can see the

daily extraterrestrial signals (500nm) obtained with the Langley plot method, after screening with the above mentioned criteria (section 4.1). Making the criteria even stricter reduces of course the number of available points, but does not reduce the variability much farther. That is the reason why many authors propose (and it is common practice) averaging a sufficient number of Langley plots to be able to achieve a satisfactory calibration (Slusser et al., 2000; Kazadzis, 2016).

For long deployments, such as the PFR's in Figure 4, the temporal fit to the extraterrestrial signals V_0 resulting from the Langley plots is better than just averaging, because it will take into account slow degradation of the optical elements (filters, detectors), which is quite clear, although small, in the plot. For instance, PFR#27 degraded by 0.4% in 5.6 years ($-0.07\%year^{-1}$). This is a successful example in long-term instrumental stability.

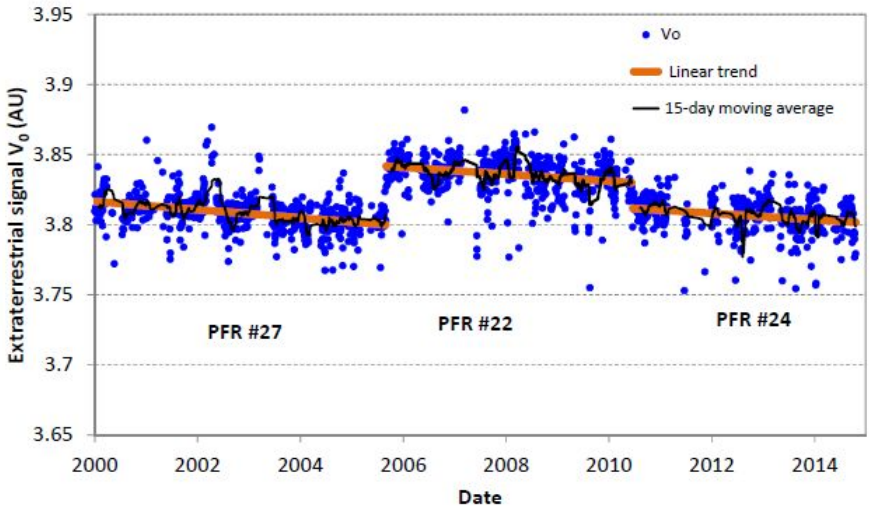

Figure 4. Daily extraterrestrial voltages (V_0) at 500nm wavelength obtained with the Langley plot method for the GAW-PFR at Mauna Loa (morning calibrations only). The temporal linear fit to the V_0's for each instrument deployment is superimposed, as well as the 15-day moving average. Note that these are instrument signals, i.e. depend on each particular instrument and are not directly comparable.

Once the slow temporal trend is taken into account, we can try to quantify the residuals in V_0 determination, as a quantification of the uncertainty of the Langley calibration at the site. The histogram of the V_0 values from the PFR (500nm wavelength), normalized to the long-term temporal trend, is provided in Figure 5a (morning Langleys only). The average of the V_0 distribution is 1.0 and the standard deviation is $\sigma = 0.0033$. In the plot we have superimposed a Gaussian distribution with the same mean and standard deviation (0.3%). The V_0 distribution does not pass a normality test mainly because the distribution has strong kurtosis (leptokurtic shape), with up to 81% of the data contained in $\pm 1\sigma$, indicating that most of the values are very close to the average. Using expanded uncertainty (k=2), which for a normal distribution corresponds to a coverage interval of approximately 95%, the Type A (The Type-A evaluation of standard uncertainty may be based on any valid statistical method for treating data (https://physics.nist.gov/cuu/Uncertainty/index.html). Standard uncertainty refers to the uncertainty for a coverage interval of 68% (±1 standard deviation, k=1), whereas expanded uncertainty, k=2, for a normal distribution corresponds to a coverage interval of approximately 95%.) uncertainty of a single Langley plot at Mauna Loa is therefore ~0.7%. The same analysis for Izaña was carried out with the data of Cimel #244, that is operated continuously since November 2011. The histogram of the residuals of the linear fit of V_0 is depicted in Figure 5b, with a relative standard deviation of 0.0046 (or 0.5%). The distribution of the residuals at Izana follows a Gaussian distribution (at 95% confidence level). Using the expanded uncertainty (k=2, 95% confidence level), the uncertainty of a single Langley plot at Izaña is therefore ~0.9%. This particular instrument (in the 500nm channel) degraded by 0.35% in 5 years (-0.07%year−1), thus showing also high stability.

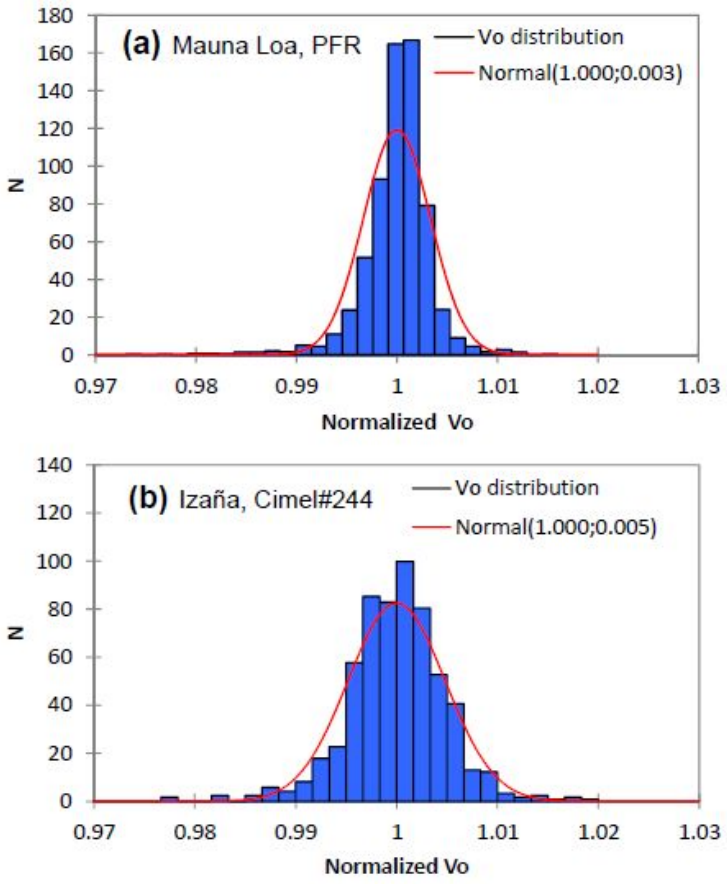

Figure 5. Histogram of daily extraterrestrial voltages (V_0) at 500nm wavelength normalized by the temporal trend: (a) At Mauna Loa using GAW-PFR data (2000-2014); (b) At Izaña using AERONET #244 (2012-2016). Red lines indicate a normal distribution (with the given parameters).

Furthermore, we can evaluate the statistical uncertainty of the V_0 determination as a function of the number of averaged Langley plots, with respect to the linear interpolation described before. For this purpose, we have computed moving averages between 2 and 20 days (number of Langley V_0's), and compared them with the reference value obtained from the linear interpolation. The 15-day moving average is also plotted in Figure 4. We basically calculate the residuals between the moving averages and the linear temporal trend, and plot them as a function of the number of Langley plots that are averaged. The result can be interpreted as the reduction in uncertainty as we average an increasing number of Langley-retrieved V_0's. Figure 6 shows the decrease in the expanded uncertainty as a function of the number of averaged Langley plots. The starting point is the uncertainty of one single Langley plot as described above. Note that the statistical uncertainty is generally expected to decrease with square root of the number measurements, in this case number of Langley plots. This is indicated in the plot as the red dashed line. In our case, the uncertainty reduction is close to this theoretical value (slope of -0.4 in log–log scale). If we average more than 10 Langley plots, then the uncertainty is <0.25%, in agreement with the calibration uncertainty at Mauna Loa reported for AERONET (Holben et al., 1998).

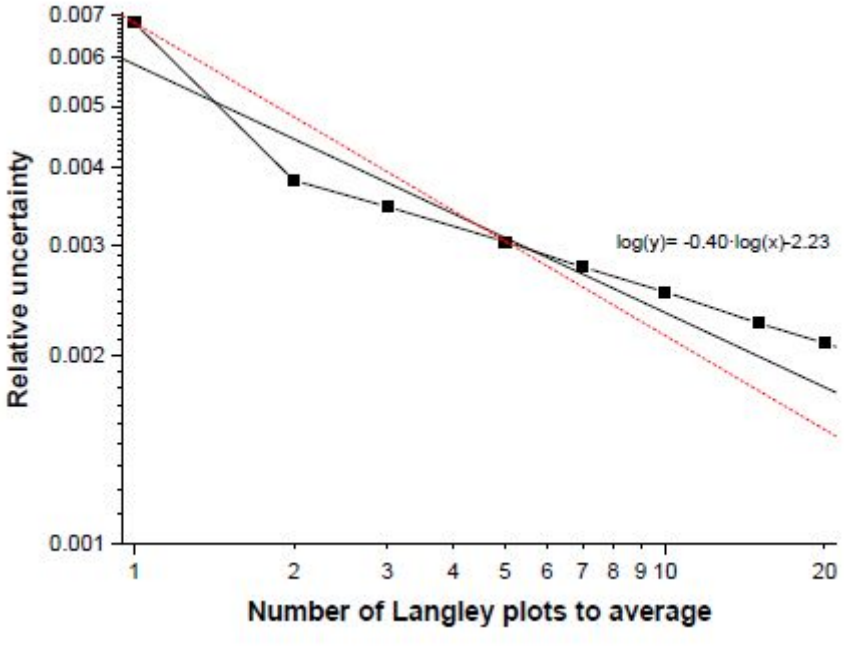

Figure 6. Uncertainty of the Langley plot calibration vs. number of Langley plot V_0's that are averaged, using GAW-PFR data (500nm) at Mauna Loa (2000-2014). Black line indicates the fit to the experimental data in log–log scale (fit result provided). Red dashed line indicates the theoretical decrease in uncertainty with the square root of the number of measurements.

We have also tried to quantify the differences that can be found between morning ('am') and afternoon ('pm') Langley plots in terms of uncertainty. The criteria applied to select afternoon Langley plots are exactly the same as above, but the number of suitable data is only 134 days per year at Mauna Loa (a factor 1.8 less). The standard deviation of the V_0's gets also higher for 'pm' Langleys ($\sigma = 0.0045$). At Izaña the decrease of 'pm' successful Langleys is not that large, with 155 days per year (a factor 1.2 less), and the standard deviation of the V_0's increases up to 0.006.

The strong requirement of AOD(500nm)< 0.025 is needed to prevent AOD variability and achieve the low uncertainty required by AERONET and GAW-PFR. A recent work by Barreto et al. (2014) included moderate, but stable throughout the day, AOD up to 0.3 in the Langley plot calibrations, that were used to recover a long-term aerosol optical depth data set at Izaña (spanning 1976-2012) from an astronomical spectrometer. The AOD uncertainty in that case gets increased but it is worth mentioning that, depending on the instrument or the intended application, the set of criteria (for instance in AOD) used to select Langley calibrations can be changed.

Finally it must be noted that the uncertainty estimations have been done for the 500nm wavelength. The standard deviation of the V_0 's in a typical ~ 20 − 30 Langley series is larger in the UV, at ~ 0.4 − 0.5%, and smaller in the NIR wavelengths (870, 1020, 1640 nm) at ~ 0.1 − 0.2%. This wavelength dependence in uncertainty occurs due to lower AOD variability at the longer wavelengths. For the UV the higher variance might be also due to filter blocking issues and also possibly to temperature effects for AERONET Cimels that have not been accounted for in the UV wavelengths (in addition to higher AOD in the UV range) .

4.3 Additional uncertainty sources

There are several other factors that can be considered in the analysis of Langley plot uncertainty. A number of authors analyzed e.g. the effect of finite bandwidth of the sun photometer channels (Box, 1981; Thomason et al., 1982), structured vertical aerosol and uncertainty in airmass determination (Thomason et al., 1983; Forgan, 1988; Russell et al., 1993), diffuse light contributions to the radiometer signal (Reagan et al., 1986) (These are Type B uncertainty estimates, not based on the statistical analysis of series of observations), and systematic

diurnal variation of optical depth (Schmid and Wehrli, 1995; Marenco, 2007). Actually these factors produce systematic errors, although the current instrument performance in terms of field of view, signal stability and time accuracy, together with the limitation of airmass range and the very low aerosol content in the selected Langley conditions for Mauna Loa and Izaña, make these errors to be <0.1% (Reagan et al., 1986)[3]. Systematic semidiurnal cycles in other components like pressure (i.e. atmospheric tide, Le Blancq (2011)), ozone, water vapor or NO_2, have very small amplitude and do not affect the aerosol wavelength channels significantly.

We have investigated other possible sources contributing to the uncertainty of the Langley plot method. First, we have analyzed the variability of the solar extraterrestrial irradiance, which is assumed as constant in our previous analysis. The measurements of the space-based photometer run by PMOD/WRC as part of the VIRGO Experiment on the ESA/NASA SOHO Mission (Fröhlich et al., 1995) were used for this purpose. The VIRGO data series comprises more than 20 years of total and spectral (in three bands) solar irradiance. It clearly shows the 11-year cycle in solar irradiance, which is in the order of 0.1%. Given the frequency of recalibration (at least 2-3 times per year) of the GAW-PFR and AERONET reference instruments, this solar cycle should not be an issue for AOD calculations.

However short-term variations in spectral solar irradiance can be as large as 0.5% (at 402 nm) in few weeks during high solar activity, as it is the case of the episode in October-November 2003, depicted in Fig. 7 for the two Sunphotometer wavelengths (500 and 862 nm). We analyzed the extraterrestrial signal provided by the PFR and the Cimel from the ground during this event, unsing the Langley plot method. The resulting (normalized) V_0's, also included in Fig. 7, are however rather noisy and do not correlate with the space-based data. Either the atmospheric variability or the instrument precission prevent the detection of this kind of abrupt changes in solar irradiance even from high altitude stations, at least with these particular instruments. Averaging several Langley calibrations is shown again necessary to overcome this possible uncertainty.

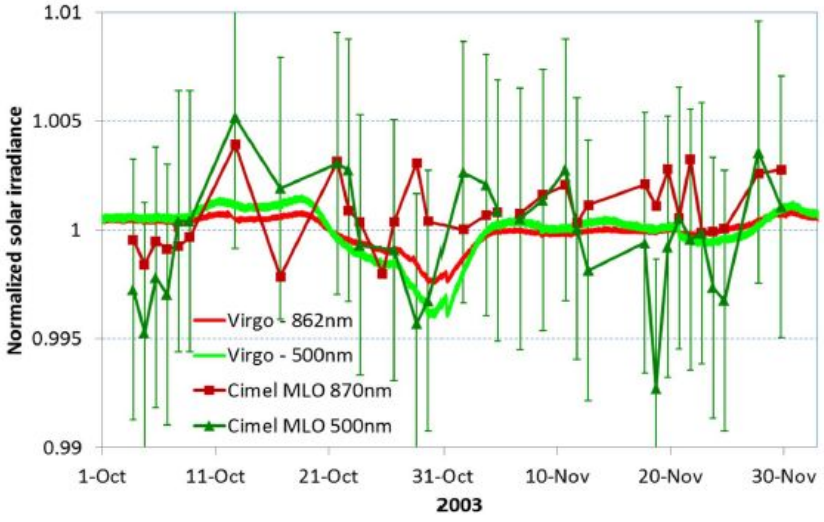

Figure 7. Solar extraterrestrial normalized irradiance as measured by the VIRGO space-based photometer during 2003-2004 at 500nm (green) and 862nm (red) wavelengths. Cimel extraterrestrial signal derived from Langley plots at 500nm and 870nm in Mauna Loa for the same period are also depicted. Error bars for 500nm channel indicate the 0.7% typical uncertainty for this spectral channel.

Another source of uncertainty that has been analyzed is the presence of the subtropical jet above Izaña in spring, which introduces strong turbulence around 12 km height. This phenomenon is well known by the astronomers of the nearby Canary Astrophysics Institute, since it produces blurring and twinkling of stars due to turbulent mixing in the Earth's atmosphere, that causes variations of the refractive index. To investigate this, we have analyzed the V_0 repeatability as in Fig. 5 but making monthly statistics, in order to check for any seasonality in the quality of the calibrations. The result is shown in Fig. 8. The variability of the Langley plots, as evaluated from the standard deviation of the V_0's (500nm wavelength), is somewhat larger in March and October-November, as compared to the rest of the year. According to Fig. 3 in (Rodríguez-Franco and Cuevas,

2013), March-April are the months with stronger winds in the upper troposphere above Izaña station, but the V_0 variability is not conclusive to confirm or discard the hypothesis. This assessment will need further investigations, but at least we can conclude that noisier Langley plots are to be expected at Izaña in March and fall. At Mauna Loa the standard deviation of the Langley plots is only higher in April, in coincidence with the higher mean AOD in this month.

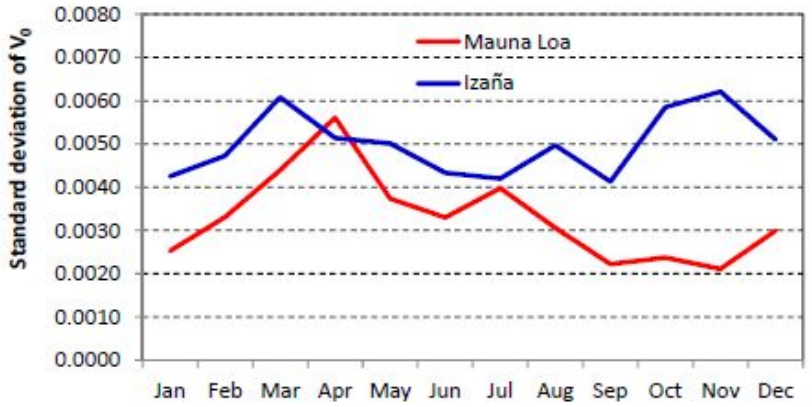

Figure 8. Standard deviation of V_0's (500nm wavelength) from Langley calibrations for every month at Izaña and Mauna Loa using AERONET data.

5 Summary and conclusions

The main aerosol optical depth characteristics of the high elevation sites Mauna Loa and Izaña have been analyzed in detail, in order to quantify the characteristics of these locations for Langley plot calibration of Sun photometers. For this purpose, we used long-term records of AERONET and GAW-PFR reference Sun photometers.

The aerosol monthly climatologies derived from both types of network instruments agree within 0.0035 optical depth at 500 nm (at both sites), and shows very low aerosol concentrations. For background conditions used in Langley calibrations, AOD (500nm) ranges from 0.01 to 0.02 for both stations. The seasonality is characterized by a spring maximum at Mauna Loa and the occurrence of Saharan dust events in summer at Izaña. Despite the different network operation (frequent swap of AERONET masters, long deployments for GAW-PFR), and data processing schemes (including cloud-screening), they are both shown to be successful in accurate aerosol monitoring in such pristine locations.

The analysis of cloudiness was accomplished by means of the cloud products OCRA and ROCCIN from GOME-2. On average, Mauna Loa and Izaña exhibit 24 and 20 clear sky days per month, respectively (very thin cirrus clouds are not included in these statistics). Therefore the clouds are not an obstacle for acquiring sufficient number of Langley plots. If we look for days fulfilling also the requirement of high atmospheric stability needed for accurate Langley plot calibration, we find a climatological average of 243 morning and 134 afternoon periods per year at Mauna Loa (about 20 morning and 11 afternoon Langleys per month). Izaña meets the criteria in 187 morning and 155 afternoon periods (about 15 morning and 13 afternoon Langleys per month on average). These conditions were established for Langley plots having standard deviation of the residuals $\sigma <$ 0.006, number of valid points > 33% of the initial number of direct Sun observations and AOD(500nm)< 0.025. Dust events at Izaña (especially in summer), reduce the number of available calibration days during those months but do not prevent from having a sufficient number of clean days for Langley calibration (13 morning Langleys in August at the minimum).

Despite the strict criteria used to select individual Langley plots, a certain noise derived from small changes in Atmospheric transmission (mainly changes in AOD), results in the time series of extraterrestrial signals to have a certain variability. This dispersion has been used to statistically provide a quantification of the calibration uncertainty. The standard deviation of the Langley-derived extraterrestrial signals is ~0.3% at Mauna Loa and

~0.5% at Izaña for 500 nm, regardless of the data set (GAW-PFR or AERONET). Applying a expanded uncertainty (k=2) criterion, the typical calibration uncertainty for a single Langley plot is 0.7-0.9% (at the 95% confidence level). The necessary averaging of at least 10 Langley-derived extraterrestrial signals reduces the statistical uncertainty to 0.25% at Mauna Loa and and 0.4% at Izaña.

Due to convective activity, morning Langley plots more often fulfill the prescribed stability conditions than afternoons. The probability to have changes in atmospheric transmission is larger in the afternoons and therefore the noise in extraterrestrial signal determination is also larger as compared to the mornings. This effect has been quantified in terms of reduction in the number of available accurate Langley plots: at Mauna Loa, a factor 1.8 less afternoon Langleys; and smaller reduction (a factor 1.2 less) is found at Izaña. It has also been found that fast variations in solar extraterrestrial irradiance, up to 0.5% in few weeks, are not easily detectable from the ground with this kind of instruments. Furthermore, more investigations are needed to explore whether the subtropical jet above Izaña is a possible explanation for the increase in the Langley plot residuals in this station during the spring months.

With this analysis we can conclude that the high-altitude stations Mauna Loa and Izaña meet the GAW-PFR and AERONET network requirements in terms of uncertainty , i.e. 0.2-0.5% in calibration factors or 0.002-0.005 in AOD (for airmass = 1). The long-term operation and maintenance of reference instruments at these unique locations is shown to be key in accurate aerosol monitoring worldwide. The stability of the reference instruments has also been proved to be very high, with signal losses due to degradation of optical components below 0.1% per year over long periods.

Acknowledgements. The authors gratefully acknowledge the effort of NOAA and AEMET to maintain the Mauna Loa and Izaña observatories. We thank the two site operators for their efforts on day to day instrument maintenance over years. Dr. Antón and Dr. Loyola provided the satellite data for the cloud analysis. We thank Dr. V. Freudenthaler for his advice on the error analysis. This research has received funding from the European Union's Horizon 2020 Research and Innovation Programme under grant agreement No 654109 (ACTRIS-2). The funding by MINECO (CTM2015-66742-R) and Junta de Castilla y León (VA100P17) is also acknowledged.

References

See references section of the PhD Thesis

Artículo 3: Advanced characterisation of aerosol size properties from measurements of spectral optical depth using the GRASP algorithm

Resumen y comentarios

El siguiente artículo evalúa el potencial uso de las medidas de espesor óptico de aerosoles dentro del algoritmo de inversión GRASP para caracterizar las propiedades microfísicas y ópticas de los aerosoles atmosféricos. Existen multitud de instrumentos que sólo son capaces de producir este tipo de medidas y por tanto, la aplicación de un algoritmo como GRASP que permita aplicar el abanico de parámetros obtenidos es especialmente interesante. El artículo propone como ejemplo el procesado de medidas de los recientes instrumentos CIMEL con capacidad para realizar medidas de extinción utilizando la radiación lunar. El artículo estudia las posibilidades de la metodología así como las limitaciones de uso mediante un estudio de sensibilidad, así como por comparación con los datos de inversión obtenidos en AERONET, que invierte conjuntamente AOD y radiancias. Como conclusión principal, los resultados muestran que a través de las medidas espectrales de AOD se pueden separar los modos fino y grueso con gran precisión y un error inferior al 1% del valor de la medida. La inversión del modo fino es muy estable, aunque la del modo grueso lo es menos, si bien el resultado se puede mejorar aportando más información de partida. Además se ha demostrado que la representación de la distribución de tamaños como una función bi-modal log-normal es adecuada especialmente cuando la hay poca información de entrada.

Este trabajo ha tenido dos aplicaciones inmediatas. La primera, cuyos objetivos son únicamente didácticos, ha sido el desarrollo de una aplicación web que permite la inversión de este tipo de medidas: www.grasp-open.com/aod-inversion. Está web puede ser utilizada para mostrar el funcionamiento general de GRASP y cómo el algoritmo va ajustando el resultado a las medidas introducidas. La figura 13 muestra una captura de pantalla de la herramienta desarrollada. Mediante un formulario de entrada se pueden insertar las medidas de AOD e índices de refracción. A modo de ayuda un selector permite elegir entre una serie de ejemplos pre-configurados. Al pulsar sobre “Progress” los datos de entrada son validados y procesados. Los resultados de la inversión se muestran iteración a iteración, siendo muy pedagógico y ayudando a entender cómo el algoritmo va ajustando en cada iteración el modelo a las medidas reales de forma que el error se minimiza.

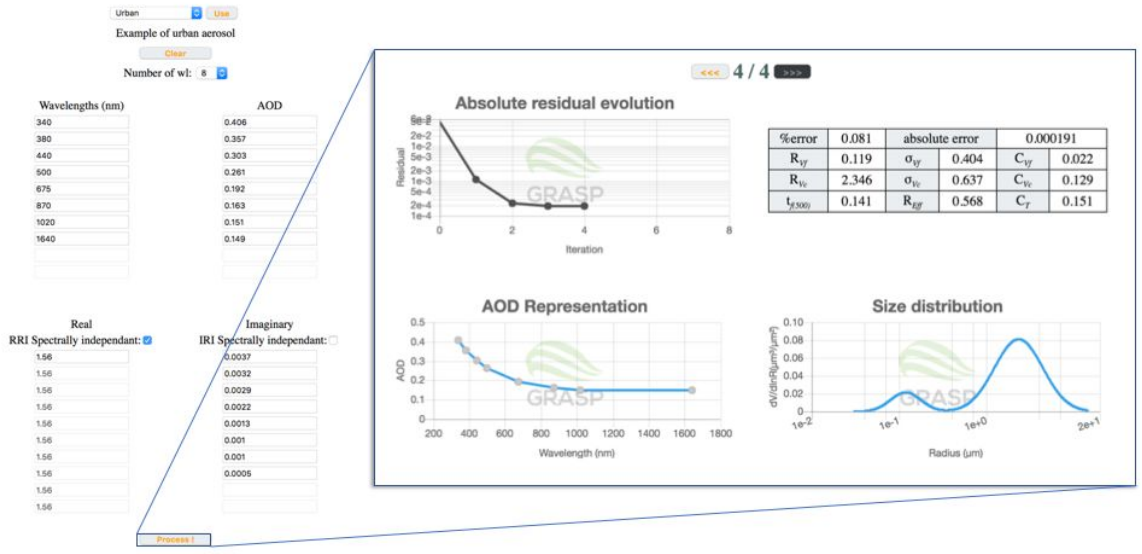

Figura 13: Captura de pantallas de la herramienta que permite procesar medidas de AOD directamente desde la web. A la izquierda el formulario que permite introducir los valores, a la derecha el resultado que se obtiene.

Por último este algoritmo y su aplicación junto al sistema CÆLIS es una muestra más del potencial de algoritmos avanzados para el estudio de los aerosoles. Como fue mostrado en la metodología, en concreto en la sección 2.1, GRASP ha sido adaptado con éxito a CÆLIS generando nuevos resultados en tiempo real que además, gracias a la potencia del motor SQL de CÆLIS pueden ser extraídos con facilidad y flexibilidad.

Artículo 3

Advanced characterization of aerosol size properties from measurements of spectral optical depth using the GRASP algorithm.

Benjamin Torres[1,2], Oleg Dubovik[1], David Fuertes[2,4], Gregory Schuster[3], Victoria Eugenia Cachorro[4], Tatsiana Lapyonok[1], Philippe Goloub[1], Luc Blarel[1], Africa Barreto[5,4,6], Marc Mallet[7], Carlos Toledano[4], and Didier Tanré[1]

[1] Laboratoire d'Optique Amosphérique, Université des Sciences et Technologies de Lille, Villeneuve d'Ascq, France.

[2] GRASP-SAS, Remote sensing developments, Université des Sciences et Technologies de Lille, Villeneuve d'Ascq, France.

[3] NASA Langley Research Center, Hampton, Virginia, USA

[4] Group of Atmospheric Optics, Valladolid University, Valladolid, Spain

[5] Cimel Electronique, Paris, France

[6] Izaña Atmospheric Research Center, Spanish Meteorological Agency, Tenerife, Spain.

[7] CNRM UMR 3589, Météo-France/CNRS, Toulouse, France

Correspondence to: Dr. Benjamín Torres (benjamin.torres@grasp-sas.com)

Abstract. This study evaluates the potential of using aerosol optical depth (τ_a) measurements to characterize the microphysical and optical properties of atmospheric aerosols. With this aim, we used the recently developed GRASP (Generalized Retrieval of Aerosol and Surface Properties) code for numerical testing of six different aerosol models with different aerosol loads. The direct numerical simulations (self-consistency tests) indicate that the GRASP-AOD retrieval provides modal aerosol optical depths (fine and coarse) to within 0.01 of the input values. The retrieval of the fine mode radius, width, and volume concentration is stable and precise if the real part of the refractive index is known. The coarse mode properties are less accurate, but they are significantly improved when additional a priori information is available. The tests with random simulated errors show that the uncertainty in the bimodal log-normal size distribution parameters increases as the aerosol load decreases. Similarly, the reduction of the spectral range diminishes the stability of the retrieved parameters. In addition to these numerical studies, we used optical depth observations at eight AERONET locations to validate our results with the standard AERONET inversion products. We found that bimodal log-normal size distributions serve as useful input assumptions, especially when the measurements have inadequate spectral coverage and/or limited accuracy, such as lunar photometry. Comparisons of the mode median radii between GRASP-AOD and AERONET indicate average differences of 0.013 μm for the fine mode and typical values of 0.2-0.3 μm for the coarse mode. The dominant mode (i.e., fine or coarse) indicates a 10 % difference in mode radii between the GRASP-AOD and AERONET inversions, and the average of the difference in volume concentration is around 17% for both modes. The retrieved values of the fine-mode $\tau_a(500)$ using GRASP-AOD are generally between those values obtained by the standard AERONET inversion and the values obtained by the AERONET Spectral Deconvolution Algorithm (SDA), with differences typically lower than 0.02 between GRASP-AOD and both algorithms. Finally, we present some examples of application of GRASP-AOD inversion using moon-photometry and the airborne PLASMA sun-photometer during ChArMEx summer 2013 campaign in the western Mediterranean.

1 Introduction

Aerosol optical depth (τ_a) measurements that are complemented with angular radiance measurements are routinely used by the scientific community to infer the microphysical and optical properties of atmospheric aerosols (e.g., the Aerosol Robotic Network, or AERONET). The availability of suitable τ_a measurements far exceeds the availability of suitable sky radiance scans, mainly because of partly cloudy conditions and scattering angle limitations. Additionally, nighttime τ_a measurements are becoming increasingly available through lunar photometry, while nighttime radiance scans are useless. Thus, it is desirable to derive meaningful aerosol information from spectral optical depth measurements when complementary radiance measurements are not available.

The goal of this work is to evaluate and demonstrate the full potential of using spectral optical depth measurement for characterizing detailed properties of aerosol. Indeed, the magnitude and spectral dependence of optical depth is known to be related to amount and size distribution of aerosol particles. Therefore, ground-based observations of solar radiation attenuation was one of the first type of measurements analyzed in pioneering studies devoted to atmospheric remote sensing algorithms (e.g. see Ångström, 1929, 1961; Yamamoto and Tanaka, 1969; Quenzel, 1970; Grassl, 1971; King et al., 1978). However, in the last few decades, the focus of remote sensing retrieval development shifted towards analysis of more complex observations: angular and polarimetric properties of transmitted and reflected diffuse radiation. In principle, such observations have high sensitivity that allows complete and accurate characterization of the aerosol features. However, modeling and interpretation of the diffuse radiation is significantly more complex than the analysis of the direct Sun beam. Therefore, the complexity and efficiency of the retrieval algorithms have significantly improved compared to the those originally developed for the interpretation of aerosol optical depth. At the same time, in a number of practical situations the interpretation of τ_a data alone remain interesting for the community. Moreover, due to evolution of ground-based instrumentation and infrastructure, the amount of available observations constantly increases. Therefore, in current study, we have decided to revisit this problem and provide a complete analysis and illustration of τ_a inversion using state-of-the-art retrieval approaches and software.

With this purpose, we make use of the recently developed GRASP (Generalized Retrieval of Aerosol and Surface Properties, see Dubovik et al. 2014) algorithm and software. The code implements statistically optimized fitting of diverse observations using multi-term least square method (LSM) concept (e.g. see Dubovik and King, 2000; Dubovik, 2004). Correspondingly the retrieval is organized as a solution search in continuous space of solutions without traditional use of pre-calculated look-up tables. The GRASP algorithm is highly versatile and can be applied to a large variety of remote sensing measurements (e.g. sun-photometer, lidars, satellite imagers, etc). The GRASP concept, originated from the Dubovik and King (2000) algorithm, has been successfully used for 15 years to process observations of AErosol RObothic NETwork (AERONET) of ground-based sun/sky-radiometers (Holben et al., 1998) engendering a large number of worldwide climatologies (to cite some Dubovik et al., 2002a; Smirnov et al., 2002a, b; Eck et al., 2005, 2010; Giles et al., 2012; Toledano et al., 2012). During this period the algorithm has certainly evolved and several useful modifications were realized (Dubovik et al., 2000, 2002b, 2006; Li et al., 2009). The GRASP development inherited of all these retrieval advances.

In addition, the GRASP algorithm has a highly flexible forward model that makes it a convenient tool for sensitivity and tuning studies (Dubovik et al., 2014). This flexibility was one of motivating factors for performing these studies. Indeed, the lack of scattering information in τ_a observation obliges the retrieval developer to search for an optimum aerosol model and an adequate set of a priori constraints (parameterization of size distribution, etc.). For example, this study suggests that reasonable results can be obtained by approximating size distributions as bimodal log-normals, which can be described with only 6 parameters (volume median radius (r_{Vi}), standard deviation (σ_{Vi}) and volume concentration (C_{Vi}) for fine and coarse mode) instead of using binned size distributions (in the case of AERONET standard inversion 22 bins logarithmically equidistant between 0.05 and 15 μm). Moreover, we assume that the complex refractive index and the sphericity parameter are known. The different assumptions and their consequences are discussed in detail in the sensitivity analysis presented in section 3.

A practical motivation for the present study is the large amount of “optical depth only" measurements that exist in the ground-based networks. For instance, AERONET includes around forty direct Sun measurements per day in its standardized sequence of measurements (in cloudless conditions); only about eight of these sequences are coincident with sky-radiance measurements that are suitable as input to the AERONET inversion code (In reality there are around sixteen sky measurements per day: eight almucantar and eight principal plane. We have counted eight set of measurements since AERONET products include only almucantar inversions to guarantee the quality of the retrievals. More information about AERONET standardized sequence of measurements can be found in http://aeronet.gsfc.nasa.gov/new_web/Documents/AERONETcriteria_final1_excerpt.pdf and about principal plane retrievals in Torres et al. (2014).). Some sites have new instruments that increase the number of valid clear-sky radiance retrievals to about sixteen per day (through the use of Hybrid scans) and the number of τ_a measurements to about two hundred per day. Nonetheless, there is still a large amount of data that do not contain the sky-radiance scans necessary for full AERONET inversions of size distributions, complex refractive indices, and single-scatter albedos. Moreover, many AERONET sites are plagued by several months of partial cloudiness. In these situations, there are no angular measurements of sky-radiance suitable for the retrieval of detailed aerosol properties, and only a few direct Sun measurements are available. As a result, the aerosol loads are the only data reported at many sites, together with the Ångström exponent that parameterize the relative fine versus coarse mode optical influence, depending on the wavelength range used in its computation (Eck et al., 1999; Schuster et al., 2006).

Similarly to AERONET, the τ_a data are often the most common measurement data provided by other ground-based networks, such as the SKYNET-PREDE network of sky radiometers (Takamura et al., 2004). Furthermore, some networks provide only τ_a data. For example, the Maritime Aerosol Network (Smirnov et al., 2009) provides τ_a measurements over the oceans taken by Microtops handheld sun-photometers. This network is federated with AERONET and uses the same calibration procedure and data processing. Another example is the Global Atmospheric Watch GAW-PFR (Wehrli, 2005), operated by the World Optical Depth Research and Calibration Center (WORCC), which provides only quality-assured spectral τ_a data, albeit with nearly continuous temporal coverage. Outside of the standardized networks, many other instruments offer only aerosol optical depth measurements at similar spectral ranges: airborne sunphotometers (AATS-14, as in Schmid et al. 2003, PLASMA by Karol et al. 2013 and others), spectroradiometers (Cachorro and De Frutos 1994, Martinez-Lozano et al. 1999), etc.

Night measurements, which have been largely developed in recent years, represent another interesting example where τ_a data are typically the only information available about the columnar aerosol properties (apart from the backscattering provided by collocated lidars). These night observations are of great interest, especially in polar regions where they offer a solution to infer aerosol loading during winter months. There are two main groups depending on the light source: star-photometry (Herber et al., 2002; Perez-Ramirez et al., 2008; Perez-Ramirez et al., 2011; Baibakov et al., 2015), and more recently, lunar photometry (Barreto et al., 2013, 2016). In some conditions, these techniques show the same accuracy as regular Sun measurements (Perez-Ramirez et al., 2008; Barreto et al., 2013), although the absence of worldwide networks with well-defined standardized protocols limits the diffusion of these results.

Aerosol optical depth measurements provide key information about climate effects, tropospheric corrections for remote sensing, visibility, etc. (Dubovik et al., 2002a). Moreover, even though τ_a refers to the total load of the whole atmospheric column, several studies have demonstrated a strong correlation of τ_a with the near-surface atmospheric concentration of particulate matter, PM_x (where x is the upper cut-off aerodynamic diameter, typically 2.5 or 10 μm, and PM_x is mass per unit volume of air, generally in $\mu g/cm^3$). PM_x has a detrimental effect on human health, and is commonly monitored at the ground level in worldwide networks (Rohen et al., 2011; Bennouna et al., 2016). For these reasons, many studies during recent decades use τ_a retrieved by satellite sensors to estimate and forecast the surface PM_x (Kacenelenbogen et al., 2006; Koelemeijer et al., 2006; Van Donkelaar et al., 2010, 2016; Vidot et al., 2007; Rohen et al., 2011).

Nevertheless, the total aerosol loading given by $\tau_a(\lambda)$ itself is not enough for complete climate studies. For instance, information about the microphysical properties of aerosols (i.e. size, shape and chemical composition) is needed to quantify the aforementioned climate effect produced by atmospheric aerosols (Mishchenko et al., 2007). However, numerous studies have demonstrated that just a set of τ_a measurements could be used for deriving more detailed information about aerosol apart from a characterization of the quantity. For example, the spectral dependence, typically given by the Ångström exponent (Ångström, 1961), is commonly used as an indicator of the predominant aerosol size (Reid et al., 1999; Eck et al., 1999, 2001; Kim et al., 2004; Toledano et al., 2007, 2009; Kaskaoutis et al., 2009; Kumar et al., 2014, etc.).

The pioneering study of King et al. (1978) showed the capacity of retrieving aerosol size distributions by modifying initial Junge distributions (Junge, 1955) through a numerical inversion. The algorithm has been used extensively for decades (for instance, Cachorro and De Frutos 1994; Liousse et al. 1995; Cachorro 1998; Martinez-Lozano et al. 1999; and Wang et al. 2006 applied the retrieval to τ_a data, while Elias et al. (1998, 2000), Vermeulen et al. (2000) combined the retrieval with radiance measurements).

O'Neill et al. (2003) developed the Spectral Deconvolution Algorithm (SDA) to discriminate fine and coarse mode extinction at a reference wavelength. That study employed the 0th, 1st and 2nd order mathematical (differential) equations describing a bi-modal particle size distribution (O'Neill et al., 2001b) to arrive at an expression for the fine Ångström exponent (a pure spectral derivative) and, in turn, the fine-mode τ_a (from the 1st order Ångström type equation) and the coarse-mode τ_a (from the 0th order τ_a equation). The set of 3 equations were then solved for fine and coarse parameters given the total τ_a along with its 1st and 2nd order spectral derivatives as input. This solution involved two 2nd order approximations: prescribing low fixed values for the coarse Ångström exponent and its derivative and the use of an empirical relation (between the fine Ångström exponent and its derivative). The algorithm is part of the AERONET processing chain: the value of the fine and coarse-mode τ_a at 500 nm is retrieved from every measured τ_a spectrum and provided as a standard product of the network (full description in http://aeronet.gsfc.nasa.gov/new_web/PDF/tauf_tauc_technical_memo1.pdf).

Several recent studies retrieve the effective radius and total aerosol concentration from aerosol optical depth measurements by using linear estimation techniques (LET), which have been largely developed for the retrieval of lidar measurements (Veselovskii et al., 2012, 2013). Kazadzis et al. (2014) applied LET retrievals to direct Sun measurements from GAW-PFR and AERONET-Cimel photometers. Pérez-Ramírez et al. (2015) extended the use of LET to star photometry measurements. They also applied LET technique to sun-photometer data from several AERONET sites influenced by different aerosol types. The retrieved effective radius and aerosol concentrations were afterwards compared to those retrieved by the operational AERONET code. The GRASP-AOD inversion, illustrated here, also allows the derivation of secondary products, such as the extinction of fine/coarse mode and the effective radius of the retrieved size distribution. We include a special emphasis on $\tau_f(500)$ (fine mode extinction at 500 nm) in this study, since it is directly comparable to the AERONET-SDA product. However, other products are systematically evaluated (such as the effective radius).

The analysis presented here is focused on τ_a measurements in the spectral range of the Cimel sun-photometers that are used in the AERONET project. This approach allowed us to compare the results obtained by the GRASP-AOD inversion with the standard AERONET inversion. Consequently, the simulation tests proposed in section 3 are done using the wavelengths in AERONET network, and the main analysis with real measurements in section 4 corresponds to AERONET data. However, we emphasize that the code is not restricted to AERONET measurements, and some example applications of the code to moon photometer data are also shown in section 4. Finally we present some retrievals from data obtained at different heights during the ChArMEx campaign (Mallet et al., 2016) with the new airborne sun-tracking photometer PLASMA (Karol et al., 2013) fully designed at the LOA (Laboratoire d'Optique Atmosphérique, University of Lille).

2 Inversion strategy (GRASP-AOD)

As commented in the introduction, we make use of the recently developed GRASP (Generalized Retrieval of Aerosol and Surface Properties, see Dubovik et al., 2014) algorithm and software (more information and a free

version of the code can be obtained in http://www.grasp-open.com/) to assess the potential of spectral aerosol optical depth measurement for characterizing aerosol properties. The main concept of GRASP is the multi-term least square method (LSM) (for details of the inversion methodology see Dubovik and King, 2000, Dubovik, 2004 and also and also King and Dubovik, 2013). GRASP is designed to be applied to a broad number of remote sensing measurements (e.g. sun-photometer, lidars, satellite images, etc).

The multiterm LSM method solves the following system of equations

$$\begin{cases} f^* = f(a) + \Delta_f \\ 0^* = Ga + \Delta_g \\ a^* = a + \Delta_a \end{cases} \quad (1)$$

The first equation in (1) describes the physical relation between the set of measurements **f** and the vector of unknowns **a**. The symbols Δ_f denote the uncertainty in the real measurements $\mathbf{f}^*$. Note that in our case, the set of measurements is only the spectral aerosol optical depths (defined in Eq. A2). In GRASP-code the atmospheric aerosol is modeled as an ensemble of randomly oriented spheroids and the aerosol optical depth is modeled as follows:

$$\tau_a(\lambda) = \int_{ln\varepsilon_{min}}^{ln\varepsilon_{max}} \int_{lnr_{min}}^{lnr_{max}} \frac{C_{ext}(\lambda,n,k,r)}{v(r)} \cdot \frac{dn(\varepsilon)}{dln(\varepsilon)} \frac{dV(r)}{dln(r)} dln(r) dln(\varepsilon), \quad (2)$$

where $v(r)$ is the volume of particle, Cext is the cross section of extinction, λ - wavelength, n and k - real and imaginary parts of the refractive index. The aerosols are approximated as spheroids (Mishchenko et al., 2002) with ε being the axis ratio (ε = a/b, a – axis of spheroid rotational symmetry, b – axis perpendicular to the axis of spheroid rotational symmetry) and r – radius of the equivalent sphere. As discussed by Mishchenko et al. (1997), the usage of r and ε is convenient for separating the effect of particle shape and size in analysis of aerosol mixture light scattering. Then the functions $\frac{dV(r)}{dln(r)}$ and $\frac{dn(\varepsilon)}{dln(\varepsilon)}$ denotes the d ln(r) d ln(ε) volume distribution of the spheroids (for the total column) and the number particle shape (axis ratio) distribution accordingly.

Dubovik et al. (2006) have demonstrated that the particle shape distribution $\left(\frac{dn(\varepsilon)}{dln(\varepsilon)}\right)$ for the non-spherical fraction of any d ln(ε) tropospheric aerosol can be approximated as constant over the particle size distribution. This assumption simplifies Eq. 2 and the aerosol extinction is calculated for the retrieval as a mixture of spherical and non-spherical fractions. Moreover, in order to perform fast and accurate calculations, the integrals are replaced by sums of pre-calculated kernels as follows:

$$\tau_a(\lambda) = \tau_{sph}(\lambda) + \tau_{nons}(\lambda) = \sum_{i=1,\ldots,N_r} (C_{sph} K_\tau^{sph}(\lambda, k, n, r_i) + (1 - C_{sph}) K_\tau^{nons}(\lambda, k, n, r_i)) \frac{dV(r_i)}{dln(r)} \quad (3)$$

where N_r is the number of bins used to represent the size distribution, C_{sph} is the fraction of the spherical particles and K_τ^{sph} and K_τ^{nons} are the kernels for spherical and non-spherical particles respectively. The complete information about the forward model and the detailed calculation of the kernels can be gained in Dubovik et al. (2006, 2011).

The second equation in (1) represents a priori smoothness constraints on the retrieved characteristics. They are typically applied to eliminate unrealistic strongly oscillating dependencies in the retrieved characteristics.

Specifically, the study of Dubovik and King (2000) showed that assuming zeros (**0*** – zero vector) for the derivatives of retrieved aerosol characteristics allows the elimination of strongly oscillating solutions with high derivatives. The matrix **G** is composed of coefficients allowing the numerical estimates of derivatives of function y(x) using discrete values $a_i = y(x_i)$. These constraints are normally used to smooth the retrieved size distribution and the spectral dependencies of the refractive index. The symbol Δ_g accounts for the uncertainties in the a priori constraints.

However, here in the so-called GRASP-AOD application, the refractive index and the sphericity parameter are assumed as known and the particle size distribution is characterized as bimodal log-normal being defined by six independent parameters: volume median radius (r_{Vi}[μm]), geometric standard deviation (σ_{Vi}) and particle volume concentration (C_{Vi}[$\mu m^3/\mu m^2$]), with i = f,c for the fine and coarse mode, respectively. Therefore, the second equation is not used in this particular application of GRASP code. It should be commented here that we initially tested binned size distributions but we rapidly observed that strong smoothness constraints were required in order to assure realistic retrievals. Hence, we decided to model the size distribution in terms of log-normal functions. Note that log-normal approximations to represent size distributions are largely used by many physical models (e.g. see Whitby, 1978; Shettle and Fenn, 1979; Koepke et al., 1997; Hess et al., 1998, etc.) and this aerosol representation generally agrees well with observations (Tanre et al., 1988; Remer and Kaufman, 1998; Dubovik et al., 2002a). Therefore, applications with a need of representing aerosol by limited number of parameters naturally choose this concept for modeling the particle size distribution. In general, bimodal lognormal functions are fully sufficient to interpret variability of aerosol optical depth (to cite some Eck et al., 1999; O'Neill et al., 2001a, b; Schuster et al., 2006, etc). However, some AERONET retrievals suggest that the particle size distribution is not always perfectly log-normal, as some size distributions are characterized by asymmetrical mode shapes (e.g. Dubovik et al., 2002a; Eck et al., 2005, 2010). Moreover, some size distribution retrievals have a pronounced tri-modal structure in the particle size range addressed by the inversion, such as observed in volcanic aerosol plumes (Eck et al., 2010) or aerosol retrievals located near fog or cloud (Eck et al., 2012; Li et al., 2014). Obviously, our strategy that is based upon simplified bimodal size distributions would not provide correct retrievals in these specialized situations.

The last equation in (1) shows the possibility of using a priori constraints on actual values of any retrieved parameter $\mathbf{a}_i$ and $\mathbf{a}^*$ is the vector of a priori estimates of $\mathbf{a}_i$. The symbol Δ_a represents the uncertainty in the a priori constraints of $\mathbf{a}^*$. For optimized accounting of those uncertainties, the solution of the system defined in (1) is given by the minimization of the following quadratic form:

$$2\Psi(a) = (f(a) - f^*)^T W_f^{-1} (f(a) - f^*) + \gamma_g a^T G^T W_g^{-1} G a + \gamma_a (a - a^*)^T W_a^{-1} (a - a^*)' \quad (4)$$

where the weighting matrices **W** and the Lagrange parameters γ are defined as follows:

$$W_f = \frac{1}{\varepsilon_f^2} C_f; \qquad W_g = \frac{1}{\varepsilon_g^2} C_g; \qquad W_a = \frac{1}{\varepsilon_a^2} C_a;$$
$$\gamma_g = \frac{\varepsilon_f^2}{\varepsilon_g^2}; \qquad \gamma_a = \frac{\varepsilon_f^2}{\varepsilon_a^2} \quad (5)$$

where ε_f^2 and ε_a^2 are the first diagonal elements of the corresponding covariance matrices C_f and C_a, respectively. During the retrieval, we assume that all input data have log-normal error distribution (Dubovik and King, 2000; Dubovik, 2004), which means that the measurements and the retrieved parameters are used in the logarithm space.

Finally, it should be indicated that one of the recent success of GRASP code has been the easy adaptation of the multipixel retrieval concept in the methodology proposed by multiterm LSM (Eq. 1). The strategy was developed by Dubovik et al. (2011) in order to overcome the difficulties related to the limited information of the

satellite observations over a single pixel. The multi-pixel retrieval regime takes advantage of known limitations on spatial and temporal evolution in both aerosol and surface properties. Specifically, a large group of pixels are inverted simultaneously, using a priori constraints on the temporal and spatial variability of the retrieved parameters. The concept has been expanded in the latest version of the GRASP-algorithm, where the measurements can also belong to different remote sensing instruments. The present study focuses on the potential of a single set of aerosol optical depth measurements, so that the multi-pixel inversion will not be used in this work. Nevertheless, in a number of recent promising applications the multi-pixel approach has been used for synergy retrievals when τ_a observations were combined with other co-located but not coincident measurements (Lopatin et al., 2013, 2016). Moreover, it appears to be a powerful capability for interpretation of τ_a-only measurements in the future.

3 Sensitivity studies

The description of any algorithm must answer several inherent questions regarding the retrieval: stability of the inversion, confidence in the retrieved products, dependence up on the a-priori assumptions, etc. In our particular case, the main challenges are to (a) identify the reliability of the six parameters which describe the bimodal log-normal size distribution (and of the secondary products derived from them), (b) check the effects of possible errors in the aerosol optical depth measurements, and finally, (c) analyze the consequences of assuming the refractive index and sphericity parameter as "known" during the retrieval process.

Several simulation tests are considered in this section to address these points. First, a self-consistency analysis, including multiple variations of the initial guess, will be carried out to check the stability of the retrieval. Next, simulated errors in the aerosol optical depth measurements will be introduced to determine the ramifications on the retrieved properties. The last two studies will include biases in the refractive index and sphericity parameter assumptions.

3.1 Aerosol models

The numerical tests in this paper are based upon the climatology provided by Dubovik et al. (2002a), which utilizes about 10 years of real aerosol retrievals with AERONET's Version 1 processing. (AERONET has subsequently implemented a Version 2 aerosol retrieval product, but the single-scatter albedo climatology that is based upon this newer processing scheme is within 0.02 of the Dubovik et al. (2002a) climatology for the same aerosol type; Giles et al., 2012). Specifically, we have selected aerosol properties from six different sites to carry out the simulations. Three of the sites are dominated by fine mode aerosols (from less to more absorbing): Goddard Space Flight Center (GSFC, Maryland, USA), which represents urban weakly absorbing aerosol, Mexico-City (Mexico) representing urban absorbing aerosol, and Mongu (Zambia) which corresponds to a strongly absorbing biomass burning aerosol. Additionally, we have selected Bahrain (Bahrain) and Solar Village (Saudi Arabia) as examples of mixed desert dust and pure desert dust, respectively. Finally, we have used the aerosol properties at Lanai (Hawaii-USA) as an example of maritime aerosol. For each example, we have considered at least three aerosol loads: $\tau_a(440) = 0.3$, 0.6 and 0.9. The $\tau_a(440) = 0.9$ case is omitted for Lanai, however, since this case would be excessively unrealistic (given the typical values observed at that site). On the other hand, we have considered four extra cases to analyze the retrievals at low and high load aerosol conditions: $\tau_a(440) = 0.1$ for Lanai and for GSFC, and $\tau_a(440) = 1.5$ for Mongu and Solar Village. In the following, those cases will be referred to as the particular test cases. Note that henceforth, we will refer the six aerosol models as: GSFC (Goddard Space Flight Center), MEXI (Mexico-City), ZAMB (Mongu), BAHR (Bahrain), SOLV (Solar Village) and LANA (Lanai). In the same way, we will use different index for the different aerosol loads: index "0" for $\tau_a(440) = 0.1$, index "1" for $\tau_a(440) = 0.3$, index "2" for $\tau_a(440) = 0.6$ index "3" for $\tau_a(440) = 0.9$, and index "4" for $\tau_a(440) = 1.5$.

The aerosol properties of all the examples considered here are represented in table 1. The first parameter is the reference value of the aerosol optical depth and the rest of the parameters are derived from the expressions in Dubovik et al. (2002a). The parameters in the top part of table 1 are used to describe the bimodal log-normal size distribution: volume median radius (r_{Vi}[μm]), geometric standard deviation (σ_{Vi}) and particle volume concentration (C_{Vi}[$\mu m^3/\mu m^2$]) for the fine and coarse modes. It also contains the sphericity parameter; we use a

sphericity parameter of 0 (i.e., all particles are non-spherical) for all the Solar Village cases except the one with $\tau_a(440) = 0.3$ (SOLV1), which has an Ångström exponent greater than 0.6 and can not be considered as pure desert dust. We use a linear approximation with respect to the Ångström exponent to select intermediate values of the sphericity parameter for the three cases with Ångström exponents between 0.6 and 1.1 (SOLV1, BAHR2, and BAHR3). That is, we use sphericity parameters of 0 and 100 for Ångström exponents of 0.6 and 1.1 (respectively), and linearly interpolate the intermediate values. The rest of the examples have Ångström exponents greater than 1.1, so we fixed the sphericity parameter at 100 (considering all the particles as spheres). Finally, the input values of the refractive index are shown in the lower part of table 1.

Model	$\tau_{aref}(440)$	r_{V_f}	σ_{V_f}	C_{V_f}	r_{V_c}	σ_{V_c}	C_{V_c}	Sph
GSFC0	0.100	0.131	0.380	0.016	3.079	0.750	0.014	100
GSFC1	0.300	0.148	0.380	0.048	3.187	0.750	0.023	100
GSFC2	0.600	0.178	0.380	0.086	3.309	0.750	0.033	100
GSFC3	0.900	0.208	0.380	0.123	3.432	0.750	0.043	100
MEXI1	0.300	0.133	0.430	0.038	2.912	0.630	0.035	100
MEXI2	0.600	0.144	0.430	0.072	3.080	0.630	0.066	100
MEXI3	0.900	0.155	0.430	0.105	3.242	0.630	0.096	100
ZAMB1	0.300	0.128	0.400	0.036	3.433	0.730	0.027	100
ZAMB2	0.600	0.134	0.400	0.068	3.621	0.730	0.051	100
ZAMB3	0.900	0.141	0.400	0.098	3.802	0.730	0.074	100
ZAMB4	1.500	0.153	0.400	0.156	4.140	0.730	0.117	100
SOLV1	0.300	0.120	0.400	0.022	2.320	0.600	0.125	60
SOLV2	0.600	0.120	0.400	0.028	2.320	0.600	0.372	0
SOLV3	0.900	0.120	0.400	0.033	2.320	0.600	0.629	0
SOLV4	1.500	0.120	0.400	0.045	2.320	0.600	1.130	0
BAHR1	0.300	0.150	0.420	0.024	2.540	0.610	0.088	100
BAHR2	0.600	0.150	0.420	0.043	2.540	0.610	0.220	80
BAHR3	0.900	0.150	0.420	0.061	2.540	0.610	0.357	60
LANA0	0.100	0.160	0.480	0.015	2.700	0.680	0.030	100
LANA1	0.300	0.160	0.480	0.044	2.700	0.680	0.088	100
LANA2	0.600	0.160	0.480	0.088	2.700	0.680	0.176	100
	$n(340)$	$n(380)$	$n(440)$	$n(500)$	$n(675)$	$n(870)$	$n(1020)$	$n(1640)$
GSFC	$1.41-0.03\tau_a$	$1.41-0.03\tau_a$	$1.41-0.03\tau_a$	$1.41-0.03\tau_a$	$1.41-0.03\tau_a$	$1.41-0.03\tau_a$	$1.41-0.03\tau_a$	$1.41-0.03\tau_a$
MEXI	1.47	1.47	1.47	1.47	1.47	1.47	1.47	1.47
ZAMB	1.51	1.51	1.51	1.51	1.51	1.51	1.51	1.51
SOLV	1.56	1.56	1.56	1.56	1.56	1.56	1.56	1.56
BAHR	1.55	1.55	1.55	1.55	1.55	1.55	1.55	1.55
LANA	1.36	1.36	1.36	1.36	1.36	1.36	1.36	1.36
	$k(340)$	$k(380)$	$k(440)$	$k(500)$	$k(675)$	$k(870)$	$k(1020)$	$k(1640)$
GSFC	0.003	0.003	0.003	0.003	0.003	0.003	0.003	0.003
MEXI	0.014	0.014	0.014	0.014	0.014	0.014	0.014	0.014
ZAMB	0.021	0.021	0.021	0.021	0.021	0.021	0.021	0.021
SOLV	0.0037	0.0032	0.0029	0.0022	0.0013	0.0010	0.0010	0.0005
BAHR	0.0035	0.0030	0.0025	0.0022	0.0014	0.0010	0.0010	0.0005
LANA	0.0015	0.0015	0.0015	0.0015	0.0015	0.0015	0.0015	0.0015

Table 1. Description of aerosol properties used for simulating the aerosol optical depth measurements. They are based on the climatology study of Dubovik et al. (2002a). The first part of the table specifies the parameters describing the aerosol load, the size distribution (modeled as a bimodal log-normal function: $r_{Vi}[\mu m]$, σ_{Vi} and $C_{Vi}[\mu m^3/\mu m^2]$) and the sphericity parameter (Sph). The second part of the table contains the refractive index (n(λ) and k(λ)) inputs for each aerosol model. Note that the values of the refractive index are constant for all the aerosol examples regardless the aerosol load except for the case GSFC where they depend on the aerosol optical depth at 440 nm represented as τ_a.

Figure 1 illustrates the size distributions for the examples with the three aerosol loads common to all sites created from the parameters described in table 1. Each aerosol load for every case is represented by different lines: the cases with $\tau_a(440) = 0.3$ by dashed line, the cases with $\tau_a(440) = 0.6$ by solid line, and cases with $\tau_a(440) = 0.9$ by dashed-dotted line. The three cases with a predominance of fine mode are plotted in the left panel. The two desert dust examples and the case of maritime aerosol are represented in the right subfigure.

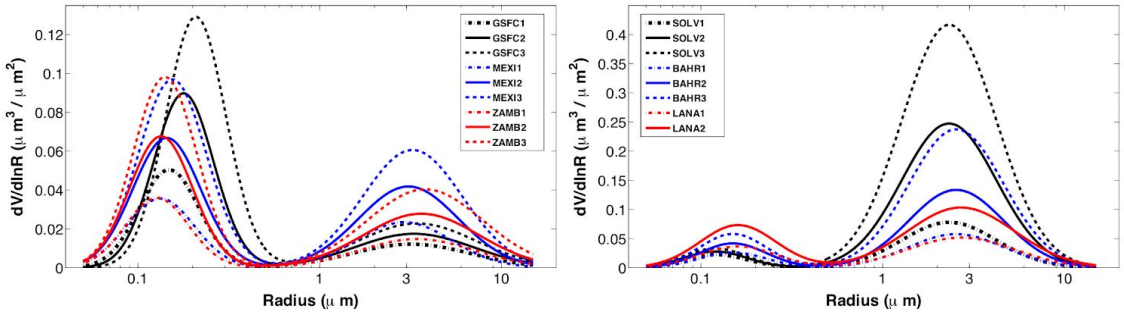

Figure 1. Representation of the aerosol size distributions used as examples in the simulation analysis (described in table 1). Aerosol models with a predominance of the fine mode are plotted in the left (subfigure a): GSFC (black lines), MEXI (blue lines) and ZAMB (red lines). The rest of the cases are plotted in the right (subfigure b): SOLV (black lines), BAHR (blue lines) and LANA (red lines). In both subfigures the cases with $\tau_a(440) = 0.3$ (index "1") are represented by dashed-dotted line, the cases with $\tau_a(440) = 0.6$ (index "2") by solid line, and cases with $\tau_a(440) = 0.9$ (index "3") by dashed line.

In the cases with a predominance of the fine mode, left panel of figure 1, the mode radii vary with τ_a for both modes. The feature was pointed in the climatology study from Dubovik et al. (2002a) and depicted in the summarizing formulas (table 1 in Dubovik et al. 2002a) from that study, which are the basis of our aerosol models here. The other three aerosol cases, which are represented in the right panel, do not present this property as can be gained from the figure (or directly from the values in table 1).

The simulated aerosol optical depth values obtained by running the GRASP-forward module with the values from table 1 are shown in table 2. We have also included the resulting Ångström exponent, which is computed as a linear regression of $\tau_a(440)$, $\tau_a(675)$ and $\tau_a(870)$. In the last two columns, the values of the fine mode aerosol optical depth at 500 nm and the effective radius are depicted since they will be analyzed in our different sensitivity studies (as derived secondary products). In order to provide a graphical representation of the tendencies from the τ_a simulated values, they are represented for the cases with $\tau_a(440) = 0.3$ and 0.6 in figure 2, in logarithmic scale. In the figures, we observe a linear relationship with slight curvature between 340 and 1020 nm for all of the sites. This curvature is negative for aerosol size distributions dominated by fine mode aerosols, and positive for the desert dust cases (especially for SOLV). This is consistent with previous works (Kaufman, 1993; Eck et al., 1999, 2001; Reid et al., 1999; Schuster et al., 2006).

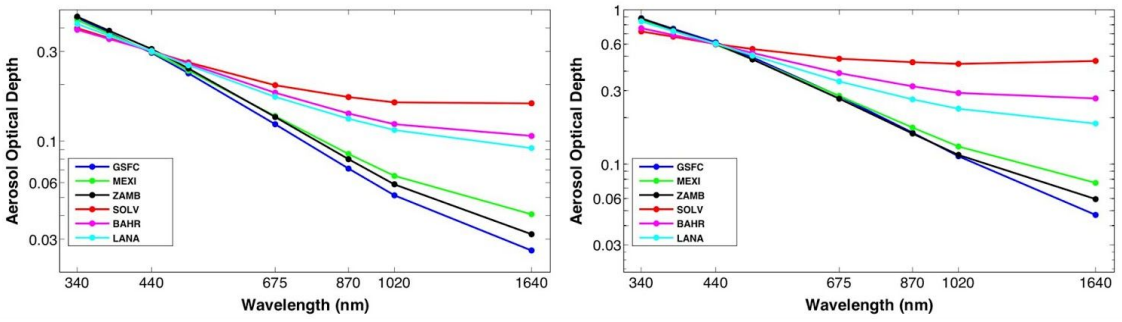

Figure 2. Spectral dependency of aerosol optical depth values of the six aerosol models represented in logarithmic scale for the cases with $\tau_a(440) = 0.3$ (on the left) and $\tau_a(440) = 0.6$ (on the right).

3.2 Self-consistency analysis

Our strategy for the simulation tests has been adapted from previous work (Dubovik et al., 2000; Torres et al., 2014). A general scheme of the procedure is drawn in figure 3. The methodology consists basically of inverting the aerosol optical depths from table 2 (which were obtained by running the forward module using the aerosol properties described in table 1), but introducing some modifications in order to "test" the sensitivity of the code regarding the different aspects already mentioned: multiple initial guesses, variation of the refractive index, and uncertainty in the aerosol optical depth data. Nevertheless, we first present a self-consistency study where we do not make any modification during the inversion process.

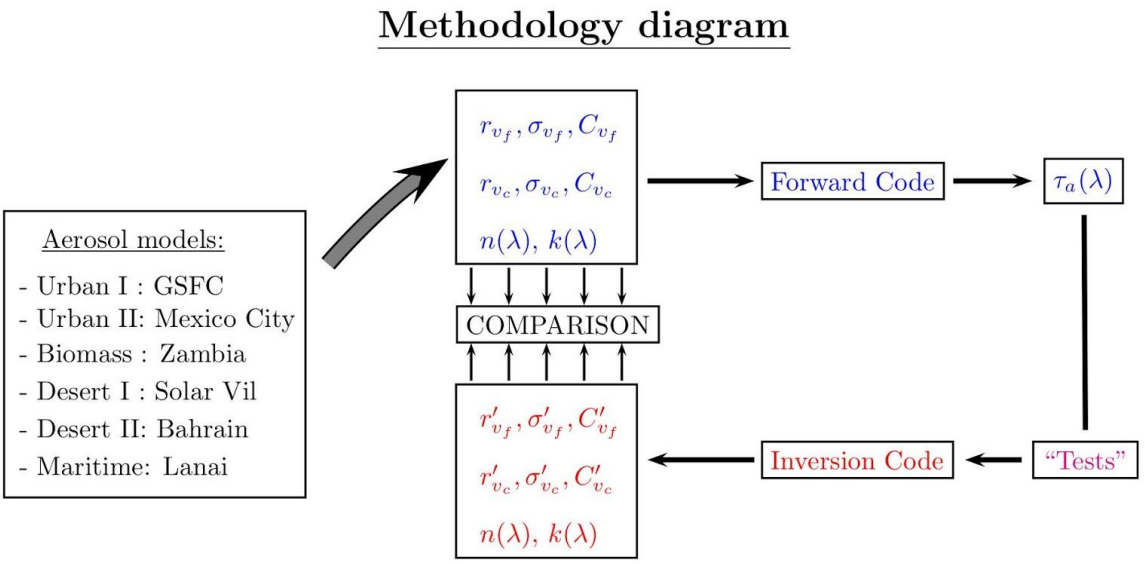

Figure 3. Methodology diagram followed to make different sensitivity "tests" on GRASP-AOD code.

The first 6 columns of table 3 represent the differences between the output of the self-consistency analysis (obtained from the inversion of the τ_a values from table 2 and considering the values of the refractive indices also from table 2) and the original values of the size distribution (table 1). In the last two columns we show the differences in the selected secondary products: $\tau_f(500)$and r_{eff} (theoretical values in table 2).

The capacity of the GRASP-AOD inversion to discriminate fine and coarse mode aerosol optical depths is one of the most important results that can be gained from table 3: differences between the reference and retrieved values of τ_f (500) are always less than 0.004. This result is even better for those cases with a predominant fine mode, where a maximum difference of 0.001 is obtained.

Model	$\tau_a(340)$	$\tau_a(380)$	$\tau_a(440)$	$\tau_a(500)$	$\tau_a(675)$	$\tau_a(870)$	$\tau_a(1020)$	$\tau_a(1640)$	α	$\tau_f(500)$	r_{eff}
GSFC0	0.158	0.130	0.100	0.078	0.043	0.028	0.022	0.015	1.899	0.067	0.198
GSFC1	0.472	0.391	0.307	0.239	0.128	0.075	0.054	0.027	2.079	0.222	0.193
GSFC2	0.867	0.739	0.602	0.480	0.269	0.157	0.111	0.047	1.967	0.457	0.223
GSFC3	1.228	1.076	0.906	0.740	0.436	0.260	0.185	0.073	1.830	0.711	0.254
MEXI1	0.442	0.372	0.298	0.237	0.136	0.085	0.065	0.041	1.837	0.212	0.211
MEXI2	0.856	0.730	0.595	0.478	0.277	0.173	0.130	0.076	1.812	0.432	0.242
MEXI3	1.263	1.091	0.903	0.733	0.432	0.269	0.201	0.110	1.770	0.671	0.260
ZAMB1	0.460	0.387	0.309	0.243	0.134	0.080	0.059	0.032	1.977	0.225	0.200
ZAMB2	0.880	0.745	0.602	0.477	0.266	0.158	0.115	0.060	1.958	0.445	0.209
ZAMB3	1.286	1.100	0.899	0.719	0.406	0.241	0.174	0.086	1.924	0.675	0.220
ZAMB4	2.080	1.807	1.507	1.221	0.707	0.422	0.303	0.140	1.853	1.156	0.237
SOLV1	0.406	0.357	0.303	0.261	0.192	0.163	0.151	0.149	0.920	0.141	0.528
SOLV2	0.724	0.670	0.601	0.557	0.482	0.458	0.446	0.466	0.410	0.174	0.907
SOLV3	1.037	0.979	0.896	0.851	0.771	0.751	0.740	0.783	0.269	0.206	1.071
SOLV4	1.682	1.611	1.497	1.444	1.346	1.334	1.322	1.409	0.178	0.279	1.204
BAHR1	0.399	0.356	0.307	0.261	0.178	0.133	0.114	0.096	1.230	0.188	0.477
BAHR2	0.765	0.690	0.602	0.522	0.375	0.298	0.265	0.240	1.023	0.334	0.635
BAHR3	1.124	1.019	0.893	0.782	0.578	0.472	0.427	0.396	0.943	0.469	0.687
LANA0	0.143	0.124	0.103	0.086	0.059	0.045	0.039	0.031	1.228	0.061	0.380
LANA1	0.420	0.364	0.302	0.253	0.172	0.132	0.114	0.092	1.228	0.179	0.380
LANA2	0.840	0.727	0.603	0.507	0.344	0.263	0.229	0.183	1.228	0.358	0.380

Table 2. Simulated aerosol optical depth values obtained from the aerosol examples described in table 1. The Ångström exponent (represented as α in the table) calculated from the 440, 675, and 870 nm wavelengths is also depicted for each aerosol example. The last two columns include the values of the fine mode aerosol optical depth at 500 nm and the effective radius.

Model	Δr_{V_f}	$\Delta\sigma_{V_f}$	ΔC_{V_f}	Δr_{V_c}	$\Delta\sigma_{V_c}$	ΔC_{V_c}	$\Delta\tau_f(500)$	Δr_{eff}
GSFC0	0.000	0.006	0.001	−0.260	−0.034	−0.001	0.000	0.007
GSFC1	0.000	0.001	0.000	−0.080	−0.007	−0.001	0.000	−0.002
GSFC2	0.000	0.000	0.001	−0.060	−0.003	−0.001	−0.001	−0.001
GSFC3	0.000	0.001	0.000	−0.056	−0.006	−0.001	0.001	−0.002
MEXI1	0.000	−0.002	0.000	0.270	0.023	0.003	−0.001	0.009
MEXI2	0.000	−0.002	−0.001	0.180	0.013	0.003	0.000	0.006
MEXI3	0.000	−0.001	0.001	0.240	0.010	0.007	0.001	0.008
ZAMB1	0.000	0.001	0.000	−0.248	−0.021	−0.002	0.000	0.006
ZAMB2	0.000	−0.002	0.000	−0.300	−0.019	−0.004	0.000	−0.006
ZAMB3	0.000	0.001	0.000	−0.312	−0.020	−0.006	0.000	−0.006
ZAMB4	0.000	0.000	0.002	−0.290	−0.050	−0.005	0.000	−0.003
SOLV1	0.000	−0.004	0.000	0.068	0.006	0.003	−0.001	0.016
SOLV2	0.000	0.007	0.000	−0.004	−0.006	−0.006	0.001	−0.012
SOLV3	0.000	−0.001	0.000	0.004	0.001	0.001	−0.004	0.002
SOLV4	0.000	−0.001	0.000	0.000	0.000	0.000	−0.000	−0.000
BAHR1	−0.002	−0.019	0.000	0.200	−0.004	0.008	0.000	0.074
BAHR2	0.000	0.001	-0.000	0.002	-0.003	-0.002	0.000	0.004
BAHR3	0.000	0.007	0.001	−0.210	−0.024	−0.020	0.003	−0.040
LANA0	−0.001	0.015	0.000	0.235	0.040	0.002	0.000	0.018
LANA1	−0.002	0.012	0.001	−0.032	−0.010	−0.001	0.001	−0.006
LANA2	0.000	−0.000	−0.000	0.004	−0.010	−0.000	0.000	0.003

Table 3. Differences obtained from the self-consistency test on GRASP-AOD code obtained by comparing parameters in tables 1 and 2. The first six columns provide parameters that represent the bimodal log-normal size distributions (volume median radius (r_{Vf}, r_{Vc} [μm]), geometric standard deviation (σ_{Vf} and σ_{Vc}) and volume concentration (C_{Vf}, C_{Vc} [$\mu m^3/\mu m^2$])).The following columns contain two secondary products derived from the GRASP-AOD inversions and the corresponding reference values: fine mode aerosol optical depth at 500 nm ($\tau_f(500)$)and the effective radius (r_{eff} [μm]).

The retrieved parameters that characterize the fine mode also show a good agreement with the reference values (from table 1). Thus, the maximum difference observed for r_{Vf} is 0.002 μm (LANA1). Once again the comparison is better for the cases with a prevailing fine mode where no difference are observed up to the third decimal. The differences in σ_{Vf} do not exceed 0.01 for the aerosol cases with a predominance of fine mode, while they are a bit higher in the rest of the cases: up to 0.015 for the maritime aerosol and a maximum difference of 0.019 for BAHR1. Finally, the divergences in the concentration (C_{Vf}) are under 0.002 $\mu m^3/\mu m^2$ in all the examples.

The retrieval of the coarse mode is less accurate than the retrieval of the fine mode. We expected this result, since the wavelengths used in this study are less sensitive to the radii in the range of the coarse mode than to those in the range of the fine mode (see, for instance, the discussion about extinction efficiency and size parameter in Lenoble et al. 2013; or in Chapter 3 of Coulson 1988). Differences in r_{Vc} are up to 0.31 μm for the cases with fine mode predominance and a bit smaller for desert dust and maritime aerosol, up to 0.21 μm, since those cases have larger coarse mode aerosol optical depth and therefore more information. The discrepancies in the concentration (C_{Vc}) are at maximum 0.007 $\mu m^3/\mu m^2$ (MEXI3) for the cases with fine mode predominance and 0.02 $\mu m^3/\mu m^2$ (SOLV2) for the cases with a prevailing coarse mode. For both cases these differences represent 6-7%.

We should point out here the strong connection between the retrievals of r_{Vc} and C_{Vc}. Those aerosol examples with the best characterization of r_{Vc} correspond as well to those with the best characterization of C_{Vc}: GSFC in the case of fine mode predominance and SOLV for the cases with a prevailing coarse mode. Those cases with an overestimation in the volume median radius also display an overestimation in the concentration: all the cases of MEXI and BAHR1. Note that for the radius range of the coarse mode, the extinction efficiency diminishes as the radius grows. Therefore an overestimation of r_{Vc} needs to be optically compensated increasing the coarse mode concentration. In the same way, the cases that present an underestimation in the volume median radius show an underestimation in the concentration: all the cases of ZAMB and BAHR3.

Finally, the effective radius is also computed and compared with the reference values in table 3. Note that this parameter is not directly derived from the inversion and is computed from the retrieved values of the bimodal log-normal size distribution. Its accuracy, therefore, will be conditioned by the accuracy of the retrieved parameters. The differences between the effective radii from the reference and those retrieved in the self-consistency are under 0.018 μm except for the cases of BAHR where differences up to 0.074 μm are obtained.

3.3 Initial guess variation

In this section, we examine the sensitivity of the inversion results to the initial guess. More specifically, we test three different initial guesses for each of the six retrieved parameters, which results in a total of 729 inversions (3^6) for the 17 aerosol examples. Note that we need not verify that the initial guesses are consistent with the inversion results; rather, we analyze the stability of the code with respect to the initial guess. That is, a perfect retrieval code would give us the same correct results, independently of the initial guess.

Table 4 shows the default initial guesses used for the first iteration of the GRASP-AOD code, which depend upon the Ångström exponent and the aerosol optical depth at 440 nm. Note that these initial guesses can be modified if ancillary information for specific applications exists. Table 5 shows the variety of initial guesses chosen for this portion of our study. These values are computed from the expressions in table 4, with a modal variation of ±25% for r_{Vi}, an absolute variation of ±25% for r_{V_i}, an absolute variation of ±0.1 for σ_{V_i} and ±40% for C_{V_i}. Here, we only show the results obtained for the examples with aerosol load $\tau_a(440)$ =0.6, since they are similar to the results obtained with the other two aerosol loads.

α	r_{V_f}	σ_{V_f}	C_{V_f}	r_{V_c}	σ_{V_c}	C_{V_c}
> 1.5	$0.13+0.05\tau_a(440)$	0.4	$0.12\tau_a(440)$	$3.0+0.5\tau_a(440)$	0.7	$(0.48–0.2\,\alpha)\,\tau_a(440)$
1.0–1.5	$0.13+0.05\tau_a(440)$	0.4	$0.08\,\alpha\tau_a(440)$	$\alpha+1.5$	0.6	$(0.78–0.4\,\alpha)\,\tau_a(870)$
< 1.0	0.12	0.4	$(0.02+0.06\,\alpha)\,\tau_a(440)$	2.3	0.6	$(0.78–0.4\,\alpha)\,\tau_a(440)$

Table 4. Initial guesses used as defaults for the GRASP-AOD retrieval. The values, as can be seen in the table, are given as a function of Ångström exponent and the aerosol optical depth at 440 nm.

Before analyzing in detail all the cases, the 729 inversion retrievals for GSFC2 and BAHR2 are represented in figure 4 to get a visual idea of the results obtained in this analysis. Black solid lines are used to represent the reference values, while the gray shadow contains all the retrievals. It can be observed how the fine mode is well characterized whereas there is a larger uncertainty in the description of the coarse mode. The better performance of the fine mode compared to the coarse mode was expected, since as commented, small particles have higher Mie extinction efficiencies at the selected wavelengths in the analysis.

Model	r_{V_f}	σ_{V_f}	C_{V_f}	r_{V_c}	σ_{V_c}	C_{V_c}
GSFC2	0.12/0.16/0.20	0.3/0.4/0.5	0.044/0.072/0.100	2.50/3.30/4.10	0.6/0.7/0.8	0.030/0.050/0.070
MEXI2	0.12/0.16/0.20	0.3/0.4/0.5	0.044/0.072/0.100	2.50/3.30/4.10	0.6/0.7/0.8	0.043/0.070/0.097
ZAMB2	0.12/0.16/0.20	0.3/0.4/0.5	0.044/0.072/0.100	2.50/3.30/4.10	0.6/0.7/0.8	0.030/0.050/0.070
SOLV2	0.09/0.12/0.15	0.3/0.4/0.5	0.016/0.027/0.038	1.80/2.30/2.80	0.5/0.6/0.7	0.220/0.370/0.520
BAHR2	0.12/0.16/0.20	0.3/0.4/0.5	0.035/0.046/0.057	2.24/2.54/2.84	0.5/0.6/0.7	0.070/0.110/0.150
LANA2	0.12/0.16/0.20	0.3/0.4/0.5	0.035/0.060/0.085	2.10/2.70/3.30	0.5/0.6/0.7	0.105/0.175/0.245

Table 5. Values used for the initial guess tests. For each aerosol example, there are three possible initial guesses for the six retrieved parameters (volume median radius (r_{Vf}, r_{Vc} [μm]), standard deviation (σ_{Vf} and σ_{Vc}) and volume concentration (C_{Vf}, C_{Vc} [$\mu m^3/\mu m^2$])).

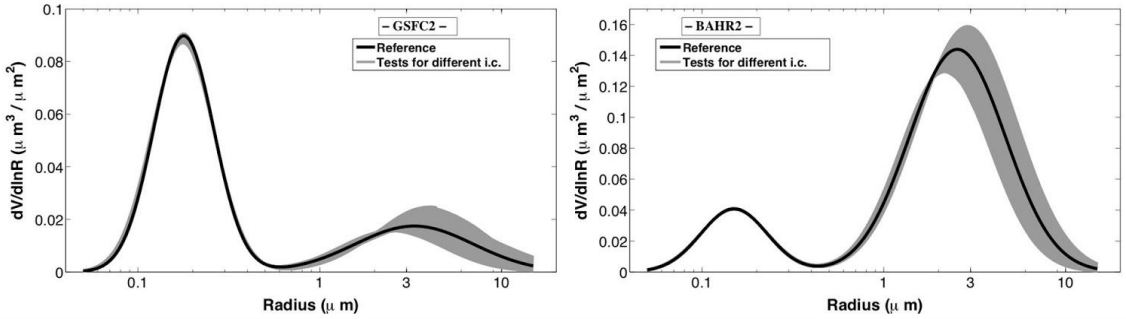

Figure 4. Size distribution retrieved in the multiple initial guess analyses for GSFC2 (left subfigure), and BAHR2 (right subfigure). Black solid lines are used to represent the reference values while the gray lines illustrates all the retrievals of the multiple initial guess analysis.

In table 6, average values and standard deviations of the retrieved parameters calculated from the 729 inversions are shown for each aerosol type. The last two columns include the secondary products: $\tau_f(500)$ and the effective radius. We focus on the standard deviations in table 6 for this second study, since they indicate the stability of the retrieved parameters. If we analyze $\tau_f(500)$, we see that the standard deviations are between 0.001-0.002 when the fine mode dominates, while they are between 0.005-0.006 for those cases when the coarse mode dominates. This result denotes that the separation of the modes is very stable regardless of the initial guess values.

Similarly, we observe that the standard deviations for r_{V_f} and C_{V_f} are less than 0.01 in all cases (units [μm] and [$\mu m^3/\mu m^2$] respectively). The variation is even smaller for the cases with a fine mode predominance, with a maximum value of 0.002 in the two parameters. In relative terms this variation is less than 3% for both cases. These results indicate that the retrieved r_{V_f} and C_{V_f} have little sensitivity to the initial guess, and the

variability is practically negligible for the cases with a dominant fine mode. The coarse modes in table 6 indicate that the standard deviations are between $10-15\%$ for both r_{V_c} and C_{V_c}, regardless of whether the fine mode or coarse mode dominates.

Model	rV_f	σV_f	CV_f	rV_c	σV_c	CV_c	$\tau_f(500)$	r_{eff}
GSFC2	0.178 ± 0.001	0.381 ± 0.009	0.086 ± 0.001	3.274 ± 0.463	0.727 ± 0.063	0.033 ± 0.004	0.457 ± 0.001	0.220 ± 0.011
MEXI2	0.144 ± 0.001	0.426 ± 0.007	0.072 ± 0.002	3.382 ± 0.435	0.648 ± 0.048	0.073 ± 0.008	0.432 ± 0.001	0.256 ± 0.021
ZAMB2	0.134 ± 0.001	0.401 ± 0.004	0.068 ± 0.001	3.407 ± 0.427	0.685 ± 0.065	0.050 ± 0.007	0.445 ± 0.001	0.208 ± 0.017
SOLV2	0.119 ± 0.004	0.416 ± 0.056	0.029 ± 0.002	2.315 ± 0.276	0.591 ± 0.029	0.372 ± 0.045	0.175 ± 0.005	0.911 ± 0.123
BAHR2	0.150 ± 0.001	0.421 ± 0.010	0.043 ± 0.001	2.507 ± 0.219	0.605 ± 0.021	0.217 ± 0.020	0.334 ± 0.002	0.628 ± 0.049
LANA2	0.160 ± 0.007	0.487 ± 0.062	0.089 ± 0.007	2.532 ± 0.316	0.649 ± 0.052	0.170 ± 0.023	0.358 ± 0.006	0.393 ± 0.053

Table 6. Sensitivity of multiple initial guesses to the GRASP-AOD inversion. The averages and the standard deviations of the retrievals are presented for six primary parameters (volume median radius (r_{Vf}, r_{Vc} [μm]), geometric standard deviation (σ_{Vf} and σ_{Vc}) and volume concentration (C_{Vf}, C_{Vc} [$\mu m^3/\mu m^2$])) in the first six columns (reference values in table 1). The last two columns contain the averages and the standard deviations of the two secondary products (fine mode aerosol optical depth at 500 nm ($\tau_f(500)$) and the effective radius (r_{eff} [μm]).

The characterization of the geometric standard deviation of fine mode, σ_{V_f}, is more sensitive to the initial guess selection than the other fine mode parameters; the standard deviation is lower than 0.01 for the cases where the fine mode dominates, and up to 0.06 for the rest of the cases. This result denotes a low sensitivity of the retrieval to the width of the fine mode. The results are a bit worse for the standard deviation of σ_{V_c}: in those cases with a predominant coarse mode the values are between $0.02-0.04$, while for the cases with a prevailing fine mode the standard deviations are up to 0.08. Therefore, a good selection of the initial guess of σ_{V_f} and σ_{V_c} is very important for a suited retrieval of both parameters.

The standard deviation of the effective radius is between $5-8\%$ in all the cases with a fine mode predominance, and between $10-14\%$ in the cases with a prevailing coarse mode. The largest influence of the predominant mode in the calculation of the effective radius explain the result obtained here and, as commented, the fine mode is better characterized than the coarse mode.

3.4 Simulation of aerosol optical depth errors

The purpose of this section is to analyze how aerosol optical depth errors affect the inversion and its products. Following the scheme in figure 2.2, we propose to introduce random variations $\Delta\tau(\lambda)$ in the aerosol optical depth values (from table 1) for each channel. The random variations are obtained from a normal distribution which has been differently defined for each wavelength, taking into the account the uncertainty estimation for AERONET field instruments. These uncertainties, ε_i, are at maximum 0.01 in the visible and near-infrared and increasing up to 0.02 in the ultraviolet wavelengths (for more information see the Appendix A and the references therein, in particular Holben et al. (1998) and Eck et al. (1999)). Due to the temperature sensitivity of the detector at 1020 nm and the water vapor absorption at this wavelength, we have also considered $\varepsilon_i = 0.02$ for this channel. To define the normal noise distribution, we have assigned $\varepsilon_i = 3\sigma$ which defines $[-\varepsilon_i \ \varepsilon_i]$ as a 86% confident interval.

The number of tests has been set to 1000 for each aerosol case. The multiterm LSM formulation (basis of GRASP-AOD inversion strategy) allows us to account for different uncertainties at each wavelength. Therefore, here and in those applications of GRASP-AOD where the errors have a spectral dependency, the known uncertainties of each wavelength can be introduced in the diagonal elements of the covariance matrix (Eq. 4 and Eq. 5), being this information used in the inversion procedure. This is the case in the analysis that follows. At the same point, we have applied a filter in the analysis, so that the retrievals with absolute residual (defined from Eq. 1 as $(f^* - f(a))/N$; with $f^* = \tau$) larger than 0.014 or relative residual (the same but dividing by $\tau(\lambda)$ for each wavelength) larger than 15% have been eliminated.

In order to summarize, only the cases with $\tau(440) = 0.3$ and $\tau(440) = 0.9$ for each type are presented in the general analysis. The particular examples with the extreme aerosol loads ($\tau(440) = 0.1$ and $\tau(440) = 1.5$) will be analyzed in a different subsection, and finally, the effects of reducing the spectral range to $440 - 1020$ nm will be discussed in the last part of the section.

3.4.1 General analysis

So as to get a visual representation of the general results, first we represent in figure 5 the retrievals for two aerosol examples (GSFC and SOLV) and two aerosol loads (τ a(440) = 0.3 and 0.9) . Black solid lines represent the reference values while black dashed lines depict the retrievals without errors. Note that both black lines are almost identical as commented in the self-consistency study. Gray regions illustrate the retrievals for the remaining combinations of random errors. Finally, we have also added the cases where all the wavelengths have the errors of $+\varepsilon_i$ and $-\varepsilon_i$, and they are illustrated with red and blue lines respectively.

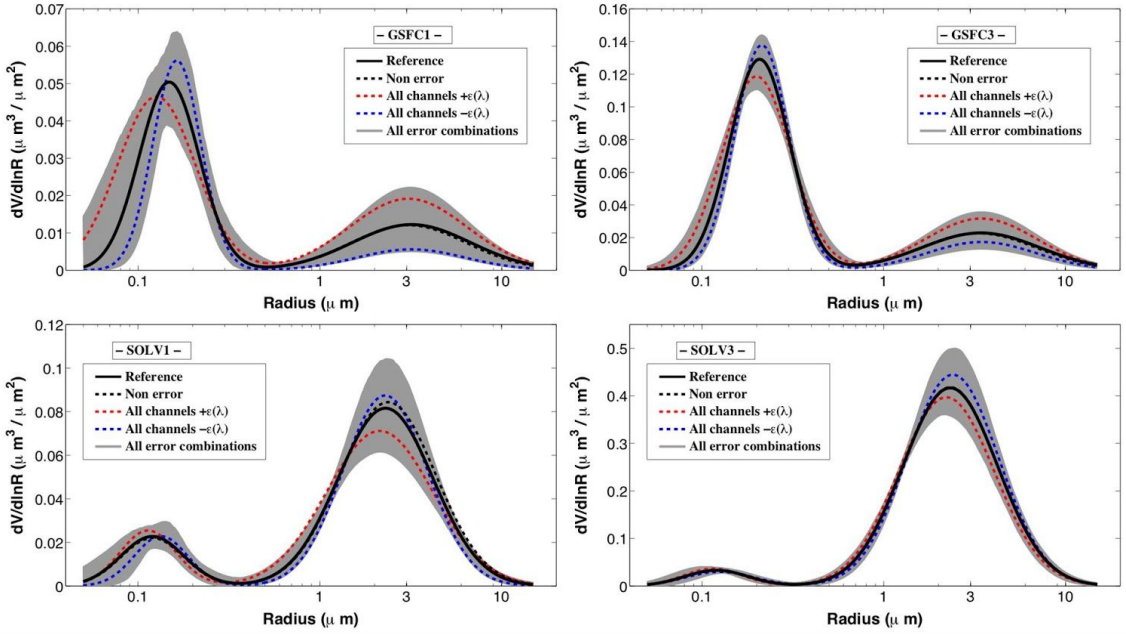

Figure 5. The effect of τ_a errors on size distributions retrieved with the GRASP-AOD code for GSFC (top panels) and SOLV (bottom). The subfigures in the left corresponds to the cases with $\tau_a(440) = 0.3$, and on the right with $\tau_a(440) = 0.9$. Black solid lines are used to illustrate the reference values while black dashed lines represent the retrievals without errors (self-consistency study). Red and blue lines are used to indicate the cases where all the wavelengths present the errors of $+\varepsilon_i$ and $-\varepsilon_i$ respectively. Gray shaded area illustrates all the retrievals for the multiple combinations of random errors.

For GSFC, we observe that the red line (all errors $+\varepsilon_i$) gives larger values of the size distribution than the reference in the coarse mode, whereas the opposite happens for the blue line. Note that the mode radii are practically the same as those obtained in the self consistency test for both the red and blue lines; the discrepancies are only observed in the concentration values. In the fine mode, however, the analysis is not that simple: for the $+\varepsilon_i$ case, the modal radii is reduced and the fine mode widens so that the concentration increases. All these effects increase considerably the volume size distribution for radii smaller than 0.12 μm. This occurs because ε_i is larger at the two ultraviolet wavelengths than at the other wavelengths, so the Ångström exponent increases and the retrieved mode radius decreases.

Similar effects are observed for the case of SOLV3 in the coarse mode. For $+\varepsilon$ case, there is a decrease in the modal radius (0.10 μm) and in the mode concentration (4%). The contrary occurs for the case with all the errors equal to $-\varepsilon_i$. In both cases, the variations in the standard deviation are under 0.01. For SOLV1, however, there is a small decrease in the concentration and in the modal radius for both the red and blue lines. The decrease in the radius is more significant for the case $+\varepsilon_i$ (0.24 μm) than for the case $-\varepsilon_i$ (0.08 μm), while the

reduction in the concentration is similar for both cases: 6% for $+\varepsilon_i$ and 7% for $-\varepsilon_i$. The standard deviation of the mode increases of 0.07 for the case $+\varepsilon_i$ and decreases 0.06 for the case $-\varepsilon_i$.

Looking at the gray area, it seems that the uncertainties in r_{Vf} and C_{Vf} are significantly reduced for the cases with the highest aerosol load, GSFC3 and SOLV3 ($\tau_a(440) = 0.9$), with respect to GSFC1 and SOLV1 ($\tau_a(440) = 0.3$). The same effect is observed in the coarse mode, for r_{Vc} and C_{Vc}, in all the cases.

Table 7 presents the values and standard deviations of the retrieved parameters calculated for the simulation of random error analysis. The scheme of the table is the same as in initial guess variation (table 6), but we have added in the last column the ratio of the inversions that pass the filters out of 1000 simulations for each aerosol case. As in the study of the initial guess variation, standard deviation values will be used to check the stability of the retrieval, though in this case, with respect to the τ_a-errors.

Average values of $\tau_f(500)$ obtained in the study do not differ by more than 0.005 from those retrieved in the self-consistency analysis (cf. table 2). The standard deviations of $\tau_f(500)$ are between 0.008-0.009. This result is consistent with the normal variations of $\varepsilon_i = 3\sigma$ introduced in the aerosol optical depth in the study.

Figure 6 summarizes the differences between the mean values obtained in the error simulation study table 7 and the values from the self-consistency for the parameters representing the bimodal log-normal size distribution. Similarly, the standard deviations obtained in the analysis for the same parameters (also in table 7) are presented in figure 7.

Model	rV_f	σV_f	CV_f	rV_c	σV_c	CV_c	$\tau_f(500)$	r_{eff}	R
GSFC1	0.147 ± 0.015	0.395 ± 0.088	0.049 ± 0.006	3.151 ± 0.044	0.699 ± 0.014	0.024 ± 0.008	0.222 ± 0.008	0.198 ± 0.030	0.86
GSFC3	0.206 ± 0.006	0.398 ± 0.047	0.125 ± 0.005	3.454 ± 0.036	0.687 ± 0.013	0.043 ± 0.011	0.711 ± 0.009	0.249 ± 0.021	0.95
MEXI1	0.133 ± 0.015	0.419 ± 0.094	0.038 ± 0.005	3.148 ± 0.046	0.681 ± 0.020	0.038 ± 0.010	0.210 ± 0.008	0.238 ± 0.047	0.91
MEXI3	0.156 ± 0.006	0.411 ± 0.046	0.103 ± 0.005	3.449 ± 0.031	0.675 ± 0.016	0.100 ± 0.010	0.669 ± 0.008	0.270 ± 0.022	0.92
ZAMB1	0.127 ± 0.013	0.404 ± 0.104	0.037 ± 0.005	3.179 ± 0.041	0.705 ± 0.020	0.026 ± 0.008	0.225 ± 0.008	0.203 ± 0.037	0.88
ZAMB3	0.142 ± 0.005	0.394 ± 0.043	0.098 ± 0.004	3.356 ± 0.028	0.712 ± 0.023	0.069 ± 0.012	0.672 ± 0.008	0.217 ± 0.018	0.99
SOLV1	0.120 ± 0.014	0.392 ± 0.073	0.022 ± 0.003	2.273 ± 0.093	0.603 ± 0.050	0.123 ± 0.010	0.140 ± 0.008	0.573 ± 0.088	0.99
SOLV3	0.120 ± 0.009	0.396 ± 0.024	0.033 ± 0.002	2.298 ± 0.070	0.597 ± 0.022	0.624 ± 0.023	0.205 ± 0.009	1.073 ± 0.072	0.99
BAHR1	0.148 ± 0.015	0.425 ± 0.121	0.025 ± 0.004	2.713 ± 0.060	0.605 ± 0.024	0.096 ± 0.008	0.187 ± 0.008	0.556 ± 0.090	0.98
BAHR3	0.150 ± 0.007	0.413 ± 0.047	0.061 ± 0.003	2.329 ± 0.057	0.600 ± 0.029	0.321 ± 0.013	0.469 ± 0.009	0.635 ± 0.045	0.99
LANA1	0.165 ± 0.018	0.475 ± 0.099	0.044 ± 0.005	2.663 ± 0.095	0.645 ± 0.050	0.089 ± 0.009	0.181 ± 0.009	0.401 ± 0.081	0.99
LANA2	0.165 ± 0.012	0.465 ± 0.057	0.087 ± 0.006	2.684 ± 0.054	0.644 ± 0.025	0.178 ± 0.009	0.363 ± 0.009	0.397 ± 0.046	0.99

Table 7. Result obtained from the simulation of errors in τ_a on GRASP-AOD code. The parameters representing the bimodal log-normal size distribution (volume median radius (r_{Vf}, r_{Vc} [μm]), geometric standard deviation (σ_{Vf} and σ_{Vc}) and volume concentration (C_{Vf}, C_{Vc} [$\mu m^3/\mu m^2$])) are shown in the first six columns (reference values in table 1). The following columns contain two secondary products derived from GRASP-AOD inversion: fine mode aerosol optical depth at 500 nm ($\tau_f(500)$) and the effective radius (r_{eff} [μm]) (reference values in table 3). The last column R indicates the fraction of the inversions that pass the filters out of the original 1000 simulations.

We can observed in figure 6 that the largest differences between the mean values of r_{Vf} in the error simulation study and the values from self-consistency is 0.007μm, and it is obtained in the case of LANA2. The standard deviations of r_{Vf} (either in table 7 or figure 7) for all of the cases are between 0.013 0.018 when $\tau_a(440) = 0.3$, and between 0.005 0.009 when $\tau_a(440) = 0.9$. There is an important diminution in the standard deviation of r_{Vf} for all examples as the aerosol load grows. This effect is more visible in the cases with a prevailing fine mode (GSFC, MEXI, and ZAMB), where the variations are around 0.015 for the cases with $\tau_a(440) = 0.3$ and diminish to 0.005 0.006 for the cases with $\tau_a(440) = 0.9$. Meanwhile, the cases with a prevailing coarse mode (SOLV, BAHR, and LANI) have r_{Vf} variability of 0.014 0.018 that diminish to 0.007 0.009.

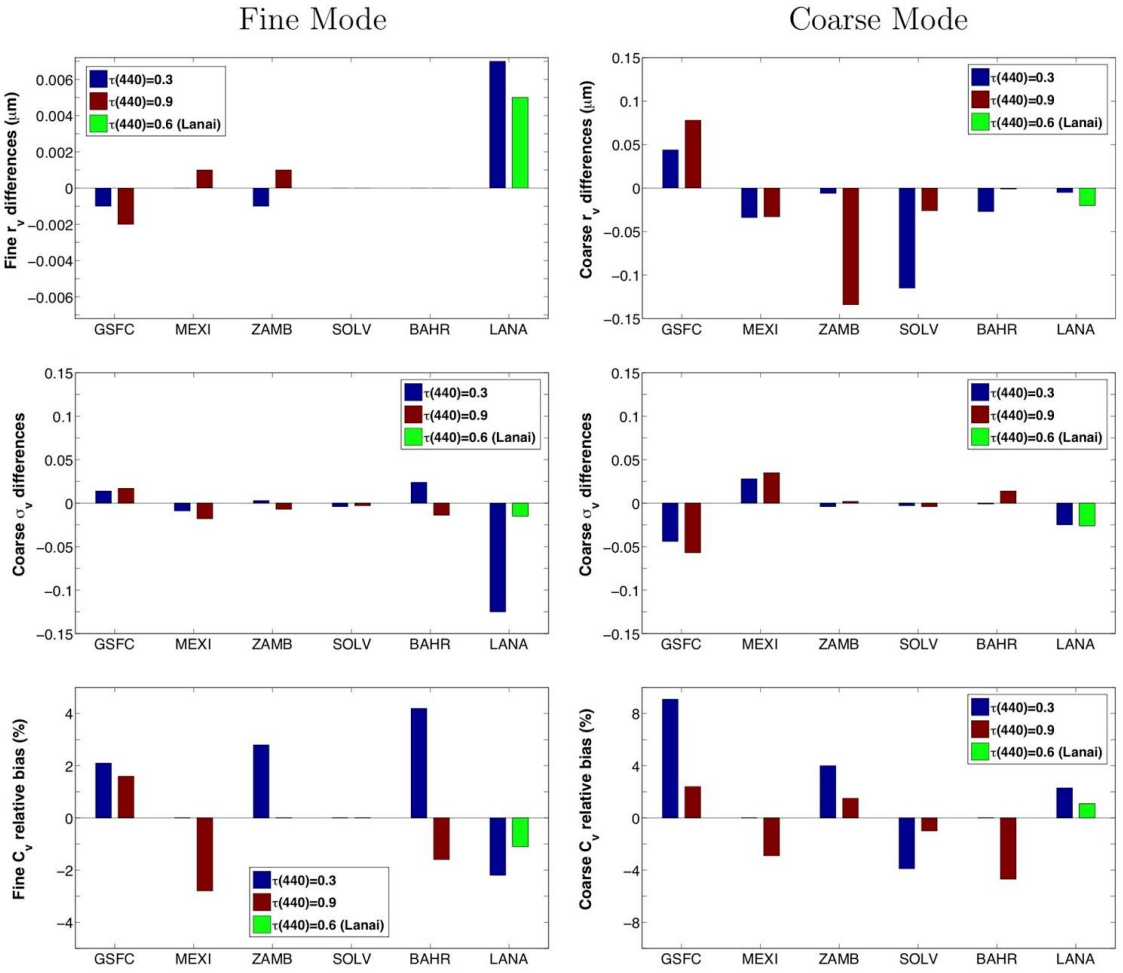

Figure 6. Differences between the averaged values obtained in the error simulation study table 7 and the retrieved values from the selfconsistency analysis (table 3) for the six parameters that describe the bimodal log-normal size distributions: volume median radius (top subfigures), geometric standard deviation (middle subfigures) and volume concentration (bottom subfigures). The differences for the latter are plotted in relative terms.

The mean values of the fine mode concentration, C_{Vf} , are almost identical to those obtained in the self consistency analysis with maximum differences of 0.002 $\mu m^3/\mu m^2$, or a 4% relative bias (figure 7). From figure 7, we can observe that the standard deviations are around 12-16% for the cases with $\tau_a(440) = 0.3$ and they decrease to 4-6% for the cases with $\tau_a(440) = 0.9$.

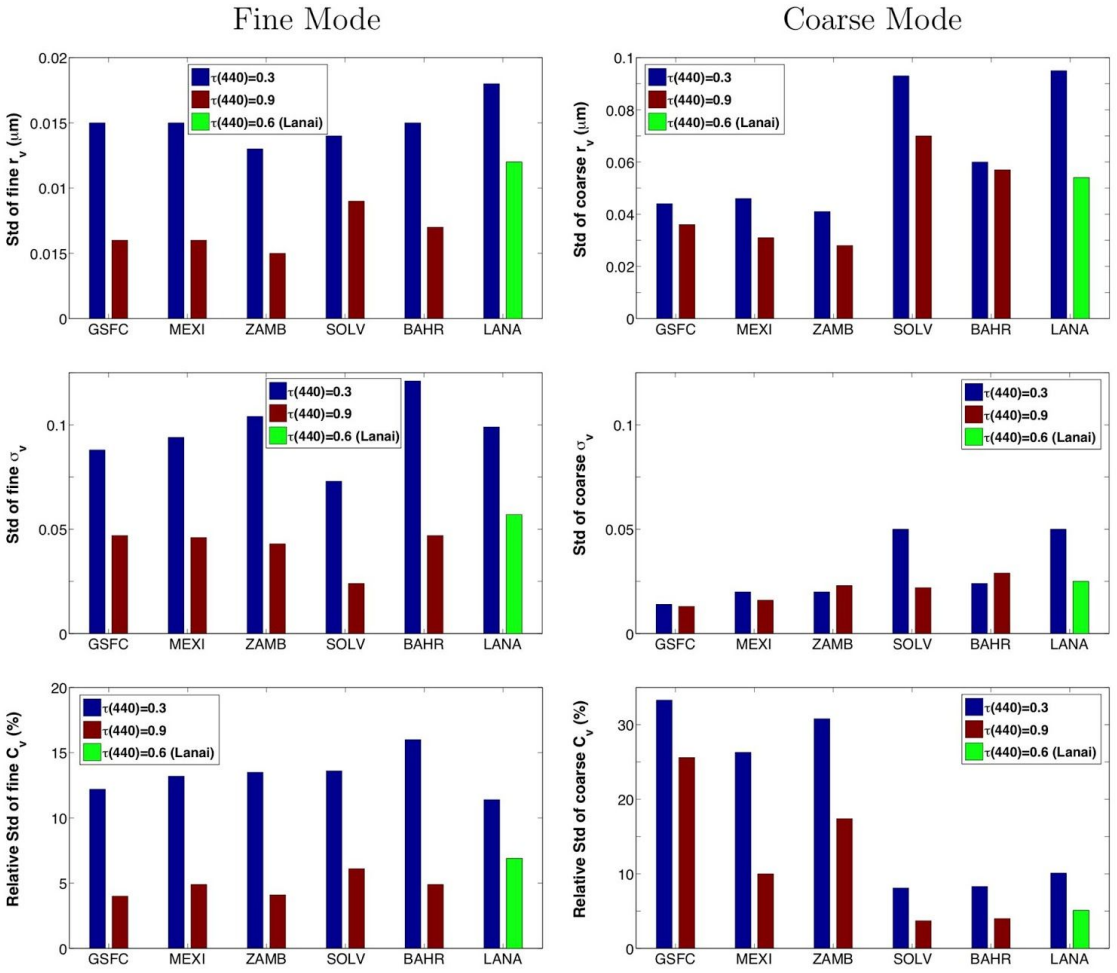

Figure 7. Standard deviation (Std) obtained in the error simulation study table 7 for the six parameters that describe the bimodal lognormal size distributions: volume median radius (top subfigures), geometric standard deviation (middle subfigures) and volume concentration (bottom subfigures). For the latter, the standard deviations are plotted in relative terms.

For σ_{Vf}, the differences between the averages in table 7 and the self-consistency analysis are typically around 0.01, except for the case of BAHR1 with a maximum difference of 0.025. The standard deviation are around 0.1 for the cases with $\tau_a(440) = 0.3$ and they are between 0.03-0.05 for the cases with the largest aerosol load in table 7.

The average values here and those obtained in the self-consistency do not differ by more than $0.15\mu m$ for all the cases. Note that if we compare the average values of r_{V_c} and the input values, the differences are much larger: around $0.4\mu m$ for the aerosol cases dominated by the coarse mode and around $0.2\mu m$ for the cases with a prevailing fine mode (similar results to those obtained between the input values and the self-consistency analysis in table 3). The standard deviation of r_{V_c} are between $0.03 - 0.1$ (see figure 8). These variations represent between the 2% and 4% in relative terms. There is, in general, a decrease in the standard deviation as the aerosol load grows but not as important as for r_{V_f}.

The analysis of C_{V_c} indicates differences of up to $0.002\ \mu m^3/\mu m^2$ between the average values in table 6 and those obtained in the self-consistency study for the cases with a prevailing fine mode. These differences can represent more than 8% of the value as can be gained in figure 7. For the cases dominated by the coarse mode, the differences are under 5%. Generally, there is a decrease in the relative differences as the aerosol load grows (except for MEXI and BAHR that do not present any errors when $\tau_a(440) = 0.3$). Back to the cases with a fine

mode predominance, table 6 shows that the standard deviations of C_{V_c} are relatively high with values around $0.01 \mu m^3/\mu m^2$. Note that for the cases with the lowest aerosol load, sometimes these variation represents around 40% of the total value as we see in figure 8. Certainly, variations of ± 0.01 for the longest wavelengths should have a large influence on the retrieval of the coarse mode considering the values of the aerosol optical depth at these wavelengths ($\tau_a(1640) \tilde{} 0.03 - 0.04$; see table 1 for GSFC1, ZAMB1 and MEXI1). The differences, in relative terms, are considerably smaller for the cases with the highest aerosol load. For the cases with a prevailing coarse mode, the standard deviations of C_{V_c} are around 10% for the cases with $\tau_a(440) = 0.3$ and between 4 - 5% for the cases with the largest aerosol load.

The differences between the mean values of the standard deviation of the coarse mode, σ_{Vc}, and those retrieved in the selfconsistency analysis are under 0.01 in all the examples, except for MEXI, LANA ,with differences around 0.025-0.03, and GSFC where differences up to 0.05 are observed. The standard deviations are under 0.025, with the exception of SOLV1 and LANA1 where a value of 0.05 is registered in both cases. For these two cases, there is a significant decrease of the standard deviation when the aerosol load grows that it is not noticeable in the rest of the aerosol models.

There is also a good agreement between the average values of the effective radius in table 7 and those retrieved in the selfconsistency test. The differences are under 0.02 μm for all the examples. The standard deviation are between 0.02-0.05 for the cases with a predominant fine mode and they are between 0.05-0.095 for the cases dominated by the coarse mode. Note that for all the cases, the variations represent between 15-20% in the cases with $\tau_a(440) = 0.3$ and between 7 – 10% for the cases with the largest aerosol load in table 7.

Almost all the inversions pass the filters for the cases with a prevailing coarse mode. For the examples dominated by the fine mode, the ratio is a little bit lower, around 90%. The filter that cuts most of the retrievals is the one imposed to the relative differences and it is due to the relative low values of τ at infrared wavelengths compare to the values of the random errors.

3.4.2 Low and high aerosol load conditions

The effects of τ_a errors on the examples with the extreme aerosol loads (GSFC0, LANA0, ZAMB4 and SOLV4) are analyzed in this subsection. Figure 8 contains the retrievals for two of our particular aerosol test cases: GSFC0 ($\tau_a(440) = 0.1$) and SOLV4 ($\tau_a(440) = 1.5$). They have been chosen since they were selected to get a visual representation in the previous subsection in figure 5. The main output from figure 5 was that the uncertainties in the characterization of the size distribution were significantly reduced for GSFC3 and SOLV3 with respect to GSFC1 and SOLV1. This tendency seems to be confirmed here if we compare SOLV4 to SOLV3, where we observe that the gray area has been significantly reduced. On the contrary, the case of GSFC0 presents larger uncertainties compared to GSFC1. Note that in the case of GSFC0, the two cases where all the wavelengths have the same error, $+\varepsilon_i$ and $-\varepsilon_i$, do not pass the filters imposed to the residuals and that explains why both lines appear out of the gray area in the coarse mode. We have preferred to keep them in the figure to point out that they follow similar patterns as their equivalents in figure 5. For instance, in the case of $+\varepsilon_i$ (red line), the modal radius decreases and the concentration increases respect to the reference. The standard deviation of the mode also rises though not as much as in figure 5. On the other hand, red and blue lines in the case of SOLV4 do not differ much from the reference in the right panel of figure 8.

The values and standard deviations of the retrieved parameters calculated for the simulation of random errors for our four particular aerosol test cases are shown in table 8. The structure of the table is the same as table 7, including the fraction of the inversions that pass the residual filters for 1000 simulations (last column); note that this ratio is particularly low for the case GSFC0 (0.39). However, ε_i represents 91% of the total value of τ_a at 1020 nm and 66% of τ_a at 1640 nm for this case with low aerosol loading. The filter imposed to the relative AOD residuals in the inversion process (i.e., relative residual < 15%) eliminates most of the retrievals.

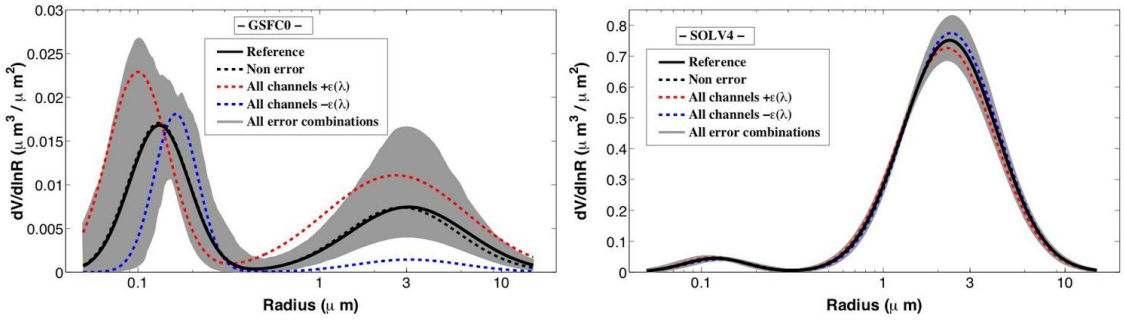

Figure 8. The effect of τ_a errors on size distributions retrieved with the GRASP-AOD code for the case of GSFC0 (low aerosol load conditions $\tau_a(440) = 0.1$), and SOLV4 (high aerosol load conditions $\tau_a(440) = 1.5$). As in figure 5, black solid lines are used to illustrate the reference values while black dashed lines represent the retrievals without errors (self-consistency study). Red and blue lines are used to indicate the cases where all the wavelengths present the errors of $+\varepsilon_i$ and $-\varepsilon_i$ respectively. Note that in the case of GSFC0, those two cases do not pass our residuals restrictions (i.e. we require total residual < 0.014 and relative residual < 15%). Shaded gray area illustrates all the retrievals for the multiple combinations of random errors.

The differences between the averaged $\tau_f(500)$ values in table 8 (with extreme aerosol loading) and those retrieved in the self-consistency analysis are all under 0.001. Moreover, the standard deviations of $\tau_f(500)$ are between 0.007-0.009 as in the general study. These same results were obtained while analyzing the 1000 retrievals without filters in the residuals. Therefore, we can conclude that the retrieval of $\tau_f(500)$ is consistent with the accuracy of τ_a measurements and independent of the aerosol load.

Similar to $\tau_f(500)$, the differences observed between the averaged values of the bimodal log-normal parameters (r_{Vi}, σ_{Vi}, and C_{Vi}) in table 8 and those retrieved in the self-consistency analysis are almost negligible. Thus, the main interest is to check the evolution of the standard deviations with respect to the general analysis.

Model	rV_f	σV_f	CV_f	rV_c	σV_c	CV_c	$\tau_f(500)$	r_{eff}	R
GSFC0	0.131 ± 0.028	0.373 ± 0.109	0.017 ± 0.003	3.027 ± 0.109	0.707 ± 0.070	0.017 ± 0.006	0.066 ± 0.007	0.237 ± 0.065	0.39
LANA0	0.164 ± 0.040	0.440 ± 0.134	0.016 ± 0.004	2.564 ± 0.183	0.630 ± 0.094	0.031 ± 0.007	0.060 ± 0.009	0.409 ± 0.147	0.74
ZAMB4	0.154 ± 0.003	0.392 ± 0.260	0.157 ± 0.004	3.854 ± 0.015	0.705 ± 0.015	0.111 ± 0.011	1.156 ± 0.008	0.234 ± 0.013	0.99
SOLV4	0.120 ± 0.006	0.400 ± 0.014	0.045 ± 0.002	2.303 ± 0.045	0.598 ± 0.012	1.123 ± 0.026	0.280 ± 0.009	1.198 ± 0.048	0.99

Table 8. Result obtained from the simulation of errors in τ_a on GRASP-AOD code for the cases with the lowest and the highest aerosol load. As in table 7, the first six columns contain the parameters representing the bimodal log-normal size distribution (volume median radius (r_{Vf}, r_{Vc} [μm]), geometric standard deviation (σ_{Vf} and σ_{Vc}) and volume concentration (C_{Vf}, C_{Vc} [$\mu m^3/\mu m^2$])). The following columns contain two secondary products derived from GRASP-AOD inversion: fine mode aerosol optical depth at 500 nm ($\tau_f(500)$) and the effective radius (r_{eff} [μm])(reference values in table 3). The last column R indicates the fraction of the inversions that pass the filters out of the original 1000 simulations.

In the cases with $\tau_a(440) = 0.1$, GSFC0 and LANA0, we observe that the standard deviations increase their values with respect to the cases with $\tau_a(440) = 0.3$. For instance, the standard deviations of r_{Vf} were 0.015 and 0.018 (in table 7) for GSFC1 and LANA1, respectively, representing the 10% in both cases. Meanwhile, for GSFC0 and LANA0 the standard deviations are 0.028 and 0.040 which represents the 25% of the averaged values of r_{Vf}. We find similar increments, from 10% to 25%, for C_{Vf}. For the coarse mode, the increment of the uncertainties is not as strong as in the fine mode though it is significant in the three parameters.

On the contrary, there is a decrease in the standard deviations of all the parameters for the cases SOLV4 and ZAMB4 $\tau_a(440) = 1.5$ with respect to the cases SOLV3 and ZAMB3 $\tau_a(440) = 0.9$. For example, the standard deviation of r_{Vf} for ZAMB3 was 0.005 (around 3.5% of the total value) while is 0.003 for ZAMB4 (the 2% of the total value). Similar results are obtained in the characterization for the coarse mode and SOLV. Thus, the standard deviation of r_{Vc} was 0.07 for SOLV3 (the 3% of total value) being 0.045 for SOLV4 (a bit under 2% of the total value).

Thus the capacity of GRASP-AOD algorithm to discriminate between fine and coarse mode extinction is robust, quite stable in absolute terms, and has a constant uncertainty linked to the value of the measurement error that does not depend upon the aerosol load. Consequently, the value of τ_f can be accurately retrieved irrespective of the value of τ_a. On the contrary, the uncertainty in the bimodal log-normal size distribution parameters dramatically increases as the aerosol load decreases. Therefore, we recommend a lower limit of $\tau_a(440)=0.2$ for the bimodal size distribution parameters in order to assure quality retrievals. We emphasize, however, that this lower limit does not apply to the τ_f retrieval.

3.4.3 Reducing the spectral range

The different sensitivity studies presented in this section have been done for the spectral range of 340 to 1640 nm using the AERONET-Extended sun-photometer channels (for more information see Appendix A). However, some instruments have a reduced spectral range that does not capture the ultraviolet or near-infrared part of this range (table A1). For instance, many sites in the AERONET network were equipped with the Cimel model 318 Polarized photometer (mainly in Africa and Europe), which only includes the 440, 670, 870 and 1020 nm channels. Likewise, measurements in the GAW-PFR network utilize a similar spectral range from 368 to 862 nm. Hence, we repeated the 1000 inversions for each aerosol case using only the wavelengths in the reduced spectral range of 440 to 1020 nm.

The increments of the average values and the standard deviations obtained in the simulation error study for the reduced spectral range (440 to 1020 nm) with respect to the reference study (spectral range 340 – 1640 nm, see values in table 7) are represented in table 9 for the six bimodal log-normal size distribution parameters and τ_f (500). In this case, we have not included the ratio of the inversions that pass the filters (now with the maximum absolute residual fixed to 0.01) since it does not change substantially with respect to the one in table 7.

The differences for the average values in table 9 are typically quite small and they do not show a clear tendency. Therefore, the discrepancies between the average values obtained in this study and those obtained in the self-consistency analysis (table 3) are quite similar to those obtained with the full spectral range. However, differences are more notable in some specific examples. For instance in the case of MEXI1, r_{Vf} was 0.133 μm in the self-consistency analysis, and presented and averaged value of 0.131 μm in the analysis with all the wavelengths. Here, in the analysis with the reduced spectral range, the averaged value is 0.145 μm; which represents a difference of 0.012 with respect to the value obtained in the self-consistency analysis and a difference of 0.014 (shown in table 9) with respect to the analysis with the full spectral range.

Model	Δ mean values							Δ standard deviations						
	r_{V_f}	σ_{V_f}	C_{V_f}	r_{V_c}	σ_{V_c}	C_{V_c}	$\tau_f(500)$	r_{V_f}	σ_{V_f}	C_{V_f}	r_{V_c}	σ_{V_c}	C_{V_c}	$\tau_f(500)$
GSFC1	−0.003	−0.012	0.003	0.001	−0.001	0.004	−0.004	0.010	−0.040	0.003	−0.030	−0.009	0.009	0.007
GSFC3	−0.005	0.013	0.003	−0.001	0.005	0.004	−0.002	0.004	−0.022	−0.001	−0.029	−0.008	0.015	0.012
MEXI1	0.012	0.079	0.002	−0.005	0.010	−0.015	0.014	0.007	−0.013	−0.002	−0.029	−0.007	0.008	0.006
MEXI3	0.004	0.004	−0.002	0.001	0.000	0.000	0.000	0.003	−0.021	−0.002	−0.024	−0.009	0.018	0.013
ZAMB1	0.003	−0.026	−0.001	0.001	0.001	0.001	−0.001	0.006	−0.046	−0.001	−0.017	−0.012	0.009	0.007
ZAMB3	0.004	−0.013	−0.003	0.002	0.001	−0.003	0.003	0.003	−0.017	−0.001	−0.015	−0.009	0.015	0.011
SOLV1	0.005	0.011	0.001	0.024	−0.003	−0.001	0.003	0.010	−0.028	0.000	−0.040	−0.026	0.005	0.007
SOLV3	0.001	0.003	0.001	−0.005	0.005	−0.005	0.001	0.005	−0.005	0.001	−0.020	−0.003	−0.004	0.004
BAHR1	0.004	−0.037	0.000	0.007	−0.005	0.000	0.000	0.011	−0.053	−0.001	−0.017	−0.022	0.012	0.011
BAHR3	−0.003	0.011	0.001	0.007	0.001	0.003	−0.004	0.005	−0.014	0.001	−0.022	−0.016	0.006	0.010
LANA1	0.006	−0.041	0.000	0.063	−0.024	0.006	−0.001	0.012	−0.040	0.002	−0.052	−0.029	0.011	0.009
LANA2	0.004	−0.041	−0.003	0.056	−0.023	0.015	−0.007	0.009	−0.027	0.001	−0.036	−0.018	0.013	0.010

Table 9. Differences in the mean values and the standard deviations between the studies of the error simulation for the spectral range 440–1020 nm and 340–1640 nm (these last values represented in table 7). As in previous tables, the first six columns contain the parameters representing the bimodal log-normal size distribution (volume median radius (r_{Vf} , r_{Vc} [μm]), geometric standard deviation (σ_{Vf} and σ_{Vc}) and volume concentration ($C_{Vf,}$ C_{Vc} [$\mu m^3/\mu m^2$])). The last column depicts the fine mode aerosol optical depth at 500 nm ($\tau_f(500)$).

If we first observe the standard deviations in table 8, we see that they are positive or negative depending upon the parameter. The standard deviation decreases for σ_{V_f}, σ_{V_c} and r_{V_c} and it increases for the rest of the parameters. The increment is particularly relevant in the case of $\tau_f(500)$: the standard deviations increase their value between $0.007 - 0.013$ with respect to the values obtained in the tests with all the wavelengths (table 6). In those tests, the standard deviations were around $0.008 - 0.009$, while here, the standard deviation of $\tau_f(500)$ exceeds 0.02 for some aerosol cases. In relative terms, the increments of the uncertainty in $\tau_f(500)$, by the fact of reducing the spectral range, goes from 5% to 10% for the cases with $\tau_a(440) = 0.3$, and from $3 - 4\%$ to $5 - 7\%$ for the cases with $\tau_a(440) = 0.9$.

For r_{V_f}, the standard deviations in the cases with $\tau_a(440) = 0.3$ was around 0.015. This value increases in average 0.01 when reducing the spectral range. The uncertainty of r_{V_f} was only of 0.005 for the cases with $\tau_a(440) = 0.9$ and for the aerosol models dominated by the fine mode (table 6). With the reduction of the spectral range this uncertainty only rises 0.003, given a maximum value in the standard deviation of 0.01.

3.5 Sensitivity to the refractive index

As it was already discussed in the introduction, the information contained exclusively in the spectral aerosol optical depth measurements is not enough to retrieve the refractive indices. We have assumed this parameter as known thus far, and at this point we wish to determine how errors in this assumption affect the characterization of the size distribution. Thus, we use the same scheme presented in figure 3 to answer this question, but this time we modify the values of the refractive indices.

We only analyze the effects on three of the aerosol cases here: GSFC and SOLV to represent the cases with fine or coarse mode predominance, respectively, and ZAMB is also included to review the effects in an absorbing aerosol.

3.5.1 Pre-analysis with the forward code

First, we use the forward code to check the variation in the aerosol optical depth generated by a modification in the refractive index. Although the retrievals for three aerosol loads were evaluated in the main study, we only evaluate variations for GSFC2, SOLV2 and ZAMB2 (cases with $\tau_a(440) = 0.6$) in this portion of the analysis.

Thus, in table 10, the change in the aerosol optical depth caused by a change of $\pm 2\sigma$ in the refractive index (in both parameters n and k) can be determined for the three examples considered. The values of 2σ are obtained as well from the climatology study of Dubovik et al. (2002a) (see table 1 in that work). In the cases GSFC2 and ZAMB2, $2\sigma_n$ is equal to 0.02 whereas it is 0.06 in the case of SOLV2. For the imaginary part, $2\sigma_k$ has values of 0.008, 0.006 and 0.002 for ZAMB2, GSFC2 and SOLV2 respectively. In all the cases, the values of 2σ are spectrally independent. Note that for SOLV2 and ZAMB2, the case with $k - 2\sigma_k$ gives a negative value of the absorption in some wavelengths. In those cases, k is fixed to zero and it is indicated with an asterisk in table 10.

An increase in the real part of the refractive index produces an increase in τ_a because more light is scattered, and consequently, the direct beam is reduced (Bohren and Huffman, 1983). This change is symmetric as it can be seen in table 10. Moreover, $\Delta\tau_a$ is linear with the increments of n considered in this study (the same results were obtained in Torres (2012) where a more detailed explanation can be found).

	GSFC2		ZAMB2		SOLV2		GSFC2		ZAMB2		SOLV2	
λ [nm]	$-2\sigma_n$	$+2\sigma_n$	$-2\sigma_n$	$+2\sigma_n$	$-2\sigma_n$	$+2\sigma_n$	$-2\sigma_k$	$+2\sigma_k$	$-2\sigma_k$	$+2\sigma_k$	$-2\sigma_k$	$+2\sigma_k$
340	−0.054	0.052	−0.042	0.040	−0.053	0.052	0.000*	0.000	0.000	0.000	0.000	0.000
380	−0.051	0.050	−0.038	0.038	−0.046	0.046	0.000*	0.001	−0.003	0.003	0.000	0.000
440	−0.046	0.046	−0.034	0.034	−0.038	0.039	−0.002*	0.004	−0.006	0.006	−0.001	0.000
500	−0.039	0.039	−0.027	0.028	−0.029	0.030	−0.003*	0.006	−0.007	0.007	−0.001	0.000
675	−0.023	0.024	−0.015	0.015	−0.012	0.012	−0.004*	0.007	−0.008	0.008	−0.005*	0.004
870	−0.013	0.013	−0.008	0.008	−0.005	0.005	−0.004*	0.006	−0.007	0.007	−0.005*	0.004
1020	−0.008	0.009	−0.005	0.005	−0.004	0.004	−0.003*	0.007	−0.006	0.006	−0.005*	0.004
1640	−0.002	0.002	−0.001	0.001	−0.002	0.002	−0.002*	0.003	−0.004	0.003	−0.004*	0.004

Table 10. Change in the aerosol optical depth (references in table 2) caused by changes of $\pm 2\sigma$ in the complex refractive index (n, k) for GSFC2, SOLV2 and ZAMB2 (reference values in table 1). The value of $2\sigma_n$ is equal to 0.02 for GSFC and ZAMB, while it is equal to 0.06 for SOLV. For the imaginary part, $2\sigma_k$ has values of 0.008, 0.006 and 0.002 for ZAMB, GSFC and SOLV respectively. Note that $k - 2\sigma_k$ can be negative at some wavelengths; for those cases, k is fixed as zero and is indicated by an asterisk in the table.

Another interesting result is the larger effect produced by an increment of n for GSFC2 and ZAMB2 compared to SOLV2: although $2\sigma_n$ is three times larger for SOLV2, the increments of the aerosol optical depth are similar for the three examples (at 440 nm the variations are 0.046 and 0.034 for GSFC and ZAMB while it is 0.039 for Solar Village). The explanation lies in the fact that most of the increment produced by the real part of the refractive index goes to increment the optical depth of the fine mode without practically changing the optical depth of the coarse mode. Only for SOLV2, there is a slight decrease in the optical depth of the coarse mode at the largest wavelengths. This property also explains the strong spectral dependence in table 10: the fine mode optical depth, τ_f, is much larger at short wavelengths with respect to long wavelengths.

Finally, it can be observed in table 10, that the variation in the imaginary part has not a big influence in the aerosol optical depth. The maximum variations, always under 0.01, were obtained for the case ZAMB, which is the case with the largest $2\sigma_k$. As expected, positive increments of the imaginary refractive index increase the absorption, and therefore, the aerosol optical depth. In this case, the variation is not only allocated to the fine mode, but it is distributed into both modes. Nevertheless, the predominant mode gets the largest variations for each particular aerosol example.

3.5.2 Retrieval analysis

Following the scheme from figure 3, GRASP-AOD code has been applied to the optical depth values for the aerosol cases GSFC, ZAMB and SOLV (table 2), considering variations of $\pm\sigma$ and $\pm 2\sigma$ (see Dubovik et al., 2002a) from the original values of their refractive index (in table 1, only the cases with $\tau_a(440)$ = 0.3,0.6 and 0.9) during the inversion procedure.

Table 11 presents the retrieved values of the fine mode aerosol optical depth at 500 nm for variations of $\pm 2\sigma$ in the real, and in the complex part of the refractive index. The maximum difference between the retrieved values with and without the variations is observed for the case SOLV3 and is equal to 0.005; however, the differences are typically around 0.001 – 0.002. A similar result is obtained for the rest of the wavelengths, although it is not presented here. Therefore, the discrimination between the extinction of fine and coarse modes does not depend upon the refractive index assumption.

Figure 9 shows the size distributions obtained by varying the real and the imaginary parts of the refractive index by $\pm\sigma$ and $\pm 2\sigma$ during the retrieval process, for the three aerosol cases (for each of them with the three different aerosol load $\tau_a(440)$ = 0.3, 0.6 and 0.9). In the figure, red lines are used to indicate the cases when the refractive index is overestimated and blue lines represent the cases when the parameter is underestimated. Variations of $\pm\sigma$ are depicted by solid lines and the ones of $\pm 2\sigma$ by dashed lines. Finally, black solid lines illustrate the reference values while gray dashed lines represent the retrievals without variations in the refractive index (self-consistency study).

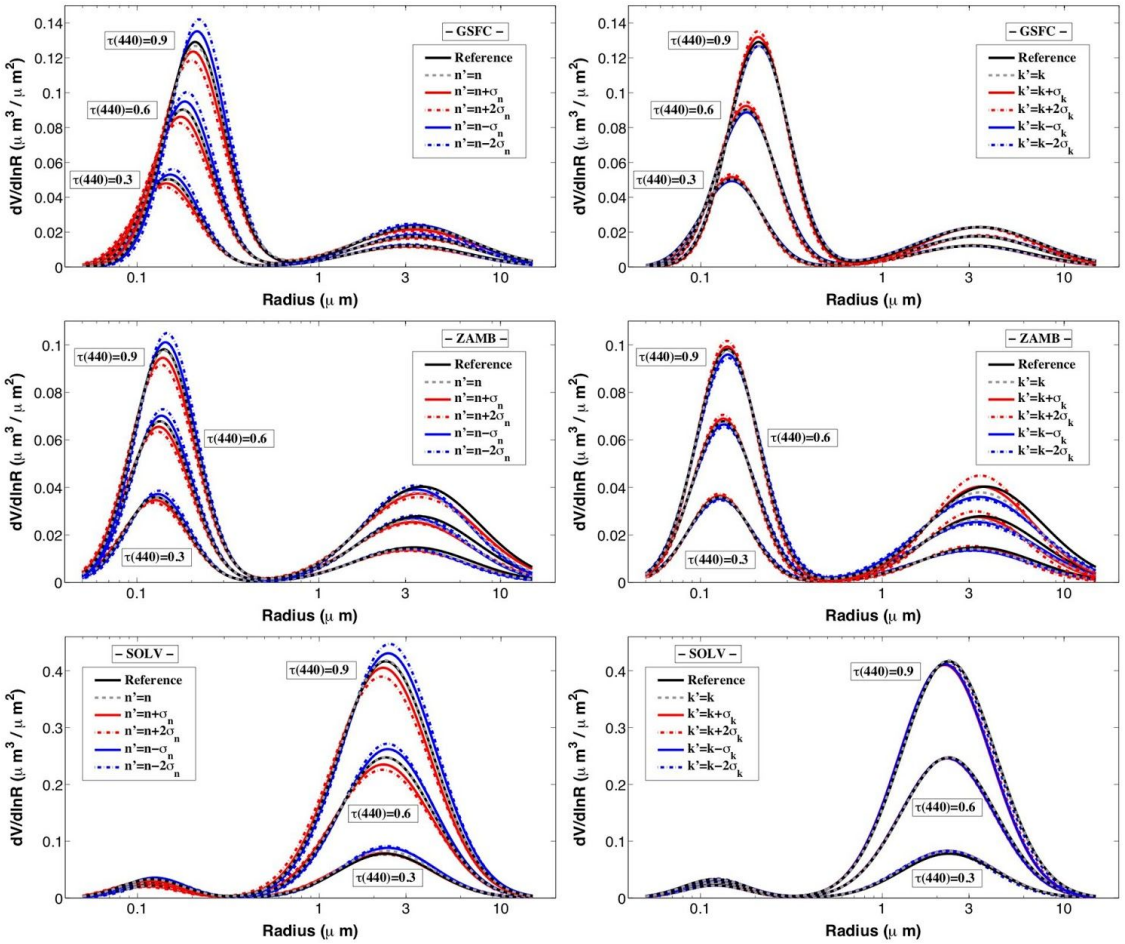

Figure 9. Sensitivity of the particle size distribution retrieval to refractive index for three of the aerosol examples: GSFC (top subfigures), ZAMB (middle subfigures) and SOLV (bottom subfigures). The subfigures on the left corresponds to the sensitivity analysis to the real part of refractive index, and on the right, to the imaginary part. Black solid lines are used to illustrate the reference values while gray dashed lines represent the retrievals without variations in the refractive index (self-consistency study). Red and blue lines are used to indicate the cases when refractive index is overestimated and underestimated respectively. In all the sub-figures, the variation of σ is represented by solid lines and the variation of 2σ by dashed lines. The value of $2\sigma_n$ is spectrally independent and equal to 0.02 for the cases GSFC and ZAMB while it is 0.06 for SOLV. For the imaginary part, $2\sigma_k$ has values of 0.008, 0.006 and 0.002 for ZAMB, GSFC and SOLV, respectively.

The retrieval behavior of the size distribution presents a similar pattern for the three analysed cases in response to the variations of the refractive index: there is a decrease in the mean radius and the volume concentration of the modes when the real part of the refractive index increases, while for negative variations both parameters increase their values. The same result was obtained in King et al. (1978), where it was pointed out that the shape of the size distribution remains the same but shifts with a varying real part. This is derived from anomalous diffraction theory of Van de Hulst (Van de Hulst, 1957), and was also discussed in Yamamoto and Tanaka (1969).

Analyzing the cases with fine mode predominance, GSFC and ZAMB, we observe that this tendency is only significant in the fine mode: the increments of r_{Vf} are between $\mp(4-5)\%$ and between $\mp(2-4)\%$ for C_{Vf} for variations of $\pm 2\sigma_n$. For the coarse mode, the variations in r_{Vc} and C_{Vc} do not show a clear behavior for GSFC and ZAMB, with values practically negligible (typically under 1%). These results are expected given the results from the pre-analysis with the forward code in the previous section and the stability of τ_f observed in table 11. As mentioned earlier, an increase in the refractive index results in a rise of the aerosol optical depth in the forward model . Since τ_f does not change in the retrieval, we expect the increase in the real refractive index to be compensated elsewhere. Figure 9 indicates that increases in the real refractive index are balanced by a

decrease in the volume of the particles and also a reduction of r_{Vf}. Note that the extinction efficiency diminishes as the radius decreases in the fine mode, especially for the shortest wavelengths.

Figure 9 seems to indicate a linear behavior in the increments of r_{Vf} and C_{Vf} against the variation of the refractive index. The differences for $\pm\sigma_n$ are half as large as for $\pm2\sigma_n$ for both GSFC and ZAMB. We have explored if this behavior continues for larger variations of the refractive index, in particular, for the case of GSFC. Note that the conditions in GSFC site are favourable to aerosol hygroscopic growth and the refractive index can suffer large variations with respect to the averaged values. Thus, we introduced differences up to $\pm5\sigma_n$ (or 0.05) for the three aerosol loads of GSFC ($\tau_a(440) = 0.3$, 0.6 and 0.9). The results of these tests have shown that the linear behavior continues with such variations of the refractive index, and that the differences in r_{Vf} and C_{Vf} can be approximated as $\Delta r_{Vf} \sim -0.04 \times \Delta n$, $\Delta C_{Vf} \sim -0.27 \times \tau_a(440) \times \Delta n$. In relative terms, these differences in r_{Vf} represents between $\mp$(12–13)% while in C_{Vf} between $\mp$(8–10)% for the maximum variation considered of $\pm5\sigma_n$. The large refractive index variation of $\pm5\sigma_n$ also perturbs the coarse mode r_{Vc} by $\mp$(3 – 5)% and C_{Vc} by $\mp$(2–4)%. The stability of τ_f observed in table 11 is still valid even with a variation of $\pm5\sigma_n$, with a maximum difference of $\Delta\tau_f = 0.005$ observed for the case GSFC3.

	GSFC1	GSFC2	GSFC3	ZAMB1	ZAMB2	ZAMB3	SOLV1	SOLV2	SOLV3
$\Delta n, k = 0$	0.222	0.457	0.711	0.225	0.445	0.675	0.141	0.174	0.206
$+2\sigma_n$	0.221	0.456	0.709	0.225	0.445	0.674	0.140	0.171	0.202
$-2\sigma_n$	0.222	0.458	0.713	0.226	0.446	0.676	0.142	0.175	0.211
$+2\sigma_k$	0.224	0.460	0.715	0.227	0.448	0.678	0.142	0.174	0.207
$-2\sigma_k^*$	0.221	0.456	0.710	0.224	0.443	0.671	0.142	0.174	0.206

Table 11. Fine mode aerosol optical depth at 500 nm ($\tau_f(500)$) obtained varying the refractive index by $\pm2\sigma$ during the retrieval process. The value of $2\sigma_n$ is spectrally independent and equal to 0.02 for GSFC and ZAMB, while is equal to 0.06 for SOLV. For the imaginary part, $2\sigma_k$ is also spectrally independent and has values of 0.008, 0.006 and 0.002 for ZAMB, GSFC and SOLV respectively. Note that $k - 2\sigma_k$ produces negative values of k for all wavelengths in the aerosol example GSFC and for some in SOLV. In those cases, k is fixed as zero in the retrieval.

For the case of SOLV, the general tendency is observed for both fine and coarse mode even with just a variation of $\pm2\sigma_n$ in the refractive index. In the fine mode, the difference in r_{Vf} and C_{Vf} are between $\mp$(8 – 9)% and $\mp$(7 – 8)% respectively. For the coarse mode, the mean radius and the volume concentration decrease between (3 – 4)% (for $+2\sigma_n$) when the real part of the refractive index increases.

The effective radius follows the same tendency as the mean radii of the modes. For the maximum increment of $\pm2\sigma_n$, it varies as $\mp$0.01μm in the three aerosol loads of GSFC and $\mp$0.006μm in those of ZAMB. These changes represent the $\mp$5% and the $\mp$3%, respectively, of the total value. In the examples of SOLV, the variations are of $\mp$3% for the two lowest aerosol loads and approximatively $\mp$7% for SOLV3.

The three sub-figures on the right in figure 9 depict the retrievals varying the imaginary part of the refractive index. The size distributions show similar patterns for the three aerosol cases: mean radii of the two modes do not have large variations with difference under 2% in the case of r_{Vf}, being a bit higher for r_{Vc} around (3 – 4)%. For both modes, these differences do not present a clear behavior being randomly positive or negative regardless the sign in the variation of the refractive index. Analyzing the concentration, however, a definite tendency can be observed: they decrease for positive variations of the refractive index and they increase for negative increments. The differences are around 1% for C_{Vf} and between (3 – 4)% for C_{Vc}. This result is expected, since when the absorption is increased there is an increase in the aerosol depth that is compensated by a reduction in the number of the particles. The behavior in the concentration, however, is not so clear in figure 9 where it seems that the opposite happens. The explanation is in the standard deviation of the modes which also diminishes for positive increments of the absorption and increases in the opposite case. Thus the maximum values in the size distribution are reached for the cases of $+2\sigma_k$ though the aerosol concentration are the lowest in these cases. The maximum variations of σ_{Vf} and σ_{Vc} are between 0.015 – 0.022 (absolute values), independently of the aerosol type. The variations in the effective radius are negligible for GSFC and ZAMB (differences under 0.5%). In the case of SOLV, differences up to 2% are observed though there is no a clear

tendency in them. This general little sensitivity for the variation of the imaginary part was also obtained in the studies of King et al. (1978) and Yamamoto and Tanaka (1969).

3.6 Variations in the sphericity parameter

We analyze the sphericity parameter assumption for our last sensitivity test. This parameter was introduced in Eq. 3 and defines the percentage of spheres in the aerosol model. The kernels of the extinction are quite similar for spheres and spheroids (unlike the kernels of angular scattering), but some small differences do appear because spheroid cross sections can not be straightforwardly calculated from equivalent sphere radii. It should also be noted that the sensitivity of extinction to particle shape is minor for small particles at the size parameters used in the retrieval, as illustrated in Figure 23 of Dubovik et al. (2006) (even the P_{11} function shows a little sensitivity as shown in Figure 27 of Dubovik et al., 2006) . Therefore, the main discrepancies produced by the uncertainty in the sphericity parameter should appear in the coarse mode.

We have selected the aerosol models of SOLV1 and BAHR3 in this analysis, since their values of the sphericity parameter is 0.6 and we can largely decrease and increase it in our tests. At the same time, the use of SOLV1 ($\tau_a(440) = 0.3$) and BAHR3 ($\tau_a(440) = 0.9$) allows us to see if the effect is more important depending on the aerosol load.

We begin with a brief comment on the variations in the aerosol optical depth caused by a modification in the sphericity parameter. We use the forward model to increase the sphericity from 0.6 to 1.0 and decrease it from 0.6 to 0.2 for both SOLV1 and BAHR3. The τ_a variations are quite similar in relative terms for both cases — increasing the sphericity parameter from 0.6 to 1 causes the aerosol optical depth to decrease by less than 1% at wavelengths less than 500 nm, to decrease by (2 – 3)% at the 675 and 870 nm wavelengths, and to decrease by about 5% at the 1020 and 1640 nm wavelengths . We also analyze the modes separately and find that the coarse mode optical depth variations are negative and almost constant at around 5% in both aerosol cases. The fine mode variations, on the other hand, are positive with values between and (1 – 2)% and a maximum at the central wavelength. Opposite results but with the same relative increments are obtained when the sphericity parameter is reduced.

We modified the reference value of the sphericity parameter for SOLV1 and BAHR3 during the inversion procedure as a second step. We reduced the sphericity to 0.4 and 0.2 and incremented it to 0.8 and 1.0, and present the variations in the resulting retrieved parameters in Table 12. As we expected from our tests with the forward mode, the differences for the fine mode are very small — the differences for r_{Vf} and C_{Vf} are negligible, and σ_{Vf} only changes at maximum by ±0.02. Similarly, no changes for the retrieved values of $\tau_f(500)$ are observed in table 12.

		Δr_{V_f}	$\Delta \sigma_{V_f}$	ΔC_{V_f}	Δr_{V_c}	$\Delta \sigma_{V_c}$	ΔC_{V_c}	$\Delta \tau_f(500)$	Δr_{eff}
SOLV1 ref.=0.6	Sph = 0.2	0.003	−0.021	−0.000	0.145	−0.001	0.008	−0.001	0.049
	Sph = 0.4	0.001	−0.009	−0.000	0.031	−0.008	−0.000	0.000	0.003
	Sph = 0.8	−0.001	0.011	0.000	−0.061	0.006	−0.001	0.000	−0.015
	Sph = 1.0	−0.002	0.006	−0.000	0.102	0.041	0.014	−0.001	0.031
BAHR3 ref. = 0.6	Sph = 0.2	0.003	−0.018	−0.000	0.056	−0.016	−0.003	0.000	0.015
	Sph = 0.4	0.001	−0.009	−0.000	0.033	−0.008	−0.001	−0.000	0.009
	Sph = 0.8	−0.001	0.009	0.000	−0.016	0.011	0.003	0.000	−0.005
	Sph = 1.0	−0.003	0.018	0.000	−0.042	0.020	0.004	0.000	−0.006

Table 12. Sphericity tests results. Differences between GRASP-AOD code with modified sphericity parameters and GRASP-AOD code with reference sphericity value of 0.6. The first six columns depict the bimodal log-normal size distribution parameters: volume median radius (r_{Vf} , r_{Vc} [μm]), geometric standard deviation (σ_{Vf} and σ_{Vc}) and volume concentration (C_{Vf} , C_{Vc} [$\mu m^3/\mu m^2$]). The last two columns contain the fine mode aerosol optical depth at 500 nm ($\tau_f(500)$) and the effective radius (r_{eff} [μm]).

On the contrary, we observe some significant differences for the parameters that define the coarse mode. These differences are more significant for SOLV1 than for BAHR3. For instance, the maximum difference for r_{V_c} is 0.145 μm for SOLV1 (6% in relative terms) and 0.056 μm for BAHR3 (about 2%). Differences in

C_{V_c} are also more significant for SOLV1 than BAHR3, with maximum differences of 0.014 $\mu m^3/\mu m^2$ (about 10% of total value) for SOLV1 and only 0.004 (1% in relative terms)for BAHR3.

As mentioned earlier, increasing the number of spheroids decreases the sphericity parameter and increases the optical depth. Since the retrieval is constrained by optical depth, the retrieval compensates for the reduction of the sphericity assumption at BAHR3 by increasing r_{V_c} (recall that the extinction efficiency diminishes as the radius increases in the coarse mode) . For SOLV1 the relation is less clear, since C_{V_c} and σ_{V_c} also suffer large variations. Nevertheless, the variations try to compensate the change in τ_a that occurs when the spheroid ratio is altered.

4 Real cases

4.1 Comparison with AERONET

We present here a comparison between the aerosol products obtained from the new GRASP-AOD inversion and AERONET products, in order to validate the results achieved in previous sections. In particular, we compare our results with: (a) size distributions obtained from the AERONET inversion code (Dubovik and King, 2000; Dubovik et al., 2006), and (b) τ_f (500) obtained from the SDA (O'Neill et al., 2003). All of the data and products used in the comparison belong to AERONET level 2.0 (quality assured data, see Smirnov et al., 2000) and can be found in the public AERONET database (http://aeronet. gsfc.nasa.gov).

4.1.1 Data selection

To homogenize the two different data sets (almucantar and spectral aerosol optical depth measurements), we propose a comparison of daily averages on days with stable aerosol conditions instead of comparing single inversions. This approach allows us to include a large number of τ_a inversions which will be useful to check the stability of the new inversion. We limit our analysis to days that fulfill three requirements:

(1) There are a minimum of 15 τ_a measurements per day; each τ_a measurement is only eligible if there is a valid almucantar within a maximum of ±30 minute delay. This requirement also improves the quality of the τ_a data selected as there are only almucantars in level 2.0 with $\theta_s > 50$. That is, a maximum delay of half an hour assures that all τ_a measurements are obtained when $\theta_s > 40$, which reduces the bias produced by errors in the calibration coefficients (see Eq. A6).

(2) In order to guarantee stable aerosol conditions, the ratio between the standard deviations and the averages of the eligible aerosol optical depths are required to be smaller than 0.1 throughout the day (evaluated for every spectral wavelengths used by the GRASP-AOD inversion).

(3) There should be a minimum of 4 valid almucantars per day.

Following these conditions, 29 days have been selected from the same six sites used as (climatological) inputs in the simulations and two additional Mediterranean AERONET sites: Rome Tor Vergata (henceforth just Rome) and the ChArMEx super site of Lampedusa. Following Mallet et al. (2013), the dominant aerosol type is background aerosols with frequent dust intrusions for Lampedusa (coarse mode predominance), while for Rome, the dominant aerosol type is urban-industrialized (fine mode predominance).

In total, 165 AERONET inversions (almucantar and τ_a) and 744 GRASP-AOD inversions have been compared. Table 13 depicts the information regarding the daily conditions of the analyzed cases. The first three columns in table 13 contains technical information about the day selected (site, photometer number, type and date). Mexico-City, Mongu, Lanai, Rome, and Lampedusa do not have extended photometers for the measurements, so we have used only standard wavelengths for the analysis at those sites. This is indicated in the second column with the label "STD" (for the standard photometers) or "EXT" (for the extended photometers) together with the AERONET number of the instrument (see table A1 in Appendix A to get more information about standard and extended photometers). The selected days for each site correspond to the same deployment period (between a common preand postcalibration). For Roma and Lampedusa, the chosen interval is coincident with the ChArMEx/ADRIMED (Chemistry-Aerosol Mediterranean Experiment/Aerosol Direct Radiative

Forcing on the Mediterranean Climate) summer campaign from 11 June to 5 July 2013 over the western Mediterranean (Mallet et al., 2016). Unfortunately, at Lampedusa site, the 340 nm channel has not passed the requirements of AERONET level 2.0 during this period, so the data at this wavelength have not been used for the GRASP-AOD inversions at this site.

Cases	Photometer	Date	$< \tau_a(440) >$	$< \alpha >$	No. ALM	No. τ_a
GSFC -A-	#451 (EXT)	22/11/2009	0.166 ± 0.015	1.639 ± 0.029	8	39
GSFC -B-		01/09/2010	0.323 ± 0.027	1.817 ± 0.025	8	30
GSFC -C-		27/08/2009	0.493 ± 0.042	1.913 ± 0.025	5	19
GSFC -D-		06/07/2010	0.590 ± 0.049	1.968 ± 0.019	4	24
MEXI -A-	#10 (STD)	05/04/2003	0.246 ± 0.009	1.556 ± 0.014	4	16
MEXI -B-		07/12/2003	0.384 ± 0.016	1.728 ± 0.029	4	16
MEXI -C-		28/04/2003	0.475 ± 0.015	1.798 ± 0.026	4	18
MEXI -D-		09/05/2003	0.686 ± 0.060	1.603 ± 0.011	4	17
ZAMB -A-	#155 (STD)	18/06/2007	0.249 ± 0.025	1.837 ± 0.055	9	43
ZAMB -B-		02/08/2006	0.422 ± 0.029	1.783 ± 0.027	10	46
ZAMB -C-		25/07/2006	0.487 ± 0.010	1.917 ± 0.019	5	23
ZAMB -D-		18/08/2006	0.733 ± 0.026	1.874 ± 0.016	9	45
SOLV -A-	#125 (EXT)	27/05/2007	0.249 ± 0.006	0.298 ± 0.006	5	20
SOLV -B-		19/05/2007	0.422 ± 0.020	0.208 ± 0.011	7	38
SOLV -C-		06/04/2007	0.532 ± 0.051	0.273 ± 0.027	8	35
SOLV -D-		06/06/2007	0.595 ± 0.020	0.089 ± 0.010	6	35
BAHR -A-	#130 (EXT)	20/04/2005	0.301 ± 0.027	0.694 ± 0.049	4	15
BAHR -B-		01/09/2005	0.423 ± 0.030	0.752 ± 0.123	4	16
BAHR -C-		12/07/2005	0.579 ± 0.014	0.512 ± 0.089	4	18
BAHR -D-		20/10/2005	0.722 ± 0.029	0.880 ± 0.050	6	24
LANA -A-	#107 (STD)	21/03/2002	0.110 ± 0.003	0.819 ± 0.048	4	18
LANA -B-		23/03/2002	0.147 ± 0.014	0.784 ± 0.108	4	17
LANA -C-		19/04/2002	0.232 ± 0.022	1.208 ± 0.054	4	17
ROME -A-	#232 (STD)	11/06/2013	0.129 ± 0.009	1.278 ± 0.074	8	32
ROME -B-		15/06/2013	0.234 ± 0.020	1.764 ± 0.037	8	34
ROME -C-		22/08/2013	0.348 ± 0.025	1.758 ± 0.010	6	30
LAMP -A-	#172 (STD)	18/03/2014	0.148 ± 0.009	0.925 ± 0.042	5	25
LAMP -B-		03/07/2013	0.304 ± 0.005	0.433 ± 0.021	4	18
LAMP -C-		20/05/2014	0.466 ± 0.013	0.098 ± 0.005	4	16

Table 13. Summary of the 29 days chosen for comparison between the new GRASP-AOD inversion and the AERONET products. The first columns depict information about the day selected: site, photometer, date, τ_a at 440 nm and Ångström exponent. The last two columns contain the number data used for each inversion type: ALM or almucantar used for AERONET inversion, and τ_a used for both GRASP-AOD inversion and SDA algorithm. STD and EXT refer to the standard and extended version of the Cimel-310 sun-photometer, respectively (see table A1). The 340-nm channel of photometer #172, at Lampedusa site, was excluded for quality assurance reason.

The daily averaged value and the standard deviation of the aerosol optical depth at 440 nm as well as the Ångström exponent (from 440 nm, 675 nm and 870 nm) are indicated in columns four and five of table 13, so as to give an idea of the characteristics of the aerosol analyzed: load and predominance of fine or coarse mode. As can be seen from the table, we covered a broad aerosol load with $\tau_a(440)$ variations by a factor of 2 (LANA) to 3.5 (GSFC) using three or four examples for each site. The last two columns indicate the number of inversions: ALM indicates the number of almucantar used for the AERONET standard inversion, AOD the number of inversions used for both GRASP-AOD inversion and SDA algorithm.

To run the GRASP-AOD inversions, we have assumed climatological values of the refractive index for the different sites in table 13. Thus, for the first six cases we have taken the values from table 1, while for Rome and Lampedusa we relied on table 2 of Mallet et al. (2013)(For the real part we have used spectrally independent values: 1.435 for Rome and 1.47 for Lampedusa. For the imaginary part, for Rome we have used 0.012 for ultraviolet and 440 nm, 0.011 for 500 nm, 0.009 for 675 nm and 0.008 for the rest of the wavelengths. For Lampedusa, we have used 0.0035 for 380 and 440 nm, 0.003 for 500 nm, 0.0018 for 675 nm and 0.001 for the other wavelengths). For the sphericity parameter, we have used values of 0 and 100 for Ångström exponents

smaller than 0.6 and larger than 1.1 (respectively), and we have applied a linear interpolation (with respect to the Ångström exponent) for intermediate values.

4.1.2 Results

Table 14 represents the daily average of the standard parameters for fine and coarse modes retrieved using AERONET-standard and GRASP-AOD inversion for the chosen days shown in table 13. While both r_{V_f} and r_{V_c} are direct outputs of the GRASP inversions, the standard AERONET inversions gives a 22-bin retrieved size distribution in the latter situation, values of r_{V_f} and r_{V_c} are estimated using the standard AERONET procedure described in http://aeronet.gsfc.nasa.gov/new_web/Documents/ Inversion_products_V2.pdf.

Figure 10 illustrates the absolute differences of the mean volume radii by using GRASP-AOD and AERONET standard inversion calculated from the values in table 14. In the left panel, the differences for the fine mode are represented, while those of the coarse mode are depicted in the right panel. Analyzing the differences of r_{Vf} at the 4 sites with fine mode predominance (GSFC, MEXI, ZAMB, and ROME), we observe an excellent agreement between both inversions, with differences under 0.015 μm except for the cases of GSFC -A(maximum difference of 0.028 μm), GSFC -D(0.018 μm) and ZAMB -A(0.020 μm). At the 4 sites with a prevailing coarse mode (SOLV, BAHR, LANA and LAMP), the differences are a bit higher, generally, ranging from 0.010 μm to 0.020 μm. The maximum difference of 0.035 μm is observed for the case LAMP -B-. Thus, the average of the differences of r_{Vf} are 0.010 μm at sites dominated by the fine mode and 0.013 μm when we include all the site.

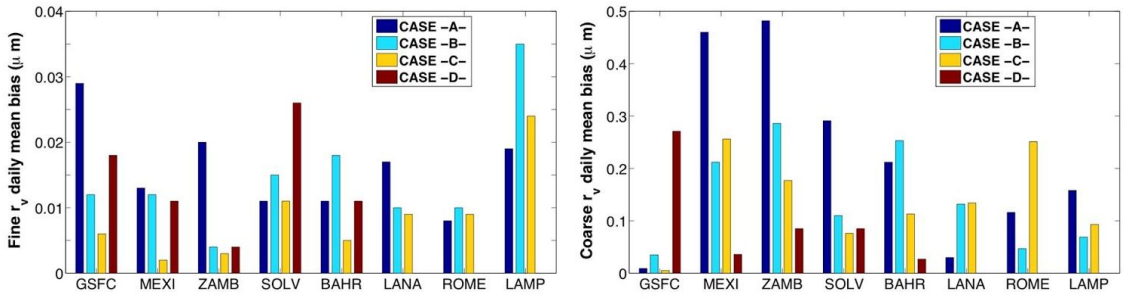

Figure 10. Absolute differences between the daily averages of the median volume radii retrieved by GRASP-AOD and AERONET standard inversions (total values can be found in table 14) for the examples considered in the analysis as listed in table 13. The differences for the fine mode are represented in the left panel and for the coarse mode in the right panel. Different days (A, B, C, and possibly D) considered at each station and are plotted with different colours.

The differences in r_{V_c} are under 0.3 μm for the cases with $\tau_a(440) > 0.3$. The maximum differences are reached for the cases with a prevailing fine mode and $\tau_a(440) < 0.3$: MEXI -A- and ZAMB -A- with values of 0.46 μm and 0.48 μm, respectively. The analysis in relative terms give similar results as in the fine mode, with differences of around 15% in our particular test cases, although they do not exceed 10% in the rest of the cases.

In the case of C_{V_f}, the largest differences are obtained for the cases with a predominant fine mode with a maximum value of 0.016 $\mu m^3/\mu m^2$ found for MEXI -D(see table 14). For C_{V_c}, the largest differences are found for the desert dust cases, with a maximum value of 0.043 $\mu m^3/\mu m^2$ (SOLV -D-). The high variability of the concentration for both modes makes the analysis more suitable in terms of relative differences. Figure 11 shows the relative differences (in modulus) of the daily volume concentration retrieved by GRASP-AOD and AERONET standard inversion for the different examples. The average differences in both C_{V_f} and C_{V_c} are around 17%. As a general result, we observe that the differences for C_{V_f} are the smallest for the cases dominated by the fine mode, and the differences for C_{V_c} are the smallest for the cases dominated by the coarse

mode. We find that the average differences in volume concentration are around 10 % for the dominant mode, whether it is the fine or coarse mode.

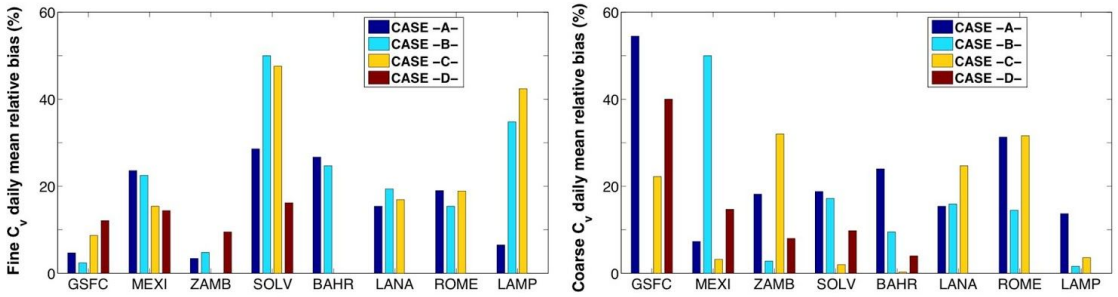

Figure 11. Relative differences between the daily averages of the volume concentrations retrieved by GRASP-AOD and AERONET standard inversions (total values can be found in table 14) for the examples considered in the analysis as listed in table 13. The differences for the fine mode are represented in the left panel and for the coarse mode in the right panel. Different days (A, B, C, and possibly D) considered at each station and are plotted with different colours.

In figure 12, the absolute differences for the daily means of σ_{Vf} and σ_{Vc}, retrieved by GRASP-AOD and AERONET standard inversions (table 14), are shown. The average difference is 0.071 for σ_{Vf} and 0.081 for σ_{Vc}, although differences larger than 0.2 are sometimes observed in both cases. These results confirm one of the outcomes from the sensitivity analysis, where we pointed out that the retrieval of the standard deviations (mode widths) is less accurate than the retrieval of the modal radii and concentrations.

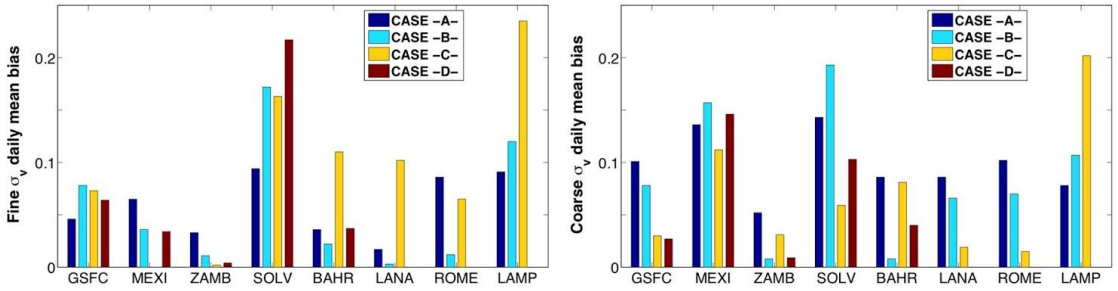

Figure 12. Absolute differences between the daily averages of the mode standard deviation retrieved by GRASP-AOD and AERONET standard inversions (total values can be found in table 14) for the examples considered in the analysis as listed in table 13. The differences for the fine mode are represented in the left panel and for the coarse mode in the right panel. Different days (A, B, C, and possibly D) considered at each station and are plotted with different colours.

Values of $\tau_f(500)$ are computed using the retrieved parameters from standard AERONET (the computation from the retrieved parameters of the standard AERONET inversion requires running the forward model with extra information about the refractive index at 500 nm. In our case, the value of the refractive index is interpolated between 440 and 675 nm for every single inversion.) and GRASP-AOD inversions. Both values are presented together with those obtained by the SDA algorithm in table 15. It can be observed that, in general, the values of $\tau_f(500)$ retrieved by GRASP-AOD are ranging between those retrieved by the standard AERONET inversion and the SDA algorithm. Analyzing the differences for the cases with a prevailing fine mode, we see that a maximum value of 0.020 is found for the case GSFC -Dbetween GRASP-AOD and the standard AERONET inversion. On the other hand, a maximum difference of 0.011 is observed between GRASP-AOD and SDA algorithm for the case GSFC -D-. The analysis of the cases dominated by the coarse mode shows difference by up to 0.034 (SOLV -D-) between GRASP-AOD and the standard AERONET inversion. The maximum difference is a bit larger for the comparison between GRASP-AOD and SDA algorithms with a value of 0.036 (BAHR -A-).

Note that computing $\tau_f(500)$ also allows us to compare the results obtained by the SDA and AERONET standard inversions for the examples presented here. This comparison was already done in O'Neill et al. (2003) (and in the technical memo of the Spectral Deconvolution Algorithm;

http://aeronet.gsfc.nasa.gov/new_web/PDF/tauf_tauc_technical_memo.pdf) and in other studies like in Eck et al. (2010). The previous studies have pointed out a negative bias for $\tau_f(500)$ calculated from SDA with respect to the AERONET standard inversion. The same general tendency is observed here for all the cases presented. For the examples with a predominance of the fine mode, absolute values of the differences are a bit smaller here than those found in O'Neill et al. (2003). Thus, a maximum difference of 0.02 is observed here (case MEXI -B-) while in O'Neill et al. (2003) the differences were ranging between 0.015-0.03, for examples of similar characteristics. This slight improvement can be justified since the AERONET Version 2 is used in the present work instead of Version 1 employed in O'Neill et al. (2003). In Version 2, the fine-coarse mode separation is done by finding the minimum value in the size distribution within the size interval from 0.439 to 0.992 μm, while in Version 1 the separation was done universally at 0.6 μm. The universal cut-off at 0.6 μm was the main source of discrepancies between the algorithms in O'Neill et al. (2003), and justified using Mie calculations in the technical memo of SDA. The results of this comparison certainly improves with the new fine-coarse mode separation in Version 2. The comparison for the cases dominated by the coarse mode shows differences between 0.01-0.05 in the values of $\tau_f(500)$. The same range is found in the study by Eck et al. (2010), which contains examples with large coarse mode (see their section 3.2: ~ 0.03 at Ilorin site and ~ 0.05 at Kanpur site).

Cases	Type	r_{V_f}	σ_{V_f}	C_{V_f}	r_{V_c}	σ_{V_c}	C_{V_c}
GSFC -A-	ALM	0.230 ± 0.016	0.503 ± 0.028	0.021 ± 0.002	2.905 ± 0.159	0.677 ± 0.019	0.004 ± 0.001
	GRASP (EXT)	0.201 ± 0.014	0.457 ± 0.053	0.022 ± 0.003	2.914 ± 0.038	0.778 ± 0.017	0.007 ± 0.001
GSFC -B-	ALM	0.180 ± 0.008	0.446 ± 0.019	0.043 ± 0.014	3.223 ± 0.075	0.608 ± 0.014	0.025 ± 0.003
	GRASP (EXT)	0.192 ± 0.011	0.368 ± 0.073	0.042 ± 0.005	3.188 ± 0.016	0.686 ± 0.006	0.025 ± 0.002
GSFC -C-	ALM	0.186 ± 0.012	0.433 ± 0.018	0.072 ± 0.022	3.256 ± 0.107	0.668 ± 0.012	0.020 ± 0.001
	GRASP (EXT)	0.192 ± 0.006	0.360 ± 0.024	0.066 ± 0.006	3.251 ± 0.002	0.698 ± 0.002	0.025 ± 0.003
GSFC -D-	ALM	0.193 ± 0.001	0.396 ± 0.015	0.070 ± 0.010	3.619 ± 0.261	0.658 ± 0.035	0.015 ± 0.002
	GRASP (EXT)	0.211 ± 0.005	0.332 ± 0.008	0.079 ± 0.013	3.348 ± 0.005	0.685 ± 0.003	0.010 ± 0.001
MEXI -A-	ALM	0.145 ± 0.002	0.363 ± 0.006	0.052 ± 0.002	3.671 ± 0.074	0.567 ± 0.008	0.057 ± 0.003
	GRASP (STD)	0.132 ± 0.009	0.428 ± 0.070	0.041 ± 0.002	3.211 ± 0.002	0.703 ± 0.005	0.053 ± 0.007
MEXI -B-	ALM	0.163 ± 0.005	0.435 ± 0.010	0.079 ± 0.003	3.425 ± 0.117	0.539 ± 0.011	0.033 ± 0.004
	GRASP (STD)	0.151 ± 0.008	0.399 ± 0.048	0.063 ± 0.007	3.213 ± 0.001	0.696 ± 0.001	0.055 ± 0.005
MEXI -C-	ALM	0.141 ± 0.004	0.376 ± 0.026	0.091 ± 0.013	3.493 ± 0.136	0.583 ± 0.015	0.062 ± 0.002
	GRASP (STD)	0.143 ± 0.003	0.376 ± 0.022	0.078 ± 0.001	3.237 ± 0.031	0.695 ± 0.001	0.064 ± 0.010
MEXI -D-	ALM	0.173 ± 0.008	0.440 ± 0.006	0.119 ± 0.014	3.401 ± 0.172	0.544 ± 0.028	0.063 ± 0.003
	GRASP (STD)	0.184 ± 0.004	0.406 ± 0.005	0.103 ± 0.005	3.437 ± 0.001	0.690 ± 0.004	0.073 ± 0.008
ZAMB -A-	ALM	0.148 ± 0.003	0.393 ± 0.027	0.029 ± 0.005	3.631 ± 0.240	0.654 ± 0.051	0.020 ± 0.002
	GRASP (STD)	0.128 ± 0.014	0.426 ± 0.096	0.030 ± 0.003	3.149 ± 0.029	0.706 ± 0.004	0.024 ± 0.005
ZAMB -B-	ALM	0.149 ± 0.003	0.367 ± 0.018	0.041 ± 0.007	3.563 ± 0.114	0.692 ± 0.024	0.035 ± 0.002
	GRASP (STD)	0.153 ± 0.004	0.378 ± 0.018	0.043 ± 0.002	3.277 ± 0.003	0.700 ± 0.001	0.036 ± 0.004
ZAMB -C-	ALM	0.141 ± 0.004	0.374 ± 0.022	0.053 ± 0.010	3.519 ± 0.074	0.734 ± 0.036	0.021 ± 0.001
	GRASP (STD)	0.144 ± 0.003	0.372 ± 0.027	0.053 ± 0.002	3.342 ± 0.002	0.703 ± 0.001	0.029 ± 0.006
ZAMB -D-	ALM	0.142 ± 0.002	0.383 ± 0.016	0.088 ± 0.008	3.496 ± 0.106	0.688 ± 0.044	0.048 ± 0.006
	GRASP (STD)	0.146 ± 0.002	0.379 ± 0.014	0.080 ± 0.003	3.411 ± 0.002	0.697 ± 0.001	0.052 ± 0.009
SOLV -A-	ALM	0.132 ± 0.006	0.537 ± 0.013	0.016 ± 0.001	2.140 ± 0.014	0.613 ± 0.011	0.140 ± 0.006
	GRASP (EXT)	0.121 ± 0.011	0.443 ± 0.044	0.012 ± 0.002	1.849 ± 0.102	0.756 ± 0.038	0.116 ± 0.004
SOLV -B-	ALM	0.144 ± 0.015	0.631 ± 0.010	0.025 ± 0.005	2.096 ± 0.081	0.570 ± 0.021	0.259 ± 0.017
	GRASP (EXT)	0.159 ± 0.010	0.459 ± 0.016	0.015 ± 0.002	1.986 ± 0.109	0.763 ± 0.052	0.218 ± 0.025
SOLV -C-	ALM	0.136 ± 0.007	0.595 ± 0.035	0.039 ± 0.003	2.102 ± 0.072	0.607 ± 0.024	0.298 ± 0.031
	GRASP (EXT)	0.147 ± 0.011	0.432 ± 0.012	0.024 ± 0.002	2.178 ± 0.070	0.666 ± 0.033	0.304 ± 0.055
SOLV -D-	ALM	0.168 ± 0.017	0.682 ± 0.024	0.020 ± 0.002	2.296 ± 0.074	0.549 ± 0.021	0.460 ± 0.029
	GRASP (EXT)	0.142 ± 0.002	0.465 ± 0.003	0.017 ± 0.002	2.211 ± 0.036	0.652 ± 0.015	0.417 ± 0.021
BAHR -A-	ALM	0.131 ± 0.010	0.521 ± 0.021	0.034 ± 0.005	1.872 ± 0.164	0.597 ± 0.039	0.077 ± 0.017
	GRASP (EXT)	0.142 ± 0.008	0.485 ± 0.043	0.026 ± 0.002	2.084 ± 0.058	0.683 ± 0.025	0.098 ± 0.018
BAHR -B-	ALM	0.137 ± 0.008	0.392 ± 0.013	0.032 ± 0.003	2.535 ± 0.042	0.644 ± 0.004	0.155 ± 0.019
	GRASP (EXT)	0.119 ± 0.007	0.414 ± 0.015	0.041 ± 0.005	2.282 ± 0.030	0.636 ± 0.015	0.141 ± 0.014
BAHR -C-	ALM	0.139 ± 0.020	0.550 ± 0.019	0.033 ± 0.001	2.077 ± 0.498	0.575 ± 0.042	0.303 ± 0.082
	GRASP (EXT)	0.134 ± 0.005	0.440 ± 0.008	0.033 ± 0.002	2.190 ± 0.044	0.656 ± 0.021	0.304 ± 0.009
BAHR -D-	ALM	0.153 ± 0.003	0.393 ± 0.013	0.060 ± 0.007	2.242 ± 0.042	0.580 ± 0.010	0.245 ± 0.018
	GRASP (EXT)	0.142 ± 0.004	0.430 ± 0.007	0.060 ± 0.001	2.269 ± 0.004	0.620 ± 0.012	0.255 ± 0.024

Table 14. Daily average of standard parameters for fine and coarse modes retrieved using AERONET-standard and GRASP-AOD inversion: volume median radius (r_{Vf} , r_{Vc} [μm]), standard deviation (σ_{Vf} and σ_{Vc}) and volume concentration (C_{Vf} , C_{Vc} [$\mu m^3 / \mu m^2$]). Additional information about the 29 chosen days is shown in table 13.

Cases	Type	r_{V_f}	σ_{V_f}	C_{V_f}	r_{V_c}	σ_{V_c}	C_{V_c}
LANA -A-	ALM	0.156 ± 0.004	0.443 ± 0.008	0.014 ± 0.002	2.236 ± 0.079	0.699 ± 0.021	0.036 ± 0.003
	GRASP (STD)	0.173 ± 0.015	0.426 ± 0.057	0.012 ± 0.001	2.266 ± 0.050	0.613 ± 0.040	0.042 ± 0.004
LANA -B-	ALM	0.168 ± 0.004	0.429 ± 0.021	0.017 ± 0.005	2.145 ± 0.057	0.672 ± 0.009	0.058 ± 0.005
	GRASP (STD)	0.178 ± 0.010	0.426 ± 0.036	0.014 ± 0.003	2.277 ± 0.027	0.606 ± 0.029	0.068 ± 0.006
LANA -C-	ALM	0.284 ± 0.016	0.441 ± 0.014	0.032 ± 0.003	2.546 ± 0.203	0.611 ± 0.035	0.032 ± 0.008
	GRASP (STD)	0.275 ± 0.009	0.339 ± 0.051	0.027 ± 0.003	2.680 ± 0.006	0.592 ± 0.008	0.041 ± 0.008
ROME -A-	ALM	0.147 ± 0.020	0.377 ± 0.031	0.023 ± 0.008	2.643 ± 0.383	0.721 ± 0.010	0.027 ± 0.002
	GRASP (STD)	0.139 ± 0.016	0.463 ± 0.122	0.019 ± 0.003	2.759 ± 0.041	0.619 ± 0.012	0.037 ± 0.004
ROME -B-	ALM	0.144 ± 0.006	0.406 ± 0.018	0.042 ± 0.009	3.161 ± 0.117	0.631 ± 0.026	0.032 ± 0.004
	GRASP (STD)	0.134 ± 0.007	0.394 ± 0.069	0.036 ± 0.003	3.114 ± 0.003	0.701 ± 0.006	0.037 ± 0.004
ROME -C-	ALM	0.172 ± 0.013	0.412 ± 0.030	0.052 ± 0.014	2.834 ± 0.123	0.677 ± 0.037	0.024 ± 0.001
	GRASP (STD)	0.181 ± 0.002	0.347 ± 0.012	0.043 ± 0.003	3.095 ± 0.005	0.692 ± 0.004	0.033 ± 0.001
LAMP -A-	ALM	0.164 ± 0.009	0.447 ± 0.029	0.016 ± 0.004	1.914 ± 0.046	0.691 ± 0.027	0.034 ± 0.005
	GRASP (STD)	0.145 ± 0.013	0.538 ± 0.061	0.015 ± 0.002	2.072 ± 0.095	0.769 ± 0.053	0.039 ± 0.005
LAMP -B-	ALM	0.142 ± 0.012	0.576 ± 0.022	0.027 ± 0.004	1.963 ± 0.018	0.630 ± 0.008	0.128 ± 0.003
	GRASP (STD)	0.177 ± 0.006	0.456 ± 0.037	0.019 ± 0.005	2.032 ± 0.020	0.737 ± 0.028	0.130 ± 0.007
LAMP -C-	ALM	0.187 ± 0.023	0.673 ± 0.041	0.020 ± 0.002	1.817 ± 0.040	0.551 ± 0.015	0.255 ± 0.013
	GRASP (STD)	0.211 ± 0.015	0.438 ± 0.035	0.013 ± 0.003	1.910 ± 0.096	0.753 ± 0.045	0.246 ± 0.031

Table 14. Continued.

Table 15 also contains the values of r_{eff} respectively retrieved by GRASP-AOD and standard AERONET standard inversion. For the cases with a prevailing fine mode, the largest differences are obtained for the cases of MEXI and ROME. Among them, the largest value is 0.06 μm, reached for the case MEXI -B-. The differences are higher in the cases with a predominance of the coarse mode. The extreme case, both in absolute and relative terms, is found for LAMP -Bwith an absolute difference of 0.196 μm which is around the 30% in relative terms. The average of the differences is 10% and it does not depend on the mode predominance.

Cases	$< \tau_f(500) >$			$< r_{eff} >$	
	AERONET	GRASP-AOD	SDA	AERONET	GRASP-AOD
GSFC -A-	0.144 ± 0.019	0.132 ± 0.013	0.129 ± 0.013	0.240 ± 0.026	0.237 ± 0.031
GSFC -B-	0.262 ± 0.022	0.250 ± 0.024	0.254 ± 0.025	0.254 ± 0.029	0.283 ± 0.026
GSFC -C-	0.402 ± 0.030	0.387 ± 0.037	0.386 ± 0.037	0.215 ± 0.020	0.245 ± 0.007
GSFC -D-	0.472 ± 0.049	0.492 ± 0.092	0.481 ± 0.093	0.214 ± 0.010	0.233 ± 0.002
MEXI -A-	0.170 ± 0.005	0.165 ± 0.008	0.156 ± 0.007	0.271 ± 0.012	0.302 ± 0.014
MEXI -B-	0.296 ± 0.007	0.279 ± 0.033	0.276 ± 0.013	0.207 ± 0.009	0.267 ± 0.040
MEXI -C-	0.347 ± 0.017	0.340 ± 0.008	0.339 ± 0.011	0.210 ± 0.013	0.251 ± 0.026
MEXI -D-	0.536 ± 0.042	0.548 ± 0.043	0.541 ± 0.040	0.235 ± 0.017	0.282 ± 0.027
ZAMB -A-	0.186 ± 0.022	0.176 ± 0.021	0.169 ± 0.017	0.226 ± 0.013	0.210 ± 0.032
ZAMB -B-	0.323 ± 0.025	0.323 ± 0.023	0.322 ± 0.024	0.245 ± 0.021	0.251 ± 0.013
ZAMB -C-	0.384 ± 0.008	0.369 ± 0.011	0.369 ± 0.008	0.182 ± 0.017	0.206 ± 0.012
ZAMB -D-	0.565 ± 0.020	0.560 ± 0.025	0.560 ± 0.022	0.199 ± 0.011	0.213 ± 0.005
SOLV -A-	0.075 ± 0.002	0.058 ± 0.008	0.062 ± 0.001	0.731 ± 0.049	0.690 ± 0.045
SOLV -B-	0.117 ± 0.003	0.094 ± 0.011	0.099 ± 0.037	0.893 ± 0.018	0.981 ± 0.018
SOLV -C-	0.164 ± 0.014	0.142 ± 0.008	0.130 ± 0.007	0.721 ± 0.054	0.950 ± 0.044
SOLV -D-	0.130 ± 0.009	0.096 ± 0.004	0.097 ± 0.007	1.249 ± 0.070	1.181 ± 0.026
BAHR -A-	0.146 ± 0.014	0.147 ± 0.011	0.111 ± 0.010	0.382 ± 0.084	0.527 ± 0.033
BAHR -B-	0.207 ± 0.025	0.200 ± 0.021	0.166 ± 0.015	0.569 ± 0.040	0.406 ± 0.033
BAHR -C-	0.211 ± 0.028	0.191 ± 0.005	0.165 ± 0.011	0.793 ± 0.131	0.766 ± 0.019
BAHR -D-	0.380 ± 0.013	0.363 ± 0.015	0.328 ± 0.013	0.550 ± 0.029	0.523 ± 0.029
LANA -A-	0.060 ± 0.002	0.056 ± 0.004	0.045 ± 0.002	0.423 ± 0.026	0.550 ± 0.098
LANA -B-	0.072 ± 0.013	0.067 ± 0.014	0.054 ± 0.012	0.527 ± 0.058	0.684 ± 0.113
LANA -C-	0.182 ± 0.018	0.168 ± 0.018	0.169 ± 0.020	0.462 ± 0.066	0.574 ± 0.045
ROME -A-	0.081 ± 0.005	0.079 ± 0.007	0.071 ± 0.006	0.311 ± 0.074	0.360 ± 0.089
ROME -B-	0.163 ± 0.014	0.161 ± 0.015	0.155 ± 0.016	0.227 ± 0.012	0.255 ± 0.024
ROME -C-	0.256 ± 0.022	0.262 ± 0.020	0.271 ± 0.024	0.245 ± 0.031	0.290 ± 0.011
LAMP -A-	0.085 ± 0.003	0.079 ± 0.005	0.078 ± 0.004	0.390 ± 0.054	0.384 ± 0.114
LAMP -B-	0.119 ± 0.003	0.103 ± 0.004	0.095 ± 0.002	0.521 ± 0.077	0.715 ± 0.058
LAMP -C-	0.114 ± 0.003	0.081 ± 0.011	0.082 ± 0.001	0.915 ± 0.087	1.012 ± 0.081

Table 15. Daily averages of the retrieved products $< \tau_f(500) >$ and r_{eff}. The values of $< \tau_f(500) >$ are computed with three different algorithms for the 29 chosen days: AERONET, GRASP-AOD, and SDA. The effective radius is computed with the standard AERONET and GRASP-AOD inversions.

4.2 Night AOD inversion from Moon photometers

The recent advances in Moon photometry (in terms of instrumentation, calibration and data treatment) have enabled the setup of night measurements at a few sites. One of the pioneer sites at Lille University has been providing regular night τ_a measurements since 2013 from a moon-photometer (Cimel model CE318-U). The typical cloudy conditions of the site and the constraints due to the moon cycle (only 14 days out of 28 valuable for night measurements) limit the study cases to a relatively small number of nights. Note that the moon measurements have a spectral range from 440 to 1640 nm (see table A1 in Appendix A) while the sensitivity analyses of section 3 were mainly done for 340-1640 nm spectral range.

The left panel of figure 13 shows the aerosol optical depth measured during one of those nights, specifically on 9th April 2015. In the same figure, we have added the τ_a values measured by the sun-photometer #741 (AERONET number) during previous evening and the following morning. Even though there is only one hour

of valid measurements (a total of six measurements), the case represents an interesting example with relatively high τ_a values due to the pollution episode that occurred in the North of France in the spring 2015 on 7th-9th of April. During those days, the values of $\tau_a(440)$ were typically ranging between 0.4 and 0.6 (with peaks up to 0.9 on 8th April) while the climatological average at the Lille site is $< \tau_a(440) >= 0.22$.

In the right panel of figure 13, size distributions retrieved by GRASP-AOD inversion for the night τ_a measurements are represented (six inversions in red solid lines). In the same figure, we have added the GRASP-AOD retrievals from the two τ_a measurements of the previous evening (blue lines) and from one of the τ_a measurement on the next morning (dashed black line). The τ_a measurement selected is the one coincident with the almucantar measurement and together they form the input of the first AERONET-standard inversion of the day and the closest to the night measurement. Note that the refractive indices retrieved from this inversion have been used in the GRASP-AOD retrievals shown in figure 13 (day and night). The 22 bins size distribution from this inversion is also illustrated in black solid line.

Observing the AERONET retrieval, we can see that the episode is characterized by a predominant fine mode (C_{vf}/C_{vc} =4) with relatively high values of r_{vf} = 0.320 µm and r_{eff} = 0.317 µm compared to the typical urban aerosols in Lille (r_{eff} < 0.2 µm see Mortier, 2013). The average of the retrieved values during the night shows similar tendencies in the fine mode with r_{vf} = 0.304 ± 0.01 µm and r_{eff} = 0.296 ± 0.012 µm. The ratio between the concentrations, however, is a bit higher C_{vf}/C_{vc} =6.94±1.45 than the one found in the AERONET retrieval. This difference is mainly due to the discrepancies in the coarse mode between both retrievals: the C_{vc} retrieved during the night is 0.009 ± 0.002 µm^3 /µm^2 while in the AERONET retrieval is 0.015 µm^3 /µm^2 . The concentration values of the fine mode are quite similar C_{vf} = 0.057 ± 0.003 µm^3 /µm^2 (GRASP-AOD) and C_{vf} = 0.06 µm^3/µm^2 (AERONET)

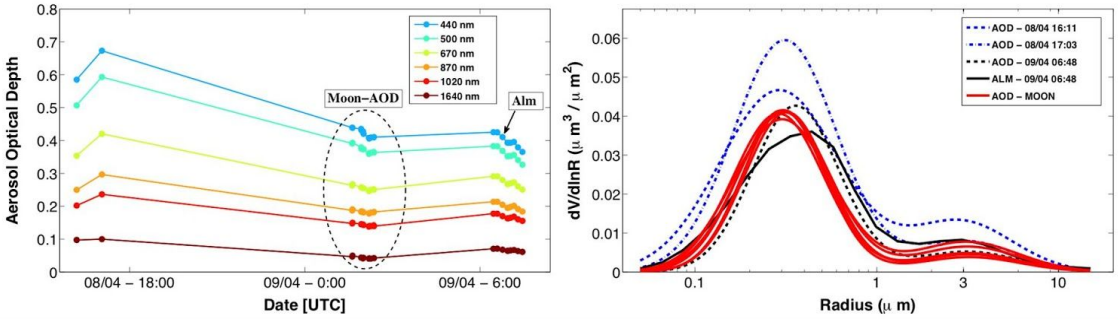

Figure 13. Left panel: aerosol optical depth values measured at the Lille site from the evening of 08/04/2015 until the morning of 09/04/2015. Measurements during daylight hours were taken with sun-photometer number #741 and nighttime measurements were obtained by moonphotometer number #841. Right panel: size distribution retrieved by GRASP-AOD inversion using τ_a from the evening of 08/04/2015 (blue lines), the measurements during the night (red lines) , and τ_a corresponding to the almucantar on the morning of 09/04/2015 (black dashed line). The size distribution from the AERONET standard inversion (6:48 AM) is also represented in the figure as a reference (black solid line).

Finally, the τ_f (500) = 0.360 ± 0.004 retrieved during the night from GRASP-AOD is in an excellent agreement with the value retrieved during the next morning by SDA, τ_f (500) = 0.337, and the one derived by the almucantar inversion τ_f (500) = 0.349.

4.3 Application of the method to the airborne PLASMA sun-photometer

The spectral optical depth measurements obtained by airborne sun-photometers represent another interesting application example of the GRASP-AOD inversion. Typically the use of airborne sun-photometers is limited to field campaigns developed in singular areas with specific research objectives such as validation of models, characterization of specific aerosol types or interactions between aerosols and other atmospheric components like clouds or gases. From the τ_a measurements taken at different heights, the derivation of the spectral aerosol extinction profile is immediate. The extinction profiles are normally available for every landing/taking off and

during pre-scheduled vertical profiles carried out by the airplanes. They give basic information for the characterization of the aerosol vertical distribution.

In the example presented here, we use the data from PLASMA airborne sun-photometer during the Chemistry-Aerosol Mediterranean Experiment/Aerosol Direct Radiative Forcing on the Mediterranean Climate (ChArMEx/ADRIMED) summer campaign that took place from 11 June to 5 July 2013 over the western Mediterranean (Mallet et al., 2016). PLASMA airborne sun-photometer was installed in the ATR-42 French research aircraft operated from Sardinia (Italy) and participated in the 18 flights of the campaign. The experimental setup also involved several ground-based measurement sites on different Mediterranean islands (Corsica, Lampedusa, Minorca and Sicily) and additional measurements from lidar and sun-photometers performed on alert during aircraft operations (at Granada and Barcelona). The meteorological conditions observed during the campaign (moderate temperatures and southern flows) were not favorable to produce large concentrations of local polluted smoke particles. However, several moderate dust plumes were observed during the campaign, with the main sources located in the north-west of the Sahara desert. Though peaks in τ_a of up to 0.6 (at 440 nm) were registered by ground-based sunphotometers during the campaign, the maximum values measured by collocated sun-photometers at the time of ATR-42 vertical profiles were around 0.3 (at 440 nm).

The τ_a values represented in the left part of figure 14 correspond to PLASMA measurements at different heights during one of the aforementioned dust plumes, specifically, in the taking off from Minorca airport on the 17 June 2013 between 11:45 and 12:00 UTC (flight 32; Denjean et al., 2016). The average values of the three τ_a data measured during this period by the ground based AERONET sun-photometer at Minorca (AERONET site Cap d'en Font; see Chazette et al., 2016) are also plotted as reference. Note that the ground-based sun-photometer is standard (see description in table A1) and does not have the 1640 nm channel. At the same time, the 340 nm channel of PLASMA suffered from instabilities during the campaign and the derived τ_a data at this channel is not represented.

One of the first conclusion obtained from figure 14 is the vertical homogeneity of the aerosol characteristics in the column up to 4000 m. The same property was observed by analyzing the coincident lidar data (figure 6 in the study by Chazette et al. (2016) on the 17 June 2013). τ_a diminishes with the height but the spectral shape of the measurements does not considerably change: the Ångström exponent (calculated like in AERONET $\tau_a(440)$, $\tau_a(675)$ and $\tau_a(870)$) varies between 0.46 at 500 m to 0.61 at 4000 m. The Ångström exponent from AERONET sun-photometer reference at ground level is 0.48. This same property is visible in the size distribution obtained by GRASP-AOD inversions and represented in the right part of figure 14: neither the mean volume radius nor the standard deviation of the modes change significantly from the retrievals at different heights. For r_{Vf} , the values span from 0.120 μm at ground level and 500 m to 0.135 μm at 4000 m, when r_{Vf} given by AERONET standard inversion is 0.134 μm. In the case of r_{Vc} , the variation goes from 2.06 μm at 4000 m to 2.21 μm at ground level, while r_{Vf} given by AERONET is 2.27 μm. The ratio between the concentrations (C_{Vf} /C_{Vc}) also maintains from 0.19 to 0.25 until 2500 m. For the last three altitude levels, it increases up to 0.4 though the concentrations are very low for both modes. The volume size distribution from the closest AERONET standard inversion (9:00 AM) is also represented in the figure as a reference. The refractive indices from this inversion are used for the different GRASP-AOD inversions of the size distributions in figure 14. Despite the low AOD levels (note that for this example are all below to the recommended lower limit of application for GRASP-AOD of 0.2 at 440 nm established in section 3.4.2), there is a consistency between the volume size distribution obtained from AERONET standard inversion and those retrieved by GRASP-AOD at different heights as can be seen in figure 14.

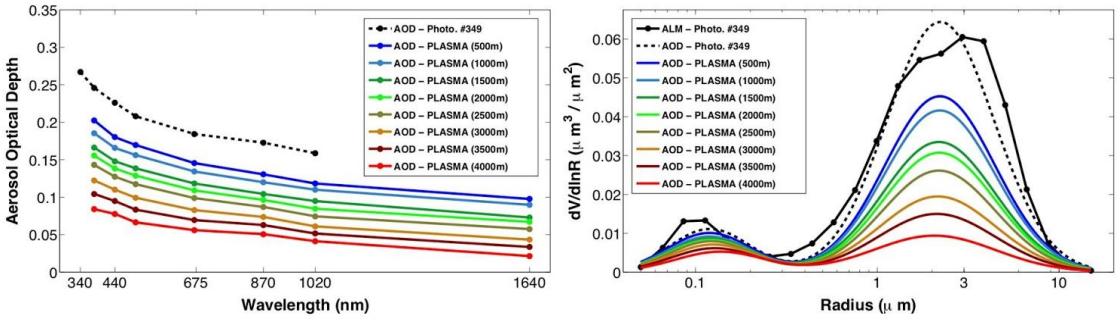

Figure 14. Aerosol optical depth values measured by PLASMA airborne photometer at different height levels in the taking off from Minorca airport on the 17 June 2013 (11:45AM) on the left, and the corresponding particle size distribution retrieved by GRASP-AOD inversion on the right. The mean values of the three τ_a data measured by the sun-photometer at AERONET site Cap d'en Font during the PLASMA profile are also represented and its corresponding GRASP-AOD inversion. The size distribution from the closest AERONET standard inversion (9:00 AM) is also represented in the figure as a reference.

5 Conclusions

The main goal of the present work was to show the potential of retrieving the total column aerosol size distributions from spectral optical depth measurements without the aid of coincident radiance measurements, and estimating a set of secondary aerosol properties (e.g. effective radius or fine mode fraction of aerosol optical depth) derived from it. The limited information content in spectral τ_a measurements results in the necessity of using a priori constraints. The utilization of the GRASP public software allowed us to test and evaluate different aerosol model descriptions and a priori constraints. The current analysis indicates that bimodal log-normal size distributions and a priori estimates of refractive indices and sphericity parameter provide a practically efficient retrieval. The validation of the retrieval has been done through a) a sensitivity analysis using 6 different aerosol models with three or four aerosol loads for each of them (section 3), and b) a comparison of the aerosol properties obtained from 744 AERONET observations using GRASP-AOD inversion to those obtained at 8 different AERONET sites through 165 almucantar AERONET standard inversion.

The simulated tests have shown that spectral τ_a measurements are sufficient for a precise discrimination between the extinction of fine and coarse modes, independently from any assumption, with maximum differences in τ_f (500) under 0.01 from the input values found in all the sensitivity tests. Specifically, the characterizations of aerosol fine mode optical properties are accurate, although they depend on reliable a-priori information about the real refractive indices and accurate measurement of aerosol optical depths. The uncertainty observed during the sensitivity tests for the fine mode r_{Vf} and C_{Vf} is between 5% for the cases with a fine mode predominance and 10% for the cases with a prevailing coarse mode. The characterization of the optical properties of the coarse mode using τ_a measurements is less accurate, but can be significantly improved using moderate a priori information about coarse mode parameters (for example, using as initial guess data retrieved from near almucantar inversions or climatological values from the given site). The study showed that a good calibration of the long wavelengths (1020 nm and 1640 nm) is essential due to its influence on the coarse mode and the typical low aerosol optical depth values presented in this spectral range. Nevertheless, in the cases where the coarse mode is predominant, the uncertainty observed in our sensitivity studies is 10% for r_{Vc} , and around 20% for C_{Vc} . The effective radius has been revealed as a quite stable parameter relatively to calibration errors (uncertainties around 15%) and bias in the assumed refractive index (differences under 10% for the analyzed cases). The simulated tests including aerosol optical errors showed that the uncertainty of the bimodal log-normal size distribution parameters dramatically increases as the aerosol load decreases. We recommend a lower limit of $\tau_a(440)$=0.2 for the bimodal size distribution parameters in order to assure quality retrievals of aerosol particle bimodal size distribution parameters. However, this lower limit does not apply to the τ_f retrieval.

Daily averaged aerosol properties obtained applying GRASP-AOD inversion to 744 AERONET observations were compared to those retrieved by 165 almucantar AERONET standard inversion at 8 selected AERONET sites with varied aerosol characteristics. The retrieved values of τ_f (500) using GRASP-AOD are generally between those obtained by AERONET standard inversion and the Spectral Deconvolution Algorithm, with differences typically lower than 0.02 between GRASP-AOD and both algorithms. In some cases with large aerosol load in the coarse mode, maximum discrepancies of up to 0.05 are observed between the three retrieval methods. The study on real cases confirms the retrieval capabilities in the fine mode: maximum differences of 0.028 μm in r_{Vf} between GRASP-AOD and AERONET inversions are observed though they are generally lower than 0.015 μm (10% of the values). In the cases with fine mode predominance, the differences in C_{Vf} are typically under 0.01 $\mu m^3/\mu m^2$, and in relative terms, the average of these differences is around 10%. The comparison of coarse mode parameters shows larger differences, however, especially at the sites with a prevailing fine mode. In these cases differences of 0.2-0.3 μm in r_{Vc} are normally obtained, although some extreme differences of up to 0.5 μm are also observed. The comparison improves significantly when limiting the study to those sites characterized by the predominance of desert dust aerosol, with differences typically under 0.2 μm between GRASP-AOD and AERONET. In relative terms, these differences are under 25% for all the dust cases, which agrees with the uncertainty estimated from the sensitivity tests. The effective radius shows average differences around 10% and it does not depend on the fine or coarse mode predominance.

Finally, we emphasize that the use of GRASP-AOD code is not restricted to the standard AERONET sun-photometer measurements. In the last part of section 4, we also show two practical applications of the GRASP-AOD code: nighttime retrievals using moon photometer data and vertically-resolved retrievals using the PLASMA airborne sun-tracking photometer.

Data availability. The AOD data used for the sensitivity studies in Sect. 3 were generated by the aerosol properties depicted in Table 1. The simulated aerosol optical depth values used in the main analyses are shown in Table 2. The AOD values used in Sect. 4 “Real Cases” are publicly available on the AERONET web page (https://aeronet.gsfc.nasa.gov/). GRASP inversion algorithm software used in this work is free and publicly available at http://www.grasp-open.com. Moreover, a web application was developed to directly use GRASP-AOD inversion without needing to install all of the GRASP code. The application can be found at www.grasp-open.com/aod-inversion.

Appendix A: Aerosol optical depth measurements.

A1 General background

Total optical depth of the atmosphere (τ) can be understood as the attenuation of light passing through the atmosphere column containing aerosol particles, molecules, and absorbing gases, and it is described by the well-known Beer-Bouguer-Lambert Law:

$$F(\lambda) = F_0(\lambda)e^{-m_s\tau}, \quad \text{(A1)}$$

where $F(\lambda)$ ($Wm^{-2}\mu m^{-1}$) and F_0 are the monochromatic direct flux densities at the Earth’s surface and at the upper limit of the atmosphere, respectively. For atmospheric applications where the Sun is the radiation source, $F(\lambda)$ and F_0 are defined as solar flux densities. We intentionally avoid the adjective ‘solar’ here, since the flux density comes from the Moon for the night observations presented in this work. Additionally, optical depth can also be derived from star radiation as well. Finally, the optical air mass (m_s) accounts for the light path in the atmosphere and can be approximated (Only valid if $\theta_s \leq 75$. The exact formulation can be found in Kasten and Young (1989)) by $m_s = 1/\cos\theta_s$, where θ_s the zenith angle of the radiation source in the sky.

Under cloud-free conditions, the total optical depth can be separated into the gaseous absorption τ_g, the molecular scattering or Rayleigh scattering τ_R, and the aerosol scattering and absorption τ_a, which is known as the aerosol optical depth. The latter can be derived, therefore, from the following expression:

$$\tau_a = \tau - \tau_R - \tau_g \quad \text{(A2)}$$

Instruments designed to derive the aerosol optical depth typically utilize wavelengths that lack significant gas absorption in the spectral region from the ultraviolet (UV) to the near infrared (NIR). This spectral region presents the highest sensitivity regarding scattering and extinction by aerosols according to the typical sizes of the natural occurring aerosols (Shaw et al., 1973; Shaw, 1983; Dutton et al., 1994).

The instruments and wavelengths used in the GRASP-AOD inversion tests with real data (section 4) are depicted in table A1. The main analysis of those tests has been done using data from the two main groups of instruments in AERONET: Cimel-318 standard version (STD) with a spectral range from 340 to 1020 nm, and Cimel-318 extended version (EXT) that includes the 1640 nm channel (for both instruments, there is an extra spectral band centered at 936 nm which is not used for the description of the aerosol properties. The channel is intentionally selected in an absorption band of water vapor in order to determine the column abundance of this gas.). The example of application of GRASP-AOD inversion to night measurements has been done with the moon photometer Cimel-318U. Given the low signal of Moon radiation in the ultraviolet spectral region, the moon photometer Cimel318U does not include the 340 nm and 380 nm channels. The last example is based on the airborne sun-tracking photometer PLASMA (Photomètre Léger Aeroporté pour la Surveillance des Masses d'Air). It has a wider spectral range (340-2250 nm) with respect to AERONET-extended instruments. Nevertheless, the calibration of PLASMA has been done using the same protocols and tools of AERONET, and therefore, only those channels of extended ground-based Cimel photometers were used in GRASP inversions of PLASMA data, with exception of the 340 nm channel due to instability during the campaign.

To summarize, the sensitivity study presented in section 3 has been mainly done only for the spectral range from 340 to 1640 nm and using the channels of AERONET-Extended sun-photometer presented in table A1.

A2 Calibration and data treatment

Calibration of the instruments is carried out by the Langley plot method (Shaw et al., 1973). The method is based on the Beer-Bouguer-Lambert law and it is directly applicable if the instrument has a linear response. In this case, Eq. A1 can be transformed to:

$$lnV(\lambda) = lnV_0(\lambda) - \tau m_s, \quad \text{(A3)}$$

where V (λ) are the digital counts measured by the instrument and $V_0(\lambda)$ is the calibration constant or the extraterrestrial signal of the instrument.

The Langley method is used to derive $V_0(\lambda)$ by means of a set of direct Sun observations performed over a range of air masses (typically from 2 to 5). The measurements provide a straight line (lnV (λ) vs. m_s), from whose intercept ($\ln V_0(\lambda)$) the calibration constant ($V(\lambda)_0$) can be extracted.

In moon photometry, calibration presents a greater complexity than the common Langley approach for sun-photometry. The main difficulty is that the moon is a highly variable source, and the illumination changes continuously with the lunar viewing geometry. Consequently, a lunar irradiance model needs to be considered. Barreto et al. (2013) developed the Lunar-Langley Method (LLM), which is a modification of the usual Langley technique that can be applied to cases with variable illumination conditions. The calibration coefficient $V_0(\lambda)$, is variable in time with the LLM, and is expressed as a function of the moon's extraterrestrial irradiance (I_0) and the instrument calibration constant ($\kappa(\lambda)$):

$$V_0(\lambda) = I_0(\lambda, t)\kappa(\lambda). \quad \text{(A4)}$$

Here, $I_0(\lambda,t)$ is is taken from the Robotic Lunar Observatory (ROLO) model, developed by Kieffer and Stone (2005). The ROLO model presents a relatively precise $I_0(\lambda,t)$, with maximum errors around 1% at any time and for all of the wavelengths. More information about the calibration process and instrument deployment can be obtained from Barreto et al. (2013) and Barreto et al. (2016).

Instrument type	Spectral channels (nm)
Cimel-318 Extended PLASMA	340, 380, 440, 500, 670, 870, 1020, 1640
Cimel-318 Standard	340, 380, 440, 500, 670, 870, 1020
Cimel-318 Polarized	440, 670, 870, 1020
Cimel-318U (moon photometer)	440, 500, 670, 870, 1020, 1640

Table A1. Instrument wavelengths used in the GRASP-AOD inversion tests with real data (section 4).

In AERONET, the inter-calibration procedure is used for the calibration of field instruments. The method is based on the realization of simultaneous co-located measurements of a so-called master instrument (calibrated by Langley method) and the field instruments under certain atmospheric conditions. The field instrument can be calibrated simply by a ratio of raw signals of each channel ($V_{field}(\lambda)$) with the master raw signal ($V_{master}(\lambda)$):

$$V_{0_{field}}(\lambda) = V_{0_{master}}(\lambda)\frac{V_{field}(\lambda)}{V_{master}(\lambda)} \tag{A5}$$

The accuracy of the master calibration is about 0.25% in the visible and NIR and 0.5% in the UV, whereas for field instruments the calibration uncertainty is 1% in the visible and NIR and 2% in the UV, due to uncertainty in the calibration transfer (Eck et al., 1999; Holben et al., 2006). Deriving Eq. A3, we obtain:

$$d\tau = \frac{1}{m_s}\frac{dV_0}{V_0} \tag{A6}$$

This means that, for instance, an uncertainty of 1% in V_0 represents a maximum error of 0.01 in the total optical depth in the extreme case of $m_s = 1$. This result is taken into the account in the sensitivity tests of section 3.

Finally, all the data used in section 4 are part of the level 2.0 quality assured AERONET data set (Smirnov et al. (2000) and http://aeronet.gsfc.nasa.gov/new_web/PDF/AERONETcriteria_final1.pdf). The measurements were done following the standard sequences of AERONET and the final values of τ_a obtained through the official data treatment of the network (http: //aeronet.gsfc.nasa.gov/new_web/Documents/version2_table.pdf).

Acknowledgements. The research has been supported by the Labex CaPPA: the CaPPA project (Chemical and Physical Properties of the Atmosphere) is funded by the French National Research Agency (ANR) through the PIA (Programme d'Investissement d'Avenir) under contract "ANR-11-LABX-0005-01" and by the Regional Council "Nord Pas de Calais Picardie" and the European Funds for Regional Economic Development (FEDER)

Acknowledgement are addressed to ESA/ESRIN for funding through the IDEAS+ (Instrument Data quality Evaluation and Analysis Service) contract.

This research has also received funding from the French National Research Agency (ANR) project ADRIMED (contract ANR-11-BS560006). This work is part of the ChArMEx project supported by ADEME, CEA, CNRS-INSU and MétéoFrance through the multidisciplinary programme MISTRALS (Mediterranean Integrated Studies aT Regional And Local Scales).

The authors acknowledge the funding provided by the European Union (H2020-INFRAIA-2014-2015) under Grant Agreement No. 654109 (ACTRIS-2). Financial support was also provided by the Spanish MINECO (CTM2015-66742-R).

We thank the AERONET principal investigators and site managers at sites Solar Village (Brent Holben and Steve Wilcox), GSFC (Brent Holben and Jon Rodriguez), Bahrain (Brent Holben and Andreas Goroch), Mexico-City (Amando Leyva Contreras and Hector R. Estevez), Lanai (Brent Holben, Chuck McClain, and Robert Frouin), Mongu (Brent Holben and Mukufute Mukulabai), Rome Tor Vergata (Gian Paolo Gobbi) and Lampedusa (Daniela Meloni). We thank the AERONET, Service National d'Observation PHOTONS/AERONET, INSU/CNRS, RIMA and WRC staff for their scientific and technical support. We acknowledge AERONET team members for calibrating and maintaining instrumentation and processing data.

Special thanks go to Michael D. King, Thomas F. Eck, Zhengqiang Li, an anonymous reviewer, and the editor, Francois Dulac, for useful comments that have helped us to improve the paper. Additional thanks are addressed to Norm T. O'Neill for helping us in the short description of the Spectral Deconvolution Algorithm (SDA).

Finally, the authors would like to acknowledge the use of GRASP inversion algorithm software (http://www.grasp-open.com) in this work.

References

See references section of the PhD Thesis

Conclusiones y líneas futuras

Esta tesis desarrolla distintas herramientas de análisis avanzado aplicadas al estudio de los aerosoles atmosféricos. El procesado del gran volumen de datos generado por las misiones satelitales y las redes de instrumentación en tierra representan un reto tecnológico y científico que debe ser superado para alcanzar un mejor entendimiento del balance radiativo terrestre. El primer artículo describe la herramienta CÆLIS que ha sido implementada con éxito y que en la actualidad está en uso. Actualmente, el sistema CÆLIS gestiona alrededor de 50 estaciones de medida y más de 100 usuarios. Además, esta herramienta cumple con los requisitos propuestos: 1) Gestión de una red de medidas 2) Obtención de productos avanzados de las medidas 3) Soporte a la investigación. La consecución del primer requisito se demuestra con los usuarios activos a diario revisando el estado de la instrumentación científica gracias a las alarmas. El segundo requisito queda recogido en el tercer artículo, donde se desarrolla una aplicación específica de el algoritmo de inversión GRASP que, junto a CÆLIS permite procesar grandes volúmenes de datos y proporcionar nuevos resultados a la comunidad científica. Por último, soporte a la investigación queda demostrado gracias al segundo artículo donde se hace un estudio científico mediante el uso de la herramienta CÆLIS, que ha permitido caracterizar las estaciones de de calibración de referencia de la red AERONET en cuanto a sus capacidades para la realización de calibraciones absolutas mediante el método de Langley.

Se han analizado 22 años de medidas de AOD en Mauna Loa y 15 años en Izaña a través de la herramienta CÆLIS, con el objetivo de analizar su calidad como estaciones de calibración. La climatología obtenida mediante las redes GAW-PFR y AERONET son similares, con diferencias en AOD por debajo de 0.0035 y muestran que el AOD (500nm) medio en Mauna Loa es de 0.016 y en Izaña es de 0.054. La estación de Izaña recibe intrusiones de aerosoles desérticos, con origen en el Sáhara, especialmente en verano. Los días con aerosol desértico no pueden ser utilizados para la calibración pero sí para comprobar que el instrumental funciona correctamente. Una vez establecidos los criterios de calidad, los datos muestran que de media en Mauna Loa se puede realizar 377 Langleys y en Izaña 343 cada año, incluyendo mañanas y tardes. En general los Langleys realizados durante la mañana son más estables que los de la tarde debido a convección atmosférica. Este efecto hace que el número total de Langleys que se pueden hacer por la tarde es un factor 1.8 menor que en la mañana para Mauna Loa y 1.2 para Izaña. La inversión atmosférica causada por los vientos Alisios es la responsable de que Izaña muestre gran estabilidad atmosférica también durante las tardes. Finalmente, el análisis permite concluir que las estaciones en altura de Mauna Loa e Izaña cumplen los criterios de calidad de las redes GAW-PFR y AERONET para la calibración de sus instrumentos de referencia (un error en AOD de 0.002 a 0.005 para masa óptica igual a 1). Estas estaciones con unas condiciones tan particulares son clave para la correcta monitorización de los aerosoles. Además, las adquisición de datos a largo plazo en la misma estación ha permitido observar la gran estabilidad de los equipos (por debajo del 0.1% anual de degradación).

El uso del algoritmo de inversión GRASP aplicado a las medidas de AOD ha sido analizado mediante tests de sensibilidad y por comparación con los datos de inversión obtenidos en

AERONET. Los resultados muestran que se pueden separar los modos fino y grueso dentro de un error menor del 1% del espesor óptico medido. Para el modo fino, la inversión del radio efectivo así como el volumen de concentración y la forma de la distribución es estable y precisa si la parte real del índice de refracción es conocida. El modo grueso es menos estable pero mejora aportando más información de partida. Los tests añadiendo errores aleatorios muestran que la incertidumbre de la distribución de tamaños modelada como una curva bimodal log-normal se incrementan si la carga de AOD disminuye. Además, si disminuye el rango espectral se pierde estabilidad. Esta técnica has sido aplicada a distintas medidas reales de AERONET demostrando que la representación de la distribución de tamaños como una log-normal bi-modal es muy útil, especialmente cuando la cantidad de información de entrada es limitada o no es muy precisa. Esta metodología de inversión es especialmente interesante para aquellos instrumentos o casos en los que sólo hay medidas de extinción, como en la emergente fotometría lunar. Las comparaciones de GRASP-AOD y AERONET muestran diferencias medias de 0.013 μm para el radio medio modal del modo fino, y valores de 0.2 a 0.3 μm para el modo grueso. Además en la comparación, el modo dominante (fino o grueso) presenta un 10% de diferencia en radios. En cuanto a la concentración, la diferencia media está en torno al 17% en ambos modos. Las diferencias obtenidas en el AOD modo fino a 500nm están dentro del rango de las mostradas por los 2 algoritmos oficiales que AERONET utiliza para el cálculo de este parámetro (la inversión regular de AERONET y el algoritmo SDA) con diferencias típicamente menores que 0.02.

El trabajo de investigación de esta tesis forma parte de una línea de trabajo desarrollada desde años en el grupo, y cuyo objetivo es el estudio de los aerosoles mediante técnicas avanzadas que permitan la explotación de grandes volúmenes de datos. Este planteamiento viene reforzado por las políticas europeas de soporte a grandes redes de observación en tierra, por su papel de medida de la composición de atmósfera así como de referencia para las misiones satelitales de las distintas agencias. Posibles líneas futuras de trabajo son, por tanto:

- Añadir más datos de otras fuentes de información atmosférica, como puede ser otro tipo de fotómetros o otros instrumentos como ceilómetro, lidar o cámara de cielo, etc.
- Añadir otros algoritmos que de forma rutinaria produzcan más productos de interés para la comunidad científica. Por ejemplo, el cálculo de AOD a través de fotometría lunar que a su vez podría ser invertido mediante GRASP-AOD.
- Cada nuevo producto añadido hay que analizarlo de manera rutinaria para detectar errores instrumentales de forma temprana, en línea con uno de los grandes objetivos de CÆLIS. Por ejemplo, la herramienta que realiza el cálculo en tiempo real de los langleys puede ser utilizada para identificar tendencias en la instrumentación.
- Desarrollar más aplicaciones de GRASP, desde aplicaciones para nuevos instrumentos como cámaras de todo cielo a, por ejemplo, la inversión combinada de instrumentos.
- Desarrollar herramientas para la validación en tiempo real de datos satelitales, puesto que tienen una mejor cobertura espacial pero carecen de la precisión de los instrumentos en tierra.

Conclusions and outlook

This PhD thesis develops different advanced software tools applied to the study of the atmospheric aerosols. The processing of large amounts of data measured by the satellite missions and the ground-based networks are a technical and scientific challenge that needs to be addressed in order to get a better understanding of the aerosol global radiative effect. The first article of this thesis describes the CÆLIS software system, a tool that has been successfully implemented and currently is under intensive use and development. CÆLIS system manages around 50 sites and more than 100 users. Additionally, this tool fulfils the requirements for which it was designed: 1) To manage a ground-based network; 2) To get advanced products from the measurements by applying complex algorithms; 3) To support research activities. The achievement of the first requirement is proved by the fact that there are active users checking routinely their instruments thanks to the alarm system. The second requirement is demonstrated by the third paper, where it is developed a specific algorithm (a GRASP application) that, jointly with CÆLIS, allows processing large amounts of data received and provides new results to the scientific community. Finally, the support to the research has been proved by the second paper where the CÆLIS system has been the main tool used to analyse the Izaña and Mauna Loa site characteristics. In that work, CÆLIS has been used to analyze the reference calibration stations of AERONET network regarding its ability to perform absolute calibrations with the Langley plot method.

Up to 22 years of optical depth measurements from Mauna Loa and 15 years from Izana have been analyzed using CÆLIS system with the goal of evaluating their quality as calibration sites. The climatology obtained from GAW-PFR and AERONET networks is similar and its differences are within 0.0035. The AOD (500nm) average in Mauna Loa is 0.016 and in Izana is 0.054. Dust aerosols, from Sahara desert, are transported over Izana, especially during summer. Those days with desert aerosols cannot be used in the calibration but they are useful to check instrumental functioning. Once the quality criteria are established, the data show that on average, having into account mornings and afternoons, at Mauna Loa is possible to perform 377 Langleys per year, and 343 at Izana. In general, Langley plots performed during the morning are more stable as those performed during the afternoon due to atmospheric convection. Due to this effect, the number of langley plots performed during the afternoon is reduced in a factor 1.8 for Mauna Loa and 1.2 for Izana. Izana is more stable in the afternoons thanks to the thermal inversion produced by the Trade winds. Finally, the analysis allows to conclude that the high-elevation sites Mauna Loa and Izana fulfil the strong quality criteria of the GAW-PFR and AERONET networks for calibrating their master instruments (uncertainty between 0.002 to 0.005 in AOD for airmass equal to 1). Those sites with such unique conditions are key for a proper global monitoring of the aerosols. Additionally, long term records allowed to observe the high stability of the reference instruments of these networks (degradation lower than 0.1% per year).

The use of the GRASP inversion algorithm applied to AOD measurements has been analyzed through sensitivity tests and by comparing the results from those of the AERONET network operational inversion. The results showed that this methodology allows to split fine

and coarse mode AOD within 1% error in the measured AOD. The fine mode retrieval is stable if the real part of the refractive index is known. The coarse mode is less stable but its retrieval improves if a priori information is known about the complex refractive index. The tests performed by adding random errors show that the uncertainty of the size distribution modeled as a bimodal log-normal increases as the AOD decreases. Additionally, if the AOD spectral range is smaller, the stability of the retrieval can get lost. This algorithm has been applied to real AERONET data, demonstrating that the representation of the size distribution as bi-modal log-normal function is very helpful, specially when the input is information is limited or not highly accurate. The methodology developed here is particularly interesting for those instruments or escenarios where only extinction measurements are available, like in the emerging lunar photometry. First comparisons of GRASP-AOD and AERONET show average differences of 0.013 μm in fine mode for the mode median radii and values between 0.2 and 0.3μm for the coarse mode. Additionally, the comparison shows a 10% difference in mode radii for the dominant mode (i.e. fine or coarse). Concentration shows average differences about 17% for both modes. The differences obtained in the fine mode AOD (500nm) are within the error described by both official AERONET algorithms, the full radiance retrieval and the spectral deconvolution algorithm (O'Neill et al., 2003) with differences typically below 0.02.

The research work of this PhD Thesis is part of the research activity performed by our group since many years, whose main goal in the study of aerosols using advanced tools that allow the analysis and exploitation of large amounts of data. This approach is reinforced by the european policies, that support large research infrastructures of ground-based observations, to promote the measurements of the atmospheric composition and support the satellite missions of the various european space agencies. Possible future works are:

- Adding new data sources with atmospheric information, e.i. new photometer types, ceilometers, lidars, all sky cameras, etc.
- Add new algorithms able to produce in near real time novel products of interest for scientific community.
- Each new product added will need to be analyzed in a routine basis, in order to early detect instrumental problems and address them as soon as they occur. This is one of the main objectives of CÆLIS, since it helps to improve the quality of the data acquired by ground-based networks. For example, the tool developed in the framework of this work for calculating the langleys can be used to identify departures in the radiometric instrumentation.
- Development of more GRASP applications, e.g. an application of GRASP for all sky cameras or new methodology for instrument sinergies.
- Development of tools for near real time satellite validation, given that those instruments have better spatial coverage but less quality than ground-based instruments.

Referencias

Andrews, E., Ogren, J., Bonasoni, P., Marinoni, A., Cuevas, E., Rodríguez, S., Sun, J., Jaffe, D., Fischer, E., Baltensperger, U., Weingartner, E., Coen, M. C., Sharma, S., Macdonald, A., Leaitch, W., Lin, N.H., Laj, P., Arsov, T., Kalapov, I., Jefferson, A., and Sheridan, P.: Climatology of aerosol radiative properties in the free troposphere, Atmospheric Research, 102, 365 – 393, doi:10.1016/j.atmosres.2011.08.017, 2011.

Ångström, A.: On the Atmospheric Transmission of Sun Radiation and on Dust in the Air, Geog. Ann., 11, 156–166, https://doi.org/10.2307/519399, 1929.

Ångström, A.: Techniques of determining the turbidity of the atmosphere, Tellus, 13, 214–223, https://doi.org/10.1111/j.2153- 3490.1961.tb00078.x, 1961.

Ansmann, A., Petzold, A., Kandler, K., Tegen, I., Wendisch, M., Müller, D., Weinzierl, B., Müller, T., and Heintzenberg, J.: Saharan Mineral Dust Experiments SAMUM–1 and SAMUM–2: What have we learned?, Tellus, 63B, this issue, 2011.

Baibakov, K., O'Neill, N. T., Ivanescu, L., Duck, T. J., Perro, C., Herber, A., Schulz, K.H., and Schrems, O.: Synchronous polar winter star photometry and lidar measurements at a High Arctic station, Atmos. Meas. Tech., 8, 3789–3809, https://doi.org/10.5194/amt-8-3789-2015, 2015.

Barreto, A., Cuevas, E., Damiri, B., Guirado, C., Berkoff, T., Berjón, A. J., Hernández, Y., Almansa, F., and Gil, M.: A new method for nocturnal aerosol measurements with a lu- nar photometer prototype, Atmos. Meas. Tech., 6, 585–598, https://doi.org/10.5194/amt-6-585-2013, 2013.

Barreto, A., Cuevas, E., Pallé, P., Romero, P. M., Guirado, C., Wehrli, C. J., and Almansa, F.: Recovering longterm aerosol optical depth series (1976–2012) from an astronomical potassium-based resonance scattering spectrometer, Atmos. Meas. Tech., 7, 4103–4116, 2014.

Barreto, Á., Cuevas, E., Granados-Muñoz, M.J., Alados- Arboledas, L., Romero, P. M., Gröbner, J., Kouremeti, N., Almansa, A. F., Stone, T., Toledano, C., Román, R., Sorokin, M., Holben, B., Canini, M., and Yela, M.: The new sun-sky-lunar Cimel CE318-T multiband photometer – a comprehensive performance evaluation, Atmos. Meas. Tech., 9, 631–654, https://doi.org/10.5194/amt-9-631-2016, 2016.

Bennouna, Y. S., Cachorro, V. E., Mateos, D., Burgos, M. A., Toledano, C., Torres, B., and de Frutos, A. M.: Long-term comparative study of columnar and surface mass concentration aerosol properties in a background environment, Atmos. Environ., 140, 261–272, https://doi.org/10.1016/j.atmosenv.2016.05.061, 2016.

Bodhaine, B. A., Mendonca, B. G., Harris, J. M., and Miller, J. M.: Seasonal variations in aerosols and atmospheric transmission at Mauna Loa Observatory, Journal of Geophysical Research: Oceans, 86, 7395–7398, doi:10.1029/JC086iC08p07395, 1981.

Bodhaine, B. A., Harris, J. M., Ogren, J. A., and Hofmann, D. J.: Aerosol optical properties at Mauna Loa Observatory: Long-range transport from Kuwait?, Geophysical Research Letters, 19, 581–584, doi:10.1029/92GL00524, 1992.

Bohren, C. F. and Huffman, D. R.: Absorption and Scattering of Light by Small Particles, John Wiley & Sons Inc, https://doi.org/10.1002/9783527618156, 1983.

Cachorro, V. E.: Simple approaches and inversion methods retrieve particle size parameters of atmospheric desert aerosols, Atmos. Environ., 32, 239–245, https://doi.org/10.1016/S1352-2310(97)00290-2, 1998.

Cachorro, V. E. and De Frutos, A. M.: Conference on visibility and fine particles Retrieval of atmospheric aerosol characteristics from visible extinction data at Valladolid (Spain), Atmos. Envi- ron., 28, 963–971, https://doi.org/10.1016/1352-2310(94)90255-0, 1994.

Cachorro, V. E., Romero, P. M., Toledano, C., Cuevas, E., and de Frutos, A. M.: The fictitious diurnal cycle of aerosol optical depth: A new approach for "in situ" calibration and correction of AOD data series, Geophysical Research Letters, 31, L12106, doi:10.1029/2004GLO19651, 2004.

Campanelli, M., Nakajima, T., and Olivieri, B.: Determination of the solar calibration constant for a sun-sky radiometer: proposal of an in-situ procedure, Appl. Opt., 43, 651–659, doi:10.1364/AO.43.000651, 2004.

Campanelli, M., Estellés, V., Tomasi, C., Nakajima, T., Malvestuto, V., and Martinez-Lozano, J. A.: Application of the SKYRAD improved Langley plot method for the in situ calibration of CIMEL sun-sky photometers, Applied Optics, 46, 2688–2702, 2007.

Carrillo, J., Guerra, J. C., Cuevas, E., and Barrancos, J.: Characterization of the Marine Boundary Layer and the Trade-Wind Inversion over the Subtropical North Atlantic, Boundary-Layer Meteorology, 158, 311–330, doi:doi:10.?1007/?s10546-015-0081-1, 2015.

Chazette, P., Totems, J., Ancellet, G., Pelon, J., and Sicard, M.: Temporal consistency of lidar observations during aerosol transport events in the framework of the ChArMEx/ADRIMED campaign at Minorca in June 2013, Atmos. Chem. Phys., 16, 2863– 2875, https://doi.org/10.5194/acp-16-2863-2016, 2016.

Chen, P. P.-S.: The Entity-Relationship Model: Toward a Unified View of Data, ACM T. Database Syst., 1, 9–36, 1976.

Chylek Petr and Wong J.: Effect of absorbing aerosols on global radiation budget, Geophysical Research Letters, 22, 8, 0094-8276, https://doi.org/10.1029/95GL00800

Cimel Electronique. Multiband photometer CE318-T. User's operation Manual. Paris, 2015.

Coulson, K. L.: Polarization and Intensity of Light in the Atmosphere, A. DEEPAK Publishing, Hampton, VA, USA, 1988.

Cuevas, E., Camino, C., Benedetti, A., Basart, S., Terradellas, E., Baldasano, J. M., Morcrette, J. J., Marticorena, B., Goloub, P., Mortier, A., Berjón, A., Hernández, Y., Gil-Ojeda, M., and Schulz, M.: The MACC-II 2007–2008 reanalysis: atmospheric dust evaluation and characterization over northern Africa and the Middle East, Atmospheric Chemistry and Physics, 15, 3991–4024, doi:10.5194/acp-15- 3991-2015, 2015.

Cuevas, E., Gómez-Peláez, A., Rodríguez, S., Terradellas, E., Basart, S., García, R., García, O., and Alonso-Pérez, S.: The pulsating nature of large-scale Saharan dust transport as a result of interplays between mid-latitude Rossby waves and the North African Dipole Intensity, Atmospheric Environment, 167, 586 – 602, doi:10.1016/j.atmosenv.2017.08.059, 2017a.

Cuevas, E., Milford, C., Bustos, J. J., del Campo-Hernández, R., García, O. E., García, R. D., Gómez-Peláez, A. J., Guirado-Fuentes, C., Marrero, C., Prats, N., Ramos, R., Redondas, A., Reyes, E., Rodríguez, S., Romero-Campos, P. M., Schneider, M., Belmonte, J., Yela, M., Almansa, F., Barreto, A., López-Solano, C., Basart, S., Terradellas, E., Afonso, S., Bayo, C., Berjón, A., Bethencourt, J., Carreño, V., Castro, N. J., Cruz, A. M., Damas, M., De Ory-Ajamil, F., García, M., Gómez-Trueba, V., González, Y., Hernández, C., Hernández, Y., Hernández-Cruz, B., Jover, M., León-Luís, S. F., López-Fernández, R., López-Solano, J., Rodríguez, E., Rodríguez-Franco, J. J., Rodríguez-Valido, M., Sálamo, C., Sanromá, E.,

Santana, D., Santo Tomás, F., Sepúlveda, E., Sierra, M., and Sosa, E.: Izaña Atmospheric Research Center Activity Report 2015–2016., Tech. rep., State Meteorological Agency of Spain (AEMET), Madrid, Spain and World Meteorological Organization, Geneva, Switzerland. (Eds.) Cuevas, E., Milford, C. and Tarasova, O. NIPO: 014-17-012-9, WMO/GAW Report No. 236, 2017b.

Denjean, C., Cassola, F., Mazzino, A., Triquet, S., Chevaillier, S., Grand, N., Bourrianne, T., Momboisse, G., Sellegri, K., Schwarzenbock, A., Freney, E., Mallet, M., and For- menti, P.: Size distribution and optical properties of mineral dust aerosols transported in the western Mediterranean, Atmos. Chem. Phys., 16, 1081–1104, https://doi.org/10.5194/acp-16-1081-2016, 2016.

Dubovik, O.: Optimization of numerical inversion in photopolarimetric remote sensing, in: Photopolarimetry in Remote Sensing, edited by: Videen, G., Yatskiv, Y., and Mishchenko, M., 65–106, Springer, New York, Oxford, 2004.

Dubovik, O. and King, M. D.: A flexible inversion algorithm for retrieval of aerosol optical properties from Sun and sky radiance measurements, J. Geophys. Res.-Atmos., 105, 20673–20696, https://doi.org/10.1029/2000JD900282, 2000.

Dubovik, O., Smirnov, A., Holben, B. N., King, M. D., Kaufman, Y. J., Eck, T. F., and Slutsker, I.: Accuracy assessments of aerosol optical properties retrieved from Aerosol Robotic Network (AERONET) Sun and sky radiance measurements, J. Geophys. Res.-Atmos., 105, 9791–9806, https://doi.org/10.1029/2000JD900040, 2000.

Dubovik, O., Holben, B., Eck, T. F., Smirnov, A., Kaufman, Y. J., King, M., Tanré, D., and Slutsker, I.: Variability of absorption and optical properties of key aerosol types observed in worldwide locations, J. Atmos. Sci., 59, 590–608, https://doi.org/10.1175/1520-0469(2002)059<0590:VOAAOP>2.0.CO;2, 2002a.

Dubovik, O., Holben, B. N., Lapyonok, T., Sinyuk, A., Mishchenko, M., Yang, P., and Slutsker, I.: Non-spherical aerosol retrieval method employing light scattering by spheroids, Geophys. Res. Lett., 29, 1415, https://doi.org/10.1029/2001GL014506, 2002b.

Dubovik, O., Sinyuk, A., Lapyonok, T., Holben, B. N., Mishchenko, M., Yang, P., Eck, T. F., Volten, H., Munoz, O., Veihelmann, B., Van Der Zande, W. J., Leon, J. F., Sorokin, M., and Slutsker, I.: Application of spheroid models to account for aerosol particle nonsphericity in remote sensing of desert dust, J. Geophys. Res.-Atmos., 111, D11208, https://doi.org/10.1029/2005JD006619, 2006.

Dubovik, O., Herman, M., Holdak, A., Lapyonok, T., Tanré, D., Deuzé, J. L., Ducos, F., Sinyuk, A., and Lopatin, A.: Statistically optimized inversion algorithm for enhanced retrieval of aerosol properties from spectral multi-angle polarimetric satellite observations, Atmos. Meas. Tech., 4, 975–1018, https://doi.org/10.5194/amt-4-975-2011, 2011.

Dubovik, O., Lapyonok, T., Litvinov, P., Herman, M., Fuertes, D., Ducos, F., Torres, B., Derimian, Y., Huang, X., Lopatin, A., Chaikovsky, A., Aspetsberger, M., and Federspiel, C.: GRASP: a versatile algorithm for characterizing the atmosphere, in: SPIE, vol. Newsroom, 2014.

Dutton, E. G., Reddy, P., Ryan, S., and DeLuisi, J. J.: Features and effects of aerosol optical depth observed at Mauna Loa, Hawaii: 198–1992, J. Geophys. Res.-Atmos., 99, 8295–8306, https://doi.org/10.1029/93JD03520, 1994.

Eck, T. F., Holben, B. N., Reid, J. S., Dubovik, O., Smirnov, A., O'Neill, N., Slutsker, I., and Kinne, S.: Wavelength dependence of the optical depth of biomass burning, urban, and desert dust aerosols, J. Geophys. Res.-Atmos., 104, 31333– 31349, https://doi.org/10.1029/1999JD900923, 1999.

Eck, T. F., Holben, B. N., Ward, D. E., Dubovik, O., Reid, J. S., Smirnov, A., Mukelabai, M. M., Hsu, N. C., O'Neill, N. T., and Slutsker, I.: Characterization of the optical properties of biomass burning aerosols in Zambia during the 1997 ZIBBEE field campaign, J. Geophys. Res.-Atmos., 106, 3425– 3448, https://doi.org/10.1029/2000JD900555, 2001.

Eck, T. F., Holben, B. N., Dubovik, O., Smirnov, A., Goloub, P., Chen, H. B., Chatenet, B., Gomes, L., Zhang, X. Y., Tsay, S. C., Ji, Q., Giles, D., and Slutsker, I.: Columnar aerosol optical properties at AERONET sites in central eastern Asia and aerosol transport to the tropical mid-Pacific, J. Geophys. Res.-Atmos., 110, D06202, https://doi.org/10.1029/2004JD005274, 2005.

Eck, T. F., Holben, B. N., Sinyuk, A., Pinker, R. T., Goloub, P., Chen, H., Chatenet, B., Li, Z., Singh, R. P., Tripathi, S. N., Reid, J. S., Giles, D. M., Dubovik, O., O'Neill, N. T., Smirnov, A., Wang, P., and Xia, X.: Climatological aspects of the optical properties of fine/coarse mode aerosol mixtures, J. Geophys. Res.-Atmos., 115, D19205, https://doi.org/10.1029/2010JD014002, 2010.

Eck, T. F., Holben, B. N., Reid, J. S., Giles, D. M., Rivas, M. A., Singh, R. P., Tripathi, S. N., Bruegge, C. J., Platnick, S., Arnold, G. T., Krotkov, N. A., Carn, S. A., Sinyuk, A., Dubovik, O., Arola, A., Schafer, J. S., Artaxo, P., Smirnov, A., Chen, H., and Goloub, P.: Fog- and cloud- induced aerosol modification observed by the Aerosol Robotic Network (AERONET), J. Geophys. Res.-Atmos., 117, D07206, https://doi.org/10.1029/2011JD016839, 2012.

Elias, T., Devaux, C., Goloub, P., and Tanre, D.: Characterization of a dust layer by inversion of ground-based photometric measurements at two altitudes in Tenerife, J. Atmos. Sci., 29, S265–S266, https://doi.org/10.1016/S0021-8502(98)00397-8, 1998.

Elias, T., Devaux, C., Goloub, P., and Herman, M.: Polarising properties of the aerosols in the north-eastern tropical Atlantic Ocean, with emphasis on the ACE-2 period, Tellus B, 52, 620–635, https://doi.org/10.1034/j.1600-0889.2000.00046.x, 2000.

Giles, D. M., Holben, B. N., Eck, T. F., Sinyuk, A., Smirnov, A., Slutsker, I., Dickerson, R. R., Thompson, A. M., and Schafer, J. S.: An analysis of AERONET aerosol absorption properties and classifications representative of aerosol source regions, J. Geophys. Res.-Atmos., 117, D17203, https://doi.org/10.1029/2012JD018127, 2012.

GRASP-SAS. The GRASP Package. An overview. Lille, France (2018). Disponible en la web: https://www.grasp-open.com/doc/

Grassl, H.: Determination of Aerosol Size Distributions from Spectral Attenuation Measurements, Appl. Optics, 10, 2534–2538, https://doi.org/10.1364/AO.10.002534, 1971.

Forgan, B. W.: General method for calibrating Sun photometers, Appl. Opt., 33, 4841–4850, doi:10.1364/AO.33.004841, 1994.

Fröhlich, C., Romero, J., Roth, H., Wehrli, C., Andersen, B. N., Appourchaux, T., Domingo, V., Telljohann, U., Berthomieu, B., Delache, P., Provost, J., Toutain, T., Crommelynck, D., Chevalier, A., Fichot, A., Däppen, W., Gough, D. O., Hoeksema, T., Jiménez-Gómez, M., Herreros, J., Roca-Cortés, T., Jones, A. R., Pap, J., and Willson, R. C.: VIRGO: Experiment for Helioseismology and Solar Irradiance Monitoring, Sol. Phys., 162, 101–128, 1995.

García, R. D., García, O. E., Cuevas, E., Cachorro, V. E., Barreto, A., Guirado-Fuentes, C., Kouremeti, N., Bustos, J. J., Romero-Campos, P. M., and de Frutos, A. M.: Aerosol optical depth retrievals at the Izaña Atmospheric Observatory from 1941 to 2013 by using artificial neural networks, Atmospheric Measurement Techniques, 9, 53–62, doi:10.5194/amt-9-53-2016, 2016.

Guirado-Fuentes, C.: Caracterización de las propiedades de los aerosoles en columna en la región subtropical, Ph.D. thesis, Universidad de Valladolid, 2015.

Guirado-Fuentes, C., Cuevas, E., Cachorro, V. E., Toledano, C., Alonso-Pérez, S., A. Barreto and, Y. H., Yela, M., and de Frutos, A.: Aerosol characterization in the free troposphere and the marine boundary layer over the subtropical Eastern North Atlantic, (in preparation), 2017. Harrison, L. and Michalsky, J.: Objective algorithms for the retrieval of optical depths from ground-based measurements, APPLIED OPTICS, 33, 5126–5132, 1994.

Herber, A., Thomason, L. W., Gernandt, H., Leiterer, U., Nagel, D., Schulz, K.-H., Kaptur, J., Albrecht, T., and Notholt, J.: Continuous day and night aerosol optical depth observations in the Arctic between 1991 and 1999, J. Geophys. Res.-Atmos., 107, AAC 6- 1–AAC 6-13, https://doi.org/10.1029/2001JD000536, 2002.

Herman, B. M., Box, M. A., Reagan, J. A., and Evans, C. M.: Alternate approach to the analysis of solar photometer data, APPLIED OPTICS, 20, 2925–2928, 1981.

Hess, M., Koepke, P., and Schult, I.: Optical properties of aerosols and clouds: The software package OPAC, B. Am. Meteorol. Soc., 79, 831–844, https://doi.org/10.1175/1520-0477(1998)079<0831:OPOAAC>2.0.CO;2, 1998.

Holben, B. N., Eck, T. F., Slutsker, I., Tanré, D., Buis, J. P., Setzer, A., Vermote, E., Reagan, J. A., Kaufman, Y. J., Nakajima, T., Lavenu, F., Jankowiak, I., and Smirnov, A.: AERONET – A federated instrument network and data archive for aerosol characterization, Remote Sens. Environ., 66, 1–16, https://doi.org/10.1016/S0034-4257(98)00031-5, 1998.

Holben, B. N., Eck, T. F., Slutsker, I., Smirnov, A., Sinyuk, A., Schafer, J., Giles, D., and Dubovik, O.: AERONET's Version 2.0 quality assurance criteria, in: Remote Sensing of the Atmosphere and Clouds, edited by: Tsay, S., Nakajima, T., Singh, R., and Sridharan, R., vol. 6408 of Proc. SPIE, Q4080, conference on Remote Sensing of the Atmosphere and Clouds, Goa, INDIA, November 13–16, https://doi.org/10.1117/12.706524, 2006.

Hyslop, N., Trzepla, K., Wallis, C., Matzoll, A., and White, W.: Technical note: A 23-year record of twice-weekly aerosol composition measurements at Mauna Loa Observatory, Atmospheric Environment, 80, 259–263, 2013.

IPCC: Climate Change 2013 – The Physical Science Basis: Working Group I Contribution to the Fifth Assessment Report of the Intergovernmental Panel on Climate Change, Cambridge University Press, Cambridge, https://doi.org/10.1017/CBO9781107415324, 2014.

Junge, C.: The size distribution and aging of natural aerosols as determined from electrical and optical data on the atmosphere, J. Meteorol., 12, 13–25, https://doi.org/10.1175/1520-0469(1955)012<0013:TSDAAO>2.0.CO;2, 1955.

Kacenelenbogen, M., Léon, J.-F., Chiapello, I., and Tanré, D.: Characterization of aerosol pollution events in France using ground- based and POLDER-2 satellite data, Atmos. Chem. Phys., 6, 4843–4849, https://doi.org/10.5194/acp-6-4843-2006, 2006.

Karol, Y., Tanré, D., Goloub, P., Vervaerde, C., Balois, J. Y., Blarel, L., Podvin, T., Mortier, A., and Chaikovsky, A.: Airborne sun photometer PLASMA: concept, measurements, comparison of aerosol extinction vertical profile with lidar, Atmos. Meas. Tech., 6, 2383–2389, https://doi.org/10.5194/amt-6-2383-2013, 2013.

Kaskaoutis, D. G., Badarinath, K. V. S., Kumar Kharol, S., Rani Sharma, A., and Kambezidis, H. D.: Variations in the aerosol optical properties and types over the tropical urban site of Hyderabad, India, J. Geophys. Res.-Atmos., 114, D22204, https://doi.org/10.1029/2009JD012423, 2009.

Kasten, F. and Young, A. T.: Revised optical air-mass tables and approximation formula, Appl. Optics, 28, 4735–4738, https://doi.org/10.1364/AO.28.004735, 1989.

Kaufman, Y. J.: Aerosol optical thickness and atmospheric path radiance, J. Geophys. Res.-Atmos., 98, 2677–2692, https://doi.org/10.1029/92JD02427, 1993.

Kazadzis, S.: WMO/GAW Aerosol Measurement Procedures, Guidelines and Recommendations. 2nd Edition, Tech. rep., World Meteorological Organization, 2016.

Kazadzis, S., Veselovskii, I., Amiridis, V., Gröbner, J., Suvorina, A., Nyeki, S., Gerasopoulos, E., Kouremeti, N., Taylor, M., Tsekeri, A., and Wehrli, C.: Aerosol microphysical retrievals from precision filter radiometer direct solar radiation measurements and comparison with AERONET, Atmos. Meas. Tech., 7, 2013– 2025, https://doi.org/10.5194/amt-7-2013-2014, 2014.

Kazadzis, S., Kouremeti, N., Gröbner, J., and Cuevas, E.: Comparisons of Aerosol Optical Depth measurements from different global Networks: the 4th filter radiometer comparison, in: CIMO TECO 2016. Instruments and Observing Methods Report No. 125., 2016.

Kazadzis, S., Kouremeti, N., Diémoz, H., Gröbner, J., Forgan, B. W., Campanelli, M., Estellés, V., Lantz, K., Michalsky, J., Carlund, T., Cuevas, E., Toledano, C., Becker, R., Nyeki, S., Kosmopoulos, P. G., Tatsiankou, V., Vuilleumier, L., Denn, F. M., Ohkawara, N., Ijima, O., Goloub, P., Raptis, P. I., Milner, M., Behrens, K., Barreto, A., Martucci, G., Hall, E., Wendell, J., Fabbri, B. E., and Wehrli, C.: Results from the Fourth WMO Filter Radiometer Comparison for aerosol optical depth measurements, Atmospheric Chemistry and Physics, 18, 3185–3201, doi:10.5194/acp-18-3185-2018, 2018a.

Kazadzis, S., Kouremeti, N., Nyeki, S., Gröbner, J., and Wehrli, C.: The World Optical Depth Research and Calibration Center (WORCC) quality assurance and quality control of GAW-PFR AOD measurements, Geoscientific Instrumentation, Methods and Data Systems, 7, 39–53, doi:10.5194/gi-7-39-2018, 2018b.

Kiedron, P. W. and Michalsky, J. J.: Non-parametric and least squares Langley plot methods, Atmospheric Measurement Techniques, 9, 215–225, doi:10.5194/amt-9-215-2016, 2016.

Kieffer, H. H. and Stone, T. C.: The Spectral Irradiance of the Moon, Astronom. J., 129, 2887–2901, https://doi.org/10.1086/430185, 2005.

Kim, D. H., Sohn, B. J., Nakajima, T., Takamura, T., Take- mura, T., Choi, B. C., and Yoon, S. C.: Aerosol optical properties over east Asia determined from ground-based sky radiation measurements, J. Geophys. Res.-Atmos., 109, D02209, https://doi.org/10.1029/2003JD003387, 2004.

Kim, S.-W., Yoon, S.-C., Dutton, E. G., Kim, J., Wehrli, C., and Holben, B. N.: Global Surface-Based Sun Photometer Network for Long-Term Observations of Column Aerosol Optical Properties: Intercomparison of Aerosol Optical Depth, Aerosol Science and Technology, 42, 1–9, doi:10.1080/02786820701699743, 2008.

King, M. D. and Dubovik, O.: Determination of aerosol optical properties from inverse methods, in: Aerosol Remote Sensing, edited by: Lenoble, J., Remer, L., and Tanré, D., Springer Verlag, Berlin, Heidelberg, 101–136, 2013.

King, M. D., Byrne, D. M., Herman, B. M., and Reagan, J. A.: Aerosol size distributions obtained by the inversion of spectral optical depth measurements, J. Atmos. Sci., 35, 2153–2167, https://doi.org/10.1175/1520- 0469(1978)035<2153:ASDOBI>2.0.CO;2, 1978.

Koelemeijer, R., Homan, C., and Matthijsen, J.: Comparison of spatial and temporal variations of aerosol optical thickness and particulate matter over Europe, Atmos. Environ., 40, 5304–5315, https://doi.org/10.1016/j.atmosenv.2006.04.044, 2006.

Koepke, P., Hess, M., Schult, I., and Shettle, E. P.: Global aerosol data set, MPI Meteorologie Hamburg, Report No. 243, p. 44, 1997.

Kumar, K. R., Sivakumar, V., Reddy, R. R., Gopal, K. R., and Adesina, A. J.: Identification and Classification of Different Aerosol Types over a Subtropical Rural Site in Mpumalanga, South

Africa: Seasonal Variations as Retrieved from the AERONET Sunphotometer, Aerosol Air Qual. Res., 14, 108– 123, https://doi.org/10.4209/aaqr.2013.03.0079, 2014.

Lenoble, J., Mishchenko, M., and Herman, M.: Absorption and scattering by molecules and particles. Aerosol Remote Sensing, in: Aerosol Remote Sensing, edited by: Lenoble, J., Remer, L., and Tanré, D., Springer Verlag, Berlin, Heidelberg, 13–51, 2013.

Li, Z., Goloub, P., Dubovik, O., Blarel, L., Zhang, W., Podvin, T., Sinyuk, A., Sorokin, M., Chen, H., Holben, B., Tanré, D., Canini, M., and Buis, J.-P.: Improvements for ground-based remote sensing of atmospheric aerosol properties by additional polarimetric measurements, J. Quant. Spectrosc. Ra., 110, 1954– 1961, https://doi.org/10.1016/j.jqsrt.2009.04.009, 2009.

Li, Z., Eck, T., Zhang, Y., Zhang, Y., Li, D., Li, L., Xu, H., Hou, W., Lv, Y., Goloub, P., and Gu, X.: Observations of residual submicron fine aerosol particles related to cloud and fog processing during a major pollution event in Beijing, Atmos. Environ., 86, 187–192, https://doi.org/10.1016/j.atmosenv.2013.12.044, 2014.

Liousse, C., Devaux, C., Dulac, F., and Cachier, H.: Aging of savanna biomass burning aerosols: Consequences on their optical properties, J. Atmos. Chem., 22, 1–17, https://doi.org/10.1007/BF00708178, 1995.

Lopatin, A., Dubovik, O., Chaikovsky, A., Goloub, P., Lapyonok, T., Tanré, D., and Litvinov, P.: Enhancement of aerosol characterization using synergy of lidar and sun-photometer coincident observations: the GARRLiC algorithm, Atmos. Meas. Tech., 6, 2065–2088, https://doi.org/10.5194/amt-6-2065-2013, 2013.

Lopatin, A., Dubovik, O., Lapyonok, T., Goloub, P., Litvinov, P., Huang, X., Torres, B., Fuertes, D., and Hu, Q.: Application of GRASP algorithm to combined day and night observations during SHADOW campaign, in: 2nd ACTRIS-2 General meeting, Frascati, 2016.

Lopez-Solano, J. e. a.: Aerosol optical depth in the European Brewer Network, Atmos. Chem. Phys. Discuss., doi:10.5194/acp-2017-1003, 2017.

Loyola R., D. G., Thomas, W., Spurr, R., and Mayer, B.: Global patterns in daytime cloud properties derived from GOME backscatter UV-VIS measurements, International Journal of Remote Sensing, 31, 4295–4318, 2010.

Mallet, M., Dubovik, O., Nabat, P., Dulac, F., Kahn, R., Sciare, J., Paronis, D., and Léon, J. F.: Absorption properties of Mediterranean aerosols obtained from multi-year ground-based remote sensing observations, Atmos. Chem. Phys., 13, 9195–9210, https://doi.org/10.5194/acp-13-9195-2013, 2013.

Mallet, M., Dulac, F., Formenti, P., Nabat, P., Sciare, J., Roberts, G., Pelon, J., Ancellet, G., Tanré, D., Parol, F., Denjean, C., Brogniez, G., di Sarra, A., Alados-Arboledas, L., Arndt, J., Auriol, F., Blarel, L., Bourrianne, T., Chazette, P., Chevaillier, S., Claeys, M., D'Anna, B., Derimian, Y., Desboeufs, K., Di Iorio, T., Doussin, J.-F., Durand, P., Féron, A., Freney, E., Gaimoz, C., Goloub, P., Gómez-Amo, J. L., Granados-Muñoz, M. J., Grand, N., Hamonou, E., Jankowiak, I., Jeannot, M., Léon, J.-F., Maillé, M., Mailler, S., Meloni, D., Menut, L., Momboisse, G., Nicolas, J., Podvin, T., Pont, V., Rea, G., Renard, J.-B., Roblou, L., Schepanski, K., Schwarzenboeck, A., Sellegri, K., Sicard, M., Solmon, F., Somot, S., Torres, B., Totems, J., Triquet, S., Verdier, N., Verwaerde, C., Waquet, F., Wenger, J., and Zapf, P.: Overview of the Chemistry-Aerosol Mediterranean Experiment/Aerosol Direct Radiative Forcing on the Mediterranean Climate (ChArMEx/ADRIMED) summer 2013 campaign, Atmos. Chem. Phys., 16, 455–504, https://doi.org/10.5194/acp-16- 455-2016, 2016.

Martinez-Lozano, J. A., Utrillas, M. P., and Tena, F.: Retrieval of the aerosol size distribution from spectroradiometer measurements at a coastal site in the Mediterranean Sea, Int. J. Remote Sens., 20, 2167–2182, https://doi.org/10.1080/014311699212173, 1999.

Mishchenko, M. I., Travis, L. D., Kahn, R. A., and West, R. A.: Modeling phase functions for dustlike tropospheric aerosols using a shape mixture of randomly oriented polydisperse spheroids, J. Geophys. Res.-Atmos., 102, 16831–16847, https://doi.org/10.1029/96JD02110, 1997.

Mishchenko, M. I., Travis, L. D., and Lacis, A. A.: Scattering, Absorption, and Emission of Light by Small Particles, Cambridge University Press, Cambridge, 1 Edn., 2002.

Mishchenko, M. I., Geogdzhayev, I. V., Rossow, W. B., Cairns, B., Carlson, B. E., Lacis, A. A., Liu, L., and Travis, L. D.: Long-Term Satellite Record Reveals Likely Recent Aerosol Trend, Sci- ence, 315, 1543–1543, https://doi.org/10.1126/science.1136709, 2007.

Mortier, A.: Tendances et variabilités de l'aérosol atmosphérique á l'aide du couplage Lidar/Photometre sur les sites de Lille et Dakar, PhD thesis, Université des Sciences et Technologies de Lille, France, 2013.

Nakajima, T., Tonna, G., Rao, R., Boi, P., Kaufman, Y., and Holben, B.: Use of sky brightness measurements from ground for remote sensing of particulate polydispersions, Applied Optics, 35, 15, 2672–2686, 1996.

O'Neill, N. T., Dubovik, O., and Eck, T. F.: Modified Ångström exponent for the characterization of submicrometer aerosols, Appl. Optics, 40, 2368–2375, https://doi.org/10.1364/AO.40.002368, 2001a.

O'Neill, N. T., Eck, T. F., Holben, B. N., Smirnov, A., Dubovik, O., and Royer, A.: Bimodal size distribution influences on the variation of Angstrom derivatives in spectral and optical depth space, J. Geophys. Res.-Atmos., 106, 9787–9806, https://doi.org/10.1029/2000JD900245, 2001b.

O'Neill, N. T., Eck, T. F., Smirnov, A., Holben, B. N., and Thulasiraman, S.: Spectral discrimination of coarse and fine mode optical depth, J. Geophys. Res.-Atmos., 108, AAC-8-1–AAC-8-15, https://doi.org/10.1029/2002JD002975, 2003.

O'Neill, N. T., Ignatov, A., Holben, B. N., and Eck, T. F.: The lognormal distribution as a reference for reporting aerosol optical depth statistics; Empirical tests using multi-year, multi-site AERONET sunphotometer data, J. Geophys. Res., 27, 3333–3336, 2000.

Perez-Ramirez, D., Ruiz, B., Aceituno, J., Olmo, F. J., and Alados-Arboledas, L.: Application of Sun/star photometry to derive the aerosol optical depth, Int. J. Remote Sens., 29, 5113–5132, https://doi.org/10.1080/01431160802036425, 2008.

Perez-Ramirez, D., Lyamani, H., Olmo, F., and Alados-Arboledas, L.: Improvements in star photometry for aerosol characterizations, J. Aerosol Sci., 42, 737–745, https://doi.org/10.1016/j.jaerosci.2011.06.010, 2011.

Pérez-Ramírez, D., Veselovskii, I., Whiteman, D. N., Suvorina, A., Korenskiy, M., Kolgotin, A., Holben, B., Dubovik, O., Siniuk, A., and Alados-Arboledas, L.: High temporal resolution estimates of columnar aerosol microphysical parameters from spectrum of aerosol optical depth by linear estimation: application to long-term AERONET and star-photometry measurements, Atmos. Meas. Tech., 8, 3117–3133, https://doi.org/10.5194/amt-8- 3117-2015, 2015.

Perry, K. D., Cahill, T. A., Schnell, R. C., and Harris, J. M.: Long-range transport of anthropogenic aerosols to the National Oceanic and Atmospheric Administration baseline station at Mauna Loa Observatory, Hawaii, Journal of Geophysical Research: Atmospheres, 104, 18 521–18 533, doi:10.1029/1998JD100083, 1999.

Prospero, J. M., Schmitt, R., Cuevas, E., Savoie, D. L., Graustein, W. C., Turekian, K. K., Volz-Thomas, A., Díaz, A., Oltmans, S. J., and Levy, H.: Temporal variability of summer-time ozone and aerosols in the free troposphere over the eastern North Atlantic, Geophysical Research Letters, 22, 2925–2928, doi:10.1029/95GL02791, 1995.

Quenzel, H.: Determination of size distribution of atmospheric aerosol particles from spectral solar radiation measurements, J. Geophys. Res., 75, 2915–2921, https://doi.org/10.1029/JC075i015p02915, 1970.

Reid, J. S., Eck, T. F., Christopher, S. A., Hobbs, P. V., and Holben, B.: Use of the Ångstrom exponent to estimate the variability of optical and physical properties of aging smoke particles in Brazil, J. Geophys. Res.-Atmos., 104, 27473–27489, https://doi.org/10.1029/1999JD900833, 1999.

Remer, L. A. and Kaufman, Y. J.: Dynamic aerosol model: Urban/industrial aerosol, J. Geophys. Res.-Atmos., 103, 13859– 13871, https://doi.org/10.1029/98JD00994, 1998.

Rodríguez, S., Alastuey, A., Alonso-Pérez, S., Querol, X., Cuevas, E., Abreu-Afonso, J., Viana, M., Pérez, N., Pandolfi, M., and de la Rosa, J.: Transport of desert dust mixed with North African industrial pollutants in the subtropical Saharan Air Layer, Atmospheric Chemistry and Physics, 11, 6663–6685, doi:10.5194/acp-11-6663-2011, 2011.

Rodríguez-Franco, J. J. and Cuevas, E.: Characteristics of the subtropical tropopause region based on long-term highly resolved sonde records over Tenerife, Journal of Geophysical Research, 118, 10 754–10 769, 2013.

Rohen, G. J., von Hoyningen-Huene, W., Kokhanovsky, A., Dinter, T., Vountas, M., and Burrows, J. P.: Retrieval of aerosol mass load (PM10) from MERIS/Envisat top of atmosphere spectral reflectance measurements over Germany, Atmos. Meas. Tech., 4,523–534, https://doi.org/10.5194/amt-4-523-2011, 2011.

Russell, P. B., Livingston, J. M., Pueschel, R. F., Reagan, J. A., Browell, E. V., Toon, G. C., Newman, P. A., Schoeberl, M. R., Lait, L. R., Pfister, L., Gao, Q., and Herman, B. M.: Post-Pinatubo optical depth spectra vs. latitude and vortex structure: Airborne tracking sunphotometer measurements in AASE II, Geophysical Research Letters, 20, 2571–2574, doi:10.1029/93GL03006, 1993.

Schmid, B., Redemann, J., Russell, P. B., Hobbs, P. V., Hlavka, D. L., McGill, M. J., Holben, B. N., Welton, E. J., Campbell, J. R., Torres, O., Kahn, R. A., Diner, D. J., Helmlinger, M. C., Chu, D. A., Robles-Gonzalez, C., and de Leeuw, G.: Coordinated airborne, spaceborne, and ground-based measurements of massive thick aerosol layers during the dry season in southern Africa, J. Geophys. Res.-Atmos., 108, D138496, https://doi.org/10.1029/2002JD002297, 2003.

Shaw, G.: Error analysis of multi-wavelength sun photometry, Pure and Applied Geophysics, 114, 1–14, 1976.

Shaw, G. E.: Aerosols at Mauna Loa: Optical Properties, Journal of the Atmospheric Sciences, 36, 862–869, 1979.

Shaw, G. E.: Sun photometry, Bull. Am. Meteorol. Soc., 64, 4–10, 1983.

Schuster, G. L., Dubovik, O., and Holben, B. N.: Angstrom exponent and bimodal aerosol size distributions, J. Geophys. Res.-Atmos., 111, D07207, https://doi.org/10.1029/2005JD006328, 2006.

Shaw, G. E.: Sun photometry, B. Am. Meteorol. Soc., 64, 4–10, https://doi.org/10.1175/1520-0477(1983)064<0004:SP>2.0.CO;2, 1983.

Shaw, G. E., Reagan, J. A., and Herman, B. M.: Investigations of Atmospheric Extinction Using Direct Solar Radiation Measurements Made with a Multiple Wavelength Radiometer, J. Appl. Meteorol., 12, 374–380, https://doi.org/10.1175/1520-0450(1973)012<0374:IOAEUD>2.0.CO;2, 1973.

Shettle, E. P. and Fenn, R. W.: Models for the aerosols of the lower atmosphere and the effects of humidity variations on their optical properties, Tech. rep., AFGL-TR-79-0214, Environ. Res. Paper 676, Air Force Cambridge Res. Lab., 1979.

Slusser, J., Gibson, J., Bigelow, D., Kolinski, D., Disterhoft, P., Lantz, K., and Beaubien, A.: Langley method of calibrating UV filter radiometers, Journal of Geophysical Research: Atmospheres, 105, 4841–4849, doi:10.1029/1999JD900451, 2000.

Smirnov, A., Holben, B., Eck, T., Dubovik, O., and Slutsker, I.: Cloud-screening and quality control algorithms for the AERONET database, Remote Sens. Environ., 73, 337–349, https://doi.org/10.1016/S0034-4257(00)00109-7, 2000.

Smirnov, A., Holben, B. N., Kaufman, Y. J., Dubovik, O., Eck, T. F., Slutsker, I., Pietras, C., and Halthore, R.: Optical properties of atmospheric aerosol in maritime environments, J. Atmos. Sci., 59, 501–523, https://doi.org/10.1175/1520- 0469(2002)059<0501:OPOAAI>2.0.CO;2, 2002a.

Smirnov, A., Holben, B. N., Dubovik, O., O'Neill, N. T., Eck, T. F., Douglas, L. W., Andreas, K. G., Pietras, C., and Slutsker, I.: Atmospheric Aerosol Optical Properties in the Persian Gulf, J. Atmos. Sci., 59, 620–634, https://doi.org/10.1175/1520-0469(2002)059<0620:AAOPIT>2.0.CO;2, 2002b.

Smirnov, A., Holben, B. N., Slutsker, I., Giles, D. M., McClain, C. R., Eck, T. F., Sakerin, S. M., Macke, A., Croot, P., Zibordi, G., Quinn, P. K., Sciare, J., Kinne, S., Harvey, M., Smyth, T. J., Piketh, S., Zielinski, T., Proshutinsky, A., Goes, J. I., Nelson, N. B., Larouche, P., Radionov, V. F., Goloub, P., Krishna Moorthy, K., Matarrese, R., Robertson, E. J., and Jourdin, F.: Maritime Aerosol Network as a component of Aerosol Robotic Network, J. Geophys. Res.-Atmos., 114, D06204, https://doi.org/10.1029/2008JD011257, 2009.

Takamura, T., Nakajima, T., and SKYNET community group: Overview of SKYNET and its activities, Optica Pura y Aplicada, 37, 3303–3308, 2004.

Tanre, D., Deschamps, P. Y., Devaux, C., and Herman, M.: Estimation of Saharan aerosol optical thickness from blurring effects in thematic mapper data, J. Geophys. Res.-Atmos., 93, 15955–15964, https://doi.org/10.1029/JD093iD12p15955, 1988.

Toledano, C., Cachorro, V. E., Berjon, A., de Frutos, A. M., Sorribas, M., de la Morena, B. A., and Goloub, P.: Aerosol optical depth and Ångström exponent climatology at El Arenosillo AERONET site (Huelva, Spain), Q. J. Roy. Meteor. Soc., 133, 795–807, https://doi.org/10.1002/qj.54, 2007.

Toledano, C., Cachorro, V. E., de Frutos, A. M., Torres, B., Berjon, A., Sorribas, M., and Stone, R. S.: Air mass classification and analysis of aerosol types at El Arenosillo (Spain), J. Appl. Meteorol. Clim., 48, 962–981, https://doi.org/10.1175/2008JAMC2006.1, 2009.

Toledano, C., Cachorro, V., Gausa, M., Stebel, K., Aaltonen, V., Berjón, A., de Galisteo, J. O., de Frutos, A., Bennouna, Y., Blindheim, S., Myhre, C., Zibordi, G., Wehrli, C., Kratzer, S., Hakansson, B., Carlund, T., de Leeuw, G., Herber, A., and Torres, B.: Overview of sun photometer measurements of aerosol properties in Scandinavia and Svalbard, Atmos. Environ., 52, 18–28, https://doi.org/10.1016/j.atmosenv.2011.10.022, 2012.

Torres, B.: Study on the influence of different error sources on sky radiance measurements and inversion-derived aerosol products in the frame of AERONET, PhD thesis, Universidad de Valladolid, https://uvadoc.uva.es/bitstream/10324/978/1/ TESIS171-120611.pdf (last access: 2 October 2017), 2012.

Torres, B., Dubovik, O., Toledano, C., Berjon, A., Cachorro, V. E., Lapyonok, T., Litvinov, P., and Goloub, P.: Sensitivity of aerosol retrieval to geometrical configuration of ground-based sun/sky

radiometer observations, Atmos. Chem. Phys., 14, 847– 875, https://doi.org/10.5194/acp-14-847-2014, 2014.

Van de Hulst, H.: Light Scattering by Small Particles, Structure of Matter Series, John Wiley & Sons, 1957.

Van Donkelaar, A., Martin, R. V., Brauer, M., Kahn, R., Levy, R., Verduzco, C., and Villeneuve, P. J.: Global Estimates of Ambient Fine Particulate Matter Concentrations from Satellite-Based Aerosol Optical Depth: Development and Application, Environ. Health Persp., 118, 847–855, https://doi.org/10.1289/ehp.0901623, 2010.

Van Donkelaar, A., Martin, R. V., Brauer, M., Hsu, N. C., Kahn, R. A., Levy, R. C., Lyapustin, A., Sayer, A. M., and Winker, D. M.: Global Estimates of Fine Particulate Matter using a Combined Geophysical-Statistical Method with Information from Satellites, Models, and Monitors, Environ. Sci. Technol., 50, 3762–3772, https://doi.org/10.1021/acs.est.5b05833, 2016.

Vermeulen, A., Devaux, C., and Herman, M.: Retrieval of the scattering and microphysical properties of aerosols from ground-based optical measurements including polarization. I. Method, Appl. Optics, 39, 6207–6220, https://doi.org/10.1364/AO.39.006207, 2000.

Veselovskii, I., Dubovik, O., Kolgotin, A., Korenskiy, M., Whiteman, D. N., Allakhverdiev, K., and Huseyinoglu, F.: Linear estimation of particle bulk parameters from multi-wavelength lidar measurements, Atmos. Meas. Tech., 5, 1135–1145, https://doi.org/10.5194/amt-5-1135-2012, 2012.

Veselovskii, I., Whiteman, D. N., Korenskiy, M., Kolgotin, A., Dubovik, O., Perez-Ramirez, D., and Suvorina, A.: Retrieval of spatio-temporal distributions of particle parameters from multi-wavelength lidar measurements using the linear estimation technique and comparison with AERONET, Atmos. Meas. Tech., 6, 2671–2682, https://doi.org/10.5194/amt-6-2671-2013, 2013.

Vidot, J., Santer, R., and Ramon, D.: Atmospheric particulate matter (PM) estimation from SeaWiFS imagery, Remote Sens. Environ., 111, 1–10, https://doi.org/10.1016/j.rse.2007.03.009, 2007.

Wang, Y., Fan, S., Feng, X., Yan, G., and Guan, Y.: Regularized inversion method for retrieval of aerosol particle size distribution function in W1,2 space, Appl. Optics, 45, 7456–7467, https://doi.org/10.1364/AO.45.007456, 2006.

Wehrli, C.: GAW–PFR: A network of Aerosol Optical Depth observations with Precision Filter Radiometers. In: WMO/GAW Experts workshop on a global surface based network for long term observations of column aerosol optical properties, Tech. rep., GAW Report No. 162, WMO TD No. 1287, 2005.

Wehrli, C. J.: Remote Sensing of Aerosol Optical Depth in a global surface network, Ph.D. thesis, ETH ZURICH, 2008.

Whitby, K. T.: Proceedings of the International Symposium The physical characteristics of sulfur aerosols, Atmos. Environ., 12, 135–159, https://doi.org/10.1016/0004-6981(78)90196-8, 1978.

WMO: WMO/GAW Experts Workshop on a Global Surface-based Network for Long Term Observations of Column Aerosol Optical Properties, GAW Report 162, WMO/TD-No 1287, Davos 2004, edited by: Baltensperger, U., Barries, L., and Wehrli, C., available at: http://library.wmo.int/pmb_ged/wmo-td_1287.pdf, 2005.

Yamamoto, G. and Tanaka, M.: Determination of Aerosol Size Distribution from Spectral Attenuation Measurements, Appl. Optics, 8, 447–453, https://doi.org/10.1364/AO.8.000447, 1969.